Hydrogen-induced Intergranular Fracture of Aluminum-Magnesium Alloys

Édouard Pouillier

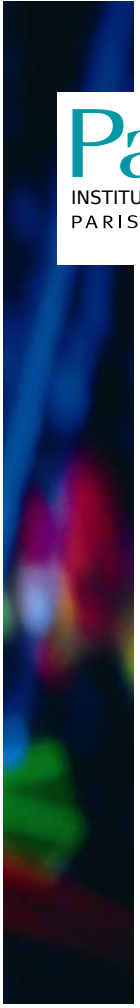

ParisTech
INSTITUT DES SCIENCES ET TECHNOLOGIES
PARIS INSTITUTE OF TECHNOLOGY

MINES ParisTech

École doctorale n° 432:
Sciences des Métiers de l'Ingénieur

Doctorat ParisTech

T H È S E

pour obtenir le grade de docteur délivré par

l'École nationale supérieure des mines de Paris

Spécialité Sciences et Génie des Matériaux

présentée et soutenue publiquement par

Édouard POUILLIER

le 16 décembre 2011

Hydrogen-Induced Intergranular Fracture Of Aluminium-Magnesium Alloys

~ ~ ~

Rupture Intergranulaire Induite Par l'Hydrogène Dans Les Alliages Aluminium-Magnesium

Directeurs de thèse: **Esteban P.BUSSO**
Anne-Françoise GOURGUES

Jury

M. François HILD, Directeur de recherche CNRS, LMT Cachan	Président
Mme Monique GASPERINI, Professeur, Université Paris XIII	Rapporteur
M. Noel O'DOWD, Professeur, University of Limerick	Rapporteur
M. Michel BORNERT, Enseignant chercheur, École des Ponts	Examinateur
Mme Anne-Françoise GOURGUES, Professeur, Centre des Matériaux, Mines ParisTech	Examinateur
M. Esteban P. BUSSO, Professeur, Centre des Matériaux, Mines ParisTech	Examinateur

T H È S E

MINES ParisTech
Centre des Matériaux
BP 87, F-91003 Evry cedex, FRANCE

Résumé

Cette étude couplant à la fois des moyens expérimentaux et numériques a eu pour but de caractériser et de modéliser l'influence de la déformation plastique à l'échelle des cristaux sur la rupture intergranulaire dans un alliage d'aluminium préalablement fragilisé par l'hydrogène. Des travaux antérieurs à cette étude ont montré que ce type de rupture peut être interprété comme une conséquence de la concentration de déformation au joint de grains due à la déformation plastique des grains. Néanmoins les mécanismes microstructuraux intervenant dans ce phénomène de rupture restent à ce jour mal définis. C'est pour cette raison qu'une procédure expérimentale a été mise en place pour obtenir sur une même surface, à la fois les champs de déformation locaux et l'orientation cristalline des grains constituant cette surface.

Les résultats obtenus ont permis de mettre en avant le mécanisme majeur intervenant dans ce type de rupture, à savoir que la rupture d'un joint est due à une configuration particulière de son voisinage. En effet les résultats de mesure des champs de déformation montrent que les grains présentant une orientation propice à la déformation vis-à-vis de la sollicitation favorisent l'amorçage de fissures dans les joints de grains adjacents. De manière plus générale, les premières fissures s'amorcent entre des grains qui se déforment peu ou pas dans un environnement granulaire relativement déformé. Ces joints de grains vont de fait subir des contraintes intergranulaires particulièrement élevées. Fort de ces observations expérimentales, un critère de rupture basé sur la contrainte normale au joint de grains a pu être proposé. Dans le but d'obtenir la valeur de contrainte limite donnant lieu à la rupture intergranulaire, des simulations numériques sur les surfaces étudiées précédemment ont été entreprises. Pour cela les surfaces étudiées par EBSD puis en traction in-situ dans un MEB ont été digitalisées puis maillées. Le comportement des grains a été modélisé à l'aide d'un modèle de plasticité cristalline préalablement calibré sur des essais de traction simple. Les conditions aux limites des calculs ont été extraites des champs de déplacements mesurés expérimentalement.

Ces simulations ont permis d'évaluer une contrainte seuil de l'ordre de 175 MPa pour laquelle les premiers joints de grains fissurent. Cette contrainte a ensuite été utilisée dans une loi de type zone cohésive pour décrire le comportement à rupture des joints de grains. L'énergie à rupture a été choisie en fonction des résultats des calculs d'atomistique menés à l'intérieur de l'ANR H-Inter. Les résultats numériques décrivent correctement les phénomènes observés expérimentalement. L'ensemble des simulations réalisées en 2D ne considérent que les surfaces étudiées expérimentalement. Afin de prendre en compte les effets de substrat, des modélisations de microstructures en 3D ont été réalisées. Ces modélisations ont principalement permis de confirmer le mécanisme de rupture intergranulaire identifié expérimentalement.

Mots clées: Rupture intergranulaire, Alliage d'aluminium, Fragilisation par hydrogène, Essais in-situ, Plasticité cristalline, Zone cohésive, Microstructure 3D

Abstract

Aluminium alloys that are strengthened by alloying elements in solid solution may present a particular sensitivity to intergranular stress corrosion cracking as a result of intergranular dissolution. In Al-5Mg alloys such as AA5083, precipitation of the β-phase (Al_3Mg_2) at grain boundaries strongly favours intergranular fracture. Previous experimental studies revealed that local plasticity seems to play a significant role in crack initiation. Nevertheless, the exact role of crystal plasticity in the vicinity of grain boundaries is not well understood. The main goals of this doctoral thesis are: (i) to study the role of the local stress and strain fields on the mechanism of intergranular stress corrosion cracking and, based on such understanding, (ii) to develop a micro-mechanics based model to predict the onset of grain boundary cracking and the subsequent intergranular crack propagation.

An experimental procedure based on in-situ tensile tests within the chamber of an scanning electron microscope was developed to measure the evolution of local strain fields at various microstructural scales and of lattice orientation using digital image correlation and electron backscatter diffraction (EBSD) techniques, respectively. Digital image correlation techniques were used over areas comprising just a few grains up to mesoscopic regions of the polycrystal to quantify the strain fields required in the multi-scale study of intergranular fracture. From these observations, it was established that interfaces between two grains which have undergone little amount of deformation but lying within a neighbourhood of significantly deformed grains are the first to develop micro-cracks. In addition, X-Ray tomography and serial EBSD sectioning analyses revealed that cracked grain boundaries were perpendicular to the applied tensile load, where maximum tensile tractions are expected.

To determine the role of local stresses and local plasticity on the mechanisms of intergranular fracture, a dislocation mechanics based crystal plasticity model was employed to describe the constitutive behaviour of each grain in the finite element model of the in-situ experiments. The model parameters were calibrated as a function of the solid solution magnesium content in the aluminium alloy. Measured EBSD maps were relied upon to define the orientation of the discrete grain regions of the in-situ specimens in the corresponding multi-scale finite element (FE) models. From the FE results, a range of threshold values of the normal grain boundary tractions needed to initiate intergranular cracks was identified. This finding is in close agreement with the predictions from an analytical solution of a simplified model of intergranular cracking based on an extension of Eshelby's theory for inclusions. Finally, a cohesive zone model calibrated with the critical grain boundary tractions and typical surface energies was added to the FE model of the polycrystal. A comparison between the experimental and numerical results reveals a good agreement with the observed experimental cracking pattern.

Keywords: Intergranular fracture, Aluminium alloys, Hydrogen embrittlement, In situ tensile tests, Crystal plasticity modelling, Cohesive zone, Microstructure 3D

Remerciements

Ma première pensée va vers mes deux directeurs de thèse, Esteban Busso et Anne-Françoise Gourgues, que je remercie très chaleureusement pour m'avoir fait confiance tout au long de ma thèse. En plus de leur grande expertise, de la justesse de leur analyse qu'ils ont su me communiquer et dont je profite chaque jour, j'aimerais saluer leur qualité humaine.

Son énergie incroyable, son engagement quotidien, sa gentillesse et sa disponibilité font d'Anne-Françoise une personne à part avec qui je suis honoré d'avoir travaillé. Le pragmatisme et la sagesse qu'incarne Esteban font souvent de ses conseils de véritables leçons de vie. Ils resteront pour moi des exemples à suivre au cours de ma carrière professionnelle.

Je souhaite remercier également Monique Gasperini et Noel O'Dowd d'avoir accepté d'être les rapporteurs de mon manuscrit, malgré les délais impartis. Merci à François Hild d'avoir présidé mon jury de soutenance et bravo à lui de laisser les sources de Correli en libre accès, cela m'a permis d'obtenir des résultats de grandes qualités. Je tiens aussi à remercier André Pinneau qui, par ses remarques a été un acteur important de ma thèse.

Ce travail a été financé dans le cadre d'une ANR blanche en partenariat avec les Mînes de St Etienne et l'Institut National des Sciences Appliquées de Lyon. Je tiens, d'une part, à remercier tous les acteurs de ce consortium, en particulier, les créateurs de ce projet ambitieux Esteban Busso et David Delafosse. Et d'autre part, je souhaite adresser un grand merci au responsable de ce projet Döme Tanguy, et à son équipe, Claire, Martial et Johan, pour m'avoir chaleureusement accueilli à St Etienne et aidé dans la préparation épique de mes petites éprouvettes.

Je remercie également le personnel du Centre des Matériaux pour son excellent travail et le cadre propice à la réflexion qu'ils m'ont ouvert. Je tiens notamment à citer Grégory et Olivier les funambules du cluster, Liliane et Véronique pour leur gentillesse et leur assistance indispensable. Un très grand merci à Konaly pour sa réactivité et sa bienveillance.

Une attention particulière pour le professionnalisme et l'enthousiasme de Franck N'Guyenne et de Maria Betbeder qui ont cru en mes projets qui semblaient trop optimistes mais qui ont pu être concrétisé grâce à eux.

Un grand merci à Antoine et Clara pour leur aide précieuse dans les moments critiques, mais aussi pour les instants de discussions et de rigolade. Ces années de thèse ont été très agréables grâce à la formidable ambiance du CdM entretenue par l'ensemble du personnel et surtout de l'atelier. Je souhaite plein de bonnes choses aux personnes avec qui j'ai passé ces trois ans et demi au CDM. Je pense en particulier, à Bahram, Guillaume, Sergei, Nicolas, Ozgur, Joao, Angélique, melkior, jadmel, Kais, Martin, Marc, Jean-Didier, Florian, Yohann, Vlad, Benoit, Clémence, Huaidong, Jianqiang, Laurent, Lingtao et tous les autres.

Je remercie ma famille et tout particulièrement mes parents et ma soeur pour m'avoir toujours soutenu dans mes choix et cela malgré les inconvénients occasionnés. C'est un cadeau

inestimable que j'ai reçu en étant continûment encouragé pendant les périodes difficiles.

Pour finir, j'adresse toute mon affection à Audrey, soutien logistique et moral indispensable pendant cette longue période de rédaction. Je la remercie tendrement pour son dynamisme et sa joie de vivre inébranlable qui nous unis.

Contents

List of Figures

List of Tables

Chapter 1

Introduction

Contents

1.1 Environment-Assisted Cracking of Aluminium Alloys

Aluminium and its alloys are widely used for their excellent mechanical properties and lightweight, and are well known for their good electrical and thermal conductivity, non toxicity and corrosion resistance. Consequently, the use of these alloys has greatly increased these last 10 years. Common applications are seen in the automotive industry, aeronautics, packaging and many others. Nevertheless, the resulting aluminium reacts quickly with oxygen, but fortunately, aluminium oxide is highly stable. Even if the oxide film is very thin (1-2 nm), it is very compact and may be considered as a strong barrier against environmental or chemical attacks. However, aluminium corrodes without the formation of a stable oxide film. In this particular state, and under a tensile stress, some aluminium alloys may exhibit stress corrosion cracking (SCC). The SCC mechanism is complex because it involves metallurgical, mechanical and chemical phenomena. SCC is known to lead to brittle fracture that initiates generally along grain boundaries.

Only those aluminium-alloys that exhibit precipitation of intermetallic phases can be affected by SCC. Another condition is that the microstructure makes the alloy sensitive to SCC. Theoretically, heat treatments that lead to the precipitation of uniformly distributed precipitates within the grains are acceptable. Precipitates lay essentially at grain boundaries and favour SCC, especially if they are closely spaced thus creating a semi-continuous or continuous network along grain boundaries. The main factors affecting SCC are the amplitude and duration of residual stress (following cooling, welding), grain size distribution, the principal stress directions and the environment (low pH, high concentration in chlorides). SCC of high strength aluminium alloys such as 2024, 7075 and 7079 is also enhanced by residual stresses and stress concentrations (around assemblies parts like rivets see Figure 1.1).

Only tensile loading triggers SCC if the stress magnitude is high enough. As a consequence, for each system (alloy sensitivity with a specific environment), there is a threshold stress that must be overcome to trigger SCC. The cause of some brittle fracture events in aluminium alloys has been attributed to hydrogen induced embrittlement (HIE) (Zapffe and Sims 1941). The resulting damage can lead to transgranular or intergranular fracture.

Figure 1.1: Example of corrosion occurred in 1988 on an aircraft flying between the Hawaiian islands. This disaster prompted the aircraft industry to investigate SCC phenomenon involved near sea environments (http://www.securiteaerienne.com).

1.2 Hydrogen Induced Embrittlement (HIE) Mechanisms

Hydrogen embrittlement is one of the most important causes of brittle fracture in mechanical parts in industry. Sources of hydrogen production causing embrittlement can be:

- Hydrogen produced during manufacturing or during heat treatments and welding.
- Use of the alloy in a gaseous environment containing hydrogen or hydrogenated compounds.
- Hydrogen produced by electrolytic reactions (e.g. surface treatments, cathodic protection).
- Hydrogen produced by corrosion (e.g. in aqueous environment).

In addition, local conditions associated with HIE involve complex material features (chemical composition, microstructure), the surrounding environment (gas, aqueous environment, temperature) and mechanical loading (applied static, dynamic, cyclic). Figure 1.2, shows a global description of hydrogen induced embrittlement interaction aspects.

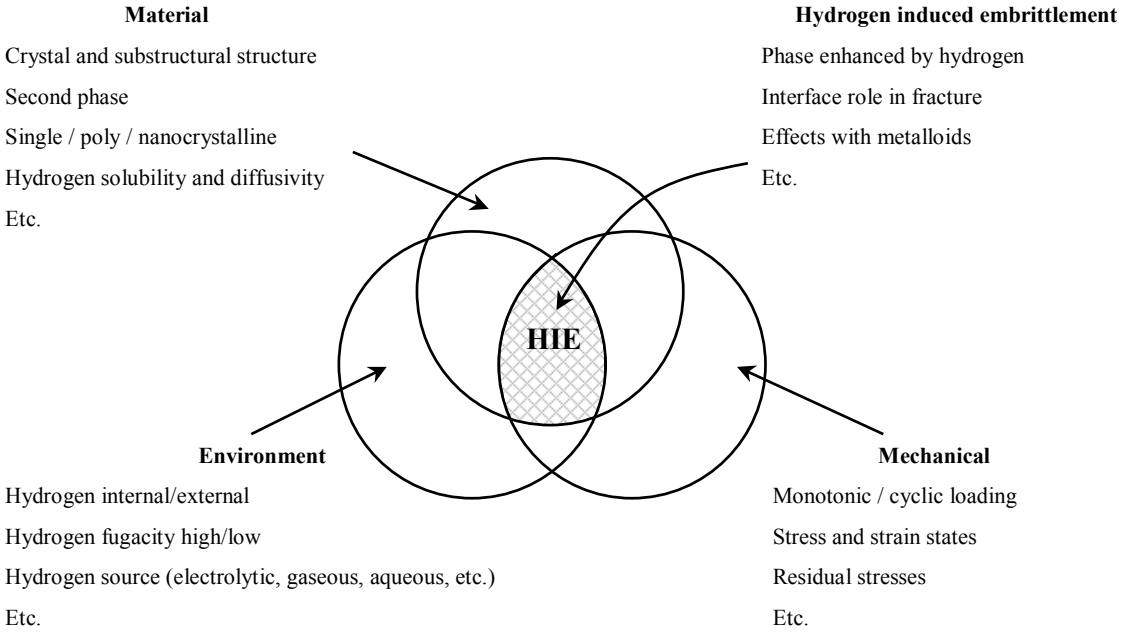

Figure 1.2: Global description of HIE interaction aspects.

Despite extensive studies since the 19th century (Johnson 1875), mechanisms of hydrogen induced embrittlement remain unclear. Several mechanisms are well understood, each one being supported by sets of experimental observations. While studies based on in-situ electron microscopy experiments and atomistic simulations of hydrogen in discrete lattices have been complementary, the majority have tended toward separate paths regarding fracture mechanisms. Moreover, some experimental studies focus on the failure behaviour of the bulk material. Three basic mechanisms associated with hydrogen embrittlement are distinguished at very local scale. (a) The first one is mostly concerned with hydrides. However, the present studied case is not concerned by hydride-induced embrittlement mechanism(s), therefore

these mechanisms will not be developed in the following overview of mechanisms of hydrogen induced embrittlement. (b) hydrogen enhanced decohesion (HEDE) that has been studied for since the sixties and (c) hydrogen enhanced localised plasticity (HELP) has been studied more recently despite the fact that Beachem (1976) discussed this phenomena thirty years ago.

1.2.1 Hydrogen solubility, diffusivity and trapping in metals

From a fundamental point of view, hydrogen embrittlement appears to be largely controlled by solubility, diffusivity and trapping phenomena. The role of the microstructure defects and, among them, of the grain boundaries, is very important in the description of the mechanism of hydrogen embrittlement.

1.2.1.1 Hydrogen solubility and diffusivity

Hydrogen dissolves in all metals to a moderate extent. It is a very small atom, and fits in between the metal atoms in the crystal (see Figure 1.3). Consequently, it can diffuse much more rapidly than larger atoms. For example, the diffusion coefficient for hydrogen in ferritic steels at room temperature is similar to that of salt in water. Hydrogen tends to be attracted to regions of high tensile stresses where the metal structure is deformed, due to a high defect concentration (e.g. dislocations). Thus, it tends to diffuse toward the regions ahead of crack tips or notches that are under stress. Dissolved hydrogen then assists the fracture of the metal, possibly by making cleavage easier or by assisting the development of intense local plastic strains. These effects lead to embrittlement of the metal; cracking may be either inter- or transgranular. Crack growth rates can be relatively fast, up to 1 mm per second in the most extreme cases.

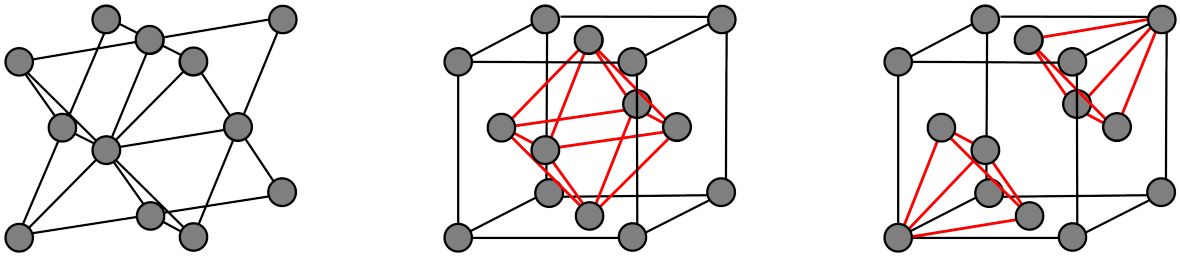

(a) (b) (c)

Figure 1.3: (a) tetrahedral sites for a face centred cubic structure, (b) and (c) octahedral and tetrahedral interstitial sites, respectively.

1.2.1.2 Hydrogen trapping

The interactions of hydrogen with lattice imperfections, such as dislocations, stacking faults, surfaces, and microcracks, determine its influence on the mechanical properties of a material. However, these interactions are far less well understood at a fundamental level than the behaviour of hydrogen in perfect crystals. In order to obtain HIE, hydrogen must be trapped by crystallographic defects in the material. It is generally admitted that there are two types of traps, low energy and irreversible traps (Vehoff and Klameth 1985). Low energy traps are constituted by dislocations (Caron 2000). Rios et al. (1995) and Magnin et al. (1996) agree that the hydrogen quantity absorbed in nickel base alloy 600 is directly linked to the imposed stress on the material and observed that the maximum quantity of

hydrogen is located at the crack tip. Concerning the irreversible traps, Shewmon (1985) states that it is due to internal surfaces (microcracks or small holes). Hydrogen can also be trapped at metal/oxide interfaces and at oxide defects resulting from a hydroxide bound (O-H) between oxygen and hydrogen (Caron 2000). Concerning, the relationship between grain boundary precipitates and hydrogen embrittlement, it can be considered that: (i) Hydrogen has a strong tendency to segregate at grain boundaries. Consequently, the solubility and the mobility of hydrogen are modified with respect to those in the bulk (ii) Interactions between intergranular precipitation of alloying elements and mobile hydrogen atoms can modify the hydrogen embrittlement susceptibility of the material.

1.2.2 Hydrogen enhanced local plasticity (HELP)

The most striking experimental observation is that hydrogen significantly increases dislocation mobility under constant stress (Birnbaum and Sofronis 1994). This hydrogen-enhanced mobility is observed for screw, edge, and mixed dislocations as well as for isolated dislocations and entangled dislocations. Other important experimental results include the observations of slip planarity and strong binding between hydrogen and dislocation cores. Theoretically, it has been proved (Takeda and McMahon 1981) within the framework of the Peierls-Nabarro model that the presence of hydrogen in pure aluminium can dramatically enhance dislocation mobility and inhibit dislocation cross slip.

Another important aspect of the behaviour of hydrogen in aluminium is the thermodynamics of H in bulk aluminium and on its {111} planes. The stability and mobility of hydrogen impurities in aluminium and aluminium alloys play an important role in HELP and more generally on HIE.

In their studies, Lu et al. (2002; 2001) and Lu and Kaxiras (2005) have computed the interaction of interstitial H with dislocations in pure aluminium using the Semi-discrete Variational Peierls Nabarro model (SVPN) with ab-initio determined parameters. They found that hydrogen can decrease the Peierls stress of dislocations by more than 50%, strongly supporting the HELP model. Additionally they noticed a strong binding of H to dislocation cores but also that the binding energy was a function of dislocation character. Their findings explain the experimentally observed restriction of cross-slip and slip planarity in the presence of hydrogen. The dislocations do not dissociate into partials even though the intrinsic stacking fault energy is reduced by 40% in the presence of hydrogen. Finally, based on the results of their calculations, they identified the following processes that could lead to HIE:

(a) H is attracted to crack tips: application of external stress produces local concentration of tensile stress in the vicinity of cracks. The captured hydrogen atoms tend to stay in slightly enlarged interstitial sites.

(b) Thinning and softening: these segregated H impurities at the crack tip can facilitate dislocation generation and enhance dislocation mobility. It will lead to an extensive plastic strains in front of the crack, causing thinning and softening of the material ahead of the crack.

(c) Lowering fracture stress: the thinning and softening processes, along with the localization of slip due to the inhibition of cross-slip, allow the crack to propagate at lower stress levels, prior to general yielding away from the crack tip.

1.2.3 Hydrogen-enhanced decohesion (HEDE)

The HEDE model is one of the first models to have been used to represent the change of properties as a result of hydrogen atom diffusing in the metal lattice. It was described first by Zapffe and Sims (1941). It is based on the increased solubility of hydrogen in a tensile strength field, for instance at the tip of a crack, in areas with internal tensile strength or in the tensile field of edge dislocations. The increased solubility of hydrogen in this tensile field results in a decrease in the atom binding forces of the metal lattice.

Birnbaum (1994) observed in a α-Ti that under a threshold bulk hydrogen concentration in the metal bulk of α-Ti, this alloy exhibits a ductile behaviour. When the hydrogen concentration becomes greater than a critical level, the material becomes brittle. They observed that the fracture mode also changes when crossing this limit. It goes from ductile microvoid coalescence to transgranular cleavage failure. The cleavage facets show evidence of plasticity in the form of slip bands, small dimples and a high density of dislocations in the vicinity of the fracture surface. During the experiments, Birnbaum (1994) found that there is no measurable changes in the Young's modulus, but the 0.2% yield strength and the fracture toughness decrease with increasing oxygen concentration.

The application of stress results either in premature brittle fracture along the grain boundaries or in weakning at lattice levels (transgranular cleavage) owing to the decrease in binding energy. In Vehoff and Rothe (1983), the mechanism is interpreted in terms of fracture energy. This energy can include the influence of elastic distortion of the two half solids, but it does not include inelastic effects. This mechanism is mainly supported by the observation that in some non-hydride forming systems, hydrogen embrittlement appears to occur in the absence of significant local strain (theoretical calculation of the effect of hydrogen on the atomic potentials and by thermodynamic arguments). However direct evidence for this mechanism has not been obtained. Measurements made on the effects of hydrogen under small strain suggest no decrease in the lattice potential.

The observed binding forces decrease and energy changes during segregation of hydrogen in interfaces and surfaces lead one to expect only a very small decrease of the separation energy due to hydrogen during transgranular fracture. A substantially larger decrease during intergranular fracture in cases where hydrogen segregation to the grain boundaries has taken place. Direct experimental characterization of this effect is currently lacking. Such weakning is in competition with hydrogen enhanced plasticity, and fractography and metallographic studies indicate that the latter process frequently intervenes, even when fracture apparently occurs along grain boundaries. The decohesion mechanism has been unambiguously observed, however, in systems where hydrogen and other embrittling solute atoms co-segregate at boundaries.

Other authors used the HEDE approach for the calculation of the cohesive energy. Van der Ven and Ceder (2003) have defined thermodynamic variables to express a "cohesive zone" that is characterised by a thermodynamic formulation. On the other hand, Tanguy et al. (2008) reported a global method to estimate the decohesion energy in case of hydrogen induced decohesion.

1.2.4 β-Mg phase precipitation and its effect on hydrogen-induced cracking

Aluminium alloys, strengthened by elements in solid solution, can be sensitive to intergranular stress corrosion cracking (ISCC) in some specific microstructural states (Hollinsworth and Hunsicker 1987). Initially, the mechanism thought to lead to ISCC was stress assisted localised dissolution (Dix 1940). It was supported by microstructural observations showing that Mg-rich (Al_3Mg_2 β-phase) precipitates form at grain boundaries during ageing. Figure 1.4 shows the corresponding Al-Mg equilibrium phase diagram. Here, locally enhanced Mg concentration was thought to create an electrochemical potential inhomogeneity that induced the anodic dissolution of the precipitate and, in so-doing, creating a preferential crack path. This understanding prevailed till the early seventies (Gest and Troiano 1974) when the crucial role of hydrogen in the fracture process was identified. Then, it was found that when a certain amount of hydrogen is absorbed from the environment into materials such as steels, it can then diffuse along grain boundaries and eventually lead to their embrittlement.

Initially, the effect of hydrogen contamination in aluminium alloys was ignored due to the vanishingly small solubility of hydrogen when the metal is in contact with the H_2 gas. Nevertheless, it was shown that a hydrogen flux can develop through Al-Zn-Mg alloys (Gest and Troiano 1974) even with a free corrosion potential. It was shown unambiguously later on (Gruhl 1984) that hydrogen can diffuse over depths of some millimeters toward regions of high stress triaxialities (e.g. notch tip region), be trapped at grain boundaries and induce intergranular fracture without any contribution of corrosion processes that may be active at the crack tip. The precise nature of "brittle" fracture, i.e. decohesion vs intense localised plasticity, is still debated nowadays. In the specific case of Al-Zn-Mg, TEM studies by Scamans et al. (Scamans et al. 1976, Scamans 1978) show that it is a true intergranular weakning mechanism (see also (Malis and Chaturvedi 1982)).

The β intergranular precipitates play multiple roles in the stress corrosion cracking (SCC) of Al-Mg alloys. It was shown (Jones et al. 2001; 2004) that they dissolve actively during SCC and that enough hydrogen must have produced to embrittle the grain boundary in between successive β particles (Jones and Danielson 2003). Furthermore, pitting tests (Tanguy et al. 2002) followed by tension in air showed that the anodic dissolution of β particles at triple junctions released enough hydrogen to embrittle precipitate free grain boundary facets. Moreover, the observations of hydrogen bubbles in Al-8%Mg (Ben Ali et al. 2011) suggests that β-precipites must indeed be preferential sites for hydrogen trapping. Such understanding and the results of numerical simulation of intergranular fracture process (Malis and Chaturvedi 1982) revealed that intergranular fracture is mostly dominated by the damage of the inter–precipitate regions. The role of plasticity in ISCC is known to be important even though it has only been studied macroscopicaly. For instance, Tanguy et al. (2002) showed that pre-straining of an Al-5%Mg alloy increases its sensitivity to ISCC under both tensile and fatigue loading conditions.

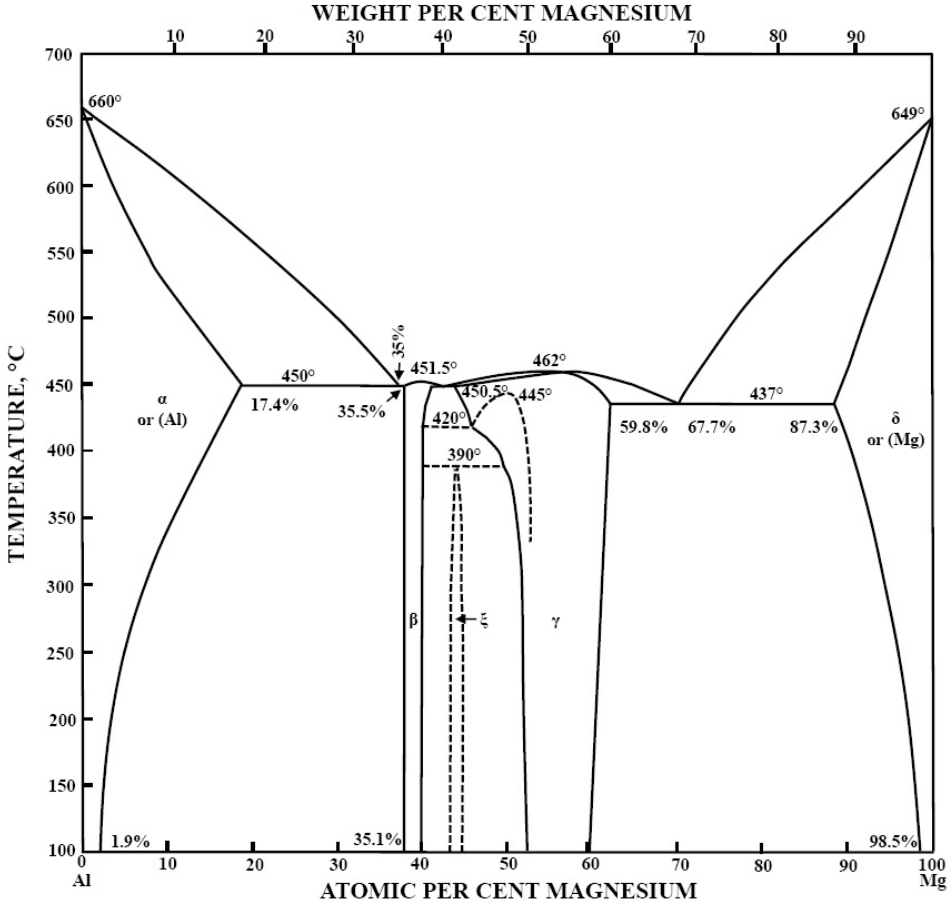

Figure 1.4: Al-Mg equilibrium phase diagram

1.3 Multiscale Modelling of Hydrogen Induced Embrittlement (HIE) by Intergranular Microcracking: The "H-Inter Project"

This thesis is part of a larger study, the "H-Inter" project, financially supported by the *French National Research Agency* (06-BLAN 0231). The "H-Inter" project relies on a multiscale approach to understand intergranular fracture due to stress corrosion cracking. Focus was made on structural aluminium alloys used in the aircraft industry. Nevertheless the same approach could have been followed with nickel based alloys for the nuclear industry and steels for hydrogen transportation and storage.

The main objective of the project was to distinguish the role of hydrogen from that of other microstructural features in intergranular failure. Hydrogen is produced during oxidation of surfaces, diffuses in the metal and is trapped at interfaces. When the material is mechanically loaded the stress distribution is no longer uniform. Locally, a grain facet, with a large local H concentration, can undergo a high tensile stress that can lead to the initiation of a crack. These different phenomena are treated by a hierarchy of simulations at different scales (Vamvakopoulos and Tanguy 2009):

- Intergranular hydrogen trapping is simulated at the atomic scale. A specific law has been established that gives the local hydrogen concentration as a function of the global concentration and the temperature. The cohesion of the hydrogen saturated grain boundary core structure is discussed based on Molecular Dynamics simulations.
- Crack propagation along a grain facet (10 ×10 µm) is modelled to take into account the fine distribution of precipitates at the nano scale by cohesive zones in an elastic medium.
- Local strain and stresses are computed by a crystalline visco-plasticity model, on a aggregate. The grain shapes are the real ones, taken from an experimental sample. This enables for a direct comparison between experiments and simulations and identify a fracture criterion for hydrogen precharged samples.

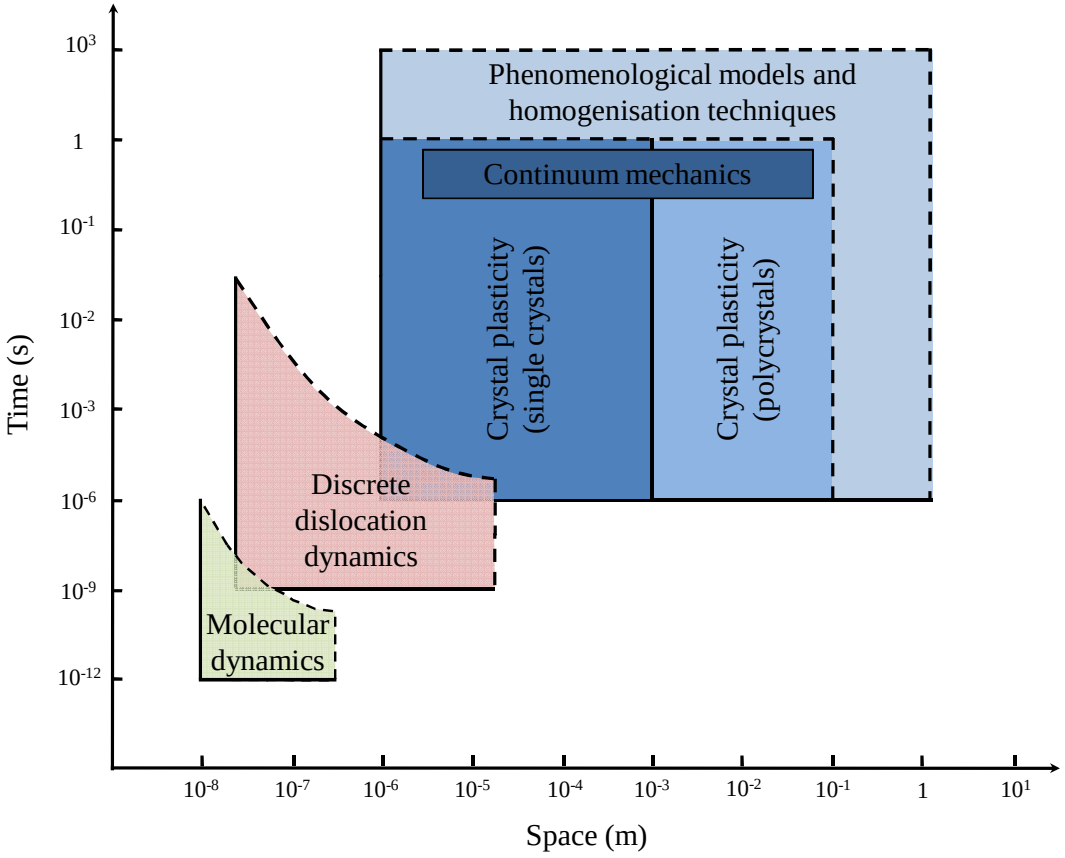

Figure 1.5: Illustration of the temporal and spatial length scales covered by typical multi-scale modelling approaches.

1.3.1 Local hydrogen segregations and vacancies for brittle fracture at the atomic scale

In the framework of atomistic molecular dynamics, critical load levels for brittle crack propagation have been investigated. In order to fully understand multiscale aspects of the concerned intergranular fracture, atomistic calculations were engaged because the details of the crack tip structure and of the interactions between the crack type and hydrogen atoms cannot be captured by continuum mechanics. In this part of the

project a Monte Carlo simulation of equilibrium thermal vacancies was extended to grain boundaries (Vamvakopoulos and Tanguy 2009). The vacancy localisation was studied by intensive molecular-dynamics simulations. Vamvakopoulos and Tanguy (2009) found that a symmetrical tilt boundary based on the coincident site lattice geometrical model is appropriate to describe the microstates of the system in the presence of vacancies. Therefore, a microstate was defined by site occupancies and continuous displacements from the lattice nodes. This microstate was used as initial state within molecular dynamics simulations for crack propagation in the plane (111) along the [111] direction of an FCC single crystal. In the framework of elasticity, obtained stress intensity factors were derived for meso-scale simulations (Tanguy et al. 2008). Figure 1.6 show three states of crack growth by molecular dynamics.

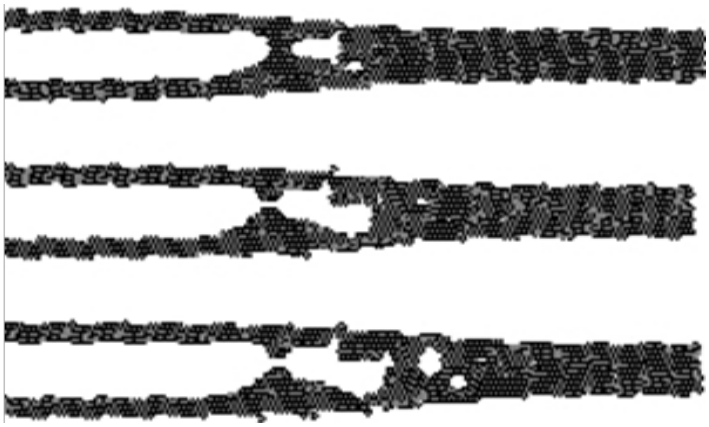

Figure 1.6: Three states of crack growth by molecular dynamics (Vamvakopoulos and Tanguy 2009)

1.3.2 Effect of nanoscale intergranular precipitate distribution on grain boundary toughness

At the scale of a single grain boundary facet of around 10 μm $\times$ 10 μm, transmission electron microscopy (TEM) observations revealed a particular sensitivity to H close to Mg rich intergranular β-precipitates. These sites between the precipitates and the matrix seem to be preferential site for microcrack nucleation. In the study of Ben Ali et al. (2011) the effect of precipitate size and density on intergranular crack propagation was investigated by a continuum mechanics approach at the scale of an individual grain boundary. Simulation was composed of 2 grains and 1 boundary, the behaviour of the boundary was modelled with a mixed cohesive zone model a first one for the interface between matrix and matrix and the other one for matrix/precipate. The matrix behaviour is assumed to be linear elastic in order to estimate the effect of grain boundary heterogeneity on the cohesive energy. Figure 1.7 shows two cases of crack initiation and propagation for different lengths of brittle precipitates. Results show a decrease by about a factor 2 in the cohesive energy for a non affected grain boundary. To complete this approach and reach experimental results, the authors add H diffusivity at the crack tip assisted by both the gradient in H concentration and stress gradient.

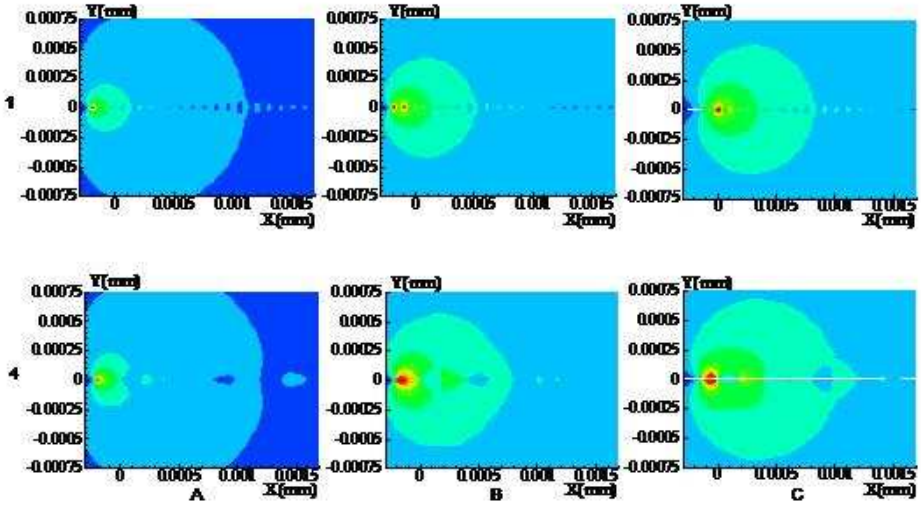

Figure 1.7: Stress field (A) at initiation (B) and (C) during crack growth, for two heterogeneous interfaces with a length of precipitates vary from (1) 50 nm and (4) 200 nm (El-Houdaigui et al. 2009)

1.3.3 Study of the mechanism of hydrogen embrittlement at the polycrystalline scale

To understand crystal plasticity effects on intergranular cracking, tensile specimens charged with hydrogen were used to quantify the effect of plastic strain at the grain scale. In a given area of a notched specimen, the evolution of strain fields at various microscopic scales by digital image correlation, as well as the crystal orientation evolution by electron backscatter diffraction after an in-situ tensile test in the scanning electron microscope. To determine the effects of local plasticity on intergranular fracture, a crystal visco-plasticity model was employed in finite element simulations of the experiments. The model parameters were first calibrated on macroscopic strain/stress curves. Then, initial EBSD maps were meshed and used as crystal aggregates in FE simulations. This methodology allows direct comparison between strain and stress fields. Consequently, it is possible to get access to a full understanding of plasticity effects on intergranular crack initiation.

1.4 Thesis Objectives and Methodology

The main objective of the thesis is to understand the effects of local plasticity on crack initiation due to hydrogen induced embrittlement in aluminium-magnesium alloys. To that purpose, the present work is conducted following four interconnected steps in which this manuscript is organised.

In order to set the framework of this study, an extensive description of the alloy and hydrogen charging procedure is presented in Chapter 2. The alloy description includes the crystallographic properties at the grain scale and macroscopic properties at the polycrystal scale.

In Chapter 3, once the notched specimens are locally charged with hydrogen, an in-situ SEM experimental procedure is then set up to observe the onset of intergranular cracking and to measure, in a given region, the evolution of strain fields at various scales using digital image correlation and the crystal orientation evolution measured by electron backscatter diffraction. From these observations, an intergranular criterion is established to understand the crack initiation mechanism.

Chapter 4 focuses on the calculation of the local stress fields to determine a range of critical values of the failure criterion identified in Chapter 3. This chapter describes the methodology used to perform an accurate calibration of the single crystal visco-plastic model. The effect of magnesium in solid solution is accounted for in the model for in terms of magnesium content.

In Chapter 5, in-situ SEM measurements of 2D displacements, crystal orientation and FE meshing are combined to determine a range of critical values of the grain boundary traction used in the proposed failure criterion. These values are then used in the fracture model in order to predict crack propagation observed in Chapter 3.

Finally, in Chapter 6 a three dimensional microstructural geometry is built to investigate the effects of grain boundary and bulk material morphologies on the intergranular initiation mechanism.

Chapter 2

Hydrogen Charging and Characterisation of the Alloy

Contents

2.1 Introduction

The present chapter focuses on the material preparation needed to perform experimental studies on hydrogen induced embrittlement. First of all, a general description of the alloy is made in terms of its industrial use and chemical composition. This information will be useful to understand the heat treatment needed to perform hydrogen charging procedure and proper conditions for future experimental studies.

Additionally, a macroscopic model will be presented and calibrated in order to obtain preliminary information on the material behaviour for in-situ tests to be discussed in Chapter 4 and on the boundary conditions to be used in crystal plasticity model of Chapters 4, 5 and 6.

2.2 Alloy Characteristics

2.2.1 Industrial applications

The AA5083 alloy is well known for its commercial use as a high strength non-heat-treatable alloy. Wrought alloys of this type are mainly those of 1xxx, 3xxx and 5xxx groups that contain chromium, manganese and magnesium, respectively. Other main properties are a high fatigue strength and the ability to retain this excellent tensile strength in the weld zone due to its as-rolled properties. Furthermore, this aluminium alloy has good weldability, good cold and stretch formability.

Despite a very good corrosion resistance, aluminium producers warm their customers against using AA5083 above 65 °C for extended periods of time in a corrosive environment. Fortunately, it is possible to use effective corrosion protection. Traditionally, anti-corrosion technologies are based on the use of Cr^{6+} formulations allowing aluminium alloys to be used in high corrosive media (e.g. chlorides solutions). However, these technologies present high toxic and carcinogenic risks. Other corrosion protections based on rare earth modified films need long processing times, high processing temperatures and even high voltage potential in some cases. Nowadays, extensive studies are still under way to develop new anti-corrosion technologies for example, with uniform deposition of CeO_2 film prepared by cathode electrophoresis process (Xiang et al. 2010).

AA5083 is available in many forms (e.g. plate, sheet, bar, wire and tube). Profile section shapes can be produced in thick plates without residual stresses. However, it is difficult to extrude the AA5083 in thin or complex sections. That is why various modified 5083 type alloys with fine microstructures (about 11 µm grain size on average) have been developed. Such microstructures allow the use of hot blow forming processes such as quick plastic forming (QPF) (Barnes 1994) and superplastic forming (SPF) (Schroth et al. 2004). In this microstructural condition, the alloy shows superplastic properties for large elongations over a wide temperature and strain rate range without developing significant cavitations. These processes are particularly interesting for automobile and aerospace applications, where forming of thin or/and complex body parts remains difficult.

Due to these good properties, particularly in SPF, AA5083 is also used in metal matrix composites. Extrusion of 5083 aluminium matrix composites provide a large scale of dynamic recrystallisation that leads to a grain size of approximately 5 µm, and limits particle clustering. Subsequent consolidation was successfully accomplished with $Al_2O_3 - TiC$, SiC, artificially

oxidized SiC particles, and A120 particles dispersed in AA5083. These advanced composite materials have shown a significant increase in the tensile elongation, yield strength and UTS compared to the monolithic AA5083 aluminium alloy (Zhong et al. (1996) and Maeng et al. (2001)).

The AA5083 alloy is most often used in structures requiring high weld efficiency and maximum weld strength:

- Structures and equipment: shipbuilding (welded components), masts, platforms. Chemical apparatus and storage tanks, cryogenics. Pressure vessels, piping and tubing.
- Automotive industry : welded tank trailers and welded dump bodies.
- Railway: welded tanks and structural components.
- Military vehicle bodies and equipment: armour plates, collapsible bridges.
- Machinery: structures, appliances, tools.
- Building and road construction: poles, pylons, towers, scaffolding.

Another main advantage of aluminium alloys is their ability to be very efficiently recycled. The recycling process involves the re-melting of used metals that is less expensive than creating new aluminium through the electrolysis of aluminium oxide (Al_2O_3), even if collection and separation costs are taken into account. Moreover, recycling aluminium and aluminium alloys require only 5% of the energy required to produce new aluminium. Today, approximately 45 (wt.%) of the aluminium produced in France comes from recycled scrap (www.af-aluminium.fr).

(a)

(b)

(c)

(d)

Figure 2.1: (a) Extruded aluminium bar (Supply HQ Australia Pty Ltd), (b) aluminium vessel (www.aluminiumleader.com), (c) location of AA5083 on the 737 wing leading edge (Hefti 2007) and (d) 777 wing tip light housing made of AA5083 aluminium alloy (Hefti 2007)

2.2.2 Chemical composition

The AA5083 alloy considered in this work belongs to the 5XXX series, which contains a range of magnesium from 0.5 to 6 wt%. The amount of magnesium in solid solution is the major factor in the increase of the tensile yield strength. Solid-solution strenghtening exhibits a quasi-linear dependency with magnesium content. The effect of magnesium in solid solution on the yield strength is illustrated in Figure 2.2.

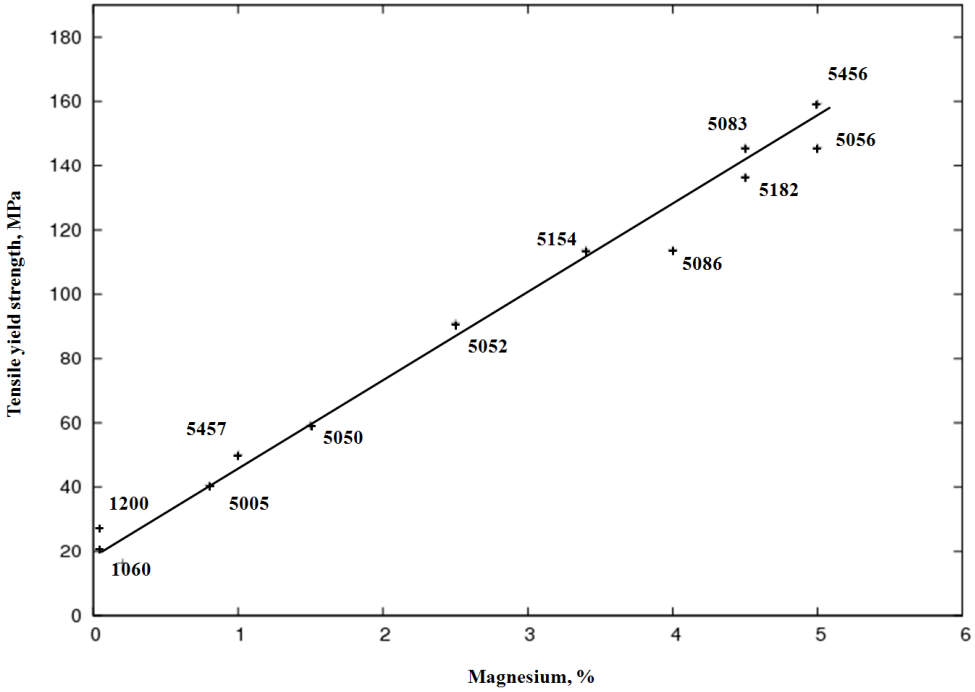

Figure 2.2: Correlation between tensile yield strength and magnesium content for some commercial aluminium magnesium alloys Lyman (1972)

The AA5083 aluminium alloy tested was cut from an extruded rod–end bar with a diameter of 15 mm that was hammered 5000 times up to 30% of strain. This alloy contains small additions of transition elements such as manganese, chromium and zirconium to retard revealed grain growth during ingot reheating. Moreover, microchemical analysis done in our laboratory exhibited some particules of intermetallic impurities of chromium, iron and silicon that do not affect the metallurgical and mechanical properties of the material. The chemical composition of the as-received material is given in Table 2.1.

Table 2.1: Chemical compositions (wt.%) of as–received Al 5083

	Si	Fe	Cu	Mn	Mg	Zn	Ti	Cr	Al
Nominal	0.40	0.40	0.10	0.70	4.50	0.25	0.15	0.25	Balance
Measured (±0.01)	0.25	0.35	0.05	0.65	4.70	0.25	0.13	0.20	Balance

2.3 Hydrogen Charging

2.3.1 Procedure

To study the influence of plastic strain on the embrittlement of grain boundaries by hydrogen, grain strain and hydrogen charging were carried out separately. Thus specimens have been pre-charged before being tested mechanically. Moreover the microstructure of AA 5083 plays a major part in the sensitivity of grain boundaries to hydrogen induced embrittlement. It is the reason why cathodic charging and the influence of the precipitation of intergranular β–particles and β–phase have to be investigated thoroughly.

There are two main methods of charging metallic materials with hydrogen. The first one consists in heating the specimen up to high temperatures and exposing it to a high H_2 gas pressure. This method requires the control of the concentration rate of hydrogen. With this method the risk of desorption is important during mechanical testing as it increases with temperature. The second one is cathodic charging. This method generally induces a concentration gradient of hydrogen in the workpiece, enables for the introduction of a high amount of hydrogen and is easier to use.

However, before polarisation, if the metal is covered by a passive film, hydrogen absorption can be governed by electronic transfer through the layer. In the case of aluminium, the alumina film constitutes an electrical isolator. One of the most plausible assumptions is that electrons travel through the layer by tunnelling. In practice, the sample surface contains cathodic precipitates, not covered by the oxide film, and the reduction of oxygen with protons from water dissociation leads to a local increase in pH around the precipitates, and yet the alumina protection film is unstable for pH, between 4 and 9. This leads to a local dissolution of the passive film and to a resumption of the matrix oxidation around precipitates. However, precipitates are rapidly lost in the aqueous medium, so that the remaining (matrix) surface repassivates quickly. Cathodic charging is therefore ineffective unless the alumina layer is made unstable over the whole free surface.

Birnbaum (1994) have developed three modes of "hydrogen electrolytic charging" in high purity aluminium with very low pH in H_2SO_4 or in HCl by using $NaAs0_2$ as a recombination poison for hydrogen, with pH ranging from 10 to 12 in a $NaOH$ solution or with a neutral pH by using an ultrasonic bath to disrupt the passive film. Figure 2.3 shows a concentration profile established by Secondary Ion Mass Spectrometry (SIMS) through the surface of a pure Al single crystal on which Rozenak et al. (2005) performed electrolytic charging and used deuterium to track hydrogen ingress into the sample. Rozenak et al. (2005) observes that, over the first µm under the free surface, a deuterium concentration 1000 times higher than deeper in the bulk. Thus, in a pH-2 deaerated aqueous solution of boric acid with H_2SO_4 at 10^{-2} mol/l, hydrogen absorption is strongly favoured (Tanguy 2001). From these methods Tanguy et al. (2002) proposed to use metallurgical conditions as well as local electrochemical conditions of grain boundary with β-precipitates to enable H^+ reduction on depassivated Al surface. Tanguy et al. (2002) used hydrogen pre–charged samples to confirm that hydrogen absorption is responsible for grain boundary failure. In their study Tanguy et al. (2002) immersed samples in an NaCl–HCl solution at room temperature (pH 1.5) and at free potential. Sample surfaces showed that after 15 days of immersion the triple junctions were preferentially corroded because of the presence of tiny intergranular precipitates and that the fracture in air was intergranular and brittle.

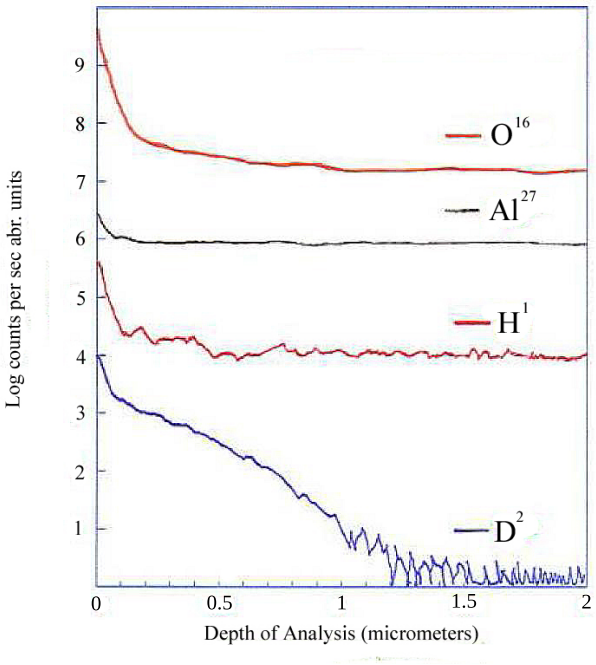

Figure 2.3: SIMS chemical composition profiles of pure Aluminium single crystal electrolytically charged during 2 h with hydrogen at room temperature (Rozenak et al. 2005).

The cathodic hydrogen charging method used here was based on a negative current imposed on the specimen in an aqueous solution of boric acid 10^{-2} mol/l and at fixed pH-2 using H_2SO_4. First, it is important to recall the chemical reactions during cathodic polarisation in a de–aerated environment.

Anodic dissolution:

$$M \Leftrightarrow M^{n+} + ne^{-1} \tag{2.1}$$

Cathodic reduction:

$$H^+ + e^- \Leftrightarrow H_{abs} \tag{2.2}$$

$$\frac{1}{2}O_2 + H_2O + 2e^{-1} \Leftrightarrow 2OH^- \tag{2.3}$$

where M is the metal and H_{abs} the absorbed hydrogen.

Additionally from Evans' diagram (Evans 1948) it can be deduced that the anodic dissolution highly decreases due to a forced cathodic polarization. Electrons consumed by cathodic reactions are delivered by the external generator. The intensity of reduction reactions is increased and the production of H_{abs} is encouraged by decreasing the O_2 content with a de-aerating environment.

During SCC studies on AA5083, Jones et al. (2004) showed that, when immersing an AA5083 sample in an aqueous $NaCl$ $30g/l$ solution, a galvanic couple is formed in which the matrix and the β–phase are the cathode and the anode, respectively. The free potential of the matrix and of the Al_3Mg_2 phase are estimated in this solution at -760 mV/SCE (i.e sell

calomel electrode) and -1290 mV/SCE, respectively.

In order to perform cathodic charging, negative current is imposed in a pH-2 solution of boric acid with H_2SO_4 at $10^{-2}mol/L$ (Tanguy et al. 2002). The assumption here is that the free potential of the aluminium matrix and the Al_3Mg_2 phase present in the AA5083 sample remain close to the values -760mV/SCE and -1290 mV/SCE that were estimated by Jones et al. (2004) in 30g/l NaCl solution. The aluminium matrix and the Al_3Mg_2 phase are, respectively, the cathode and the anode of the galvanic couple formed. At the same time the Al matrix and the Al_3Mg_2 phase are both cathodically polarised.

2.3.2 Effect of Al_3Mg_2 precipitation on the mechanism of hydrogen induced embrittlement

Ohnishi and Higashi (1981) focused on possible links between intergranular β precipitation and hydrogen concentration. Tests were conducted with specimens aged for 1, 24 and 100 hours at temperatures ranging from 100°C to 300°C that allow for three different precipitation states in the form of "low precipitation", "continuous precipitation" and "large precipitation". In Figure 2.4(a) large and (b) continuous β precipitations are shown. Then specimens were cathodically charged in a solution of $2N - H_2SO_4$ with $1g/L$ of $Na_2HAsO_47H_2O$, and with an imposed cathodic current of $-5mA/cm^2$. Desorbing measurements showed that hydrogen penetration along grain boundaries is massive in the case of continuous precipitation (Ohnishi and Higashi 1981).

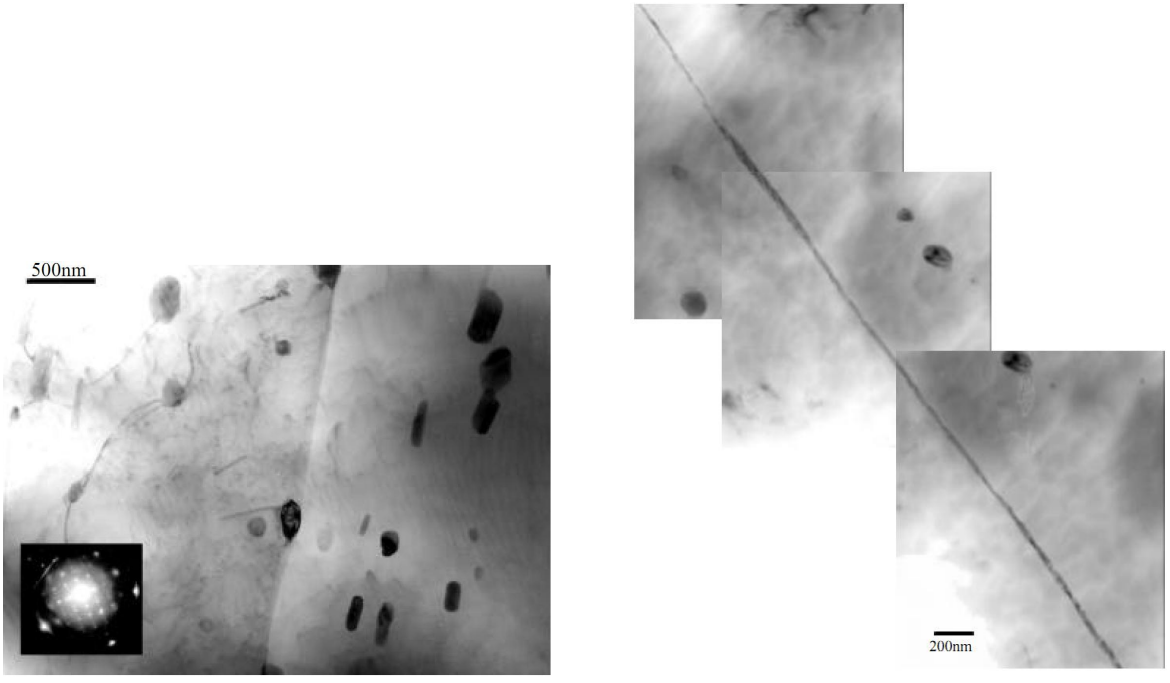

(a) (b)

Figure 2.4: (a) TEM micrograph of a 82.5 hour sample showing coarse discrete β–precipitates at grain boundaries with associated diffraction pattern along the <110> zone axis (Searles et al. 2001), and (b) a TEM composite micrograph of a 189 hour sample showing continuous β film along the matrix grain boundaries (Searles et al. 2001).

Furthermore, Malis and Chaturvedi (1982) observed bubble formation at grain boundaries by TEM, which showed a particularly high concentration in magnesium. Microchemical analysis revealed that the higher the ratio of magnesium to aluminium content, the higher the number density of hydrogen bubbles. The authors concluded that Al_3Mg_2 precipitation along grain boundaries allows for penetration and trapping of hydrogen at grain boundaries and an embrittling effect of hydrogen at grain boundaries.

To confirm that grain boundaries had actually been embrittled over a few µm under the surface, a smooth tensile specimen was prepared and cathodically charged with hydrogen, tested in tension till intergranular cracking at the free surface (see Figure 2.5), and in order to compare brittle and ductile surfaces the specimen was loaded in bending fatigue till the ductile fracture of the specimen (see Figure 2.6). Interrupted tensile test conducted up to an elongation of 10% confirmed HIE over a depth of about 5 µm and showed that charged specimens exhibit marked sensitivity to intergranular fracture after a few percent of plastic strain (see Figure 2.6).

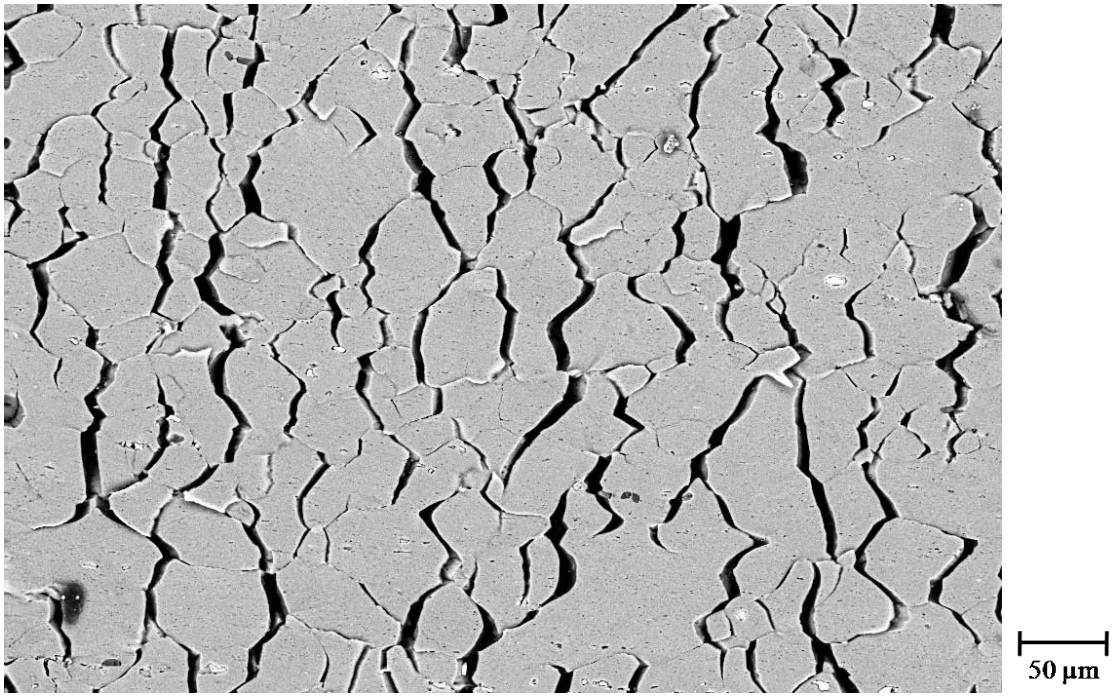

Figure 2.5: SEM Observations of the free surface of tensile specimen showing intergranular fracture after a 10% of imposed tensile elongation at room temperature. The tensile axis is horizontal.

At low magnifications, ductile fracture of the bulk and brittle fracture of embrittled grain boundaries was observed on the fracture surface (see Figure 2.6(a)). This observation confirmed the ductile behaviour of the bulk aluminium alloy and the hydrogen embrittlement of grain boundaries over a depth of 5 µm. These observations validate the above mentioned hydrogen charging procedure to be used for the remainder of the study.

Note that, at a higher magnification, at embrittled grain boundaries in Figure 2.6(b), the fracture surface showed micronmeter-sized cavities. Thus, the fracture that seems to be brittle at low magnifications is in fact a nano-localised crack. Figure 2.6(b) illustrates that

intergranular fracture of embrittled grain boundaries results from the growth and coalescence of nanocavities. Cavity initiation sites are associated with the embrittlement of discontinuous Al_3Mg_2 precipitates at grain boundaries.

These observations are in good agreement with the work of Ben Ali et al. (2011) at lower scales. In its work Ben Ali et al. (2011) a grain boundary is assumed to be composed of alternate brittle and bulk layers every 200 nm.

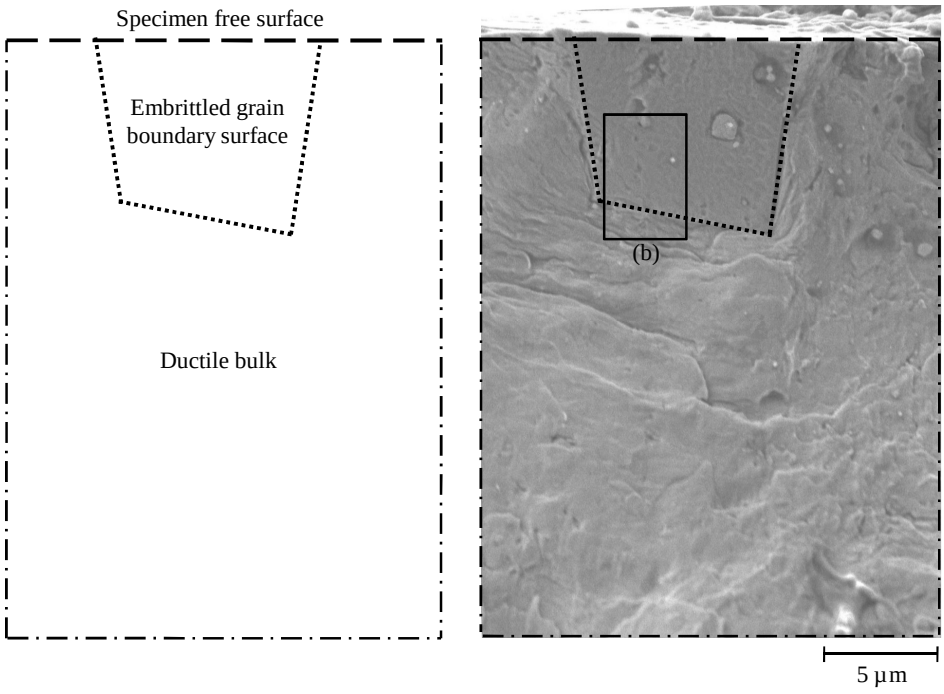

(a)

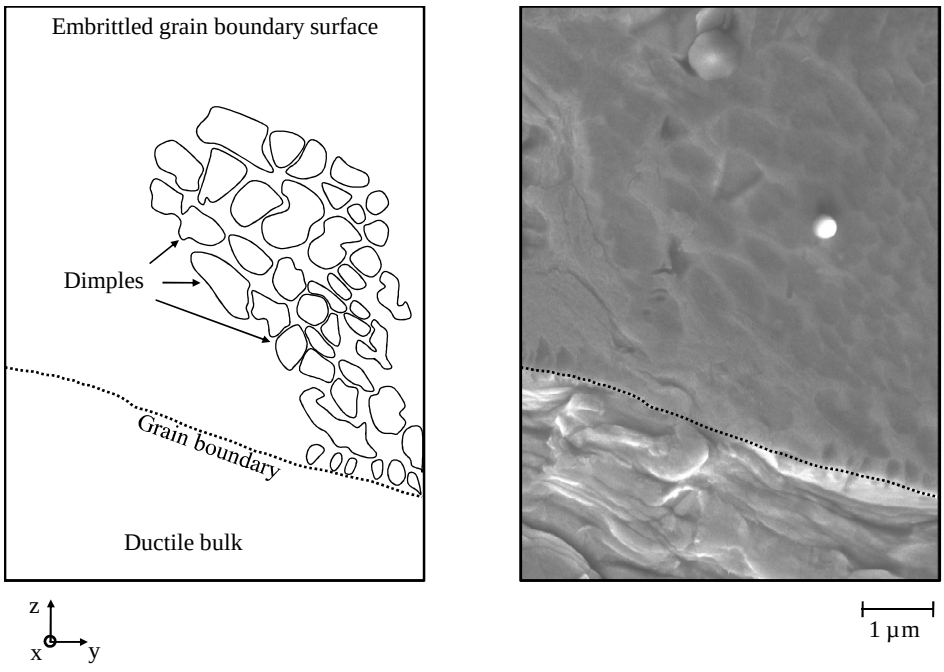

(b)

Figure 2.6: SEM secondary electron images and corresponding schematic drawing of the fracture surface of a smooth tensile specimen charged with hydrogen and then loaded to fracture at room temperature, (a) general view showing the thickness of the embrittled layer and (b) a close-up view of micrometer-sized dimples on the fractured grain boundaries.

2.4 Crystallographic Properties

2.4.1 Electron backscatter diffraction mapping

Several techniques can be used to provide the crystal orientation in a polycrystal. Over the past 20 years, the Electron Backscatter diffraction technique (EBSD), also called Backscatter Kikuchi diffraction (BKD), has become a very popular tool for microtexture measurements. The EBSD technique provides detailed crystallographic and spatial information and microstructure imaging of many types of materials and minerals. In the case of our polycrystalline material, the EBSD technique was used to study the crystal orientation distribution, grain boundary morphologies, microstrain and local crystallographic heterogeneity, both before and after plastic deformation.

2.4.1.1 Principles of EBSD

For EBSD measurements, the specimen surface to be analysed was tilted by 70° from the horizontal position toward the phosphor screen in order to optimise the contrast in the resultant electron backscatter diffraction pattern.

In the scanning electron microscope (SEM), the atoms in the probed region inelastically scatter a fraction of the incident electron beam with a small loss of energy to form a divergent source of electrons close to the surface of the sample. Some of these electrons are incident on atomic planes at angles that satisfy Bragg's equation. These electrons are diffracted to form a set of paired large angle cones corresponding to each diffracting plane. When used to form an image on an appropriate "phosphor", the regions of enhanced electron intensity between the cones produce the characteristic Kikuchi bands of the electron backscatter diffraction pattern.

Then an electron backscatter diffraction pattern is formed when many different planes diffract different electrons to form Kikuchi bands that correspond to each of the lattice diffracting planes. If the system geometry is well described, it is possible to relate the bands present in the EBSP to the underlying crystal phase and orientation of the material within the electron interaction volume. Each band can be indexed individually by Miller's indices of the diffracting plane family that formed it. In cubic materials, only three bands with no unique intersection are required to describe a unique solution to the crystal orientation (based upon their interplanar angles) and commercial systems use look–up tables with international crystal data bases to perform the indexing.

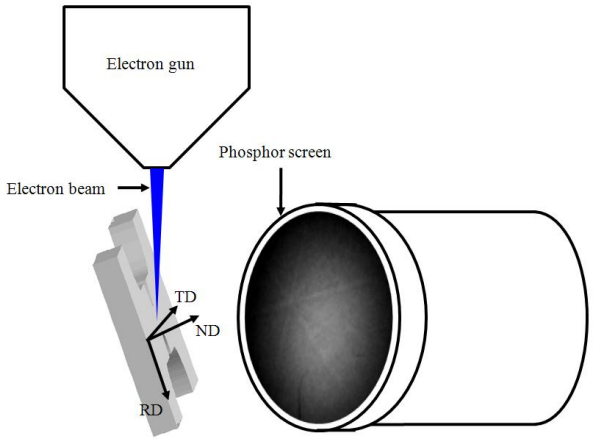

Figure 2.7: Schematics of the EBSD operating system with corresponding sample coordinates (tilt axes parallel to the axes of the tensile specimen)

In the present study, EBSD measurements were carried out using a Zeiss DSM982 Gemini field emission gun SEM, with a high voltage of 20kV, a tilt angle of 70°, a working distance of 19mm, a probe current of less than 1nA, an aperture diameter of 1 µm and a square scanning grid. To accurately represent the distribution of crystal orientations within grains while investigating a significant number of grains for the texture to be determined, a step size of 0.8 µm was chosen. The EBSD facility was an EDAX TSL OIM 2.6 system together with a CCD digital camera. A minimum of three bands (max 7) was used to index EBSPs.

2.4.1.2 Sample preparation

To obtain optimised EBSD patterns, the surface preparation of EBSD samples has to be carefully performed. With deformation introduced during sectioning and grinding, patterns are not visible. That is why samples require several degrees of polishing. There are three main steps to maximize pattern quality, called Image Quality (IQ) in the used system, they are:

- First, large machining scratches are removed with 4 types of abrasive silicon carbide papers and then an annealing treatment is performed in order to relieve the deformed layer.
- Then samples are polished with diamond pastes (1 µm and 0.3 µm). The resulting surface is nearly acceptable for pattern acquisition but pattern quality can still be improved.
- Finally a polish is performed using colloidal silica with an automated vibrating machine. This technique provides excellent EBSD patterns. The samples are fixed on a brass cylinder and immersed into colloidal silica. The weight of the cylinder was carefully chosen in order to both allow the circular displacement of the cylinder and to avoid surface deformation. The colloidal silica solution consists of negatively charged particles of silicon dioxide (SiO_2) with a pH value of 8.

Despite good results with electropolish, this latter technique was abandoned because of the deep etching over approximatively 20 µm. Such etchings remove fiducial indentation marks used for the localisation of the studied surface and introduce a significant shadowing relief in which the IQ of EBSD patterns are vastly decreased.

2.4.2 Mathematical procedures for texture analysis

2.4.2.1 Coordinate systems and crystal orientation

Crystal orientation describes the orientation of the principal crystal axes (e_i^c in Figure 2.8) relative to the principal sample axes (e_i^s in figure 2.8). Euler angles ϕ_1, Φ and ϕ_2 represent a set of three rotations that are needed to make the principal axes of the crystal coincide with those of the sample. In this work, Bunge's description of the Euler angles was used. In the case of Bunge's form of the Euler angles, a rotation (ϕ_1) about the e_3^s axis is followed by a rotation Φ about rotated e_1^s axis and finally a rotation ϕ_2 about rotated e_3^s axis are successively performed.

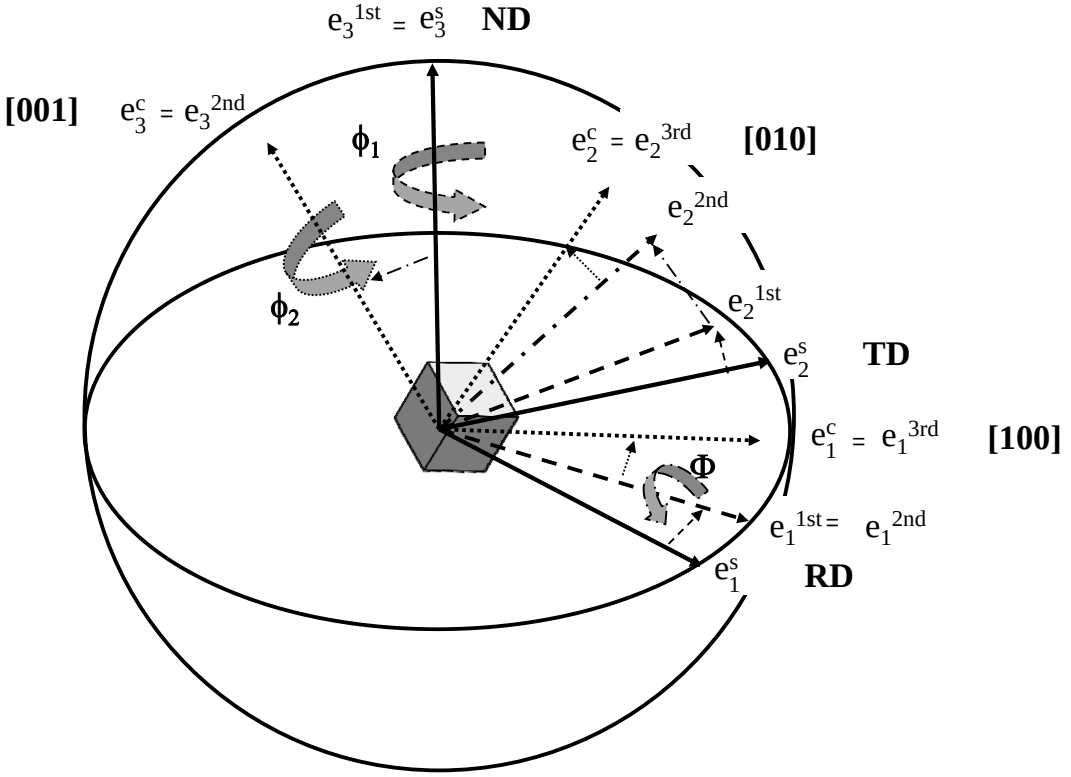

Figure 2.8: Euler space rotations to define Euler angles

2.4.2.2 Misorientation

Consideration of the misorientation or orientation difference is important in order to investigate coincidence between two grains at their common grain boundary. Symbol Δg_{12} in Eq.(2.4) is used to represent the misorientation at the boundary separating two crystals with orientations g_1 and g_2. The rotation matrix Δg_{12} is expressed by:

$$\Delta g_{12} = g_2 . g_1^{-1} \tag{2.4}$$

Misorientation Δg_{12} can also be represented by Euler angles. In the axis/angles representation, a common (rotation) axis of neighbouring grains is used and an misorientation angle θ is then calculated to make the two crystal lattices coincide.

2.4.2.3 Representation of crystal orientation data used in the present study

In sciences, common two dimensional representations include pole and inverse pole figures and inverse pole figure mapping. Pole figures are based on reference directions that coincide

with the sample coordinate system and single crystals are projected. Inverse pole figures and inverse pole figure mapping are based on the reference given by the crystal coordinates and where one of the sample directions is projected. Only one direction (TD) is used to illustrate the microtexture for each analysed region. According to most studies in material science, projections concern the upper hemisphere of the unit sphere. A stereographic projection and a definition of the standard triangle used in this work is given in Figure 2.9.

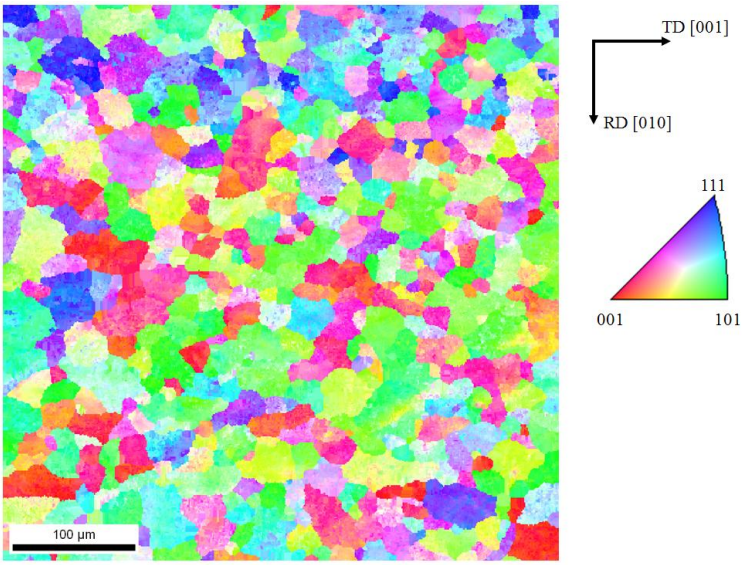

Figure 2.9: Typical inverse pole figure map and definition of the standard colour code triangle used in the work.

2.4.2.4 Orientation distribution function (ODF)

The orientation distribution function (ODF) expresses the statistical distributions of crystal orientation in the investigated region (Bunge and Morris 1982). In this work, ODFs were calculated with the help of series expansion method. This method is based on the principle that the discrete distribution of Euler angles measured by EBSD mapping can be expanded into a series of continuous generalised spherical harmonic functions. The form of this series expansion is given by:

$$f(g) = \sum_{l=0}^{\infty} \sum_{m=-l}^{l} \sum_{n=-l}^{l} C_{mn}^{l} T_{mn}^{l}(g) \tag{2.5}$$

where the generalized spherical harmonics, $T_{mn}^{l}(g)$, are calculated for each orientation (g) and C_{mn}^{l} are the series coefficients. The maximum value of l was typically set to 22. This default value gives accurate results with an acceptable computation time.

As a probability density function, the ODF should be positive everywhere. However, the use of a Dirac function in Fourier series expansion leads to negative values. To overcome this negativity problem, a Gaussian spread function K is usually introduced into the C_{mn}^{l} coefficients. The value of K is calculated as follows,

$$K = \frac{exp[(\frac{-l^2\omega^2}{4}) - exp(\frac{-(l+1)^2\omega^2}{4})]}{1 - exp(\frac{-\omega^2}{4})} \tag{2.6}$$

where ω, the half-width of the Gaussian peak, has to be manually set by the user. The optimal setting of K depends on the number of measured orientations. In this work, K was fixed to 5° following common practice.

2.4.3 Microtexture of the aluminium alloy before and after deformation

The objective of this section is to examine the microstructure and texture of the studied material associated with deformation mechanisms. EBSD analyses will provide the evolution of microtexture and boundary misorientation during deformation. In order to get statistically significant measurements, four regions of at least 500 grains for each were chosen for examination (see Figure 2.10(3)) on a smooth tensile specimen (see Figure 2.10(1)). The surface of the specimen was examined, both before and after an axial tensile elongation of 5% at strain rate $10^{-4}s^{-1}$ and at room temperature. The value of 5% was chosen because both intergranular cracking can be largely observed and EBSD mapping can be performed without new polishing.

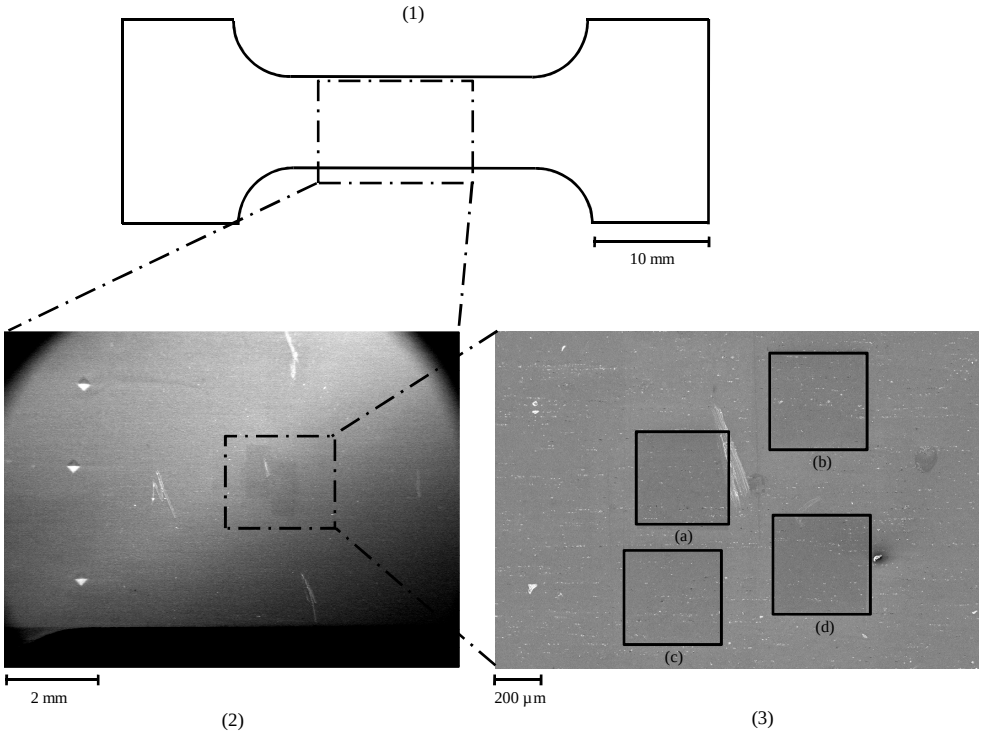

Figure 2.10: Successive close–up views of the smooth tensile specimen showing the studied zones. Fiducial indentation marks and scratches are visible in (2) and (3), respectively : (1) schematic drawing and (2), (3) secondary electron SEM images.

In Figure 2.11, grains exhibit a large distribution in grain size and wavy grain boundaries that revealed a shape and orientation gradient in grains at the surface may be due to polishing. The inverse pole figure maps of Figure 2.11 are not completely sharp, i.e. they exhibit diffuse orientation (colour levels) within grains. Together with the wavy shape of grain boundaries, this suggests that residual (plastic) crystal rotations still exist and that the recrystallisation

process may not have been completely achieved. One can notice that in this work the lower cut–off value of grain boundaries disorientation angles was set to 5°following minimum observed desorientation angles between identified grains.

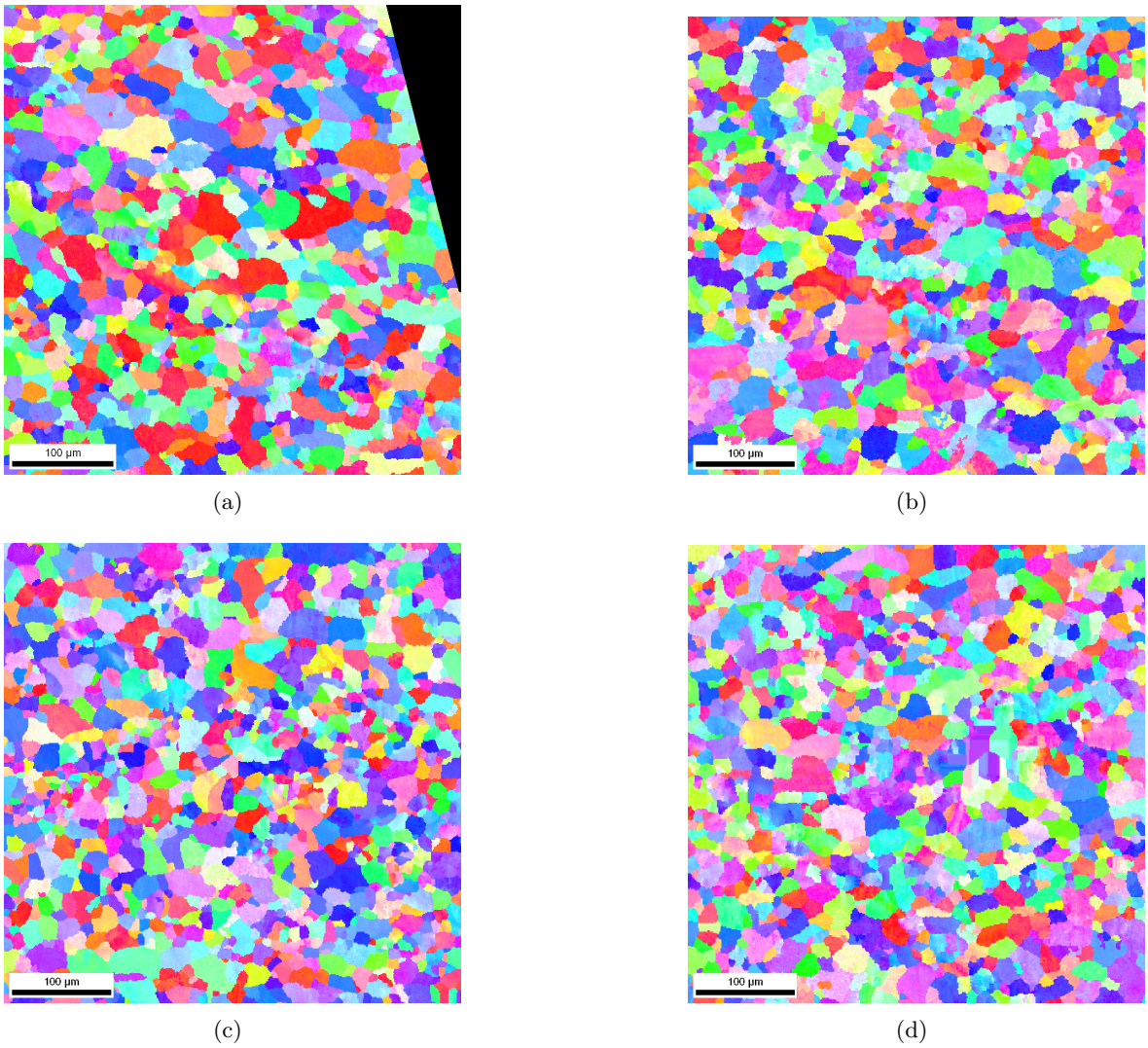

(a) (b)

(c) (d)

Figure 2.11: (a)(b)(c)(d) respective inverse pole figure maps (ND direction) of the four regions of Figure 2.10, undeformed sample. The black triangle in (a) is due to poor EBSD quality next to the scratch (see Figure 2.10(3)).

The grain size distributions given in Figure 2.12 reveal a complex microstructure composed of mean grain size of 27 µm according to ASTM. Moreover, the standard deviation of 8.5 µm shows that the grain size distribution is scattered. Together with their orientation illustrated in Figure 2.11, heterogeneous distributions of larger and smaller grains can significantly influence local strain field distributions.

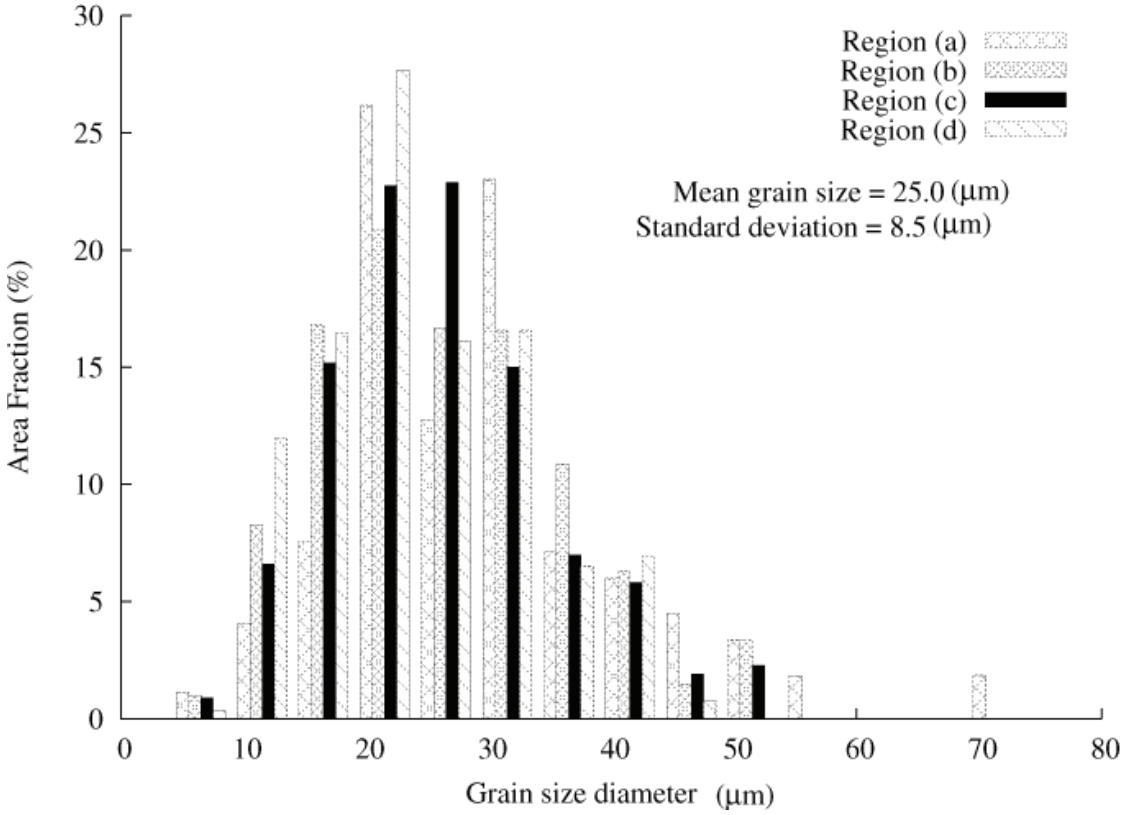

Figure 2.12: Grain size distribution for the four studied zones.

In Figure 2.13 the distribution of disorientation angles lies in the range of 10° up to 60°, with no evidence of any texture in the matrix of the whole material (i.e. close to random misorientation (Mackenzie 1958)). The analysed surfaces of approximatively 500 grains (i.e. Figure 2.10) was assumed to be representative for the study of intergranular fracture in next parts of this work.

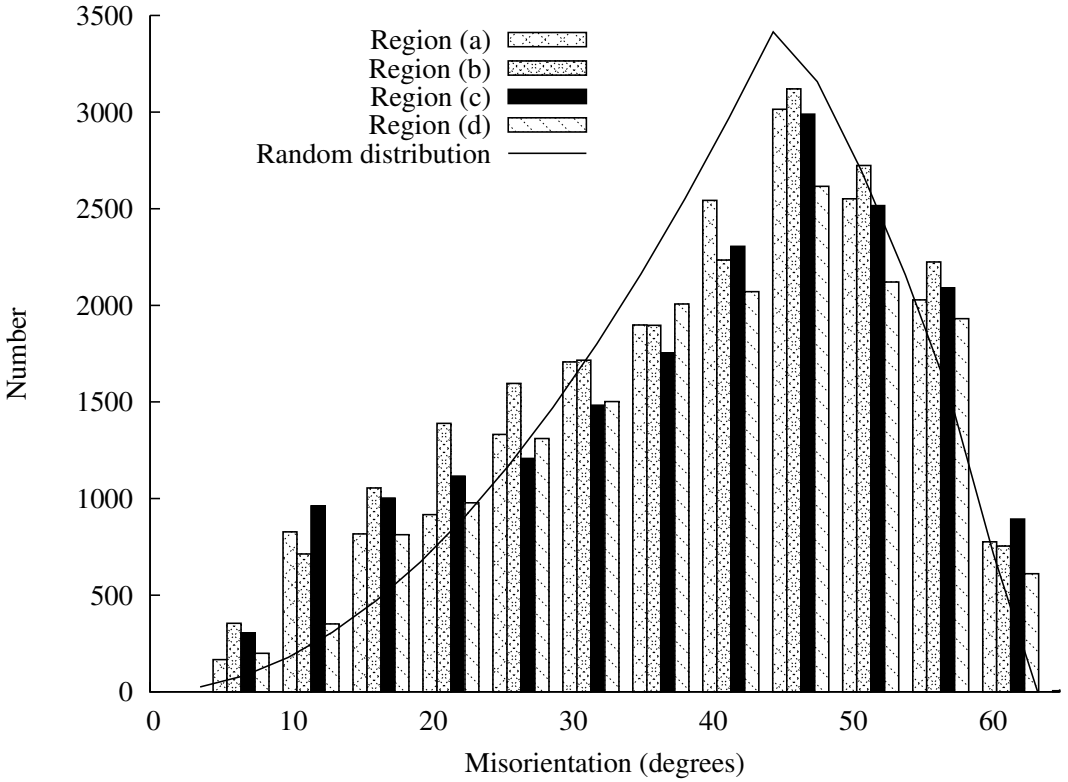

(a)

Figure 2.13: Misorientation distribution at grain boundary. Number of measured points ãs function of misorientation angles at grain boundaries.

Calculation of ODFs allowed plotting pole figures with an intensity (contour) scale (see Figure 2.14). These pole figures do not reveal a particular concentration of orientation that could have induced significant anisotropy of the macroscopic mechanical response of the material. Pole figures are in agreement with literature data (Pérez-Prado et al. 2001) obtained on a textureless AA5083 aluminium alloy.

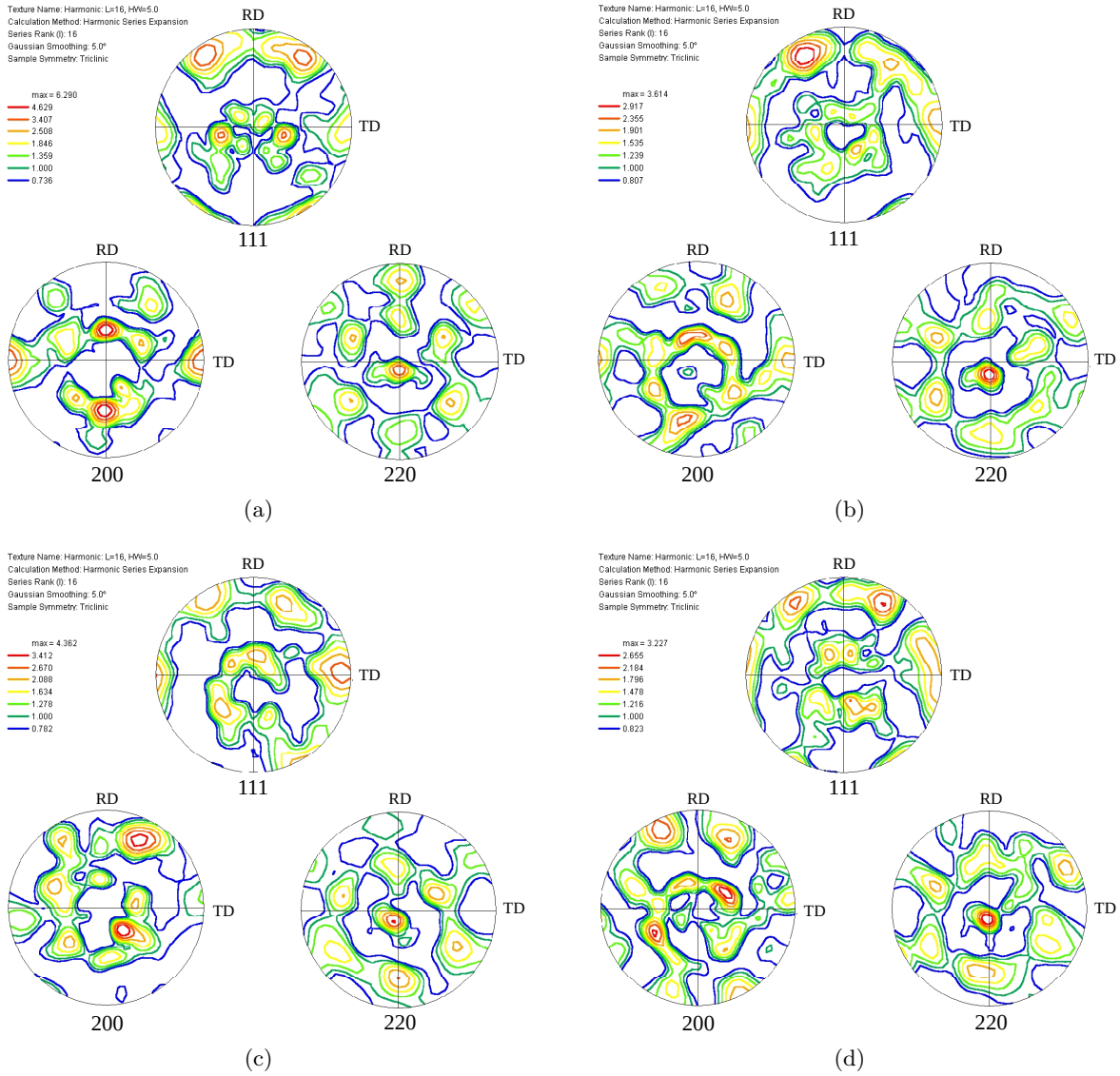

Figure 2.14: (a)(b)(c) and (d) pole figures [001] of undeformed sample for the four regions of Figure 2.10. The reference direction TD with respect to the pole figure is the tensile axis of the specimen.

Pole figure and ODF are represented in Figure 2.15 and Figure 2.16 for the four investigated regions of Figure 2.10. Results suggests that at low deformation state no particular orientation fiber was developed. This result validates the use of phenomenological model presented in Section 2.5.

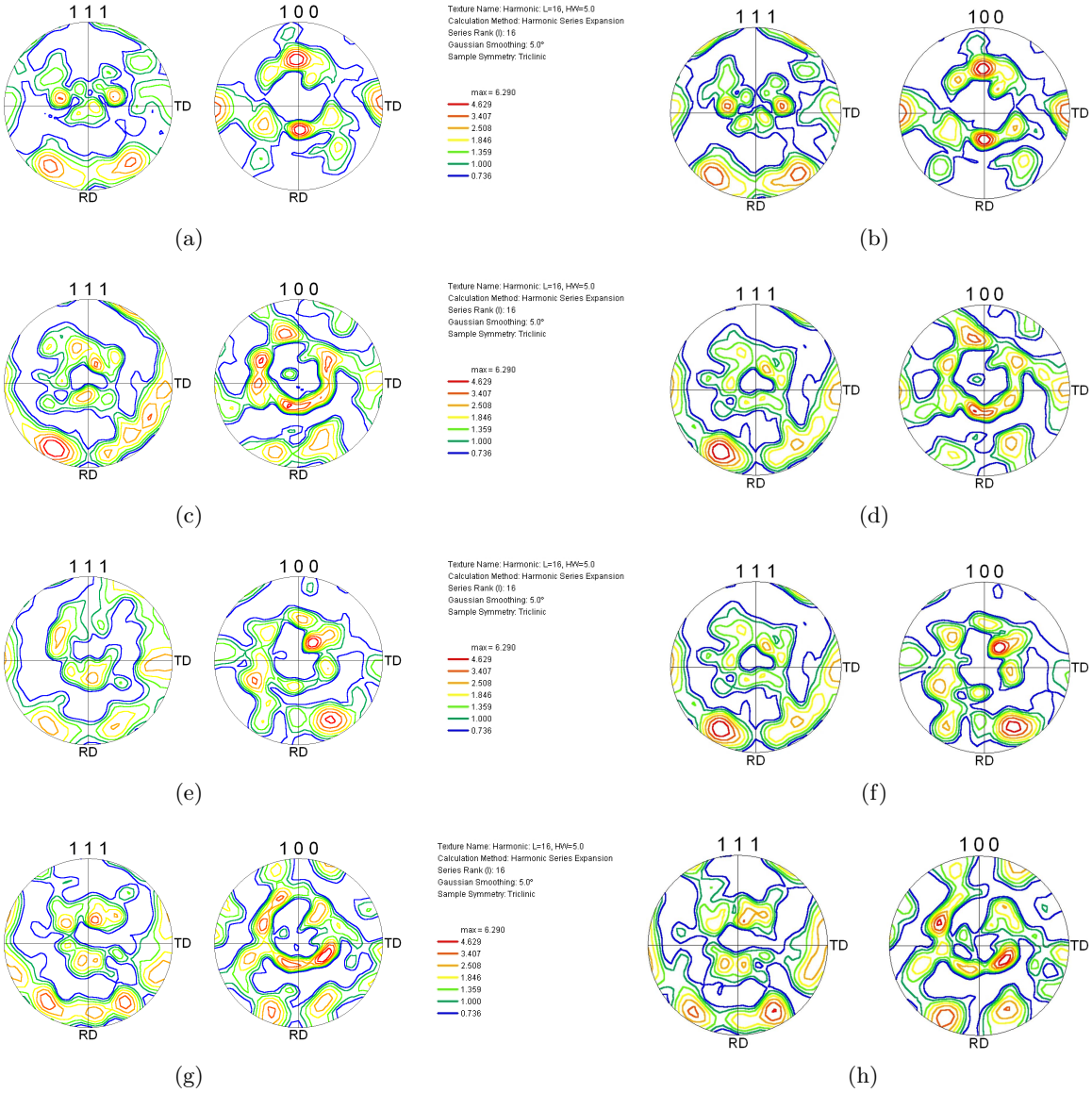

Figure 2.15: Texture data for the annealed AA5083 aluminium alloy in the form of pole figure [001], for the four regions of Figure 2.10, (a),(c),(e) and (g) undeformed sample and (b),(d),(f) and (h) deformed sample 5% applied strain. The reference direction TD with respect to the pole figure is the tensile axis of the specimen. [(a),(b)], [(c),(d)], [(e),(f)] and [(g),(h)] are the four regions designated as (a), (b), (c) and (d) in Figure 2.10.

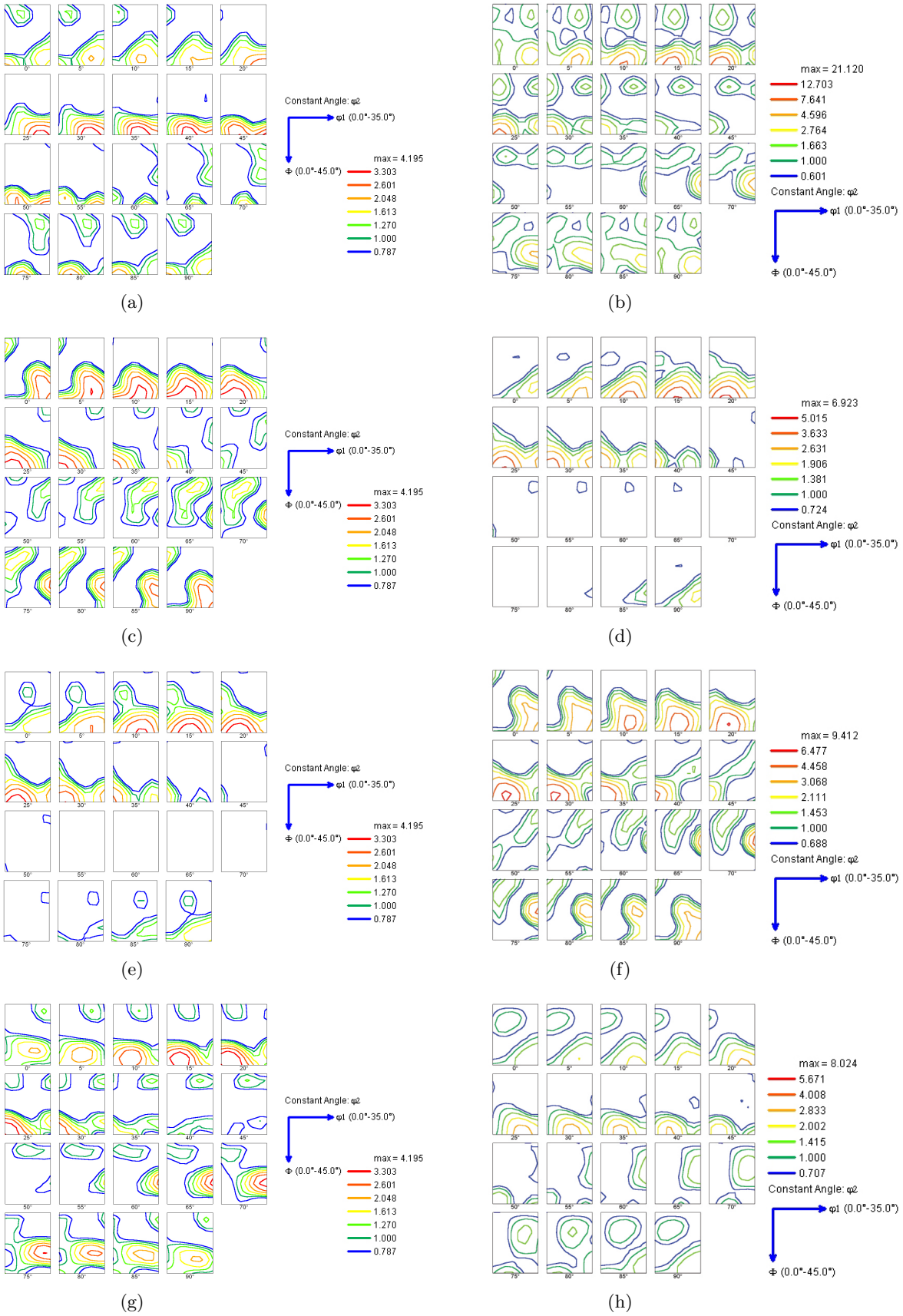

Figure 2.16: Texture data for the annealed AA5083 aluminium alloy in the form of ODF determined by EBSD, for the four regions of Figure 2.10's, (a),(c),(e) and (g) undeformed sample and (b),(d),(f) and (h) deformed sample 5% applied strain. [(a),(b)], [(c),(d)], [(e),(f)] and [(g),(h)] are the four regions denoted by (a), (b), (c) and (d) in Figure 2.10.

2.5 Macroscopic Behaviour of the Alloy

In order to quantitatively describe hydrogen induced embrittlement with a crack initiation and propagation criterion, notched tensile specimens were chosen as described in Chapter 3. To accurately assess boundary conditions that are applied to the regions of interest, stress and strain fields have to be determined for the notched specimens. To this aim, the macroscopic behaviour of the considered material was investigated by the use of tensile tests on the above mentioned smooth specimens (Figure 2.17). As the thickness of the embritlled region is very small (5 µm) compared to the specimen thickness (1 mm), only the "bulk" material (i.e. non affected by hydrogen ingress) was considered in this part of the study.

2.5.1 Uniaxial tensile test results

The focus of the uniaxial tensile tests presented here is the plastic behaviour at room temperature of the studied material determined from the stress-strain relationship under prescribed elongation rate. Tensile tests were conducted for three values of the strain rates ($\dot{\varepsilon} = 10^{-3}s^{-1}, 10^{-4}s^{-1}, 10^{-5}s^{-1}$) for the as-received material and after heat treatment in order to quantify softening induced by solution annealing and further tempering. Specimen drawing is illustrated in Figure 2.17.

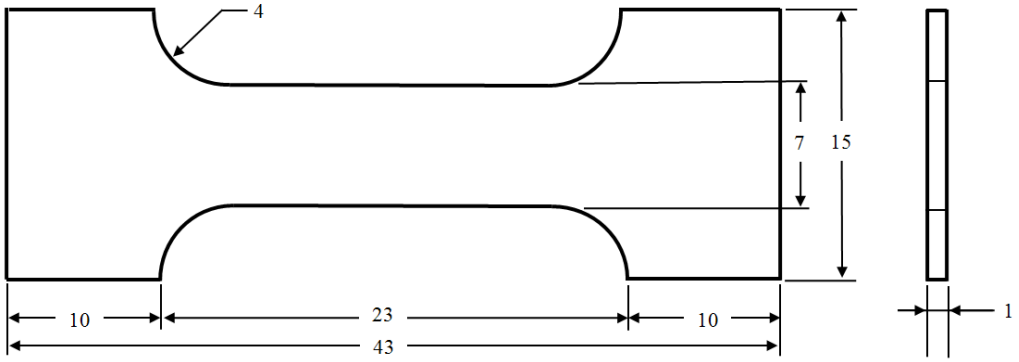

Figure 2.17: Smooth tensile specimen drawing

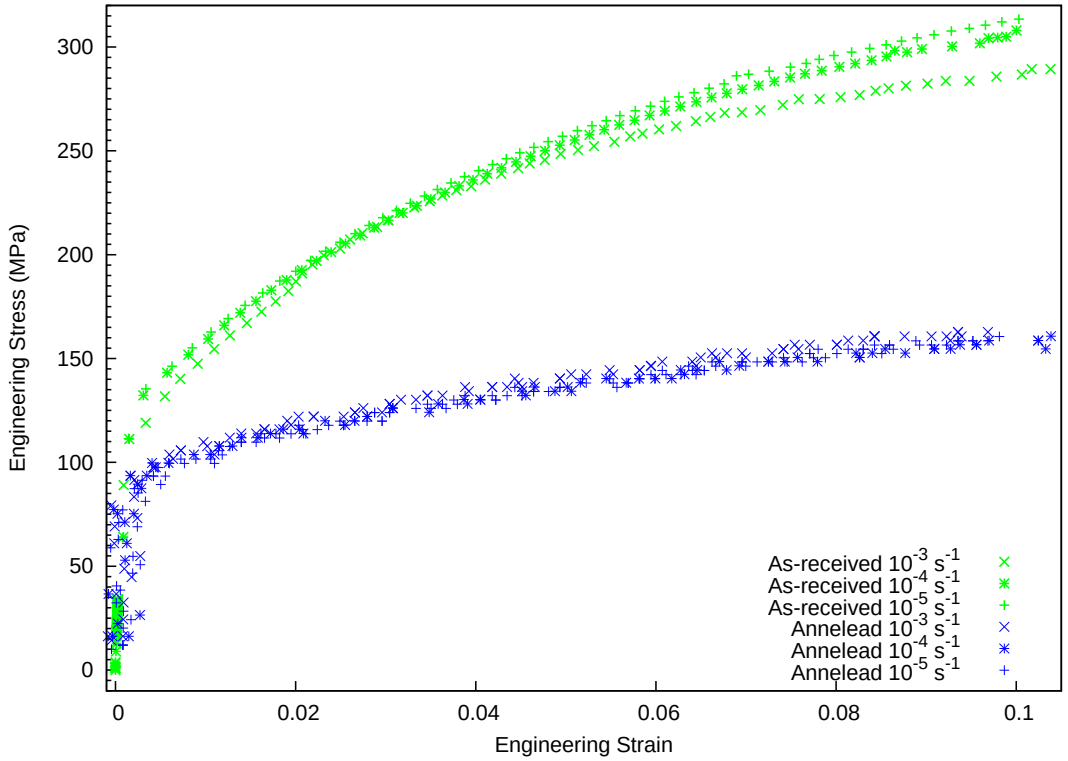

Figure 2.18: Tensile curves at different strain rate and at 25°C

Results show a significant decrease of the tensile strength, thus confirming the softening effect of the heat treatment used to precipitate Al_3Mg_2 at grain boundaries. Despite this softening treatment, the vast majority of magnesium atoms are still in supersaturated solid solution within the grains. This softening effect mainly affects strain hardening and, to a much lower extent, the yield strength of the material. Tensile curves exhibit a very low effect of strain rate on the tensile behaviour as expected at room temperature. It can be noticed that the wavy shape of the tensile curve in the elastic domain is due to the noise in load cell measurement.

2.5.2 Preliminary macroscopic model to describe the alloy homogeneous behaviour

A simple mechanical analysis of the smooth specimen was used in order to get (i) boundary conditions for the finer more localised study and verify the level of triaxiality and (ii) a reference for the calibration of the crystal plasticity model (Chapter 4). To obtain a satisfactory computational stability, a macroscopic model considering viscoplasticity as the inelastic deformation regime was used. Parameters were calibrated in order to reduce viscosity effects according to experimental observations of the material behaviour. A von Mises yield criterion was chosen to represent simply the viscoplastic potential. Norton flow rule and an isotropic non-linear hardening rule were used as shown by Eq. (2.7). Optimized parameters are reported in Table 2.2. The model equation are:

$$R = R_0 + Q(1 - e^{-bp}) \tag{2.7}$$

where material coefficients R_0, Q and b are the initial yield, strength the maximum amount of hardening and the rate of saturation respectively. Variable p is the cumulated plastic strain.

Finally the isotropic hardening is integrated to the viscoplastic potential as follows:

$$f = \sigma_{eq} - R \tag{2.8}$$

$$\dot{p} = \left\langle \frac{f}{K} \right\rangle^{n}, \dot{\varepsilon}^{\mathbf{p}} = \dot{p}\mathbf{n} \tag{2.9}$$

Equation (2.9) corresponds to the classical Norton creep power law. K and n are viscoplastic Norton law coefficients, the coefficients K and n must be non-zero. n is the local normal to the viscoplastic potential surface and $\dot{\varepsilon}^{p}$ is the von Mises equivalent viscoplastic rate. The coefficients are chosen to normalize the stress term, $< f >$ denotes the positive part of f.

Table 2.2: Macromechanical constitutive equation parameters

Elasticity	Norton law	Isotropic hardening
E 72 GPa	n 2.6	R_0 75 MPa
ν 0.33	K 830	Q 155 MPa
		b 7.7

Model simulations with optimised parameters fit experimental tensile curves well for the three values of strain rate (see Figure 2.19). However, as stress and strain anisotropy were not considered either the experiment or in the proposed model (see Figure 2.20), particular attention was paid to the model predictions of the plastic behaviour of notched specimens, which may be strongly affected by in–plane anisotropy (see Chapter 3).

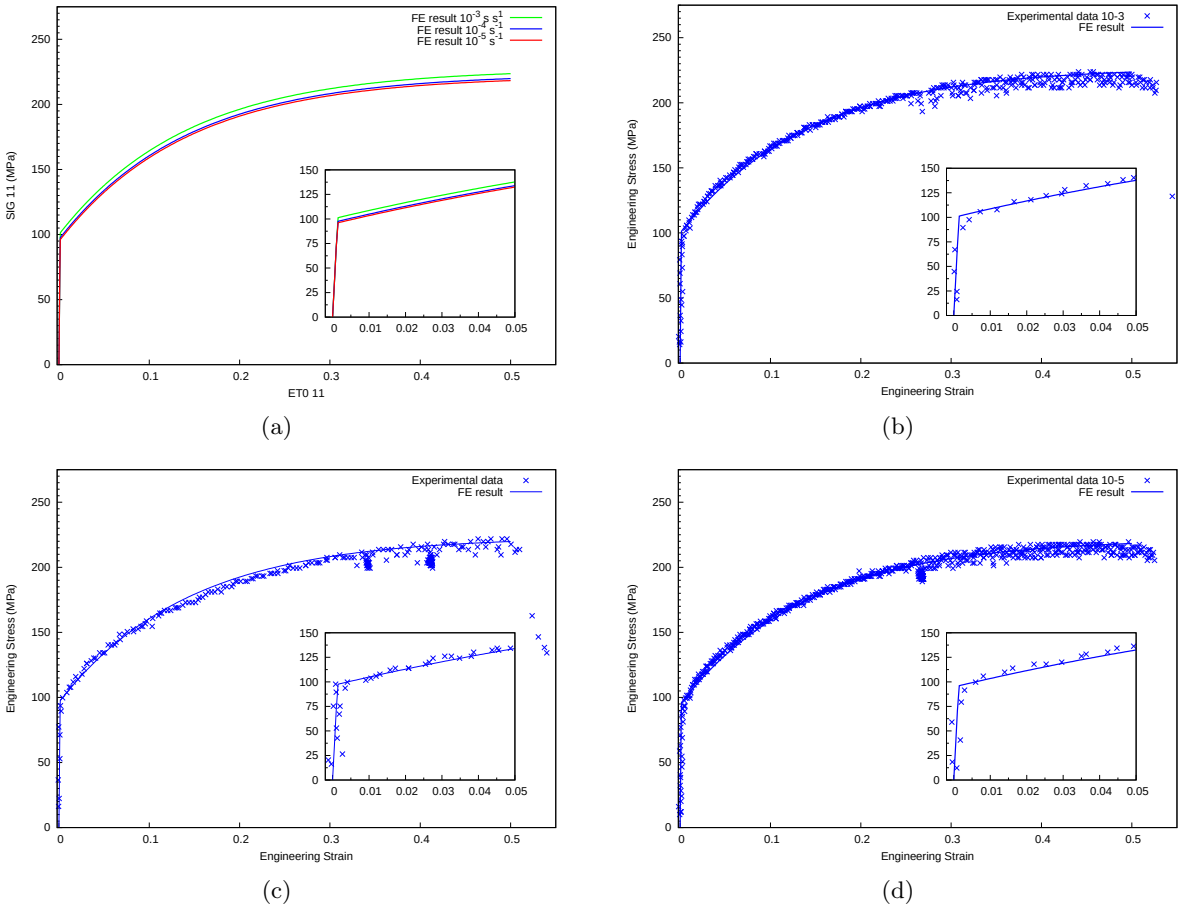

Figure 2.19: Comparison between experimental data with FE results for the different tensile tests

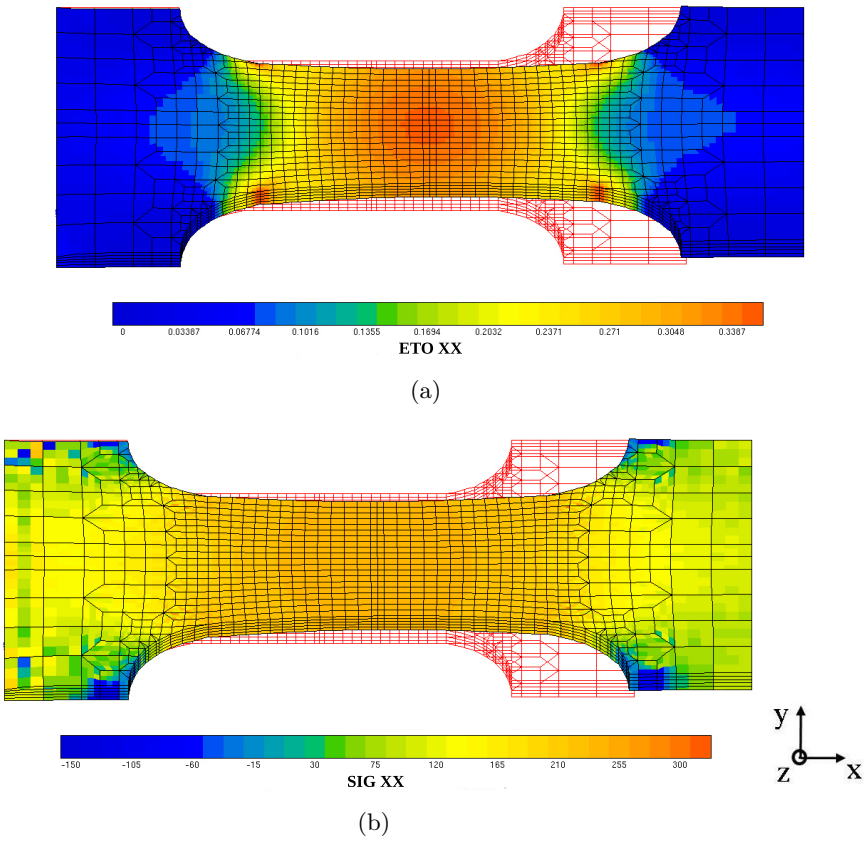

Figure 2.20: (a) Total strain distribution along direction x and (b) axial stress maps after 30 % applied strain

It can be noticed that for large amounts of strains, the wavy shape of the tensile curve is due to the Portevin–Le Chatelier effect. Intergranular fracture occurs at low strain state, thus the Portevin–Le Chatelier effect will not be taken into account in this study.

2.6 Conclusions

It was shown in this chapter that despite its excellent corrosion resistance, the surface of AA5083 becomes brittle over a depth of 5 µm when exposed to: (i) β phase precipitation at grain boundaries, (ii) cathodic hydrogen charging as proposed by Tanguy et al. (2002) and (iii) plastic strain < 5 %. Moreover, observations of surface cracked grain boundaries reveal that the fracture mechanism is microductile for the metallurgical state and hydrogen charging conditions used in this study.

Additionally, microstructure and texture analyses reveal that surfaces of an amount of 500 grains can be considered as representative of the material for in-situ characterisation and analysis of grain boundary cracking during a tensile test. Furthermore, texture of the material both before and after a small tensile strain show any prefered orientation up to 5 % applied strain. This result supports the use of an isotropic macroscopic model to describe the plastic flow behaviour at the macroscopic scale.

To this aim, this plastic flow behaviour of the material was characterised and modelled in uniaxial tension, to be applied to the mechanical analysis of the notched specimens in the

next chapter and as a reference for the calibration of the crystal plasticity model in Chapter 4.

Résumé

Ce chapitre part du fait que malgré son excellente résistance à la corrosion, l'alliage AA5083 peut devenir fragile en surface sur une profondeur de 5 µm. Pour obtenir ce type de fragilisation le matériau doit (i) présenter une précipitation de phase bêta continue ou semi-continue aux joints de grains ; (ii) être chargé en hydrogène et (iii) être soumis à une déformation plastique (typiquement de quelques % en traction uni-axiale).

Les premières analyses des facettes de rupture intergranulaire après essai interrompu, puis poursuivi par une fissuration en fatigue révèlent que le phénomène de rupture étudié est de nature micro ductile aux joints de grains pour l'état métallurgique et les conditions de chargement en hydrogène utilisés dans cette étude. Les analyses de la texture et de la microstructure du matériau démontrent qu'une surface englobant 500 grains peut-être considérée comme une surface représentative à la fois en termes de nombre d'événements de rupture observables et en termes de comportement du matériau en surface.

L'analyse de l'évolution de la texture du matériau avant et après une déformation de 5% montre l'apparition d'une faible texture d'orientation. En admettant que cet effet de texture est négligeable il devient possible dans un premier temps de modéliser le comportement du matériau à l'aide d'une loi de comportement macroscopique et isotrope.

Ce modèle macroscopique, une fois calibré pour décrire le comportement du matériau en traction uni axiale, a été utilisé sur une éprouvette à double entaille identique à celle utilisée expérimentalement. Le modèle macroscopique pourra ainsi être considéré comme une référence pour la calibration du modèle de plasticité cristalline mis en œuvre pour les calculs à l'échelle microscopique du chapitre 4.

Chapter 3

Experimental Study of Crack Initiation

Contents

3.1 Introduction

In order to qualitatively investigate the microcrack initiation process (e.g. fraction of grain boundaries that are sensitive to cracking, local crystal orientation and strain distributions at the onset of cracking) and to provide quantitative data that are useful for modelling (e.g. strain fields, local orientation of grain boundaries that crack first), this chapter reports an experimental investigation on the grain-level heterogeneous plastic deformation behaviour under uniaxial tension in order to identify the deformation conditions that could be related to the microcracks initiation phenomenon.

The experimental methodology of this work consists of interrupted tensile tests of the aluminium multicrystal with the help of electron backscattered diffraction for local texture measurements (Adams 1993, Schwartz et al. 2000) and with digital image correlation for local in-plane surface deformation measurements (Bruck et al. 1989, Vendroux and Knauss 1998, Tong 1997, Smith et al. 1998, Li 2000, Schroeter and McDowell 2003). A schematic representation of the experimental strategy is shown in Figure 3.1.

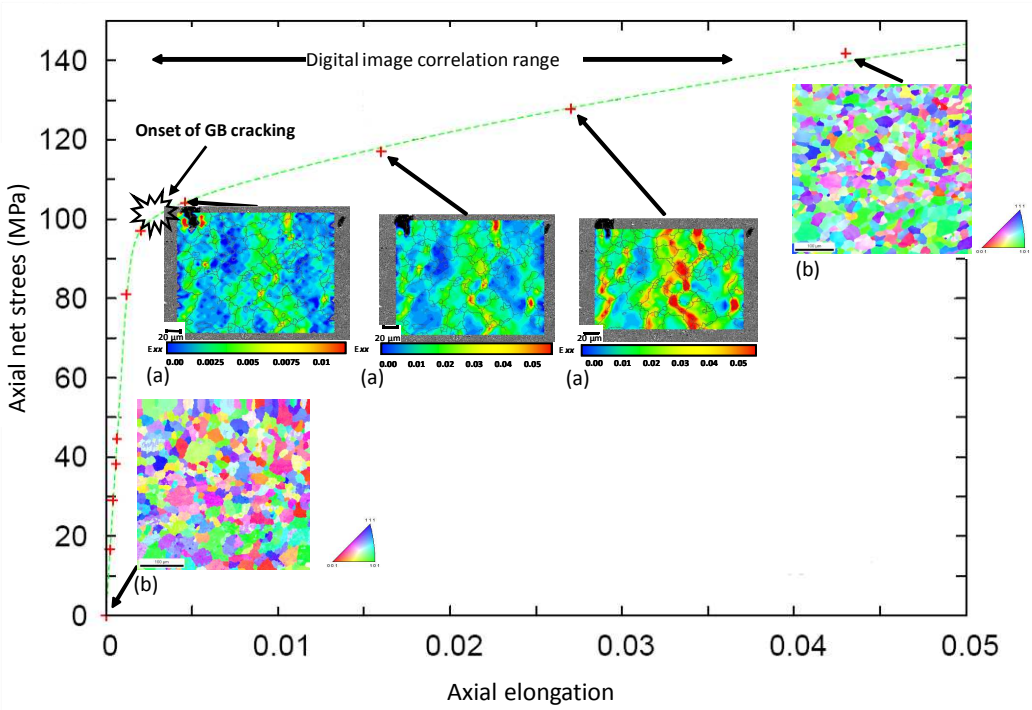

Figure 3.1: Schematic representation of the experimental strategy. (a) Image correlation results (ε_{xx}) and (b) EBSD measurements before and after the test.

3.2 Experimental Procedure for Crystal and Strain Field Measurements

3.2.1 Strategy for experimental measurements

Tensile test specimen with double notch at the centre were used in order to localise strains in the central zone of 1 mm^2 (see Figure 3.2). After the above mentioned surface preparation the studied zone was delimited by fiducial microindentation marks (see Figure 3.3). This microindentation markers were used as optical extensometer (see Figure 3.3) to confirm average results obtained by digital image correlation. The applied macroscopic forces was also confirmed with the use of the macroscopic model calibrated in Chapter 2 (see Figure 3.4). Duplication of strain/stress measurements during in-situ tensile test assured correct results and highlight potential sources of errors.

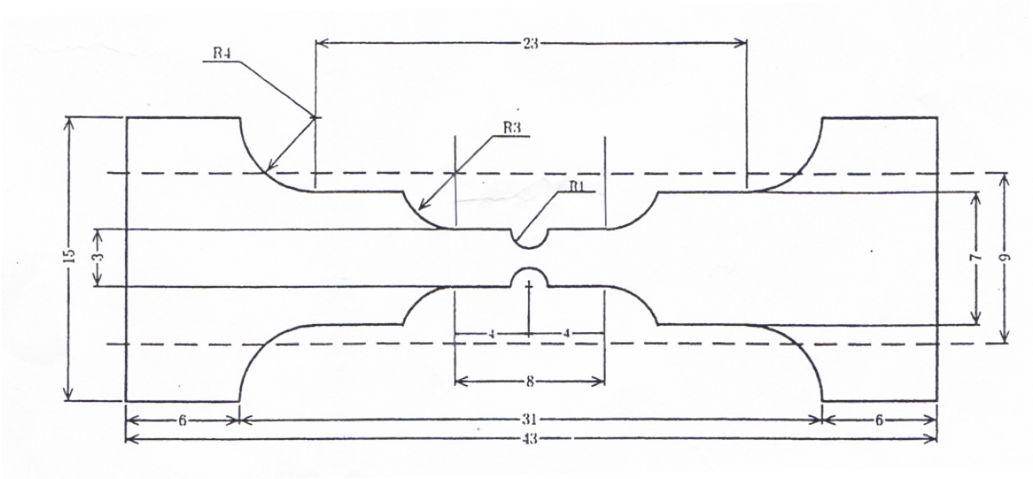

Figure 3.2: In-situ specimen geometry. Dimensions are in mm (thickness 1mm).

For each tests a 450×450 µm region was selected for analysis at the "mesoscopic" scale and crystal orientations were determined by EBSD mapping (see Figure 3.3(b)) before and after the applied total strain of 5%. In average the EBSD analyses revealed that the regions with 500 grains constitute a representative region of the material both in terms of its deformation and microcrack behaviour (see Chapter 2).

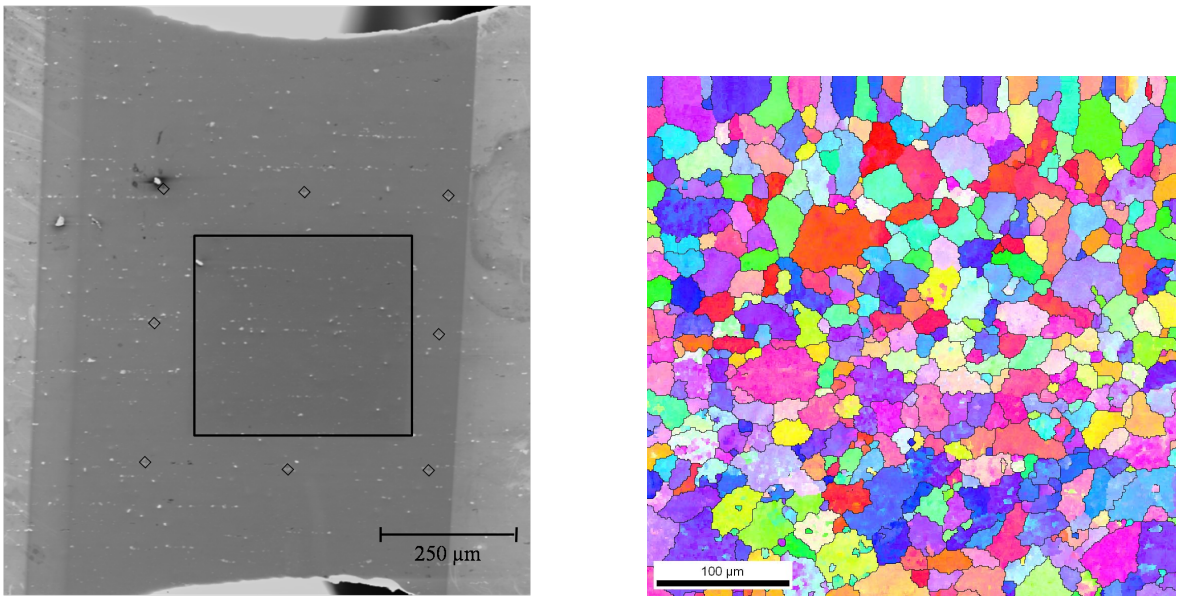

(a) (b)

Figure 3.3: Region of interest: (a) Region delimited by micro-indentation marks (empty diamonds) used to calculate the average strain conditions to be applied to the FE model and (b) region analysed by EBSD in the black square.

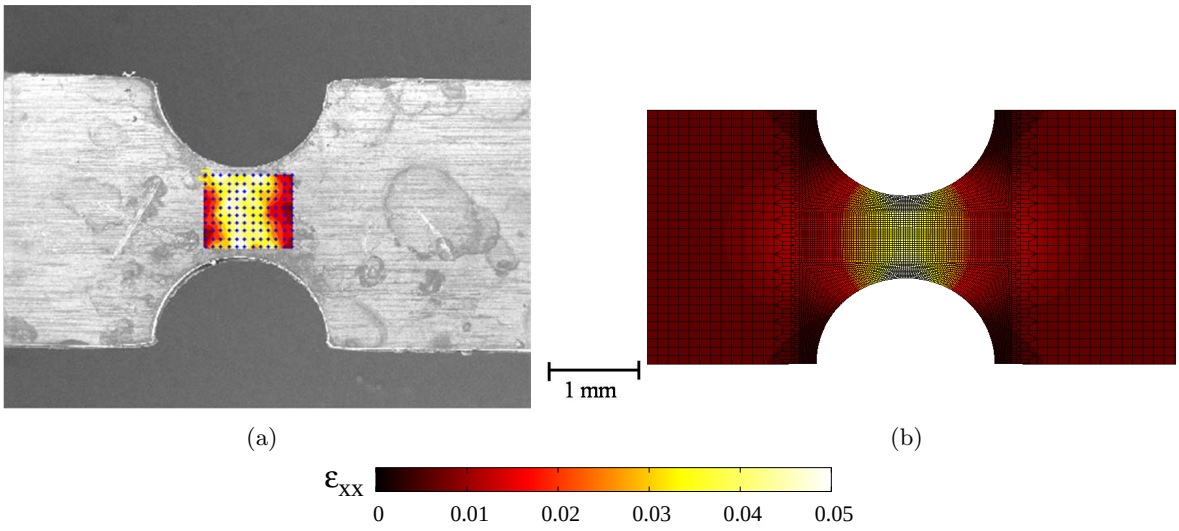

(a) (b)

Figure 3.4: Comparison between macroscopic measurements of ε_{xx} at 4.5% applied macroscopic strain (a) experimental measurements (b) prediction by using the "macroscopic model".

3.2.2 Specimen preparation

The use of both EBSD analysis and DIC techniques required a specific surface finish. After machining, specimens were recrystallized at 460 °C for 1 h and water quenched to keep Mg in solid solution as explained in the previous section. Then a mechanical polish was performed down to 1 µm in order to remove surface damage. The specimens were then tempered at 150°C for 7 days in order to precipitate the Al-Mg β-phase and relieve any residual stresses that may have been introduced due to mechanical polishing. A final polishing step was applied from 1 µm down to 1/4 µm before a chemical polish with colloidal silica to optimize the surface state for EBSD scanning (see Figure 3.5(a)). After EBSD mapping, the region of interest was precharged with hydrogen as described previously. To be able to measure the strain heterogeneities inside the grains, the surface of interest had to be patterned with a specific speckle. To get efficient results by digital image correlation at this scale, surface heterogeneities have to be less than 200 nm in size. Slight corrosion pits observed after hydrogen charging were kept and employed as surface heterogeneities as shown in Figure 3.5(b), micrograph acquired with backscattering electron emission (QBSD) was also used in order to easily detect microcracks initiation (Figure 3.5(d)).

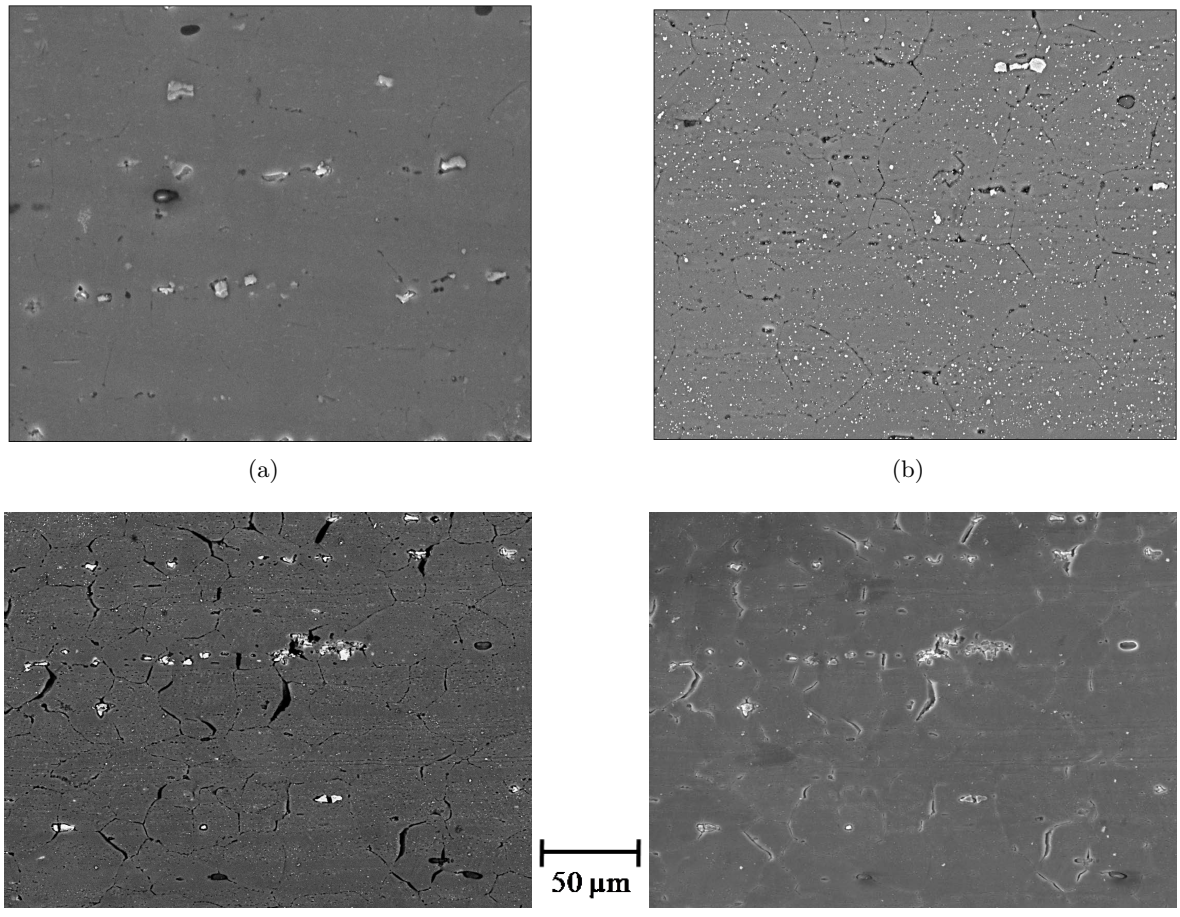

Figure 3.5: Optimum surface preparation for (a) EBSD (before hydrogen charging), (b) for digital image correlation (after hydrogen charging), micrograph after 5% applied strain by (c) secondary electrons (SE) and (d) backscatering electron emission (QBSD).

3.2.3 Multi-scale approach

The complexity of intergranular microcracking involved many mechanical problems at very different scales from atomic to microscopic and then macroscopic scales. Thus, experimental investigations presented here were conducted through the spatial resolution range allowed by digital image correlation used with Scanning Electron Microscopy (SEM)

In such experimental technique a compromise has to be found between resolution and recording time for SEM images. Recording time increase drastically with the image resolution from 5 seconds for images composed by 1024 × 768 pixel to 50 seconds for 2048 × 1536 pixel images. The time needed for image recording required interrupting the tensile test with a prescribed constant displacement. Such interruptions of the tensile test affect kinematic mechanism of the material behaviour and may induce stress relaxation that can be sources of mismatch in the intergranular cracking identification. In order to minimise this disadvantage tests with 2 different resolutions were conducted and compared. Image resolution and considered region of interest are illustrated in Figure 3.6, 3.7, 3.8. 10 in-situ tensile tests were performed in this work, among them 3 representative tests, namely for specimen (I, II, III), are presented here after. For each specimen presented digital image correlation parameter and resolution are reported in Table 3.1.

With the approach proposed by Bergonnier et al. (2005), for a ZOI of 32 × 32 pixels and an average displacement equal to 0.5 pixel, the displacement resolution is equal to 1.4×10^{-2} pixel. Since the pixel size is about 0.12×0.12 µm the displacement resolution for each magnifications is about 0.5 µm, 0.12 µm, 0.07 µm for respectively large, medium and low magnification images of Specimen (I). Despite the optimistic calculation of spatial resolution proposed by Bergonnier et al. (2005), in this work the spatial resolution was identified as 3 times the ZOI size (see Tab. 3.1). With this method, DIC results inside a range of 0,5% up to 3% of macroscopic strain can be used according to a computed relative error less than 3%, between the first recorded image and other images.

Table 3.1: Digital image correlation parameters

Specimen number	ROI number	ROI size		ZOI size		resolution (µm)
		in pixels	in µm	in pixels	in µm	
I	1	2048 × 1536	800 × 600	36 × 36	14 × 14	4.6
	2, 3	2048 × 1536	250 × 150	36 × 36	4.4 × 4.4	1.4
	4, 5	2048 × 1536	150 × 100	36 × 36	2.6 × 2.6	0.7
II	1	2048 × 1536	800 × 600	128 × 128	25 × 25	8.4
	2, 3, 4, 5	2048 × 1536	250 × 150	128 × 128	10 × 10	3.3
III	1	1024 × 768	500 × 520	64 × 64	25 × 25	8.4

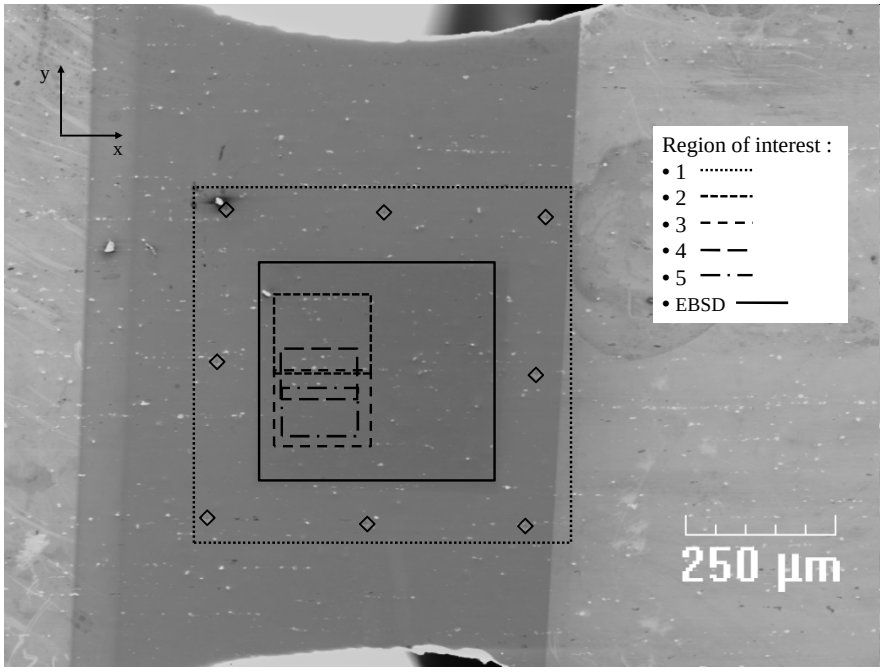

Figure 3.6: Region of interest for Specimen (I): region delimited by micro-indentation marks, region analysed by EBSD (empty diamonds), and SEM image acquisition regions for digital image correlation for (1) low (2, 3) medium and (4 ,5) high magnifications.

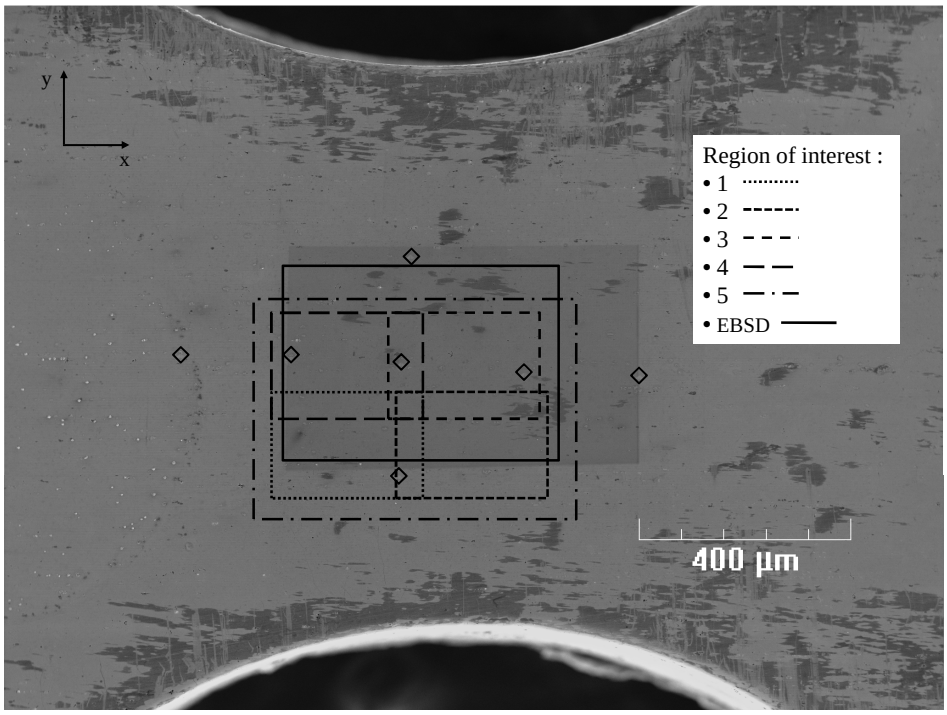

Figure 3.7: Region of interest for Specimen (II): region delimited by micro-indentation marks, region analysed by EBSD (empty diamonds), and SEM image acquisition regions for digital image correlation for (1) low and (2, 3, 4, 5) medium magnifications.

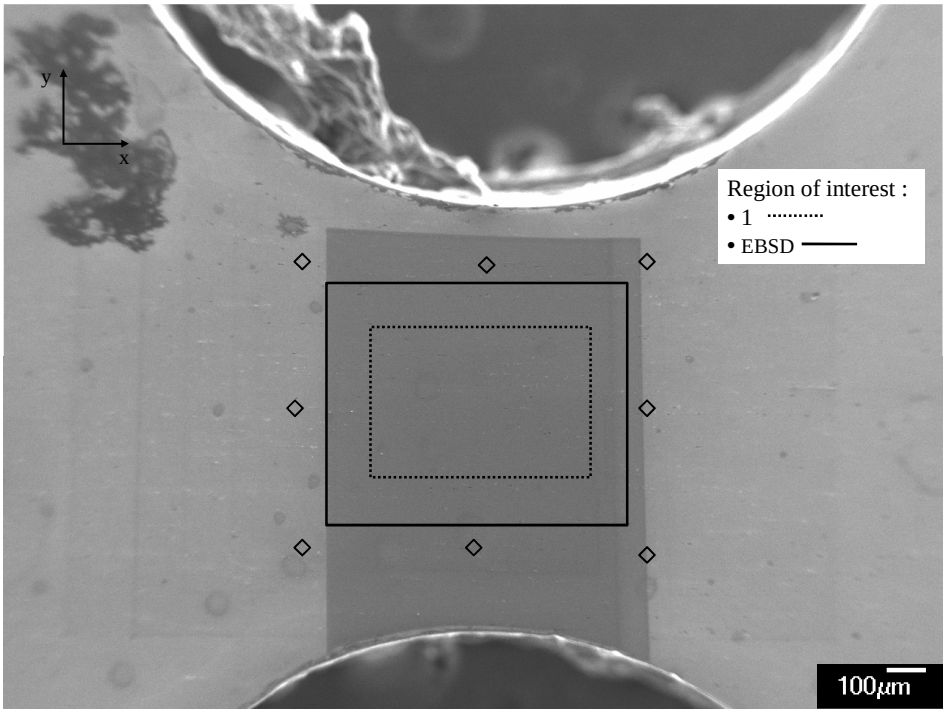

Figure 3.8: Region of interest for Specimen (III): region delimited by micro-indentation marks, region analysed by EBSD (empty diamonds), and SEM image acquisition regions for digital image correlation for (1) low magnifications.

3.2.4 Uniaxial in-situ tensile test

The double notched tensile specimens (Figure 3.2) were pulled using a mini-tensile testing machine in SEM vacuum chamber. The machine has a dimension of 502×327×250 mm, a total screw travel of 150 mm, and a maximum load capacity of 5000 N. A computer integrated stepping motor control was used to carry out the tensile test at an imposed displacement rate of 0.36 mm/min equivalent to an average strain rate of $4.10^{-4}s^{-1}$ in the regions that were chosen for in-situ observations. The microindented decorated specimen surface was imaged under both secondary electron (SE) and backscatter electron (BSE) imaging modes and a set of 8-bit gray scale digital images was obtained. The specimen was then loaded up to a total strain of 5%. A series of digital images of the microindented decorated surface were acquired in-situ at several deformation levels in order to record the in-plane strain field evolution and identify intergranular crack initiation phenomenon.

3.2.5 Displacement field measurement by Digital Image Correlation

In order to investigate possible relationship between strain field heterogeneity and initiation of intergranular microcracks, displacement fields measured during mechanical tests were analysed at the grain scale. Various optical techniques can be use to achieve this goal (Rastogi 2000). Recent advances in digital image acquisition, in terms of fine spatial resolution and quality allow for strain field measurements for scale of observation ranging from nanoscopic to macroscopic observations, through the Digital Image Correlation (DIC) technique (Sutton et al. 2000). The digital image correlation technique has been applied successfully to a number of different materials and geometries even containing cracks (McNeill et al. 1987, Forquin et al. 2004, Réthoré et al. 2005, Kuntz et al. 2006, Roux and Hild 2006).

The technique consists in analyzing displacement fields from textured surface images through the estimate of displacement by cross–correlation of zones of interest or mimimization of the sum of differences. Under loading the observed surface moves and deforms, by acquiring images for different load steps by using scanning electron microscopy, it is possible to determine the in–plane displacement field. To increase the measurable displacement range, a multiscale setting developed algorithm by Hild et al. (2002) was used. This enriched cross–correlation function is quickly evaluated by using Fast Fourier Transforms (FFT). The displacements can also be assumed to be described by Q4P1–shape functions relevant to finite element simulations (Zienkievicz and Taylor 1989). Consequently the displacement evaluation is formatted to be easely used for further finite element modelling.

In this section, the general concept of the digital image correlation is first introduced. Then, a particular attention was made on developements achieved by Besnard et al. (2006), which allow for successful investigation at microscopic scale with a very high spatial resolution accuracy.

3.2.5.1 Correlation principle

The aim of the digital image correlation method is to match square regions call Zones Of Interest (ZOI), from a reference to a deformed surface of the region of interest (ROI). For example in Figure 3.9 the correlation mesh used for the DIC computation is shown. Grey level scalar functions $g(\mathbf{x})$ and $f(\mathbf{x})$, respectively, for the reference image and the deformed image give the grey level at each pixel coordinate. The two grey–level functions f and g are related through the conservation of the gray level by the displacement field $\mathbf{u}$ with:

$$f(\mathbf{x}) = g[\mathbf{x} + \mathbf{u}(\mathbf{x})] \tag{3.1}$$

In the following, the noise induced by image acquisition can be neglected because of its low amplitude compare to those of f and g. By making the assumption that the reference image is differentiable, a first order Taylor expansion yields

$$f(\mathbf{x}) \simeq g(\mathbf{x}) + u(\mathbf{x}) \cdot \nabla f(\mathbf{x}) \tag{3.2}$$

The displacement field is only measurable along the direction of the intensity gradient. Thus, additional assumptions have been proposed by Besnard et al. (2006) to regularize and solve the problem. It consists in mimimizing the sum of squared differences. To determine u with a reasonable accuracy, an objective function Φ is introduced and integrated over the whole studied domain and then minimized:

$$\Phi = \iint (f(\mathbf{x}) - g(\mathbf{x} + \mathbf{u}(\mathbf{x})))^2 dx \tag{3.3}$$

The strategy chosen by Besnard et al. (2006) to solve the problem consists in decomposing the displacement field as a linear combination of scalar shape functions $\psi_n(x)$:

$$\mathbf{u}(\mathbf{x}) = \sum_{\alpha,n} a_{\alpha n} \psi_n(x) \mathbf{e}_\alpha \tag{3.4}$$

The linearized quadratic form of the objective function is thus expressed as:

$$\Phi = \iint \left[\sum_{\alpha,n} a_{\alpha n} \psi_n(\mathbf{x}) \mathbf{e}_\alpha \nabla f(\mathbf{x}) + f(\mathbf{x}) - g(\mathbf{x}) \right]^2 d\mathbf{x} \tag{3.5}$$

The minimization is then computed from the solution of a linear system of equations:

$$\sum_{\beta m} a_{\beta,m} \iint_{\Omega} \left[\psi_m(\mathbf{x})\psi_n(\mathbf{x})\partial_\alpha f(\mathbf{x})\partial_\beta f(\mathbf{x})\right] d\mathbf{x} = \iint \left[f(\mathbf{x}) - g(\mathbf{x})\right] \psi_n(\mathbf{x})\partial_\alpha f(\mathbf{x}) d\mathbf{x} \tag{3.6}$$

This system can be written in a matrix form as

$$[\mathbf{M}]\{\mathbf{w}\} = \{\mathbf{m}\} \tag{3.7}$$

where $\{\mathbf{w}\}$ is a vector containing all the unknown components, matrix $[\mathbf{M}]$ and vector $\{\mathbf{m}\}$ are quantities dependent upon f, g, and ψ_n directly read from Equation (3.6):

$$M_{\alpha n \beta m} = \iint \left[\psi_m(\mathbf{x})\psi_n(\mathbf{x})\partial_\alpha f(\mathbf{x})\partial_\beta f(\mathbf{x})\right] d\mathbf{x} \tag{3.8}$$

and

$$m_{\alpha n} = \iint \left[g(\mathbf{x}) - f(\mathbf{x})\right] \psi_n(\mathbf{x})\partial_\alpha f(\mathbf{x}) d\mathbf{x} \tag{3.9}$$

The displacement field is then evaluated through the minimization of the global error density by successive iterations.

3.2.5.2 The Q4P1–shape function

A large variety of function ψ_n can be applied in Equation (3.4). Finite element shape functions are particularly attractive because of the interface they provide between the measurement of the displacement field and a micromechanical modelling based on the same mesh and using constitutive equations.

Moreover, since the digital image is naturally partitioned into pixels, it is appropriate to choose a square shape for each element (see Figure 3.9). The displacement decomposition is therefore particularized to account for the previous shape functions of a finite element discretization. Each component of the displacement field is treated in a similar manner, and thus only scalar shape functions $N_n(x)$ are introduced to interpolate the displacement $u_e(x)$ in an element of the region of interest (Besnard et al. 2006).

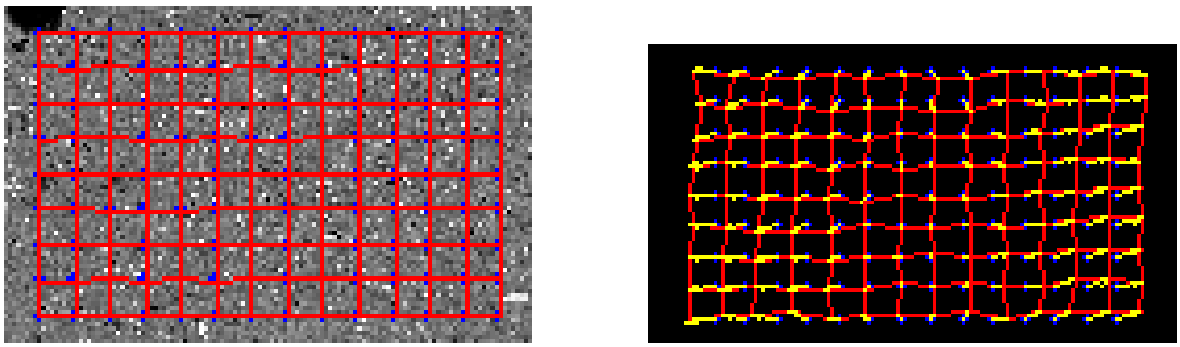

(a) (b)

Figure 3.9: For a region similar to ones use in this study (a) initial mesh in blue dots and deformed mesh in red line (b) amplified correlation mesh

The interpolated displacement field is thus globally continuous as in FE computations. Consequently, there is only one correlation parameter defined by the element size, l. As

previously discussed, the very first step is a determination of the global displacement performed on coarse images, so as to capture the large amplitudes of the displacement field, and progressively finer details are restored. This linear system naturally leads to subpixel displacements.

3.2.5.3 Sub–pixel interpolation

As explained previously f represents the so-called 'texture' of the initial image, discretized at the pixel level. Gradient $\nabla f(x)$ is then used in a Taylor expansion. However, the definition of a gradient requires some care to be taken. In Schreier et al. (2000) a cubic spline was argued to be very convenient and to give accurate results. In CorreliQ4 a different approach is proposed, namely, a Fourier decomposition. From such approach a mapping can be more easily defines an interpolated value of the grey level at any point between two given pixels (i.e. sub–pixel interpolation). Moreover, sub–pixel interpolation results can further be processed to computing a gradient at any point.

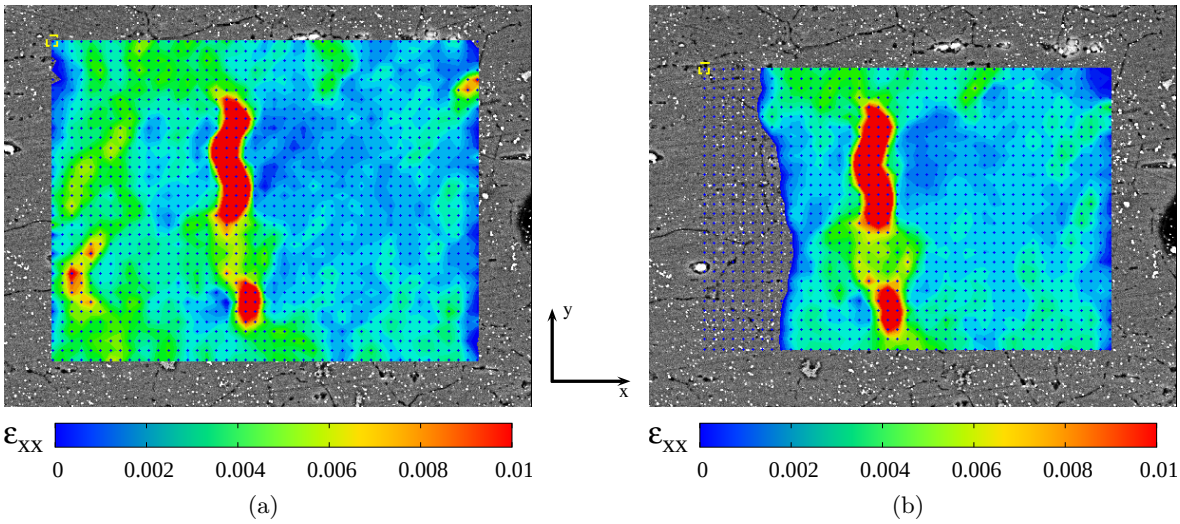

Figure 3.10: Strain distributions (a) with sub–pixel interpolation (b) without sub–pixel interpolation

However, Fourier transforms over a finite interval implicitly assume periodicity. Thus, differences between left–right and up–down border induce artefacts close to edges (Figure 3.10). In order to reduce this edge effects, Hild et al. (2002) has proposed to enlarged by two the integer power for zone of interest (ZOI) and consider a new frame around each element. The enlarged ZOI is only used for FFT purposes, with this new approach gradients are better estimated (Figure 3.10). Finally, only original ZOI are considered and edge artefacts are significantly reduced.

3.3 Identification of Crack Initiation Criterion

3.3.1 Effect of local strain incompatibilities at grain boundaries

It is now well documented that grain boundary constraint can play an important role in the deformation behaviour of polycrystalline materials. This constraint effect is known to result from the requirement of continuity of stress and strain across a grain boundaries (Hirth 1972). Elastic and plastic deformation in the vicinity of grain boundaries are incompatible due to the different elastic constants and slip geometry on either side of the grain boundary. Consequently additional internal stresses are induced in order to satisfy the continuity requirements.

3.3.1.1 Effect of crystal orientation

The local study of misorientation profiles before and after deformation across an uncracked grain boundary and a not cracked grain boundary, respectively, before and after deformation (Figure 3.11 and 3.12) does not highlight the role of disorientation grain boundary in the intergranular fracture. This finding indicates that strain incompatibility at the grain boundary in this case is not a sufficient criterion of intergranular cracks, as sometimes observed in intergranular fracture (see a review in Gourgues (2002)).

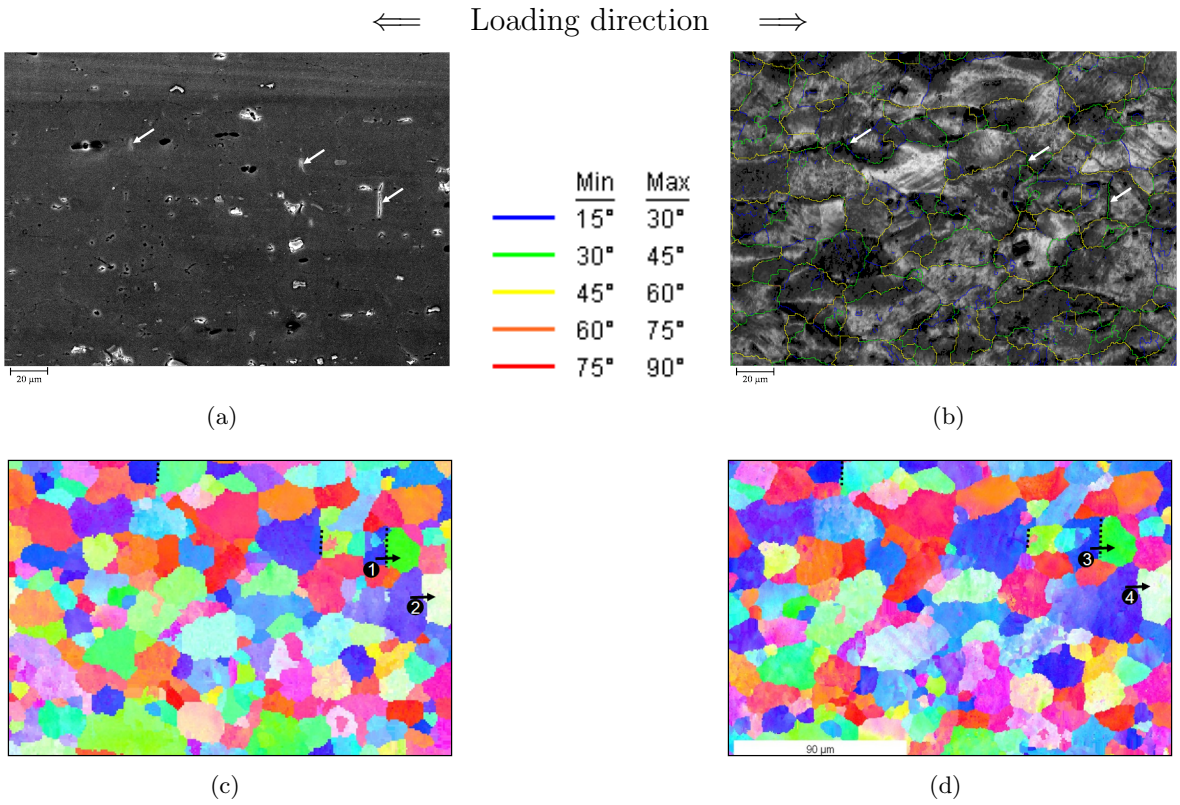

Figure 3.11: For Specimen (II) (a) SEM after 5% axial elongation, (b) misorientation angle, (c) and (d) inverse pole figure map before and after 5% axial elongation.

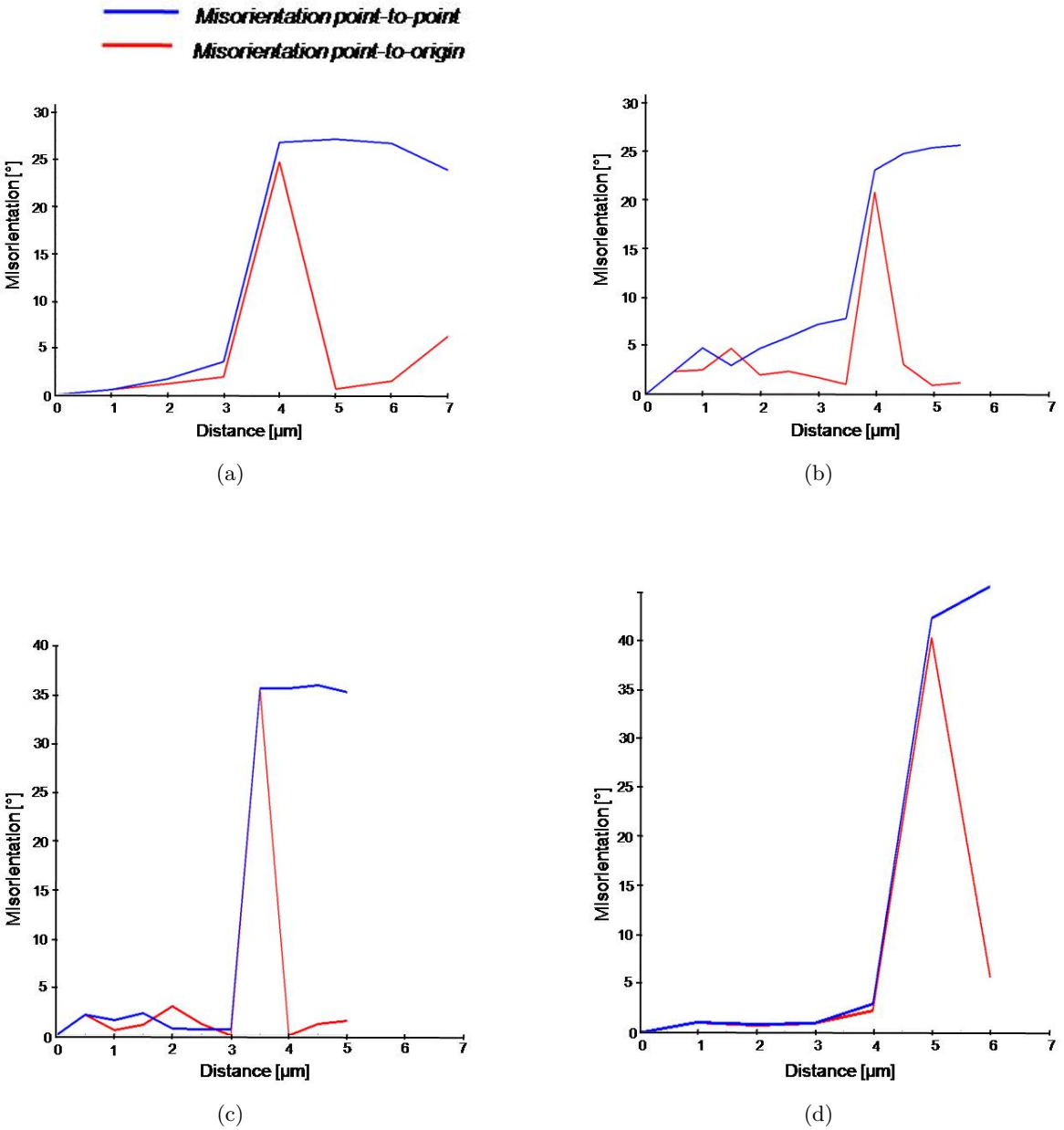

Figure 3.12: For Specimen (II), misorientation profile (a) and (b) for cracked grain boundary namely (1) and (3) in Figure 3.11, and (c) and (d) for not cracked grain boundary namely (2) and (4) in Figure 3.11

3.3.1.2 Effect of misorientation angles

In order to understand the effects of grain boundaries misorientations as well as grain orientation on the microcrack initiation, orientations of more than 2000 grains were measured by using the EBSD method. Apart from the grains that were involved in microcracking, some other grains without microcracks were also examined for the purpose of comparison.

Commonly grain boundaries are classified into high– and low–angle boundaries according to the misorientation angle value. Boundary with a misorientation angle value below 15° are considered as low angle grain boundary and accepted to be due to edge dislocation arrays. Moreover an often used separation takes into account both the misorientation angle and the

rotation axis, this classification distinguishes random and coincidence site lattice (CSL) grain boundaries. However, due to the specific nature of the industrial aluminium alloy used in this work coincidence site lattices with Σ–values below 49 are very rare and that previous work conducted by Wang et al. (1986) found that for FCC polycrystals fatigue microcraks preferentially initiate at random grain boundary.

From misorientation measurements as illustrated in Figures 3.13 and 3.11 one can conclude that microcracks initiate for high–angle grain boundaries with a misorientation angle between 30°and 60°that constitute in average 72% of grain boundaries in the studied material. It is widely accepted that is due to the fact that to be cracked these high–angle grain boundaries need less fracture energy. However all these high–angle grain boundaries do not cracked at the same time during the mechanical loading, that means that another mechanism dominates microcrack initiation and that a misorientation based criterion is not sufficient to understand the intergranular microcracking mecanism.

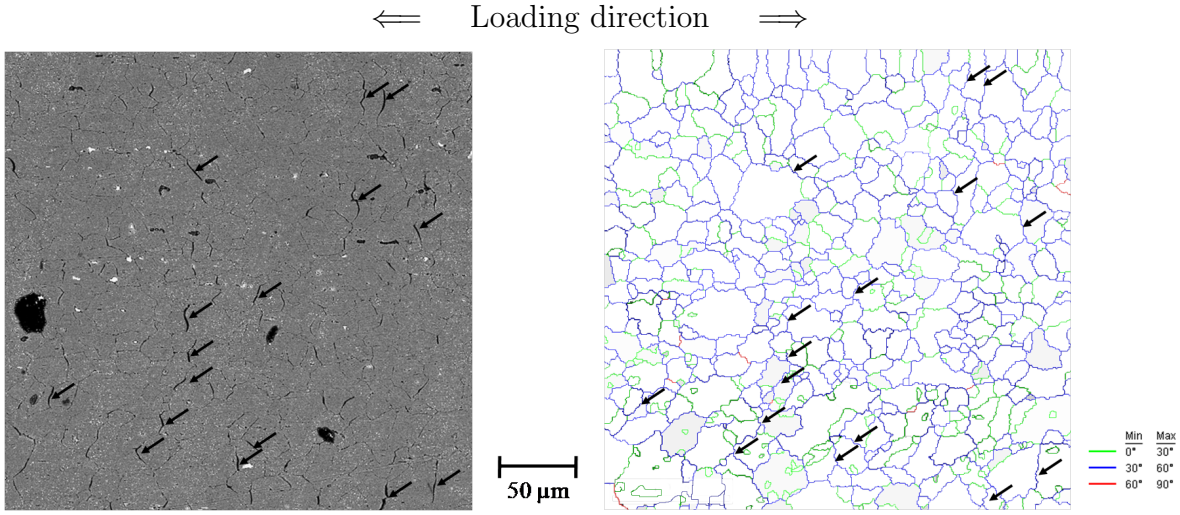

Figure 3.13: For Specimen (I), (a) Scanning electron micrograph of a studied region after 5% macroscopic strain, (b) misorientation angle map

3.3.1.3 Effect of Schmid factor gradient

Grain boundary character can play an important role in the microcracking process due to microstructural differences among various grain boundaries. Therefore, statistical characterization of grain boundary properties can be useful for understanding the mechanisms involved in microcrack initiation. First microstructural investigation have been looked at schmid factor, degrees of misorientation, misorientation angle variation, and the textural homogeneity and or heterogeneity across the grain boundary.

The Schmid factor is a geometrical relationship between the corresponding deformation mode and the direction of the applied force. Thus, Schmid factor mapping can provide a representation of grain that are preferentially oriented to be deformed first and highlight possible deformation mechanisms responsible of microcrak initiation.

The Schmid factors of each of the grains in the scanned regions were determined by defining the 12 slip systems along the 111 planes in the [110] directions. The orientation image mapping analysis software was then used to determine the Schmid factors of each of the 12 slip systems. The Schmid factor of the slip system with the highest resolved shear stress for the defined tensile direction was then reported as the Schmid factor of the grain. An example of a region examined in this work is presented in Figure 3.14. Microcracks are reported on corresponding grain boundaries in Schmid factor map with the help of the micrograph at 5% macroscopic strain (Figure 3.14(a)).

Figure 3.14 shows a surface of 480 × 480 µm with 16 microcraks. Schmid factor mapping Figure 3.14(b) does not show any repetive configuration that exhibits a particular configuration for microcrack initiation. Microcracks appeared indifferently between high and low, low and low or high and high Schimd factor averaged by grain.

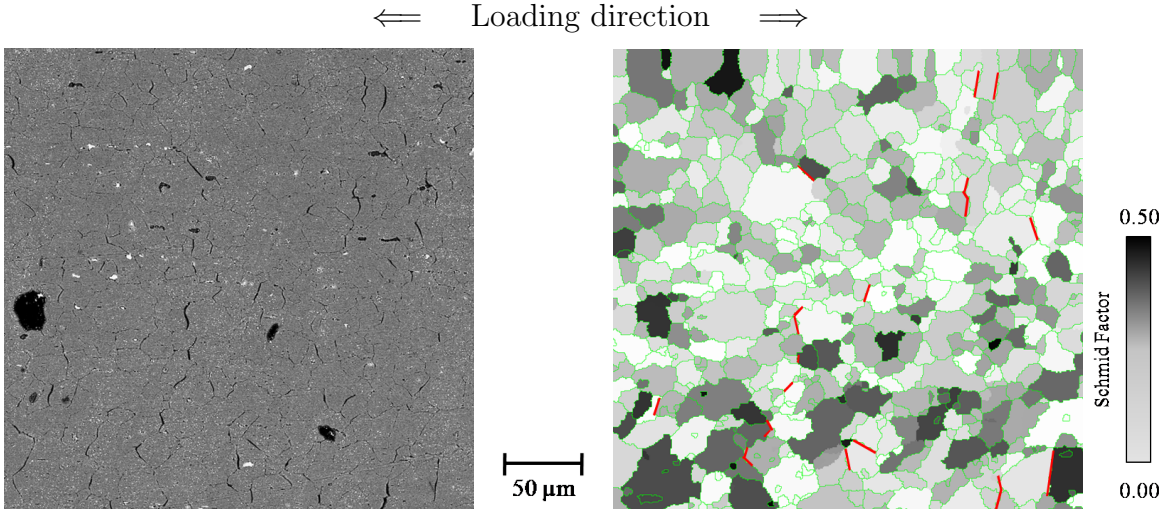

Figure 3.14: For Specimen (II) (a) Scanning electronic micrograph of a studied region after 5% macroscopic strain, (b) corresponding Schmid factor map

However, Schmid factors are based on single crystal under uniaxial loading to predict quantitatively the operating deformation system on the basis of estimations of critical shear stress. Schmid factor does not take into account multiaxial stress conditions due to the

tortous shape of grains. One can conclude that Schmid factor cannot be a proper criterion for microcraks initiation (Gourgues 2002), unlike what was observed in irradiated 316L stainless steel (West and Was 2010).

3.3.1.4 Effect of local strain concentration at grain boundaries

One can observe strain field localisation at some grain boundaries with no resulting intergranular cracking in Figure 3.15. This phenomenon remains unclear but it can be supposed that intergranular constraints remained low because of the capacity of adjacent grains (i.e. grain 1 and 2 in Figure 3.15) to accommodate strains in the same manner. This accommodation probably results from the fact that each grain on either side of the grain boundary are very close or symmetric in terms of orientation and thus are supposed to deform in the same way (i.e. with same slip systems).

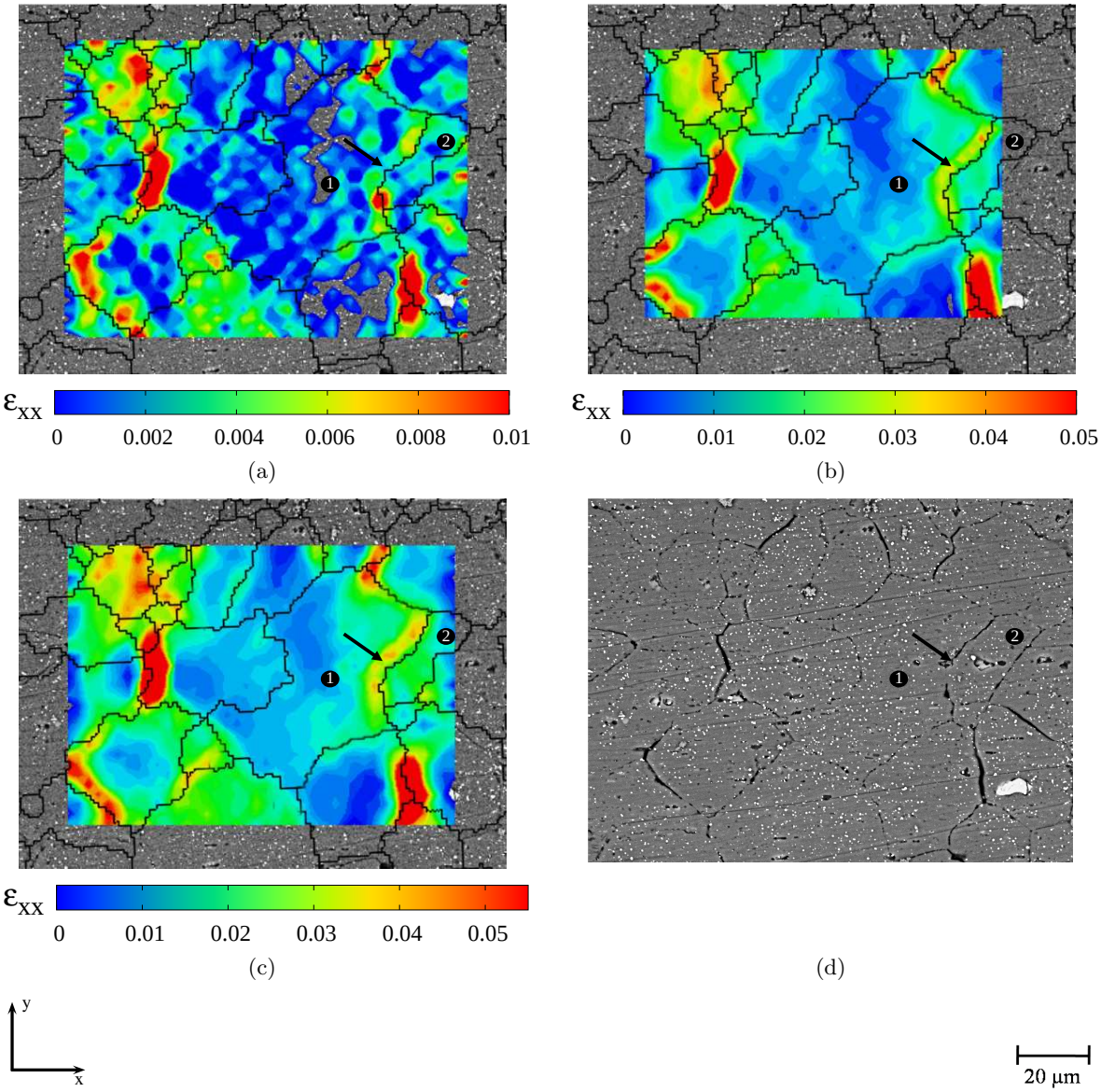

Figure 3.15: Strain distributions for Specimen (I) at small magnification along the x direction for macroscopic applied strains of (a) 0.5%, (b) 1.6% and (c) 2.6%, and (d) SEM image taken after 4.5% applied strain. Black arrow indicates a region with high strain level at a grain boundary that did not crack.

3.3.2 Effect of strain incompatibilities at the aggregate scale

3.3.2.1 Persistant strain band observations

At low magnification, strain field measurements (Figure 3.16) clearly show localised deformed bands oriented 90° and 45° with respect to the loading direction classically observed at this scale (Barbe et al. 2009). The approximate width of the deformed bands is 100 µm (i.e. 4 times the average grain size). The distribution of deformed bands shows a periodic pattern as illustrated in Figure 3.16 and 3.17.

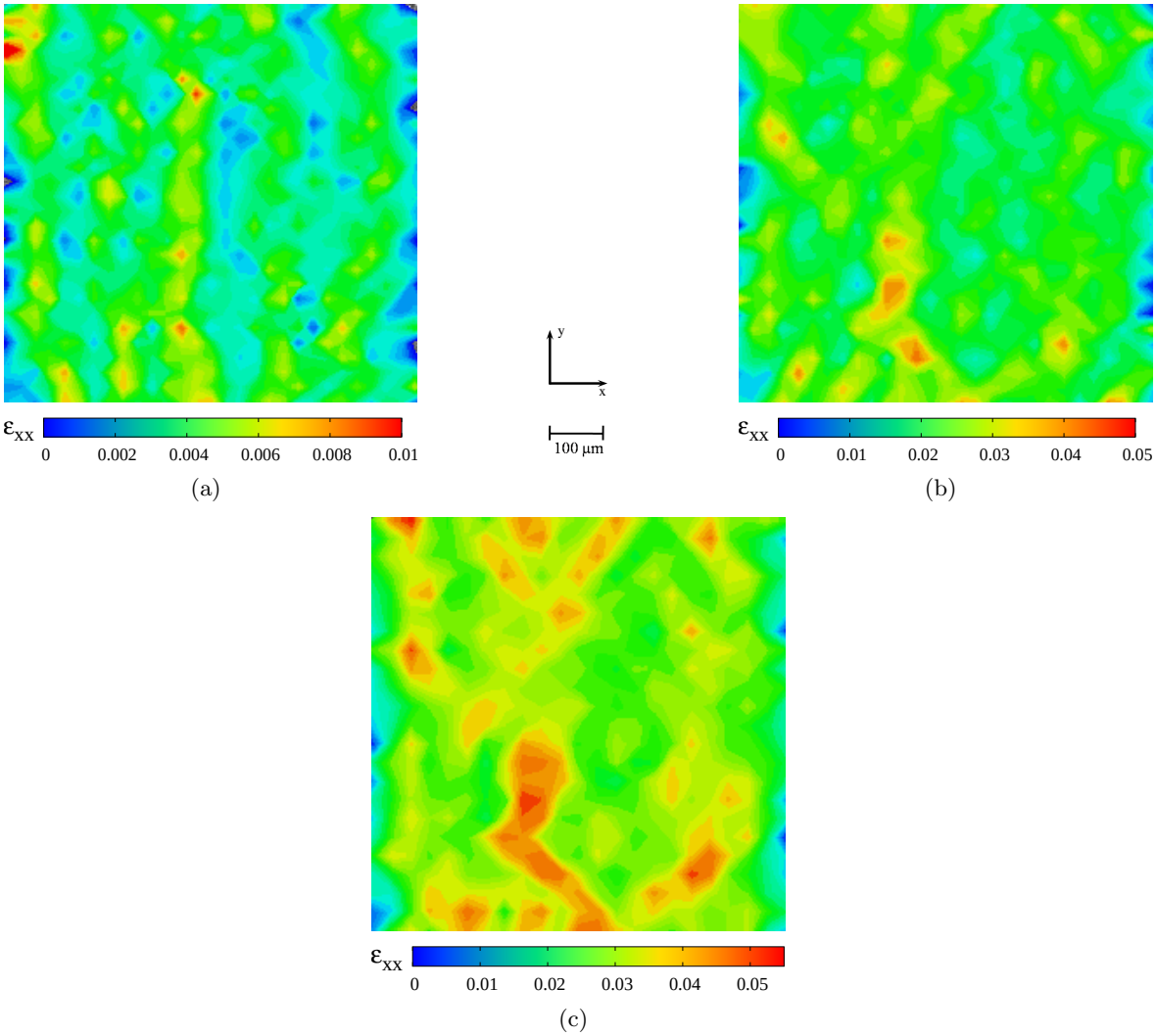

Figure 3.16: Strain distributions on Specimen (I) at low magnification along the x direction for macroscopic applied strains of (a) 0.5%, (b) 1.6% and (c) 2.6%.

In Figure 3.17, we can see that microcracks are located in large deformation bands, which proves that cracks initiation needs a given level of strain. Furthermore, first cracks are observed to nucleate preferentially at grain boundaries normal to the tensile direction at least in the plane of the images (see Figure 3.17). To conclude about the relationship between grain boundary orientation and cracks initiation, the 3D grain boundary morphology will be studied in Chapter 6. These first observations of grain boundaries able to fail confirm that the cracking mechanism is in close relationship with both the grain boundary morphology and the plastic strain of grains.

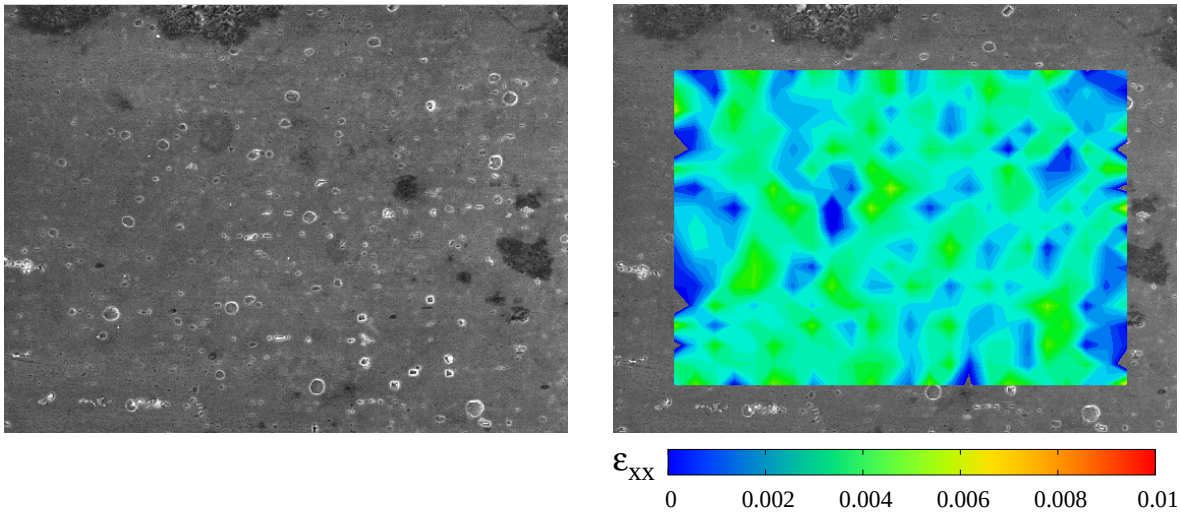
ε_xx
0
0.002
0.004
0.006
0.008
0.01

(a) (b)

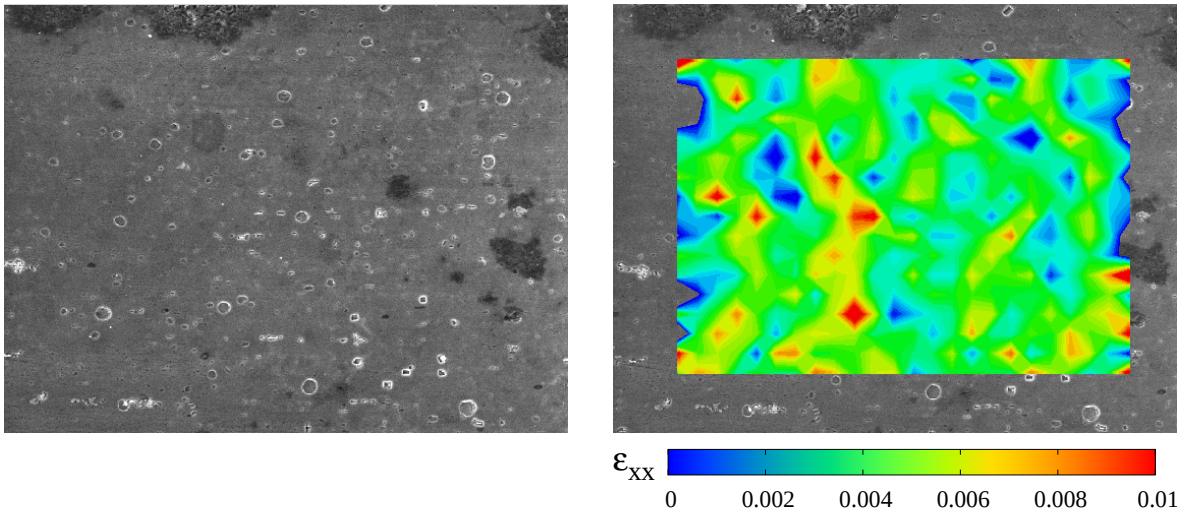
ε_xx
0
0.002
0.004
0.006
0.008
0.01

(c) (d)

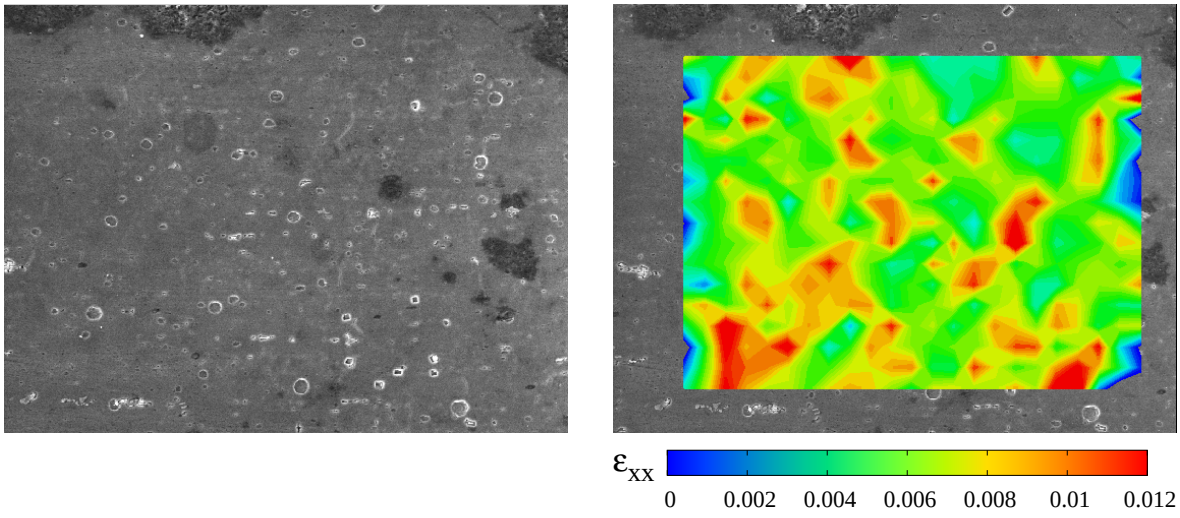
ε_xx
0
0.002
0.004
0.006
0.008
0.01
0.012

(e) (f)

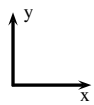
y
x

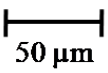
50 µm

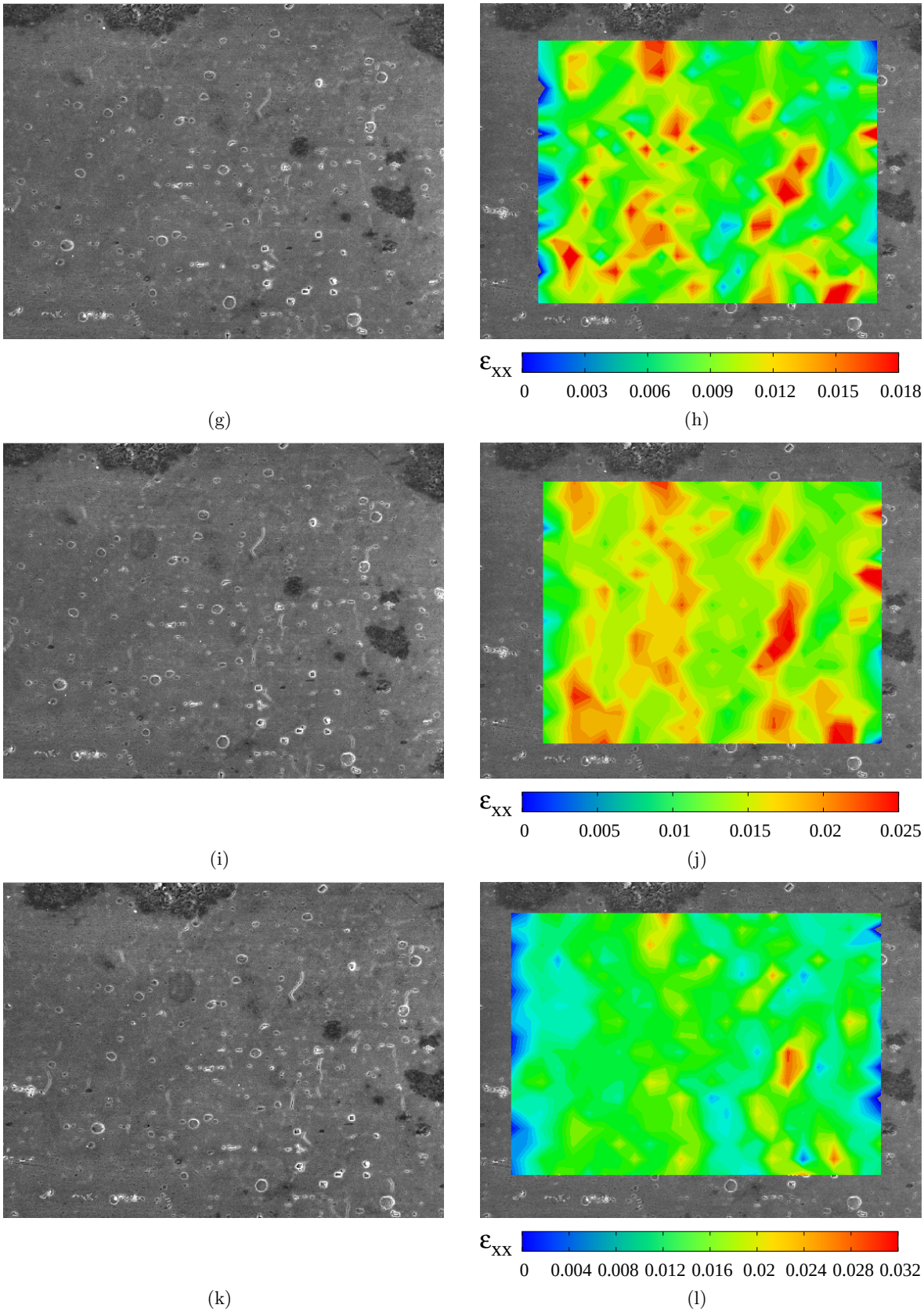

Figure 3.17: Strain distributions in region 1 of Specimen (III) along the x direction for macroscopic applied strains of (b) 0.4%, (d) 0.5%, (f) 0.6%, (h)1.0% (j)1.1% (l)1.6% and (a), (c), (e), (g), (i) and (k) SEM images.

SEM images displayed in Figure 3.17 were continuously acquired i.e. without interrupting the mechanical test. Although such images are of lower quality, they allowed to investigate the onset of surface microcracking.

The intergranular mechanism can be divided into 3 main steps as illustrated in Figure 3.17:
i) Till an applied strain of 0.4% the free surface of the specimen is not affected by the hydrogen embrittlement (Figure 3.17(a) and (c)).
ii) First cracks appear at grain boundaries normal to the applied load direction at an applied strain higher than 0.5% (Figure 3.17(e) and (g)).
iii) Several new grain boundaries failed (Figure 3.17(i) and (k)).

It can be notice that the detection of the exact moment of the crack initiation is difficult, due to the large field of SEM images compared to the small opening of microcracks (Rupil et al. 2011).

3.3.2.2 Development of intergranular cracking at the embrittled specimen surface

The microcracks are found within the localised deformation bands, which suggests that crack initiation needs a minimum level of strain to occur. The first cracks also appeared on grain boundaries oriented normal to the tensile direction. Thus, intergranular crack initiation seems to be related to both strain level and grain boundary orientation.

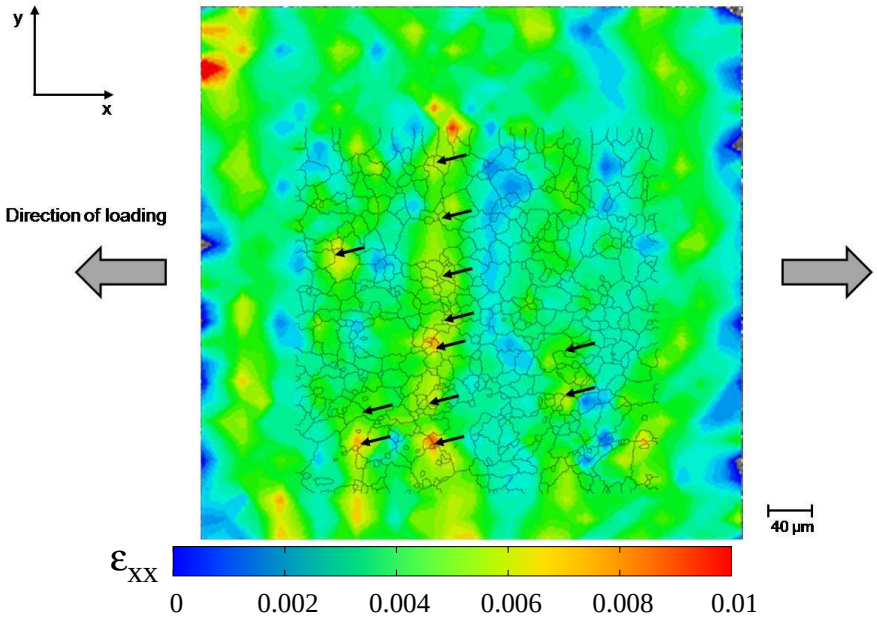

Figure 3.18: DIC measured axial strain field ε_{xx} for Specimen (I) after 0.0045 macroscopic strain along the x-axis. Black arrows indicate the grain boundaries where crack initiation was observed.

The strain field was then studied at a finer scale in regions (2) and (3) (Figure 3.6) to investigate what happened within a given deformation band. The measured strain distributions at medium magnification for specimen (I) are shown in Figure 3.19 for macroscopic applied strains of (a) 0.5%, (b) 1.6%, (c) 2.6%.

DIC computations at higher magnification (see Figure 3.19 and 3.20) show that microcracks appeared between grains that were less deformed compared to neighbouring grains, after a small amount of macroscopic plastic strain. Strain field measurements at this scale showed that grain boundaries between not or less deformed grains do not necessarily crack. Consequently, in order to describe the cracking phenomena correctly, the vinicity of the cracked grain boundaries has to be taken into account. DIC results also show that these surrounding grains are deformed (see white arrows Figure 3.19 and 3.20). Strain field computations at smaller scale confirm the identified kinematic environment (see Figure 3.22).

Results also show that grain boundaries between undeformed or slightly deformed grains do not necessarily crack. This implies that, the grains surronding the cracked grain boundary region need to be taken into account. DIC results also showed that grains surrounding the ones whose boundaries have cracked were more highly deformed. As it will be discussed below, measured strain fields at finer scales confirm these experimental results.

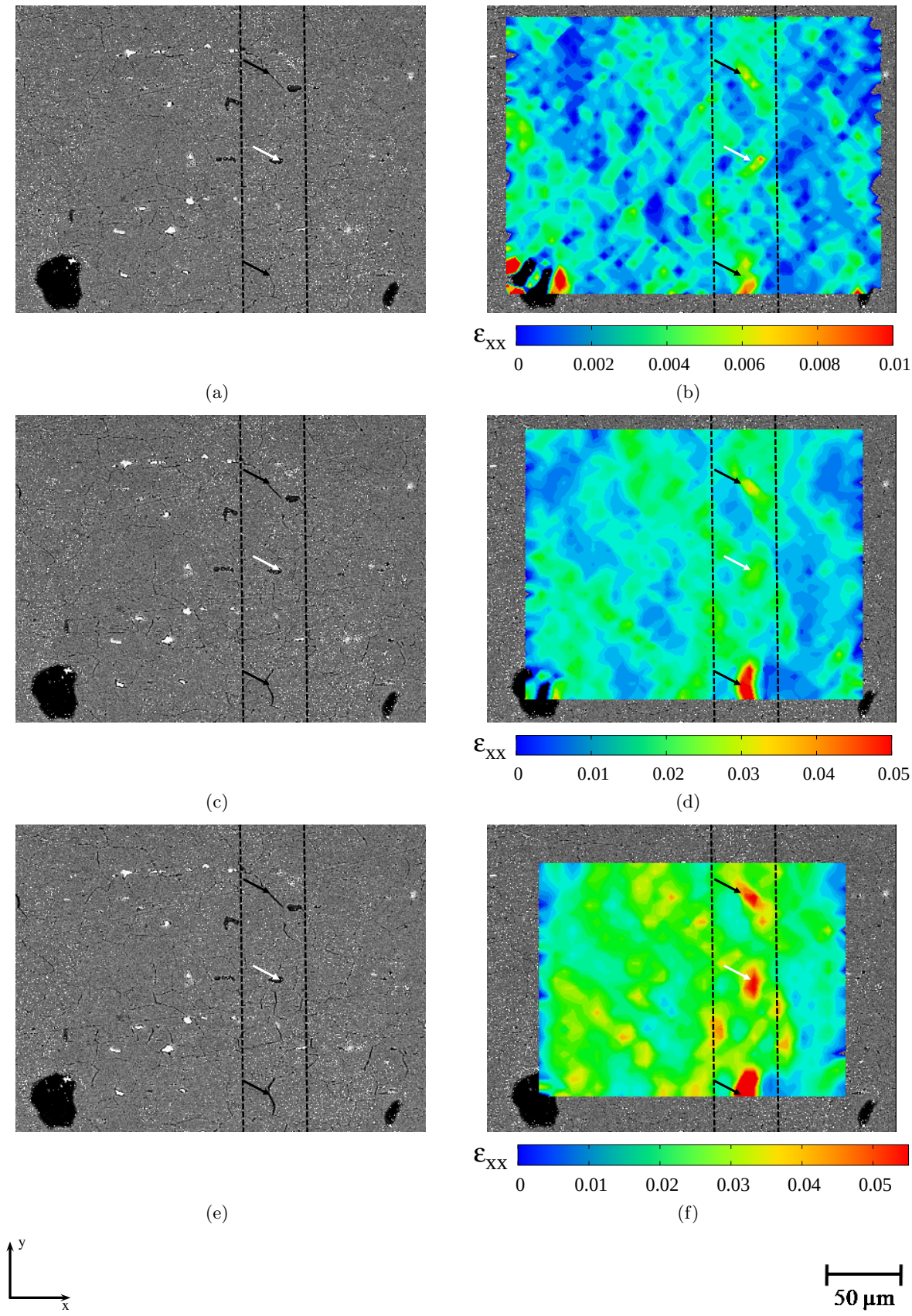

Figure 3.19: Strain fields for Specimen (I) at medium magnification along the x direction for macroscopic applied strains of (b) 0.5%, (d) 1.6% and (e) 2.6%, and (a),(c) and (d) respective SEM micrograph. White arrows indicate the strongly deformed region and black ones the cracked grain boundaries.

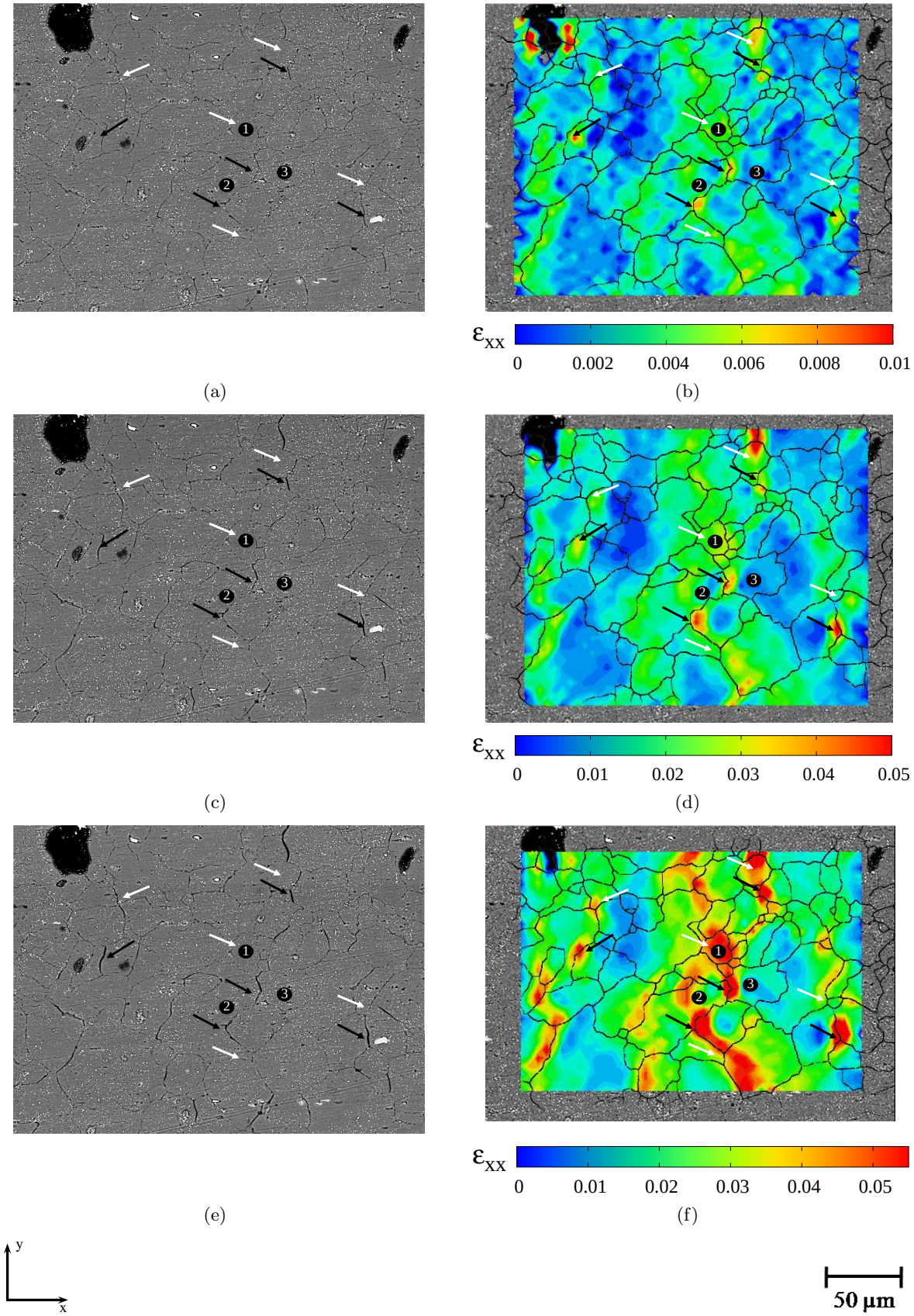

Figure 3.20: Strain distributions for Specimen (I) at medium magnification along the x direction for macroscopic applied strains of (b) 0.5%, (d) 1.6% and (e) 2.6%, and (a),(c) and (d) respective SEM micrograph. White arrows indicate the strongly deformed region black ones the cracked grain boundaries.

To confirm these results, the level of lattice rotation due to plastic deformation was investigated within each individual grain. Figure 3.21 shows the crystal orientation evolution of Grains 1, 2 and 3 identified in Figure 3.20 before and after deformation. It can be seen that Grains 2 and 3 undergo a very small amount of rotation, whereas Grain 1 rotates considerably more towards the [101] orientation. These EBSD results are in good agreement with the fact that Grains 2 and 3 are less deformed than Grain 1, as revealed by Figure 3.20.

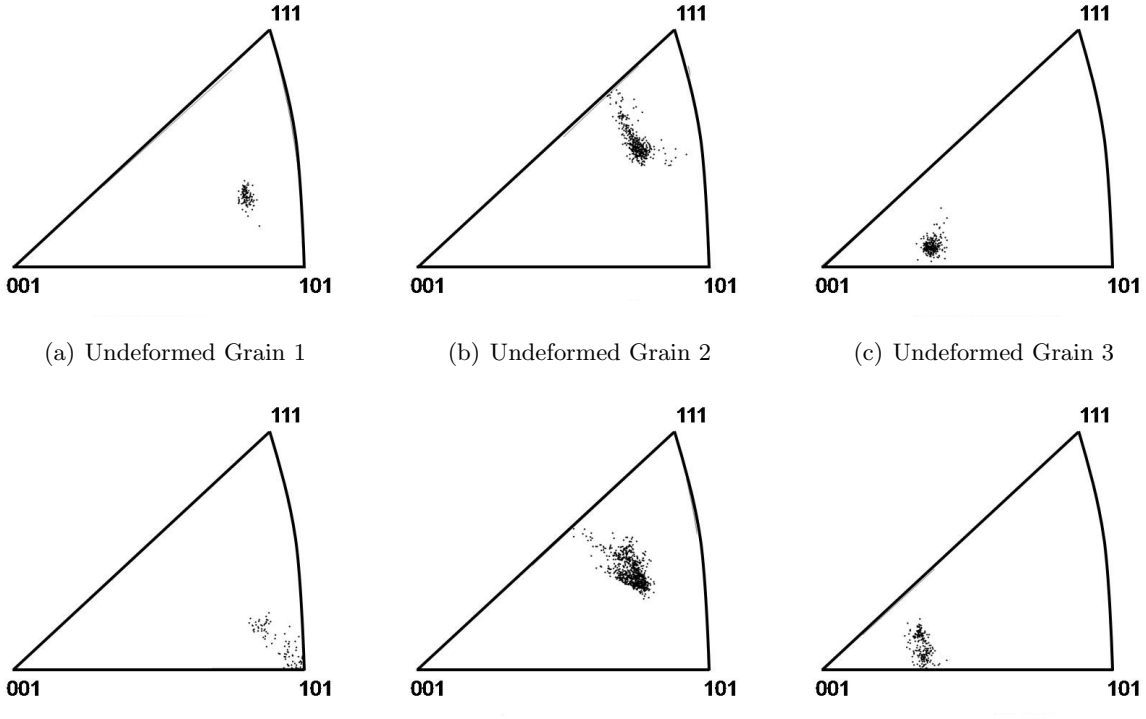

(a) Undeformed Grain 1 (b) Undeformed Grain 2 (c) Undeformed Grain 3

(d) Deformed Grain 1 (e) Deformed Grain 2 (f) Deformed Grain 3

Figure 3.21: Comparison between the inverse pole figures for (a) and (d) Grains 1, (b) and (e) Grain 2, and (c) and (f) Grain 3 identified in Figure 3.20(c) before (a,b,c) and after (d,e,f) 4.5 % applied strain

These observations also reveal that grain boundaries between undeformed or only slightly deformed grains do not necessarily crack. This implies that, in order to describe the cracking phenomena correctly, grains neighbouring the failed grain boundaries need to be taken into account. The DIC results also showed that grains surrounding the failed grain boundaries deformed more than those where cracks were found (white arrow in Figure 3.22).

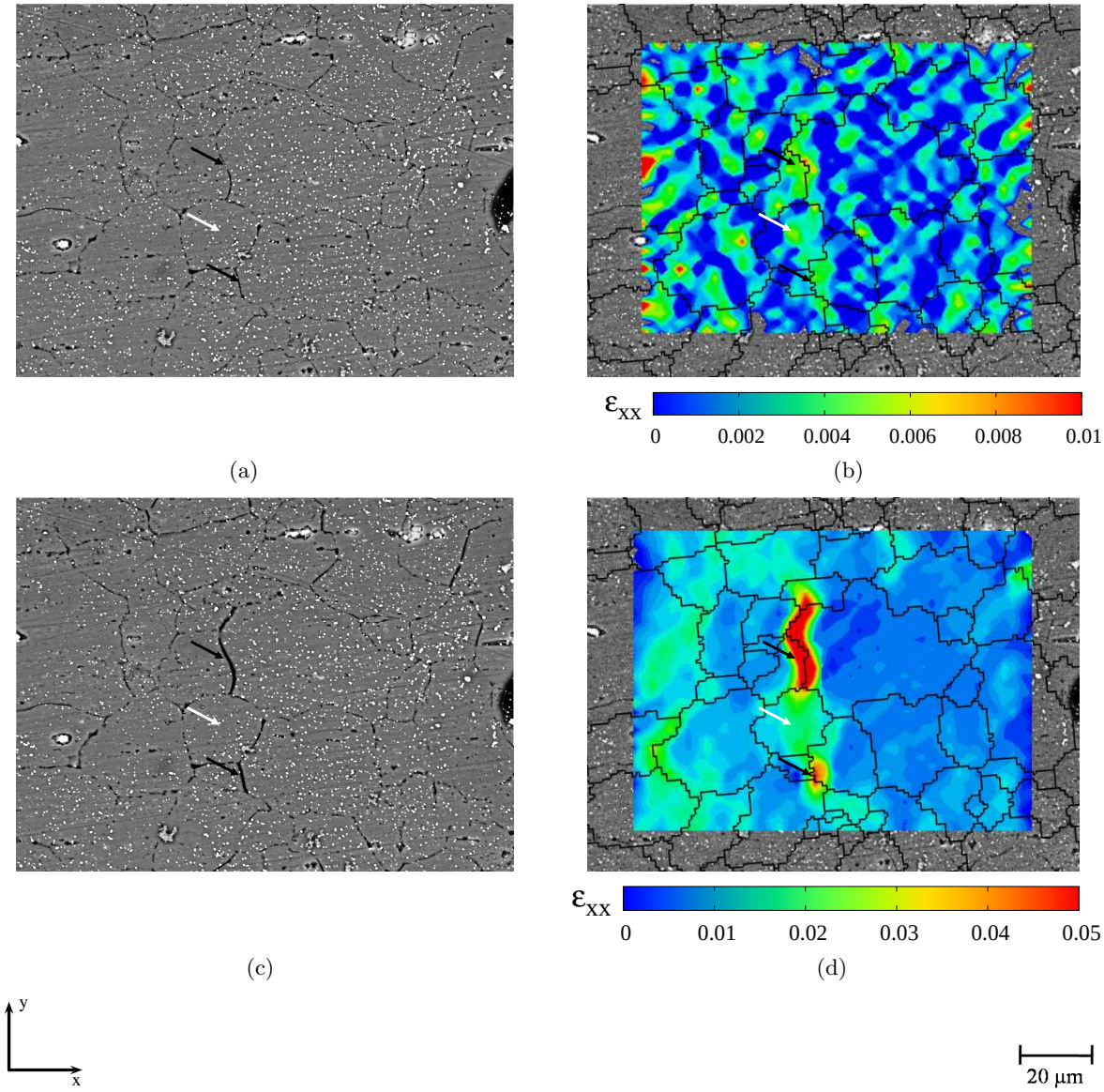

Figure 3.22: Strain distributions for Specimen (I) at small magnification along the x direction for macroscopic applied strains of (b) 0.3%, (d) 1.6%, and (a),(b) respective SEM micrograph. White arrows indicate the strongly deformed region and black ones the cracked grain boundaries.

In summary, micro-cracks seem to initiate at boundaries (i) contained within a strongly deformed region, (ii) oriented perpendicular to the loading direction, at least at the specimen surface, and (iii) located at the boundary between two "hard" grains that are, in turn, contained within a larger "softer" region. This is schematically illustrated in Figure 3.23.

Within the studied region of Specimen (I) described in Figure 3.6, 12 events of fracture characteristics have been analysed. The study of cracked grain boundaries shows that all of them were located within a highly deformed region, and secondly at the interface between grains with that had undergone only low strain levels as represented in Figure 3.23.

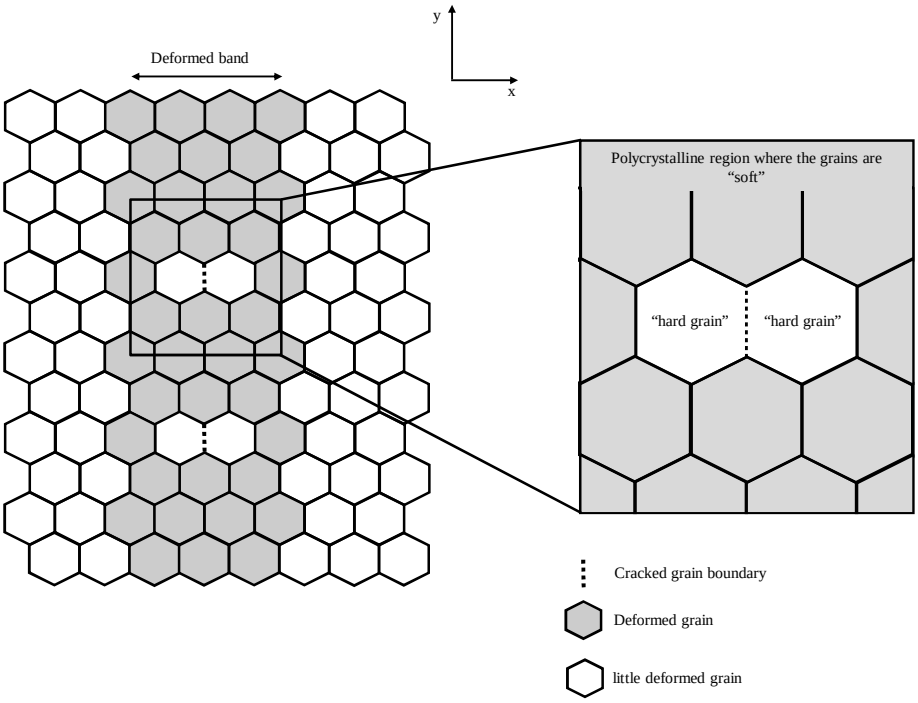

Figure 3.23: Schematics of the typical grain configuration observed around a cracked grain boundary (indicated by the dashed line): (a) large polycrystalline idealised configuration and (b) local polycrystalline idealised configuration. The dashed line delimits the boundary that is assumed to fail.

3.4 Conclusions

In-situ tensile tests showed that intergranular cracking initiates between "harder" grains that are embedded in a "softer" deformation band. This was shown by both local crystal rotation analysis and strain field measurements. Involved grain boundaries were, in addition, found to be perpendicular to the loading axis at least at the specimen surface.

Short-range strain incompatibility between the two grains that are separated by a grain boundary is not the relevant phenomenon to be considered in intergranular cracking of the hydrogen embrittled material. On the other hand, strain incompatibility over a longer range, i.e. between the "harder" pair of grains involved in intergranular crack initiation and the surrounding "softer" band, leads to a load transfer to this "harder" inclusion and to high grain boundary tractions that seem to promote crack initiation.

Since grain boundaries were found to fail in a brittle manner, a crack initiation criterion needs to be formulated in terms of grain boundary tractions. This requires an evaluation of the local stress fields and thus, a detailed mechanical analysis of the test over the regions that were experimentally investigated. This will be the aim of the micromechanical study presented in the next chapters.

Résumé

Ce chapitre regroupe l'ensemble des résultats expérimentaux qui ont permis de mettre en évidence le mécanisme de rupture intergranulaire. Les résultats de calcul de champs de déformation ainsi que plusieurs types de mesures cristallographiques de caractérisation des joints de grains obtenues lors d'essais in-situ ont permis de montrer que la fissuration intergranulaire étudiée dans ce travail s'amorce entre deux grains présentant de faibles niveaux de déformation et situés à l'intérieur d'une bande de forte déformation. Il est également important de souligner qu'une forte proportion de joints de grains rompus sont perpendiculaires à l'axe de traction (grande face de l'éprouvette).

L'effet d'incompatibilité de déformation à courte distance entre deux grains n'est pas le phénomène prédominant dans le cas de la rupture intergranulaire due à l'hydrogène étudié ici. Néanmoins, on peut considérer qu'il s'agit d'un effet d'incompatibilité de déformation à longue distance puisqu'il faut considérer un îlot de grains faiblement déformé mais situé dans un milieu plus fortement déformé que la moyenne. Ce milieu plus étendu correspond à une bande de forte déformation composée de plusieurs dizaines de grains. Etant donné que la microstructure est continue, les grains plus fortement déformés ont ainsi la capacité de transférer leur chargement aux îlots de grains durs. C'est la raison pour laquelle on peut supposer que les grains et les joints de grains composant les îlots de grains durs subissent un fort chargement qui entraîne in-fine l'initiation de fissure intergranulaire. Ce constat permet de conclure que les joints de grains se fissurent suivant un mode de rupture fragile.

Du fait que les joints de grains se fissurent de manière fragile, on choisit de formuler le critère de rupture associé en termes de contrainte normale aux joints de grains. Afin de déterminer la valeur critique de cette contrainte normale, il est indispensable de réaliser une analyse mécanique à l'échelle microscopique des champs de contraintes sur les surfaces qui ont permis d'obtenir expérimentalement le champ de déformations à l'origine de l'établissement du critère de rupture.

Chapter 4

Constitutive Behaviour of Al-Mg Polycrystalline Aggregates

Contents

4.1 Literature review

As seen in the previous chapter, local texture and stress fields play a prominent role in the nucleation and propagation of localised intergranular cracks aluminium alloys due to hydrogen embrittlement. In order to examine local stress fields in the vicinity of grain boundaries, a constitutive crystallographic slip based model is needed. In this work, an existing rate-dependent dislocation mechanics-based crystallographic model, originally proposed by Busso and McClintock (1996) was adopted. This model is based on the experimental and mechanistic studies conducted by Busso (1990), Busso et al. (1992), Busso and McClintock (1994).

In the crystallographic slip theory (e.g. Hill (1965)), macroscopic single crystal behaviour can be predicted from the deformation phenomena on individual crystallographic slip systems through appropriate flow and evolutionary equations. In order to obtain the macroscopic single crystal inelastic strain rate, the slip rate contributions from all the operative slip systems need to be summed up. In most of crystallographic models for pure metals (e.g. Peirce et al. (1983), Bassani (1990), Cuitifio and Ortiz (1992)), single phase materials (e.g. Cuitifio and Ortiz (1993)), and precipitation hardened alloys (e.g. Sheh and Stouffer (1990), Meric et al. (1991), Jordan et al. (1993)), the evolution of the critical resolved shear stress is often expressed in terms of a hardening modulus that affects hardening through the evolution of the slip system flow stress. Based on experimental latent hardening measurements at macroscopic level, calibrated hardening coefficients can only describe the homogeneous material behaviour.

In the dislocation mechanics-based theory proposed by Busso and McClintock (1996), the description of the flow and hardening behaviour of the crystal is based on a study of dislocation interaction from an idealization of the dislocation population and stress-dependent activation concepts. The dominant contributions to the total slip plane glide resistance makes use of the statistical description of the obstacle density in the slip system originally proposed by Kocks and Brown (1966). The theory considers, in addition to discrete obstacle resistance, the mechanism of lattice friction resistance to dislocation motion as a major contributor to the overall slip plane glide resistance. Finally, the reversible hardening associated with the polarization of the dislocation structure in the glide plane at small strains is accounted for through a saturation-hardening recovery law, hence the theory allows multiaxial loading conditions representative of the strain fields measured in the previous chapter.

To accurately represent the heterogeneous behaviour of AA5083 aggregates, the influence of microstructural parameters such as grain shape and size and crystallographic texture have to be taken into account. Hence, EBSD inverse pole figure maps were discretised to depict the grain shape and assess the corresponding grain orientations. A particular attention was also paid to the boundary conditions needed at each scale of the representative simulations.

4.1.1 Crystallographic slip systems

Metals with high or moderate stacking fault energies such as aluminium alloys of interest deform by slip. Thus, in the framework of continuum mechanics, an accurate prediction of the deformed state requires the modelling of such behaviour by a crystallographic formulation. In FCC crystals, slip takes place on the most densely packed planes <111> and along the most densely packed <110> directions, even at low temperatures. Therefore, crystallographic slip is assumed to occur on the 12 octahedral 111<110> slip systems. For each slip system α, $\mathbf{m}^{\alpha}$,

the slip direction and, $\mathbf{n}^\alpha$, the normal to the slip plane, represent the unit vectors. Schmid and Boas slip system convention is used here to identify individual slip systems, Table 4.1.

Table 4.1: Octahedral slip system, using Schmid–Boas notation

Notation : α	$\mathbf{m}^\alpha$	$\mathbf{n}^\alpha$
A2	$[\bar{1}11]$	$(0\bar{1}\bar{1})$
A3	$[\bar{1}11]$	(101)
A6	$[\bar{1}11]$	(110)
B2	$[111]$	$(0\bar{1}1)$
B4	$[111]$	$(\bar{1}01)$
B5	$[111]$	$(\bar{1}10)$
C1	$[\bar{1}\bar{1}1]$	(011)
C3	$[\bar{1}\bar{1}1]$	(101)
C5	$[\bar{1}\bar{1}1]$	$(\bar{1}10)$
D1	$[1\bar{1}1]$	(011)
D4	$[1\bar{1}1]$	$(\bar{1}01)$
D6	$[1\bar{1}1]$	(110)

4.1.2 Representative volume element definition

A representative volume element (RVE) is the smallest statistical representation of a material microstructure. It should contain enough information about the microstructure to be macroscopically representative and smaller than the macroscopic structural dimensions (Bornert et al. 2001). In the case of heterogeneous materials with non linear properties (hardening and softening materials), it must be ensured, usually through simulations, that a large enough polycrystalline aggregate is identified as a representative volume element (RVE), see Figure 4.1. To be a valuable RVE, a polycrystalline aggregate needs to have a proper size to incorporate statistically the microstructure intrinsic length scale such as grain size, mean deformation band spacing as well as texture anisotropy if present.

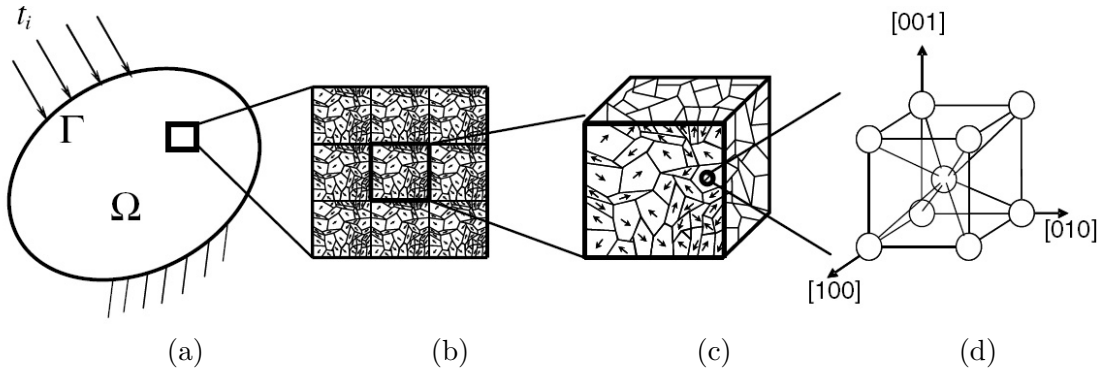

Figure 4.1: Macro continuum and micro polycrystal structures: (a) macro continuum, (b) microstructure, (c) RVE and (d) crystal lattice (Nakamachi et al. 2007)

Over the last decade, several studies have been carried out to find appropriate RVE size for specific mechanical properties. Ren and Q.S. (2002) showed that the minimum RVE size for the effective shear modulus G exhibits a close linear dependence with the degree of

anisotropy for single crystals. In the case of a linear property, Kanit et al. (2003) introduced the notion of an integral range $\mathcal{A}$, which allows to relate the RVE volume V, the number of independent realizations, N, and the estimation error, ϵ, through:

$$N = 4D_Z^2(\mathcal{A}/V)^\alpha/(\epsilon/\mathcal{Z})^2 \tag{4.1}$$

where $4D_Z^2$ is the point variance, α a constant. $\mathcal{A}$ and $\mathcal{Z}$ are deduced from stabilised mean and variance values. In the case of non linear properties, Gitman et al. (2007) have investigated the possibility to determine the RVE size by using a statistical analysis based on a Chi-square criterion. In polycrystalline aggregates, a suitable RVE ensures the reproducibility of the macroscopic behaviour, a good description of the grain morphology is required to predict an accurate localisation of strain to study nucleation or stress driven fracture problems.

Polycrystalline aggregates contain a large number of grains of various shapes that remain difficult to model. Thus, in this work, digitally generated microstructures will be relied upon to calibrate crystal plasticity model. One of the simplest methods is to consider the grain shape as cuboidal in order to obtain the main deformed features and the macroscopic stress-strain response of the aggregates. However, more realistic three-dimensional grain morphologies have been produced containing a large number of random grains generated using Voronoi polyhedra models (Barbe et al. 2001a), as used in this work, while dodecahedral-shaped crystals have been investigated to built up realistic polycrystals (Mika and Dawson 1998).

4.1.3 Local crystallographic constitutive laws formulation

4.1.3.1 Dislocations interaction

The concept of a dislocation in a 1D crystal was first proposed in 1926 by Frankel (1926). It was used to explain the lower shear strength measured in copper and more generally in crystalline materials that till there had relied on theoretical estimates based on atomic bonding considerations. In 1934, Orowan (1934), Harder (1934), Taylor (1934), almost simultaneously, proved that plastic deformation could be explained by the motion of dislocations. A new approach was then introduced, with the concept of edge dislocation to explain the decrease of the mechanical strengthening (Orowan 1934, Harder 1934, Taylor 1934). Additionally, the description of screw dislocations was later introduced by Burgers (1939). The applied stress required to move a dislocation in an otherwise perfect lattice depends on the binding forces between atoms and was called the *Peierls stress* or *Peierls-Nabarro stress*. The force required to move a dislocation was evaluated by Peierls (1940) and modified by Nabarro (1947) without taking into account the effect of other dislocations.

It was assumed that each dislocation glides when the shear stress, τ, reaches a critical value. For single-phase metals, forest dislocations (defined as dislocations on other slip systems threading the slip plane of a moving dislocation) can be considered as the main resistance to dislocation motion. Assuming that forest dislocations are the only obstacles and since the shear strain and stress fields around a dislocation are proportional to $1/r$, where r is the distance from the dislocation core, the shear stress required to move per unit length of dislocation past another of opposite sign is defined as,

$$\tau \propto \frac{\mu b^2}{2\pi r} \tag{4.2}$$

where, μ, is the shear modulus and, r, the average spacing between dislocations. Based on the assumption that dislocations are regularly arranged in the slip plane, then τ is inversely proportional to the square root of the dislocation density ρ:

$$\tau \propto \mu b^2 \rho^{1/2} \tag{4.3}$$

This relationship was first estimated by Orowan (1940). Dislocations in each slip system are taken into account through Schmid's law described in Section 3.3.1.3. Orowan's relationship was modified to describe the slip resistance on crystallographic slip system, α, by:

$$S^{\alpha} \propto \alpha \mu b \sqrt{\sum_{\beta=1}^{N} h^{\alpha\beta} \rho^{\beta}} \tag{4.4}$$

where, ρ^{β}, is the dislocation density on an arbitrary slip system, β. The extra dislocations introduced by strain due to the mutual interaction between dislocations is described by the dislocation interaction matrix, $h^{\alpha\beta}$. Many theories have been suggested and new theories are proposed as new experimental observations yield new physical insight. In this work, the dislocation interaction matrix, $h^{\alpha\beta}$, is described by two coefficients. One for the diagonal terms representing the self hardening interaction strength between dislocations on the same slip system, and the second one for the off-diagonal terms to describe the work hardening interaction strength between dislocations on dissimilar slip systems. To predict the work-hardening behaviour, it is essential to know how the dislocation density and distribution change with plastic strain. Evidence of work-hardening anisotropy during single slip obtained in work hardening experiments (Kocks and Brown 1966, Franciosi et al. 1980) and dislocation dynamic works (Madec et al. 2003, Devincre et al. 2005) showed that each element of the interaction matrix describes the cross-interaction between dislocations on two different slip systems and that these parameters are sensitive to variables such as crystal structure, stacking fault energy, temperature and strain rate.

4.1.3.2 Flow rule

Rate-dependent plasticity describes the flow rule of materials, which depends on time. When the dislocation reaches the crystal boundary, slip will have occurred on the entire slip plane. Suppose that the length of the slip plane is s, and that an edge dislocation moves through a distance x in that slip plane; then it contributes a displacement bx/s, where b is the magnitude of Burgers vector, so that n dislocations moving an average distance x produce a displacement $u = nbx/s$. If the average spacing between slip planes is l, then the plastic shear strain is express as:

$$\gamma = \frac{nb\overline{x}}{ls} \tag{4.5}$$

However, n/ls is the average number of dislocation lines per unit perpendicular area. Equivalently, the following expression is obtained for the total length of dislocation lines of a given family per unit crystal volume, ρ (i.e. the density of dislocations),

$$\gamma = \rho b \overline{x} \tag{4.6}$$

the strain-rate is then expressed as (Orowan 1940),

$$\dot{\gamma} = \rho b \overline{\nu} \tag{4.7}$$

where, $\overline{\nu}$ is the mean velocity. For the case of steady state, $\dot{\gamma}$ is a function of the shear stress and temperature only. Thus, from Equation (4.3), it is found that

$$\rho = \alpha \left(\frac{\tau}{\mu b} \right)^2 \tag{4.8}$$

where μ is the shear modulus. Since the rate dependent viscoplastic flow rule is based on the thermally activated motion of dislocations, the mean velocity of a dislocation segment, $\overline{\nu}$, follows the kinetic equation proposed by Frost and Ashby (1982),

$$\overline{\nu} = \beta b \nu \ \exp\left(-\frac{\Delta G^{\alpha}}{kT} \right) \tag{4.9}$$

where β is a dimensionless parameter, and ν a frequency. The stress dependente activation energy, ΔG^{α}, for each slip system α is a function of the distribution of obstacles and of the internal stresses. Assuming that point obstacles are randomly distributed, Kocks (1977) described the quantity ΔG^{α} by the general equation:

$$\Delta G^{\alpha} = F_0 \left(1 - \left\langle \frac{\tau^{\alpha}}{\hat{\tau}} \right\rangle^{p} \right)^{q} \tag{4.10}$$

Here, F_0 is the activation energy which depends on obstacle type, the quantity $\hat{\tau}$ is the athermal flow strength, equivalent to the shear strength in the absence of thermal energy, and parameters p and q define the shape of the energy-barrier profile. The quantities p, q and F_0 are bounded by:

$$0 \leq p \leq 1 \tag{4.11}$$

$$1 \leq q \leq 2 \tag{4.12}$$

$$0.2 \leq F_0 \mu b^3 \leq 2 \tag{4.13}$$

Equation 4.10 was first used within the context of crystal plasticity by Busso (1990). With Equations (4.7), (4.8), (4.9) and (4.10), the kinetic equation for each slip system, $\dot{\gamma}$, represents the flow characteristics on an arbitrary slip system α,

$$\dot{\gamma}^{\alpha} = \dot{\gamma_0} \exp \left[- \frac{F_0}{kT} \left(1 - \left\langle \frac{\tau^{\alpha}}{\hat{\tau}} \right\rangle^{p} \right)^{q} \right] \tag{4.14}$$

where $\dot{\gamma_0}$ is a constant. Most of physics-based flow rules used in single crystal models are based on the theory described previously (Busso 1990, Balasubramanian and Anand 2002, Ma and Roters 2004). Otherwise, more phenomenological viscoplastic flow rules have been developed (for example Cailletaud (1992)) proposed a single crystal model containing isotropic and kinematic hardening by means of the two internal variables, r^{α} and x^{α} for each slip system:

$$\dot{\gamma}^{\alpha} = \left\langle \frac{|\hat{\tau}^{\alpha} - x^{\alpha}| - r^{\alpha}}{K} \right\rangle^{n} \tag{4.15}$$

4.1.3.3 Hardening description

Hardening phenomena are due to interactions between gliding dislocations and obstacles that they need to overcome. In single-phase alloys, the main obstacles are forest dislocations. Figure 4.2 show a typical of face-centred cubic single crystals and high purity body-centred cubic single crystals. Three main stages of plastic deformation can be distinguished in the curve of an initial resolved stress vs. shear strain.

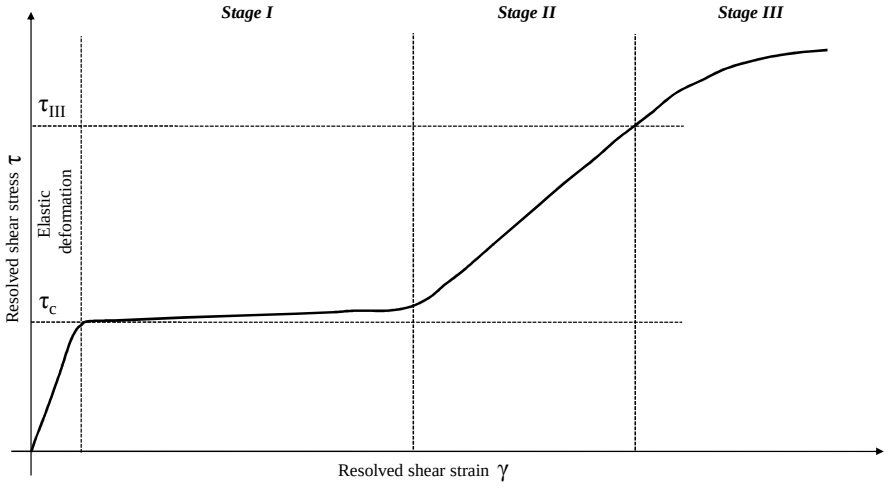

Figure 4.2: Critical RSS vs shear strain in FCC single crystals

In Figure 4.2, the following stages are identified: Stage I or easy glide, Stage II or linear hardening and stage III which is approximately parabolic hardening. The length of Stage I and the onset Stage III are sensitive to temperature, composition and crystal dimensions whereas Stage II is insensitive to these parameters. Polycrystalline FCC metals do not show an easy glide stage and deform primarily in a way equivalent to Stage III exhibited by single crystals.

Two main types of models have been developed to describe the hardening behaviour in crystal plasticity, namely, models with phenomenological internal state variables and models

with dislocation densities as internal state variables. For instance, in the first category, (Busso 1990, Kumar and Yang 1999) slip resistances are used as state variables. Cailletaud (1988) transferred macroscopic laws to the single crystal scale and showed that a phenomenological approach can also predict monotonic and cyclic behaviour accurately. For a more detailed modelling of the deformation behaviour in single and polycrystals, an appropriate description has to be based on microstructural state variables that are affected by the deformation history of the material. Therefore, models that rely on an internal–state variable approach are developed based on the understanding of microstructural evolution and the interaction of dislocations with short and long-range obstacles.

Zikry and Kao (1996) defined a constitutive formulation where mobile and immobile dislocation densities are used as internal state variables. Similarly, Roters et al. (2000) defined mobile and immobile dislocations in cell interiors and immobile dislocations inside cell walls to be the internal state variables. Alternatively, dislocation can be also discretised into edge and screw dislocations. When dislocations intersect, jogs and kinks are formed. A kink is a step in the dislocation line in the slip plane where the dislocation moves while a jog is a step in dislocation line onto another slip plane. Kinks form on edge dislocations after intersection and are always glissile and consequently do not affect the subsequent glide of dislocation. In contrast, jogs with edge character formed in screw dislocations cannot glide since the glide plane for the jog is different from that of the main dislocation line. The jog is pinned and the dislocation is said to be sessile. In this case, motion can only occur by the dislocation line moving out of its existing glide plane, this is known as a non-conservative motion. Here, the length of the dislocation line is not preserved. Therefore, the mobility of screw dislocations is markedly lower than that of an edge dislocation since its movement is more severely impeded. Arsenlis and Parks (2002), Cheong and Busso (2004) have used edge and screw dislocation densities as internal state variables and assigned them different mobilities.

4.1.4 Non-local formulation with strain gradient concepts

Size-dependent effects have been observed in a wide range of experiments. The more typical examples are the grain size dependence of initial yielding and work-hardening in polycrystalline aggregates, a behaviour known as the Hall-Petch effect (Hall 1951, Petch 1953, Hansen 1977). In these examples, for a given strain, the smaller the grain size, the harder the material response. A phenomenological expression of the Hall-Petch effect is:

$$\sigma(\epsilon) = \sigma_0(\epsilon) + kd^{-1/2} \tag{4.16}$$

where d is the grain size, σ_0 the friction stress and k the Hall-Petch factor. The length scale dependency results from the presence of strain gradients due to lattice incompatibilities associated with inhomogeneous plastic deformation. When strain gradients are of the order of the dominant microstructural length scale (small grain size), the macroscopic stress-strain response is affected. Nye (1953) was the first to give a measure of the plastic deformation incompatibility through Nye's tensor.

In order to better understand the interplay and mechanism of dislocations in macroscopic hardening, Ashby (1970) considered that dislocations can be composed of statistically-stored dislocations (SSDs) and geometrically necessary dislocations (GNDs) (see Figure 4.3). The SSDs are considered to be inherently present in homogeneously deforming material, where they accumulate in numbers by randomly impeding and trapping other moving dislocations.

On the other hand, GNDs are considered to be "necessary" in order to accommodate lattice incompatibilities in regions where strain are inhomogeneous, resulting in the curvature of the crystal lattice. Therefore, GNDs are essentially localised near grain boundaries where lattice discontinuities are found.

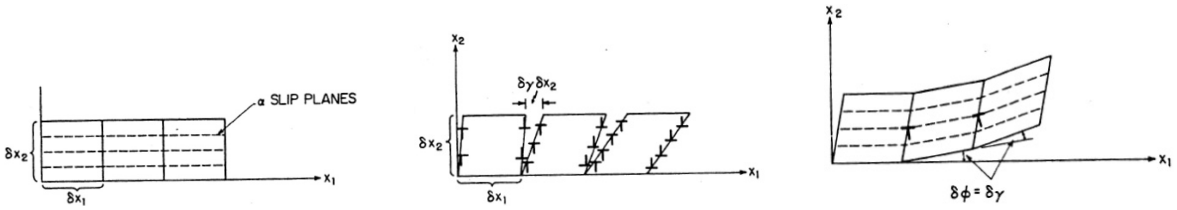

Figure 4.3: Crystal under a shear gradient (Ashby 1970)

Higher order theories such as Cosserat media have also been developed in a single crystal framework incorporating coupled stress to take into account the length scale dependency (Forest et al. 2001). Although motivated from dislocation mechanics concepts, an approach to describe strain gradient effects without additive higher order stresses has been developed by Arsenlis and Parks (1999), Busso et al. (2000), Acharya et al. (2003). These non-local theories rely on an internal state variable approach to determine the macroscopic response of the material whereby strain gradient effects are introduced directly into the evolutionary laws of the state variables. Strain gradient theories based on Nye's tensor show good agreement with experimental work (Busso and McClintock 1996, Dai and Parks 1997, Acharya and Beaudoin 2000). Contrary to the second gradient and Cosserat theories, they are relatively easy to implement numerically and do not require higher order stresses and additional boundary conditions.

4.1.5 Solid solution strengthening

Solid solution strengthening is a type of alloying that can be used to enhance the strength of a pure metal. The technique works by adding atoms of one element (e.g. magnesium in the present case) to the crystalline lattice of another element (e.g. aluminium). The alloying element diffuses into the matrix forming a solid solution. For this strengthening mechanism, solute atoms are added to the matrix, resulting in either substitutional or interstitial point defects in the crystal. Addition of solute atoms **B** in a crystalline matrix **A** will modify its volume and its modulus. A first approximation can be made by assuming that the solid solution atom is spherical with a radius r_B and a modulus, μ_B, inserted in a hole with a radius r_A, where r_A and μ_A are the matrix atomic radius and modulus, respectively. In the elastic assumption, the equilibrium radius r'_B can be approximated if the solute atoms and the matrix are placed side by side. According to Friedel (1965a), this elastic approximation is well predictive for substitution mechanism in metals. The elastic interaction was defined with the size factor μ, and the relative modulus variation, δ. Then,

$$\mu = \frac{r'_B - r_A}{r_A} = \frac{1}{a}\frac{da}{dc} \tag{4.17}$$

where a is the crystalline parameter and c the solute concentration, and:

$$\delta = \frac{\mu_B - \mu_A}{\mu_A} \backsimeq \frac{1}{\mu}\frac{d\mu}{dc} \tag{4.18}$$

where μ is the solid solution shear modulus. When solute and solvent atoms differ in size, local stress fields are created. Depending on their relative locations, solute atoms will either attract or repel dislocations in their vicinity. This is known as the size effect. A first order approximation of the interaction energy was proposed by Friedel (1965a) in which only edge dislocations were taking into account. The geometric problem is illustrated in Figure 4.4. The interaction energy for the size effect was written as follows,

$$W_\eta = \frac{1}{\pi}\frac{1+\nu}{1-\nu}\mu\nu v\frac{b\sin\theta}{r} \tag{4.19}$$

where, v, is the atomic volume and, ν, the Poisson's ratio.

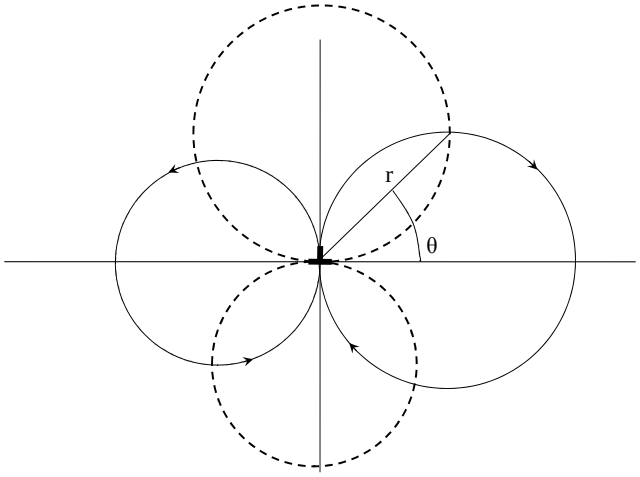

Figure 4.4: Interaction between an edge dislocation and a solute atom (Friedel 1965a)

The solute atoms cause a local change in the elastic modulus that also creates an interaction energy. This effect was estimated by Crussard (1950) with the difference in stacking fault energies between the configuration with and without solute atoms. In a perfect crystal the dissociation of a perfect dislocation into two partial is unlikely and the material deforms only by dislocation glide. Lower stacking faults energy materials display wider stacking faults and have more difficulties for cross-slip and climb. The resulting interaction energy is expressed as follows,

$$W_{\mu M} \backsimeq \frac{\nu\mu\delta}{36\pi^2 K} \tag{4.20}$$

where, K = 1 - ν, for edge dislocations and, K= 1, for screw dislocations. Generally, the modulus effect is very low compared to the size effect.

4.2 Non-Local Single Crystal Constitutive Formulations

The single crystal model based on dislocation mechanics used here was proposed by Busso and Cheong (2001). After its initial implementation in the finite element code Abaqus, it has been successfully used in a series of studies (Cheong and Busso 2004, Busso and Cheong 2005, Cheong and Busso 2006). In the model, dislocations are discretised into edge and screw components with intrinsically different relative mobilities and are subject to different dynamic recovery processes. The individual roles played by each dislocation type in contributing to the overall deformation behaviour are distinguished.

4.2.1 Finite strain kinematics

The description of the constitutive model for single crystal elasto-viscoplastic finite strain kinematics follows the approach originally proposed by Mandel (1973). The basic feature of the formulation relies on the multiplicative decomposition of the total deformation gradient for isothermal conditions, $\mathbf{F}$, as illustrated in Figure 4.5,

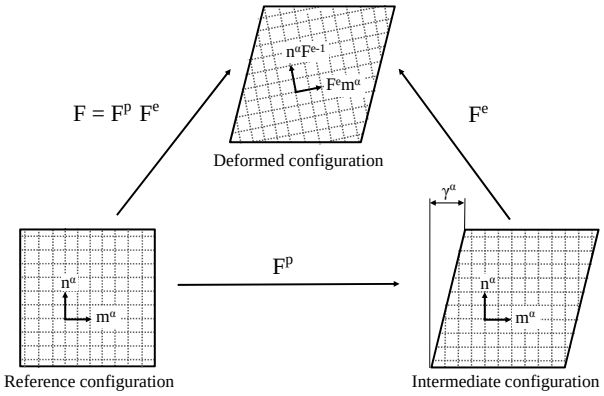

Figure 4.5: Multiplicative decomposition of the total strain gradient, $\mathbf{F} = \mathbf{F^e F^p}$. The rotation and stretching of the lattice are taken into account through the elastic deformation gradient $\mathbf{F^e}$ (after Asaro and Rice (1977)).

The total deformation gradient is multiplicatively decomposed into $\mathbf{F^e}$, associated with the stretching and the rotation of the crystal lattice, and $\mathbf{F^p}$ which describes the crystallographic slip while the lattice remains undistorted and unrotated,

$$\mathbf{F} = \mathbf{F^e F^p} \tag{4.21}$$

In order to get the deformation history, the total deformation gradient $\mathbf{F^e}$ is expressed in rate-form,

$$\dot{\mathbf{F}} = \mathbf{L F} \tag{4.22}$$

The term $\dot{\mathbf{F}}$ is the rate of the total deformation gradient and $\mathbf{L}$ the spatial velocity gradient. From Equations (4.21) and (4.22), the additive decomposition of $\mathbf{L}$ into its elastic ($\mathbf{L^e}$) and plastic ($\mathbf{L^p}$) contributions can be shown to result in:

$$\mathbf{L} = \dot{\mathbf{F}}^e\mathbf{F}^{e-1} + \mathbf{F}^e\dot{\mathbf{F}}^p\mathbf{F}^{p-1}\mathbf{F}^{e-1} = \mathbf{L}^e + \mathbf{F}^e\mathbf{L}^p\mathbf{F}^{e-1} \tag{4.23}$$

The plastic flow is assumed to be the result of crystallographic slip. Thus, $\mathbf{L^p}$ is considered as the sum of crystallographic slip rates on N number of activated slip systems (Asaro and Rice 1977),

$$\mathbf{L}^p = \sum_{\alpha=1}^{N} \dot{\gamma}^\alpha \mathbf{P}^\alpha \tag{4.24}$$

where, $\dot{\gamma}^\alpha$, is the crystallographic slip rate on an α-slip system and, $\mathbf{P}^\alpha$, the generalised Schmid tensor formed from the dyadic product of the crystallographic slip direction vector, $\mathbf{m}^\alpha$, and slip plane normal unit vectors, $\mathbf{n}^\alpha$, in the reference configuration:

$$\mathbf{P}^\alpha = \mathbf{m}^\alpha \otimes \mathbf{n}^\alpha \tag{4.25}$$

The time rate of change of the plastic deformation gradient, $\dot{\mathbf{F}}^p$, is defined by:

$$\dot{\mathbf{F}}^p = \mathbf{L}^p\mathbf{F}^p \tag{4.26}$$

It hyperelastic behaviour is considered, the lagrangian strain is given as

$$\mathbf{E}^e = \frac{1}{2}(\mathbf{F}^{eT}\mathbf{F^e} - \mathbf{I}) \tag{4.27}$$

where, $\mathbf{I}$, denotes the second-order identity tensor. Since the Cauchy stress tensor, σ, is not work-conjugate to a convenient measure of strain, the tensor $\mathbf{T}$, defined as the second Piola–Kirchhoff stress, $\mathbf{T}$, the work conjugate of $\underline{\mathbf{E}^e}$ (the Green–Lagrange strain tensor $\mathbf{E}^e$) is relied to describe the mechanical response of the single crystal through a hyperelastic constitutive law. Here,

$$\mathbf{T} = (\det \mathbf{F}^e)\mathbf{F}^{e-1}\sigma\mathbf{F}^{e-T} \tag{4.28}$$

This result allows the total stress-strain relationship to be obtained from the Helmholtz free energy density of the lattice per unit reference volume, U,

$$\mathbf{T} = \frac{\partial U}{\partial \mathbf{E^e}}. \tag{4.29}$$

Differentiating Equation (4.29) with respect to $\mathbf{E^e}$ yields a fourth order tensor $\mathcal{K}$,

$$\frac{\partial \mathbf{T}}{\partial \mathbf{E^e}} = \mathcal{K} \quad \text{where} \quad \mathcal{K} = \frac{\partial^2 U}{(\partial \mathbf{E^e})^2} \tag{4.30}$$

In the material of interest and in most metals, the assumption that the elastic deformation

range is infinitesimal when compared to the plastic strains is made. Therefore, $\mathcal{K}$ is assumed to be the fourth-order anisotropic elasticity tensor $\mathcal{C}$. Finally the constitutive law given in Equation (4.29) becomes,

$$\mathbf{T} \approx \mathcal{C} : \mathbf{E}^{\mathbf{e}}. \tag{4.31}$$

The evolution of the slip system internal variables are introduced in the constitutive formulation through suitable growth laws. The mechanisms by which dislocation density governs inelastic flow is presented in the next section.

4.2.2 Kinetics of plastic flow

The associated flow rule governing the kinetics of plastic flow is considered rate-dependent due to dislocation motion even at low homologous temperatures (Orowan 1940). The kinetic equation used for the crystallographic slip rate describes the flow characteristics on an arbitrary slip system α, for a given temperature, structure and applied stress taking into account the thermal and athermal components (Busso 1990, Busso and McClintock 1996). From Equation (4.15) and extrapolating the slip resistance and lattice stress at 0 K, the crystallographic slip rate $\dot{\gamma}^{\alpha}$ follows a function of the form (Busso 1990),

$$\dot{\gamma}^{\alpha} = \dot{\gamma}_0 \exp\left[-\frac{F_0}{kT}\left\{ 1 - \left\langle \frac{|\tau^{\alpha}| - S_0^{\alpha}\mu/\mu_0}{\widehat{\tau}_0\mu/\mu_0} \right\rangle^{p} \right\}^{q} \right] sgn(\tau^{\alpha}) \tag{4.32}$$

where F_0, $\dot{\gamma}_0$, p, q are the flow rule parameters while κ is Boltzmann's constant and θ is the absolute temperature. Here F_0 is defined as the Helmholtz free energy of activation, which is the total energy needed to overcome obstacles without the aid of an applied shear stress. The parameter $\widehat{\tau}_0$ represents the lattice friction at 0 K and S_0^{α} is the total athermal slip resistance to dislocation motion. The shear moduli ratio at T is μ and at 0 K μ_0 are used to obtain the lattice friction stress and the slip resistance at the considered temperature T. The constants p and q are parameters which defined the shape of the energy–barrier profile. The sign of τ^{α} is taken into account in order to distinguish positive and negative slip on the slip system.

The main contributions of the slip resistance to plastic flow, S_c^{α}, is composed of the friction stress due to Mg atoms in solid solution, S_{ss}^{α} and of a the athermal slip resistance S_T^{α}. As the slip resistance contributions are assumed to be additive, then:

$$S_c^{\alpha} = S_{ss}^{\alpha} + S_T^{\alpha} \tag{4.33}$$

As only a small part of the Mg atoms precipitate during the heat treatment, the concentration of Mg in solid solution is set to be equal to the average concentration in the material. Thus the friction stress due to Mg atoms in solid solution (S_{ss}^{α}) is calculated based on the atomic size and concentration of Mg in the alloy (Table 2.1) as proposed by Saada (1968) and detailed in Section 4.2.5.

From the assumption of Ashby (1970) the total dislocation density was split into two categories, statistically stored dislocations (SSDs) and geometrically necessary dislocations (GNDs). The GNDs are distinguished from the SSDs as they are only present in regions of

non-homogeneous plastic deformation to accommodate geometric incompatibilities or strain-gradients within. Therefore, the total dislocation density can be additively decomposed into statistically-stored and geometrically necessary parts,

$$\rho_T^\alpha = \rho_S^\alpha + \rho_G^\alpha \tag{4.34}$$

Thus, both categories contribute to the total athermal slip resistance S_T^α defined as,

$$S_T^\alpha = \sqrt{(S_S^\alpha)^2 + (S_G^\alpha)^2} \tag{4.35}$$

with,

$$S_S^\alpha = \lambda_S \mu b_S^\alpha \sqrt{(\sum_{\beta=1}^{N} h^{\alpha\beta} \rho_S^\beta)} \tag{4.36}$$

$$S_G^\alpha = \lambda_G \mu b_G^\alpha \sqrt{(\sum_{\beta=1}^{N} h^{\alpha\beta} \rho_G^\beta)} \tag{4.37}$$

Here, μ is the shear modulus while b_S^α and b_G^α are their corresponding Burgers vector magnitude. The terms λ_S and λ_G are statistical coefficients that account for the deviation from regular spatial arrangements of the SSD and GND populations, respectively. In what follows, it will be assumed for simplicity that $b = b_S^\alpha = b_G^\alpha$ and $\lambda = \lambda_S + \lambda_G$. In Equation (4.38), $h_S^{\alpha\beta}$ and $h_G^{\alpha\beta}$ represents the the respective SSD and GND dislocation interaction matrices defined as,

$$h_k^{\alpha\beta} = \omega_{k1} + (1 - \omega_{k2})\delta^{\alpha\beta} \quad \text{for} \quad k = S, G \tag{4.38}$$

where ω_{k1} and ω_{k2} are two cross-hardening constants and $\delta^{\alpha\beta}$ the Kronecker symbol. The overall dislocation density for a given slip system β, ρ_T^β , is obtained from a discretisation of the dislocation structure into pure edge and pure screw types, of densities ρ_{S_e} and ρ_{S_s}, respectively:

$$\rho_S^\beta = \rho_{S_e}^\beta + \rho_{S_s}^\beta \tag{4.39}$$

$$\rho_G^\beta = \rho_{G_{en}}^\beta + \rho_{G_{et}}^\beta + \rho_{G_s}^\beta \tag{4.40}$$

The subscripts en and et refer to edge components resolved along the slip direction m and perpendicular to it, $t^\alpha = m^\alpha \times n^\alpha$. Edge and screw dislocations act as obstacles to dislocation motion in the form of forest dislocations and they contribute to the athermal slip resistance in the following way:

$$S_T^\alpha = \lambda \mu b^\alpha \sqrt{(\sum_{\beta=1}^{N} h^{\alpha\beta} \rho_{S_e}^\beta + \rho_{S_s}^\beta)} \tag{4.41}$$

To complete the set of constitutive relations, separate evolutionary equations are developed for both dislocation densities, with dislocation multiplication and annihilation forming the bases of their evolutionary behaviour.

4.2.3 Dislocation mechanics based crystallographic formulation

4.2.3.1 Main Dislocation Generation Mechanism

Dislocation generation is assumed to be associated with the expansion of dislocation loops originating from existing Franck-Read sources. Figure 4.6 shows an idealised, expanding dislocation loop on a arbitrary active slip system α during a time dt. The loop is assumed to be rectangular, with straight edge and screw sides of lengths L_e^α and L_s^α respectively.

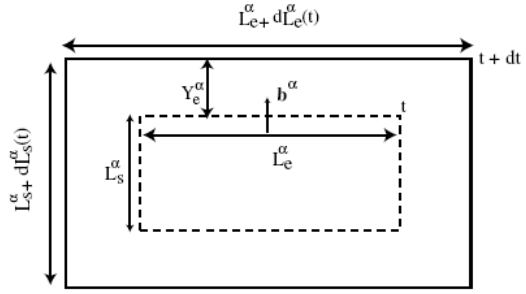

Figure 4.6: Dislocation multiplication - schematic diagram of an idealised expanding dislocation loop during a time interval dt (Cheong and Busso 2004)

The change in dislocation densities ($d\alpha$), where i refers to either edge (e) or screw (i) dislocations, is attributed to the increase in length of the individual dislocation segments (dL_i^α) expanding simultaneously within a control volume V,

$$d\rho_i^\alpha = \frac{dL_i^\alpha(t)}{V} \quad \text{for} \quad i = e, s \tag{4.42}$$

Considering an edge segment of the dislocation loop, its contribution to the plastic strain increment after a time interval dt is,

$$d\rho_e^\alpha = b^\alpha Y_e \alpha \Big[\frac{L_e^\alpha + dL_e^\alpha}{V}\Big] \tag{4.43}$$

Here, Y_e^α is the mean free path of the edge dislocation segment, defined to be the distance travelled by the segment before its motion is arrested by forest dislocations. Differentiating Equation (4.43) with respect to time yields the rate of generation of edge dislocation density,

$$\dot{\rho}^{\alpha}_{e,gen} = \frac{C_e}{b^{\alpha} Y^{\alpha}_{e}} \dot{\gamma}^{\alpha} \tag{4.44}$$

and similarly for the generation of screw dislocations,

$$\dot{\rho}^{\alpha}_{s,gen} = \frac{C_s}{b^{\alpha} Y^{\alpha}_{s}} \dot{\gamma}^{\alpha} \tag{4.45}$$

where C_e and C_s are parameters that scale the magnitudes of the slip rate contributions from the edge and screw segments, respectively.

4.2.3.2 Main dislocation annihilation mechanism

Mutual annihilation between parallel dislocations of the same character but opposite sign is assumed to be the predominant mechanism. An annihilation event occurs when two dislocation are drawn towards each other by their attractive forces in order to reduce their line energies. Through this combination process, the opposing dislocations mutually annihilate. The probability of such an event occurring is determined by the cross sectional area for annihilation. Such a region is illustrated by the dashed line around a gliding screw dislocation, which moves from the position at time "t" to "$t + dt$".

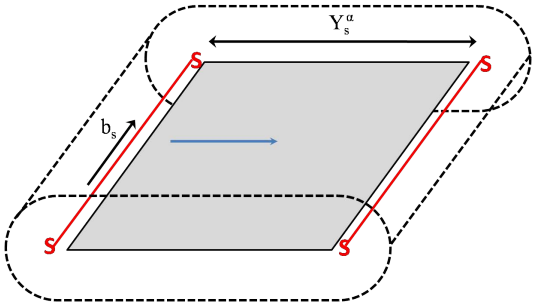

Figure 4.7: Dislocation annihilation - Schematic diagram of the annihilation region for a screw dislocation after a time interval dt (Cheong and Busso 2004)

The symbol b_s represents the critical distance for mutual annihilation between two anti-parallel screw dislocations to take place. Based on the region outlined in the figure, the annihilation area A^{α}_{s} for a screw segment gliding on an arbitrary slip system (α) is:

$$A^{\alpha}_{s} = [2 d_s Y^{\alpha}_{s} + \pi d^2_s] \tag{4.46}$$

The probability of an annihilation event is:

$$P_{ann} = \frac{1}{2} \frac{A^{\alpha}_{s} L^{\alpha}_{s}}{V} = \frac{A^{\alpha}_{s} \rho^{\alpha}_{s}}{2} \tag{4.47}$$

The screw dislocation density annihilation rate is:

$$\dot{\rho}^{\alpha}_{s,ann} = \frac{C_s}{b_{\alpha}} \left[\frac{\pi d^2_s}{Y^{\alpha}_{s}} + 2 d_s \right] \rho^{\alpha}_{s} \dot{\gamma}^{\alpha} \tag{4.48}$$

The dislocation density annihilation rate for edge dislocations does not include the additional term $\pi d_S^2 Y_S^\alpha$ because of their inability to cross-slip. Therefore, the edge dislocation annihilation rate is,

$$\dot{\rho}^\alpha_{e,ann} = \frac{C_s}{b_\alpha}\Big[2d_s\Big]\rho^\alpha_s|\dot{\gamma}^\alpha| \tag{4.49}$$

To express the evolutionary laws for edge and screw dislocations in terms of their dislocation densities, Y_e^α and Y_s^α are linked to the mean obstacle spacing, l_m^α, where the dominant obstacles are forest dislocations. A relationship between Y_i^α and l_m^α is written as,

$$Y_i^\alpha = \frac{l_m^\alpha}{K_i} \quad \text{for} \quad i = e, s \tag{4.50}$$

where K_i is a dimensionless proportionality constant controlling the mobility of dislocations. Since a moving dislocation will be affected by the nature of the forest obstacle, i.e. edge and screw dislocations, the mean obstacle spacing l_m^α should be a function of the total dislocation density, ρ_T^α. Here, l_m^α follows the inverse squareroot relationship obtained from geometric considerations,

$$l_m^\alpha = \frac{1}{\sqrt{\sum_{\beta=1}^{N}\rho_T^\beta}} \tag{4.51}$$

4.2.3.3 Dislocation density evolutionary equations

The evolutionary behaviour of both edge and screw SSDs follows from the work of Cheong and Busso (2004). They were formulated as balance equations between dislocation generation and dislocation annihilation. From Equations (4.44), (4.45) and (4.48), (4.49), one obtains

$$\dot{\rho}^\alpha_e = \frac{C_e}{b^\alpha}\left[K_e\sqrt{\sum_{\beta=1}^{N}\rho_T^\beta} - 2d_e\rho_e^\alpha\right]|\dot{\gamma}^\alpha| \tag{4.52}$$

$$\dot{\rho}^\alpha_s = \frac{C_s}{b^\alpha}\left[K_s\sqrt{\sum_{\beta=1}^{N}\rho_T^\beta} - \rho_s^\alpha\left(\pi d_s^2 K_s\sqrt{\sum_{\beta=1}^{N}\rho_T^\beta} + 2d_s\right)\right]|\dot{\gamma}^\alpha| \tag{4.53}$$

4.2.4 Slip rate gradients for non-local constitutive behaviour

The strain gradient theory here follows the work of Busso et al. (2000), Meissonnier et al. (2001), Busso and Cheong (2005), where the evolution of the GND structure is linked to local slip rate gradients. During plastic deformation of crystalline materials, GNDs accommodate orientation gradients within single crystals in the material. This dislocation structure is necessary to maintain lattice continuity. By definition, the density of the GNDs is related to the net Burgers vector of all dislocations piercing an infinitesimal surface (S) with normal $\mathbf{n}$, and enclosed counter-clockwise by a circuit (G) in the intermediate configuration associated

with $\mathbf{F}^p$. The resulting discontinuity $\mathbf{G}$ on completion of a Burgers circuit around the path is then defined through Nye's dislocation density tensor ∇ (Nye 1953) using Stoke's theorem,

$$\mathbf{G} = -\int_{\Gamma} \mathbf{F}^p dX = \int_S \Lambda.\mathbf{n} ds, \quad \text{where} \quad \Lambda = curl\,(\mathbf{F}^p) = \nabla \times \mathbf{F}^p \tag{4.54}$$

The evolution of GNDs can be then obtained by differentiating Equation (4.54) with respect to time. Here,

$$\mathbf{G} = \int_S \dot{\Lambda}.\mathbf{n} dS = \int_S \sum_{\alpha} \dot{\Lambda}^{\alpha}.\mathbf{n} dS, \quad \text{where} \quad \dot{\Lambda}^{\alpha} = \text{curl}\{(\dot{\gamma}^{\alpha}\mathbf{m}^{\alpha} \otimes \mathbf{n}^{\alpha})F^p\} \tag{4.55}$$

Considering that there exists a vectorial field of GNDs for every slip system, the GNDs can be represented by a generic GND line vector $\mathbf{G}$ with Burger's vector $\mathbf{b}$. This dislocation line vector can be further discretised into its edge and screw components by solving along axes of the coordinate system defined in terms of the slip directions $\mathbf{m}^{\alpha}$, its slip plane normal $\mathbf{n}^{\alpha}$ and a third orthogonal direction $\mathbf{t}^{\alpha} = \mathbf{m}^{\alpha} \times \mathbf{n}^{\alpha}$.

$$\rho_G^{\alpha} = \rho_{G_S}^{\alpha}\mathbf{m}^{\alpha} + \rho_{G_{en}}^{\alpha}\mathbf{n}^{\alpha} + \rho_{G_{et}}^{\alpha}\mathbf{t}^{\alpha} \tag{4.56}$$

Here, G_s refers to its screw component parallel to $\mathbf{m}^{\alpha}$ while G_{en} and G_{et} are the edge components parallel to $\mathbf{n}^{\alpha}$ and $\mathbf{t}^{\alpha}$, respectively (see Figure (4.8)).

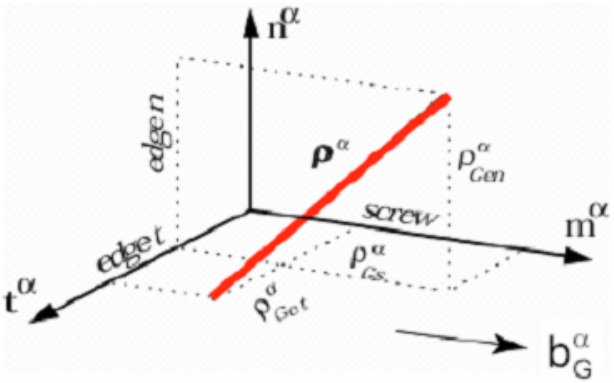

Figure 4.8: Local orthogonal coordinate system for a generic geometrically necessary dislocation line in an arbitrary slip system α (Busso et al. 2000)

The Burgers vector discontinuity associated to the density of the GNDs crossing a unit area (S) with normal $\mathbf{r}$ is given by

$$G = \int_S (b_G^{\alpha} \otimes \rho_G^{\alpha}).\mathbf{n} dS \tag{4.57}$$

Differentiating Equation (4.57), a second expression of the rate of G is obtained

$$\dot{G} = \int_S (b_G^{\alpha} \otimes \dot{\rho}_G^{\alpha}).\mathbf{n} dS \tag{4.58}$$

By equating Equations (4.55) and (4.57), the final expression for the GND evolution written

in tensorial form becomes

$$\dot{\rho}^{\alpha}_{G_S}(b^{\alpha}_{G}\otimes\mathbf{m}^{\alpha})+\dot{\rho}^{\alpha}_{G_{en}}(b^{\alpha}_{G}\otimes\mathbf{n}^{\alpha})+\dot{\rho}^{\alpha}_{G_{et}}(b^{\alpha}_{G}\otimes\mathbf{t}^{\alpha})= \quad \text{curl} \quad [(\dot{\gamma}^{\alpha}\mathbf{m}^{\alpha}\otimes\mathbf{n}^{\alpha})F^{p}] \tag{4.59}$$

4.2.5 Solid solution strengthening contribution

Let us consider a dislocation and a solute solution atom in the same slip plane, if interactions are attractive (size effect and modulus effect), dislocations will store energy when they are deformed to pass in the neighbourhood of solute solution atoms.

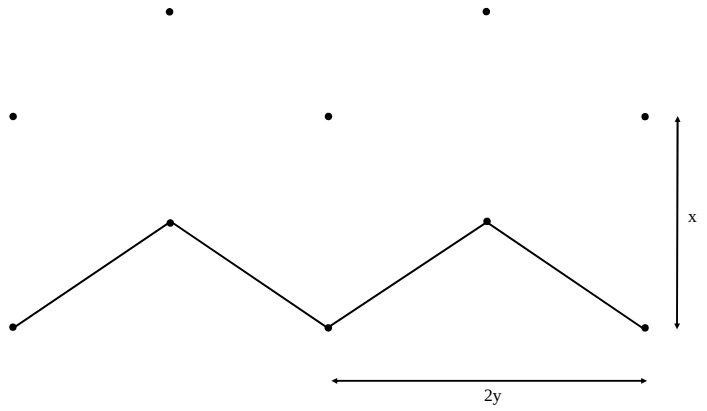

Figure 4.9: Dislocation pinning (Saada 1968)

This energy E is defined as the difference between E_1 the energy capted by unity of length when the dislocation path in the neighbourhood of solute solution atoms, and E_2 the line energy lost due to dislocation pinning (see Figure 4.9).

$$E = E_1 - E_2 \tag{4.60}$$

$$E_1 = \frac{W_M}{y} \tag{4.61}$$

$$E_2 \approx \frac{\mu b^2}{2y}\left[\left(x^2+y^2\right)^{1/2}-y\right] \tag{4.62}$$

$$xy = \frac{a^2}{c} \tag{4.63}$$

where a^2 is the average surface by atoms in a perfect die. E show a minimum for:

$$x = \left[\frac{\alpha|W_M|}{\mu c}\right]^{1/3} \tag{4.64}$$

where α is a geometric constant equal to $\frac{\sqrt{3}}{2}$ for a perfect dislocation and $\frac{\sqrt{3}}{6}$ for a Shockley dislocation along the close packed plane in compact structure. From Equations (4.63) and (4.64) y can be calculated in the case of predominant size effect:

$$x \approx \left(\frac{|\eta|}{\alpha' c}\right)^{1/3} b \approx \frac{1}{2}\left(\frac{\eta}{c}\right)^{1/3} b \tag{4.65}$$

where b is Burgers vector and α' a geometric constant which is equal to $8\frac{\sqrt{2}}{\sqrt{3}}$ for a perfect dislocation and equal to $8\frac{\sqrt{2}}{3}$ for a Shockley dislocation in a compact structure. In both case $\alpha'^{1/3} \approx 2$. From Equation (4.65) it can be shown that x is small (i.e. some interatomic length). With a modulus effect $W \approx \frac{\mu\nu\delta}{36\pi^2}$, σ_M the stress needed to move dislocations pinned on impurities at 0 K can be calculated in writing the energy needed to transfer a dislocation from the stable position to unstable position, and it is equal to the work of the applied stress.

$$(\sigma_M - \sigma_i)bxy = (E_1 - 2E_2)y \tag{4.66}$$

where σ_i is large distance stresses. With Equations (4.64) and (4.65), σ_M is expressed as follows:

$$\sigma_M = \sigma_i + \frac{|W_M c_0|}{2a^2 b} \tag{4.67}$$

Thus, the size effect is written as:

$$\sigma_M = \sigma_i + \frac{1}{4}\mu\eta c\frac{\mu}{a^2 b} \approx \sigma_i + \frac{1}{4\alpha''}\mu\eta c \tag{4.68}$$

where α'' is a geometric constant for compact structure equal to $\sqrt{\frac{3}{2}}$ for perfect dislocations, and $\frac{1}{\sqrt{2}}$ for not perfect dislocations.

It was observed that elastic limits for very low temperature ($\approx$ 4 K) are proportional to the concentration and factor size in precipitates. Nevertheless, observed values are lower than those obtained with Equation (4.68). This is due to the fact that distances between precipitates are not constant and fluctuate around an average. The previous calculation can be generalised for temperatures higher than 0 K with:

$$\sigma = \sigma_i + \sigma_M\left(1 - \frac{T}{T_c}\right) \quad \text{for} \quad T \leqslant T_c \tag{4.69}$$

$$\sigma = \sigma_i \quad \text{for} \quad T \geqslant T_c \tag{4.70}$$

$$\text{with} \quad kT_c = \frac{|W_M|}{2\log(\rho_D \mu b x^2 C_0/\dot{\epsilon})} \tag{4.71}$$

where $\dot{\epsilon}$ is the strain rate, ρ_D the density of mobile dislocations and μ the Debye frequency ($\approx 10^{13} s^{-1}$). With common parameter T_c is fund to be in a range of 100 to 200 K.

Finally, S_{SS}, the friction stress due to Magnesium in solid solution was approximated as, (Friedel 1965b):

$$S_{SS} = \frac{1}{4}\mu(\eta c)^{\frac{4}{3}} \tag{4.72}$$

Due to the lack in experimental data, the cross–hardening matrix was set to that found in (Busso and Cheong 2005, Cheong and Busso 2006) so that the only influence of magnesium that was taken into account was that on the lattice friction stress.

4.3 Calibration of the Single Crystal Model

4.3.1 Flow rule parameters for aluminium single crystals

The material constants for Al come from published values (Busso and Cheong 2005, Cheong and Busso 2006). The anisotropic elasticity tensor of FCC crystals was defined by three independent parameters, C_{11}, C_{12} and C_{44}. Values of the elastic parameters for aluminium vary significantly with temperature, θ in the temperature range of interest. All three parameters were approximated by a polynomial relation (Simmons and Wang 1971) in GPa units, θ in K:

$$C_{11} = 123.32 + (6.70 \times 10^8)\theta^3 - (1.13 \times 10^4)\theta^2 - (7.88 \times 10^3)\theta \tag{4.73}$$

$$C_{12} = 70.65 + (4.41 \times 10^8)\theta^3 - (7.55 \times 10^5)\theta^2 - (4.00 \times 10^3)\theta \tag{4.74}$$

$$C_{44} = 31.21 + (7.05 \times 10^9)\theta^3 - (1.22 \times 10^5)\theta^2 - (8.33 \times 10^3)\theta \tag{4.75}$$

$$\mu = 29.16 + (9.00 \times 10^9)\theta^3 - (2.00 \times 10^5)\theta^2 - (73.00 \times 10^4)\theta \tag{4.76}$$

The flow rule defined by Equation (4.32) contains five material parameters ($\dot{\gamma}_0$, F_0, $\widehat{\tau}_0$, p, q) that have been determined by Balasubramanian and Anand (2002). For the hardening-recovery laws defined by Equations (4.52) and (4.53), the relevant parameters are the annihilation distances for the edge and screw dislocations, d_e, d_{sw}, and the constants defining the mean free paths of the respective dislocation types, namely K_e and K_{sw}. These parameters were chosen to be compatible with physical observations made at the microstructural level. The selected values for d_e and d_{sw} are 7.0 and 35.0 nm, respectively. This value of d_e was determined by calibrating the macroscopic response of the constitutive model with [100], [111] and [112] Al single crystal tensile test data at 273 K (Busso and Cheong 2005, Cheong and Busso 2006). A higher value of 35 nm was taken for d_{sw} based on the fact that screw dislocations have the ability to cross-slip, thus increasing the spontaneous annihilation between screw dislocations of opposite sign (Busso and Cheong 2005). Previous slip line work on Cu by Rebstock (1957), Mader (1957) estimated the distance travelled by edge dislocations to be approximately twice that of screw types. As this is associated with the mean free path of the dislocations, K_{sw} was set to be twice the value of K_e so that, in Equation (4.53), the relationship between the mean free paths of the two dislocation types agree with these physical observations, and that their respective mean free paths evolve at a constant ratio. Consequently, $K_{sw} = 2K_e$ and a value of $K_e = 15.7 \times 10^{-3}$ was calibrated based on the single crystal stress-strain data (Busso and Cheong 2005, Cheong and Busso 2006), while C_e and C_{sw} were set to 0.5 to keep the slip contributions from both edge and screw dislocations equal. The initial total dislocation density specified is 8000 mm^{-2}, which is in the same order as that measured in pure FCC metallic single crystals (Honeycombe 1968). The total density is equally made up of edge and screw types and assumed to be equivalent in each of the twelve octahedral slip systems.

To confirm the validity of the calibrated parameters, finite-element (FE) simulations of single crystals under uniaxial tensile loading were performed in Zebulon. As shown in Figure 4.10, the mesh consists of $5 \times 5 \times 50$ elements. Quadratic brick elements with reduced integration were used. Boundary conditions are described in Figure 4.10, a true strain rate of $10^{-4}s^{-1}$ was applied to nodes of the top face and nodes of the bottom face were locked in z direction. As measured in (Hosford et al. 1960), initial misalignment of 0.5 $^\circ$ in the Al

single crystals from the [100], [111] and [112] ideal orientations is introduced in the simulations carried out, see Table 4.3. As shown in Figure 4.11, good agreement was obtained between the predicted single crystal response and the tensile test data from [100], [111] and [112] oriented Al single crystals (Hosford et al. 1960). The calibration was carried out at a temperature of 298 K. A summary of the material constants and model parameters at 298 K, was shown in Table 4.2.

Table 4.2: Single crystal model parameters

Elastic constants (GPa)	Flow rule (Equation (4.32))
$C_{11} = 112.9$	$F_0 = 3 \times 10^{-19}$ J
$C_{22} = 66.4$	$\widehat{\tau}_0 = 8.0$ MPa
$C_{33} = 27.9$	$\dot{\gamma}_0 = 1.73 \times 10^6 s^{-1}$
	$p = 0.141$
	$q = 1.10$
Evolutionary laws (Equations (4.36),(4.52)and(4.53))	
$b = 2.57 \times 10^{-7}$ nm	$C_e = C_{sw} = 0.5$
$d_e = 7.0$nm; $d_{sw} = 35$ nm	$K_{sw} = 2K_e$; $K_e = 15.7 \times 10^{-3}$
$\omega_1 = 1.5$; $\omega_2 = 1.2$	$\lambda = 0.3$

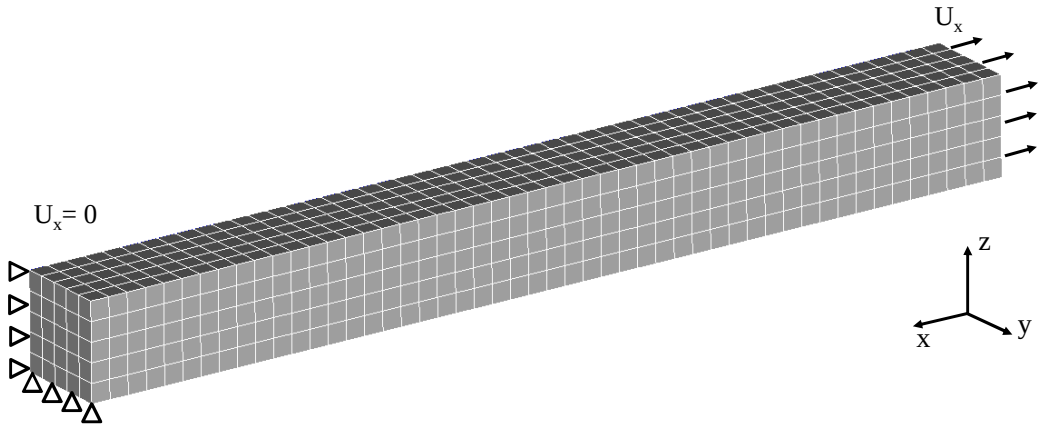

Figure 4.10: FE mesh used to simulate uniaxial tensile tests

Table 4.3: Al single crystals orientation

Orientation	$\phi_1(^\circ)$	Φ $(^\circ)$	ϕ_2 $(^\circ)$
[100]	0.4	10.0	0.0
[111]	54.8	135.01	180.0
[112]	61.1	69.7	281.0

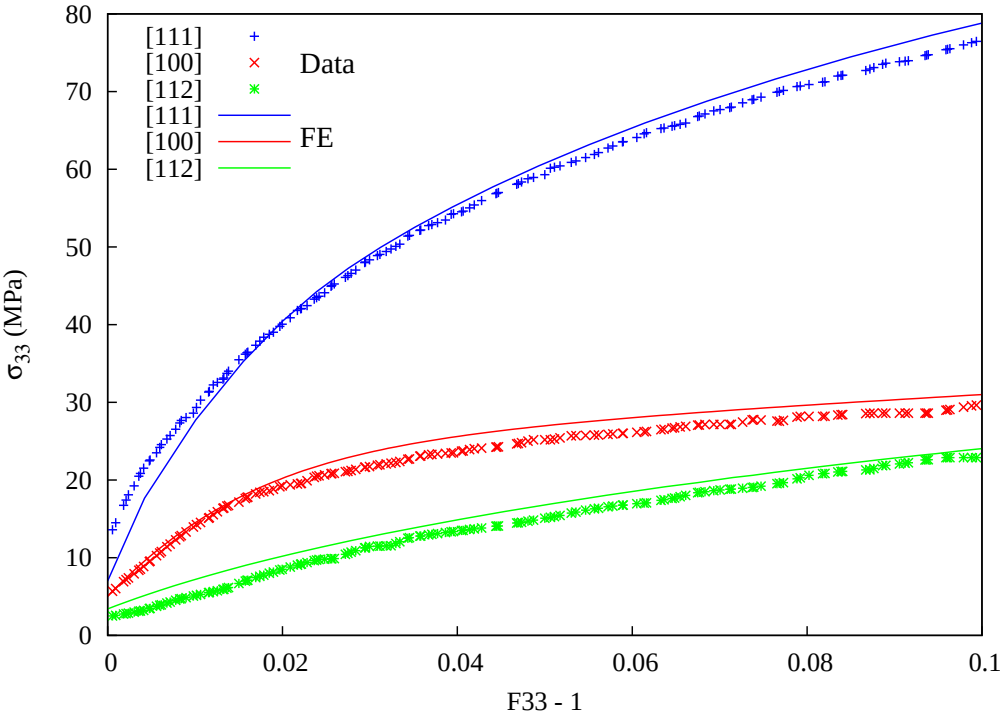

Figure 4.11: Comparison of true-stress true-strain prediction along [100], [111] and [112] with experimental data at 298 K (Hosford et al. 1960).

4.3.2 Identification of a representative volume element

It was adopted in this work the use of finite element models that are able to describe non-homogeneous deformation at both the intragranular and intergranular levels. When using finite-elements (FE) to model polycrystalline aggregates, the constitutive response at each integration points of a finite element is determined using a single crystal constitutive model. In this approach, the transition from the constitutive response of each crystal to the response of a polycrystalline aggregate is shown in Figure 4.12. Typically, the single crystal accounts for deformation and for the associated lattice rotations through crystallographic slip (see Section). The distinct advantage of finite-element models compared to the other polycrystal plasticity models is that morphological effects such as grain size, shape and topology can be accounted for.

Polycrystalline aggregates were obtained from a digital microstructure generated from mathematical models based on Poisson's distribution of the grain nuclei. This algorithm is based on an isotropic growth of seeds distributed inside the volume and it is supposed to reproduce the crystallization phenomenon observed during the cooling from the liquidus state to the solid state for crystalline materials. However, it creates geometrical equiaxed grains as illustrated in Figure 4.12 and only the first order of the experimental grain boundary morphology is obtained.

Figure 4.12 presents a microstructure composed of 100 grains obtained with Voronoi tessellation. Grains are defined as groups of elements with common randomly assigned orientations. Parallel computations were carried out to solve the resulting non linear system. The FE code Zebulon used is fully parallelised thanks to Feyel (1998). The algorithm is based on a subdomain decomposition method called FETI (Finite Element Tearing and

Interconnecting method proposed by Fahrat and Roux (1991)). After the decomposition of the structure into subdomains, the sub-problems into each domain are solved independently and an iterative scheme is employed to obtain the solution of the global problem, and to merge the results of all subdomains.

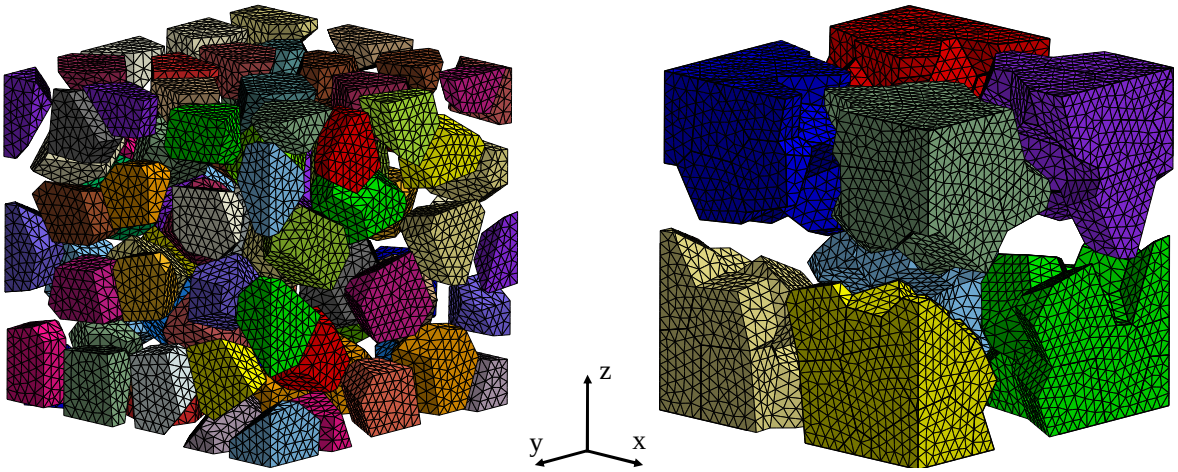

(a) (b)

Figure 4.12: Exploded view of (a) a cubic aggregate of 100 grains (b) the corresponding subdomains decomposition for parallel computations.

4.3.2.1 Effect of grain morphology

The grain morphology was investigated to evaluate macroscopic and local behavior obtained with two aggregates of Al-Mg polycrystalline aggregates. Both have an initial cubic geometry with different grain morphology, see Figure 4.13. In both cases, grains are defined by groups of elements with randomly assigned orientations. Boundary conditions are described in Figure 4.13. A true displacement yielding an average strain rate of $10^{-4}s^{-1}$ was applied on the top surface at a temperature of 298 K. A constant value of crystal orientation was assumed inside each grain. In order to study locally the effect of grain morphology, the grain rotation distribution (Figure 4.14), the accumulated plastic strain distribution (Figure 4.15), the dislocation density (Figure 4.16) and von Mises stress distribution (Figure 4.17) were plotted after 5% applied strain for both polycrystals. The resulting stress-strain response is given in Figure 4.18.

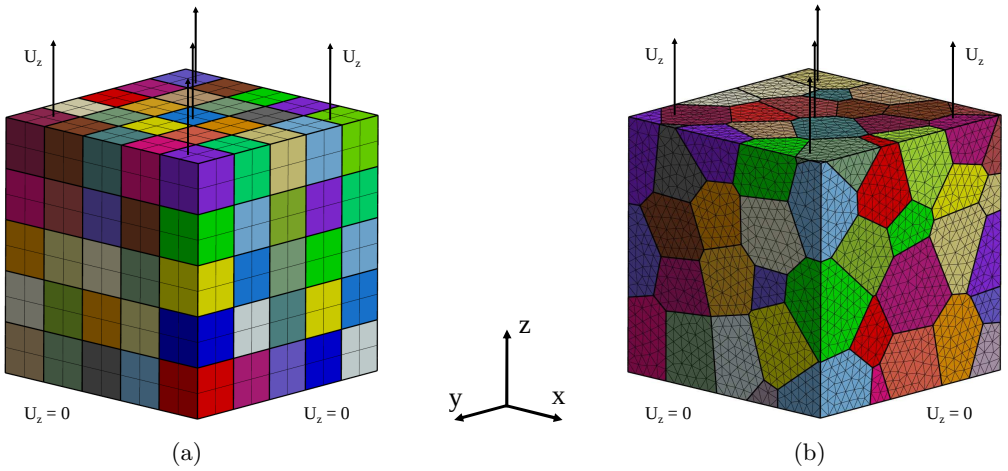

Figure 4.13: Polycrystalline aggregates used to simulate uniaxial tensile tests with (a) a regular mesh and cubic grains, and with (b) a free mesh and Voronoi tessellation. U_z is applied on the top of aggregate to prescribe an average true strain rate of $10^{-4}s^{-1}$.

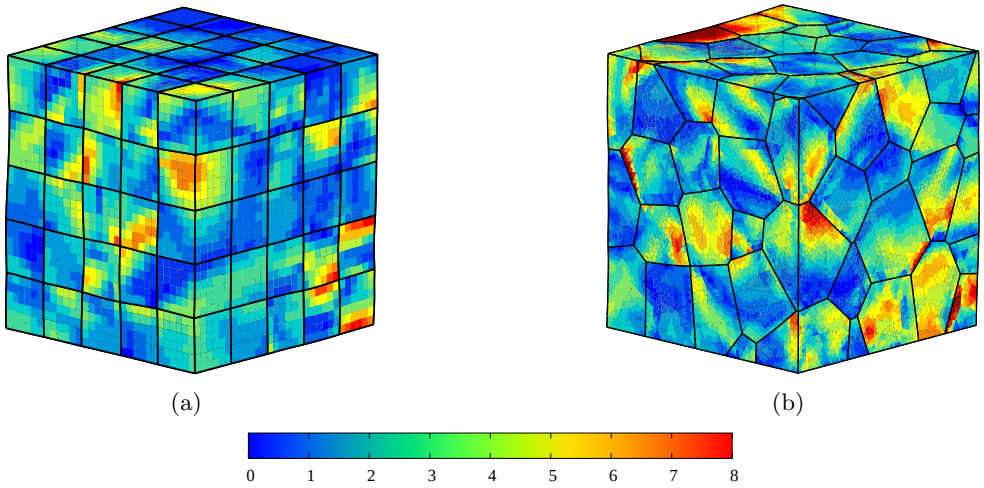

Figure 4.14: Grain rotation distribution (in degrees) after 5% applied strain.

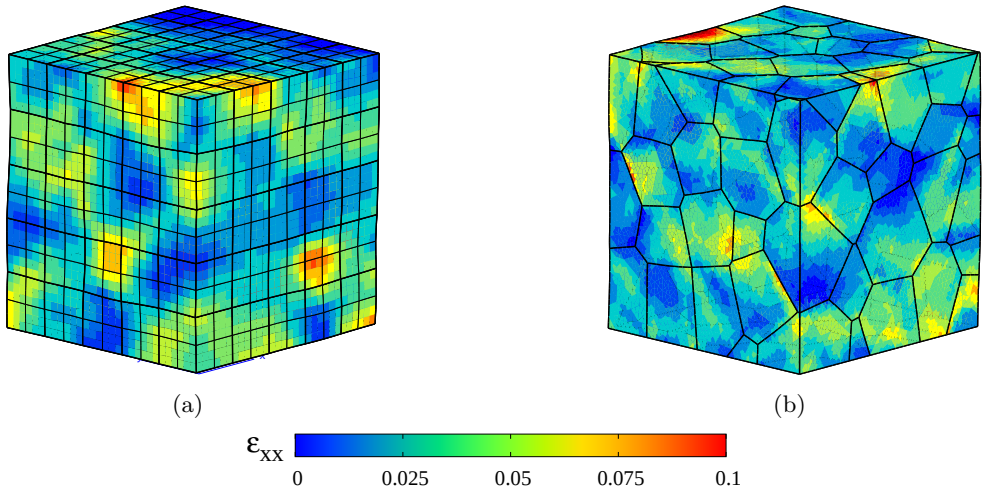

Figure 4.15: Accumulated plastic strain distribution after 5% applied strain.

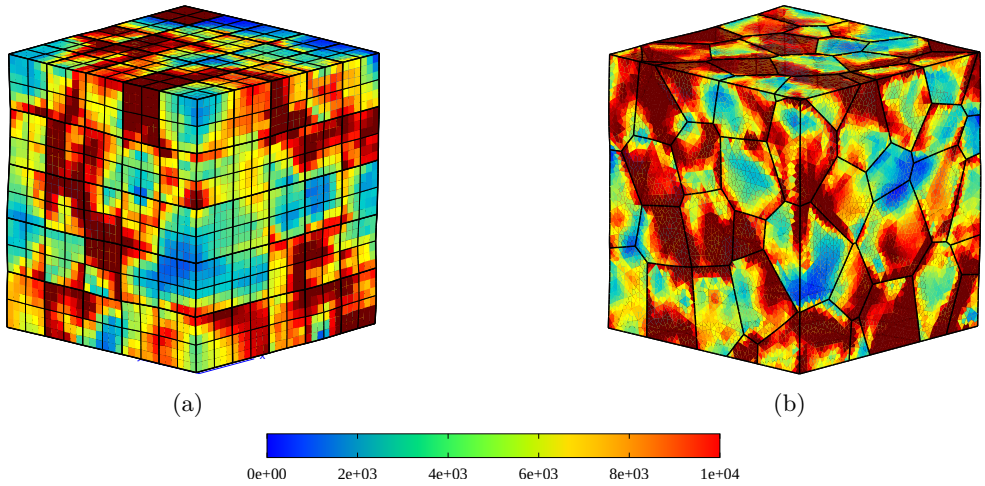

Figure 4.16: Dislocation density (in mm^{-2}) after 5% applied strain.

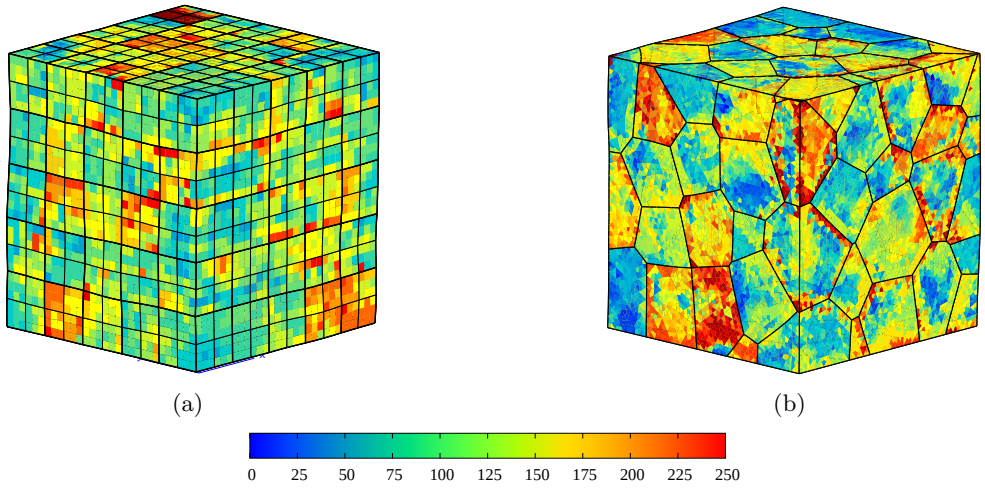

Figure 4.17: Von Mises stress distribution (in MPa) after 5% applied strain.

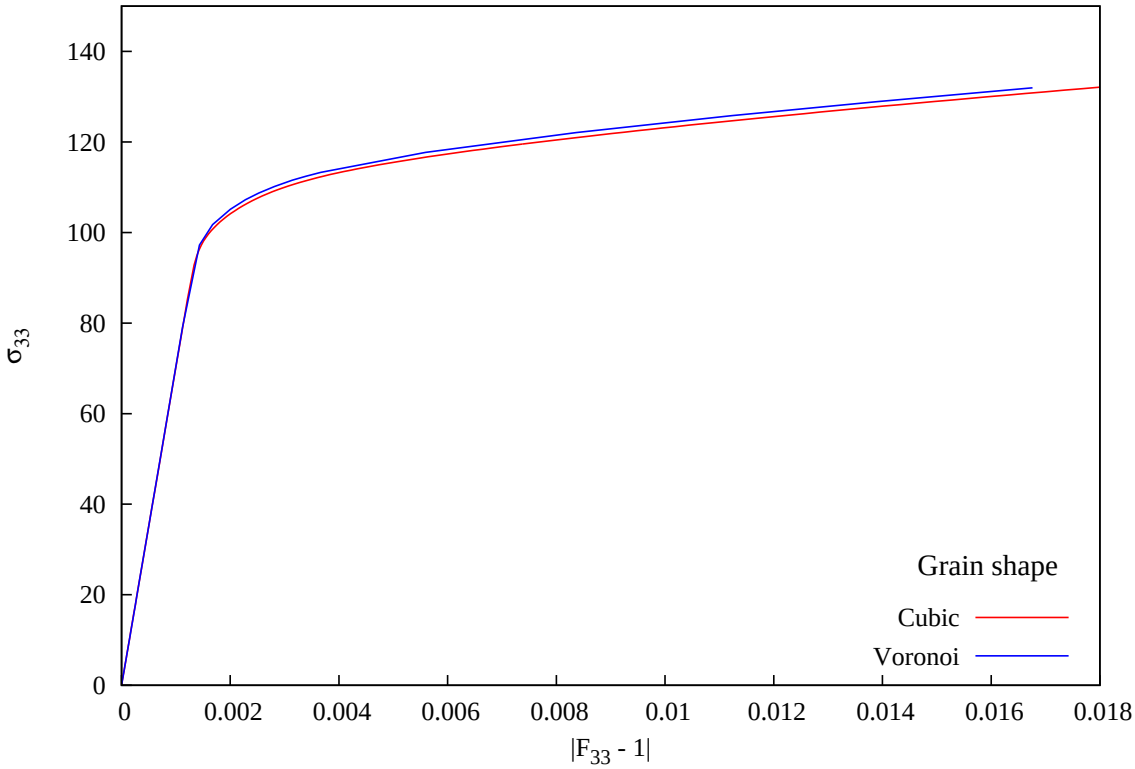

Figure 4.18: Predicted macroscopic stress-strain responses of both aggregates of Figure 4.13 (σ_{33} in MPa).

The predicted accumulated grain rotation is shown in Figure 4.14. In both cases rotations are heterogeneous inside each grain giving a misorientation development. Only few grains keep their initial orientation as seen in Figure 4.14. In both aggregates it can be observed the growth of deformed bands with a size close to the grain size as observed in the experimental part of the study (see Chapter 3). Maxima of dislocations density are more localised in cubic grains. Moreover, the dislocation density is more confined in specific grains in contrast with more homogeneous dislocation density over the whole Voronoi aggregate. The same observation can be done in terms of von Mises stress distribution. This contrast between results obtained from both aggregates can be interpreted as a consequence of the use of a lower number of grains in cubic simulations and higher fraction of grains belonging to the free surfaces and thus not constrained by other grains to rotate. However, in Figure 4.18, both polycrystalline aggregates predicted similar average macroscopic stress-strain curves.

One can conclude from the analysis of grain morphology effect that the macroscopic behavior is similar in both cases. This proves that cubic grains can be used to calibrate the crystal plasticity model as well as equivalent Voronoi aggregates (i.e. in number of grains) since the only experimental data that are used are average stress-strain curves. The use of cubic grains will decrease calculations time by a factor of 10. However cubic grains with such a low number of elements per grain do not yield accurate local stress–strain states.

4.3.2.2 Effect of number of considered grains

Here, the effective number of cubic grains needed to accurately predict the macroscopic behaviour of the alloy was studied. Six cubic aggregates composed of 27, 64, 125, 216, 343 and 512 cubic grains were considered, see Figure 4.19. In both cases, grains are defined by groups of 8 quadratic elements with common randomly assigned crystal orientation. Boundary conditions are described in Figure 4.13. A displacement leading to an average true strain rate of $10^{-4}s^{-1}$ was applied on the top surface at a temperature of 298 K. In order to study the effect of the number of considered grains locally, the grain rotation distribution (Figure 4.20), the accumulated plastic strain distribution (Figure 4.21), the dislocation density (Figure 4.22) and the Von Mises stress distribution (Figure 4.23) were plotted after 10% applied strain. The resulting stress-strain response is given in Figure 4.24.

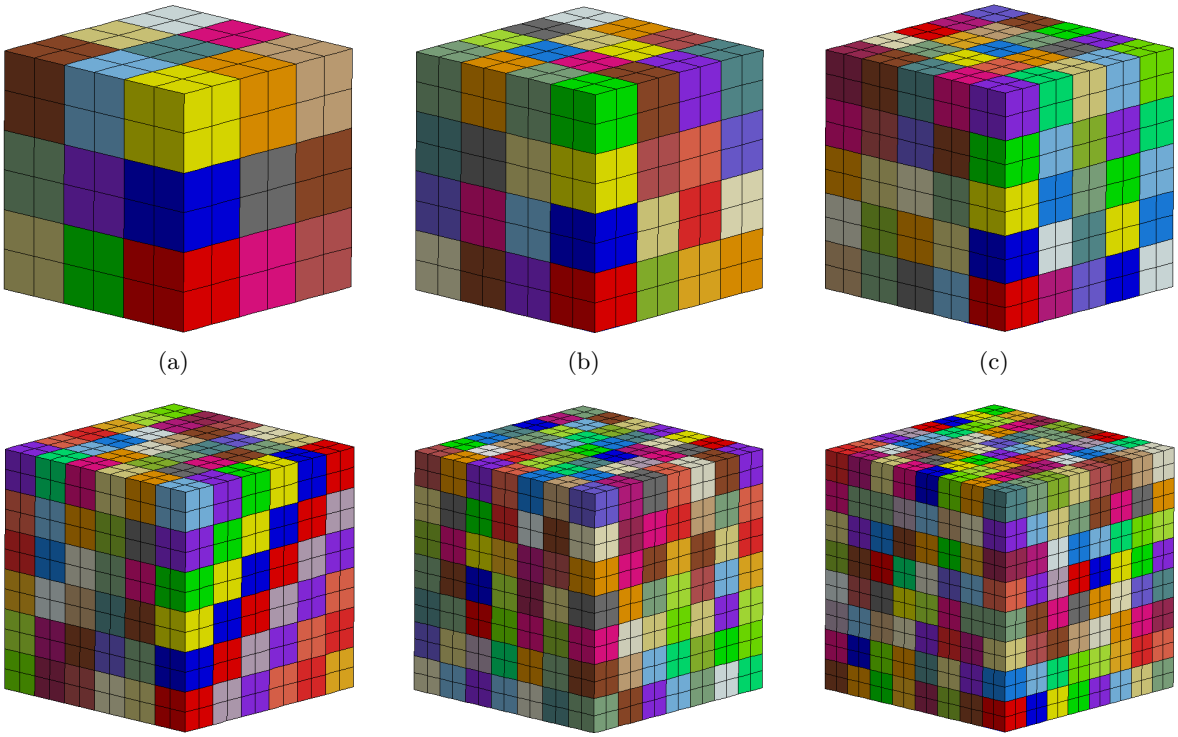

Figure 4.19: Polycrystalline aggregates used to simulate uniaxial tensile tests with a regular mesh and (a) 27, (b) 64, (c) 125, (d) 216, (e) 343 and (f) 512 cubic grains

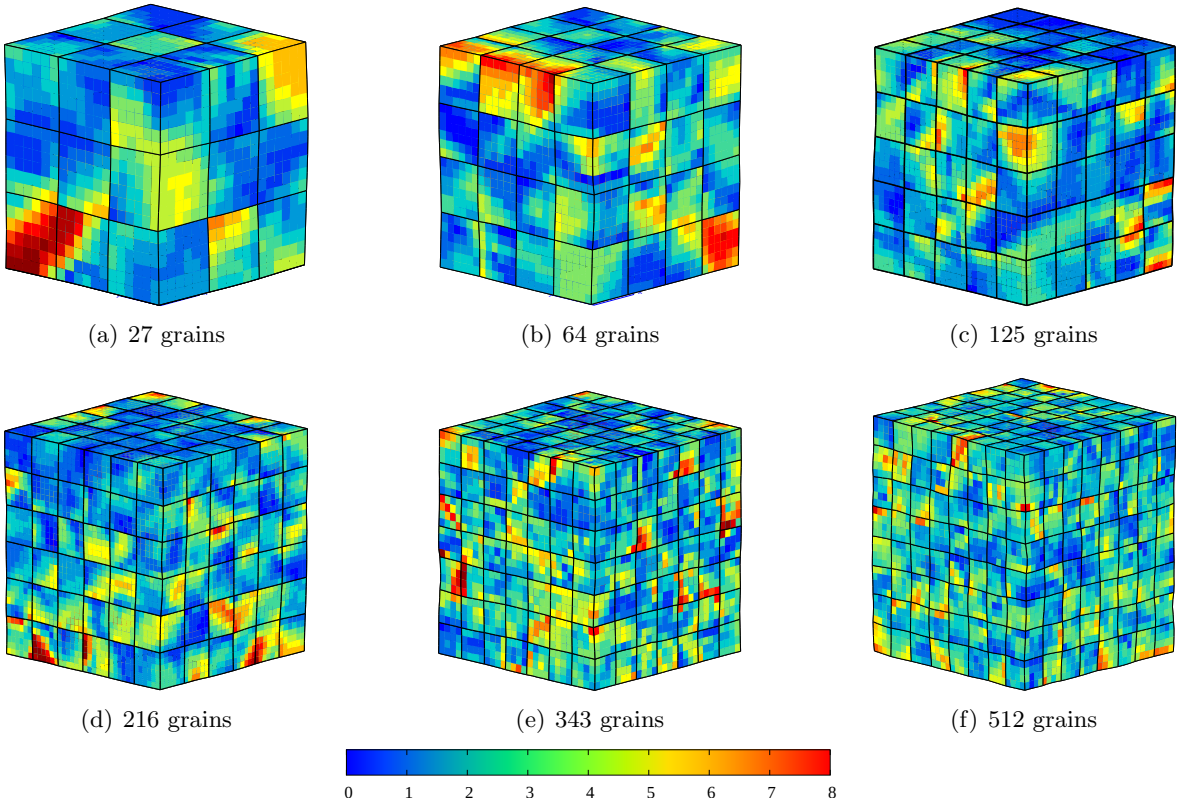

(a) 27 grains (b) 64 grains (c) 125 grains

(d) 216 grains (e) 343 grains (f) 512 grains

Figure 4.20: Grain rotation distribution (in degrees) after 10% applied strain

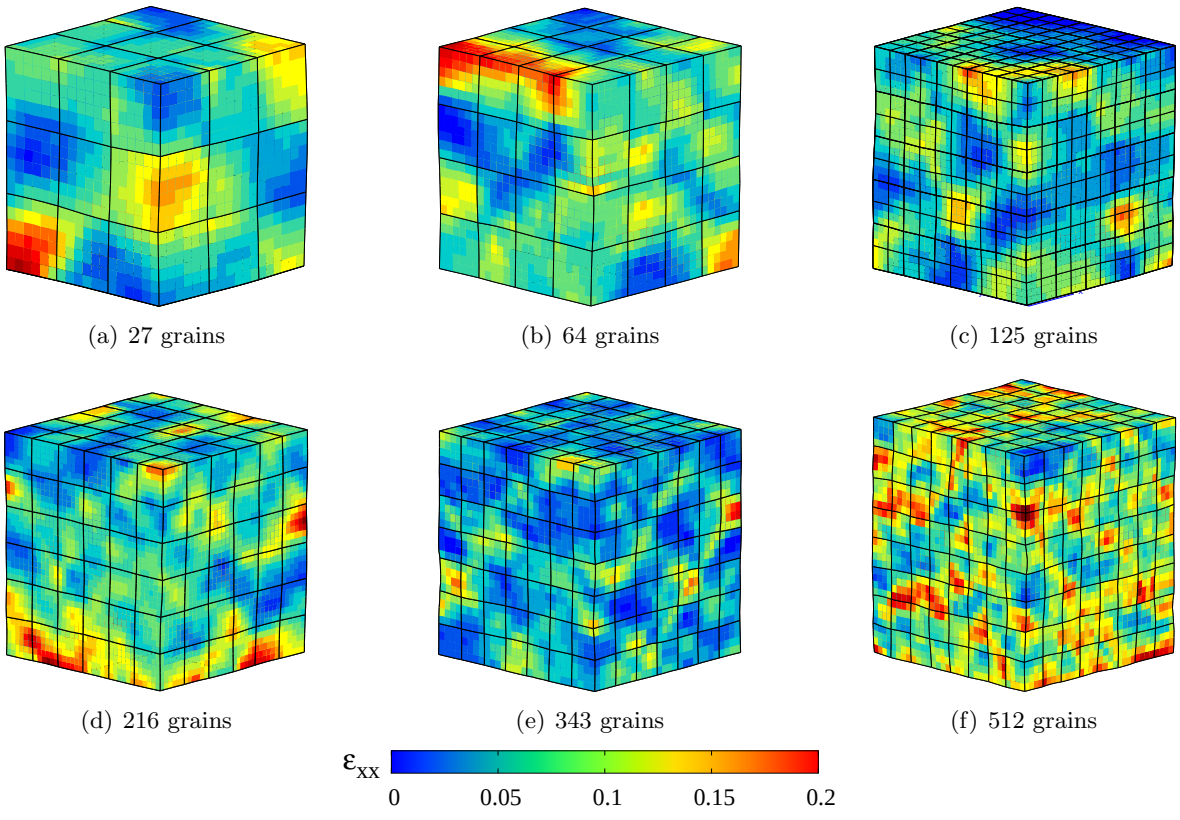

(a) 27 grains (b) 64 grains (c) 125 grains

(d) 216 grains (e) 343 grains (f) 512 grains

Figure 4.21: Accumulated plastic strain distribution after 10% applied strain

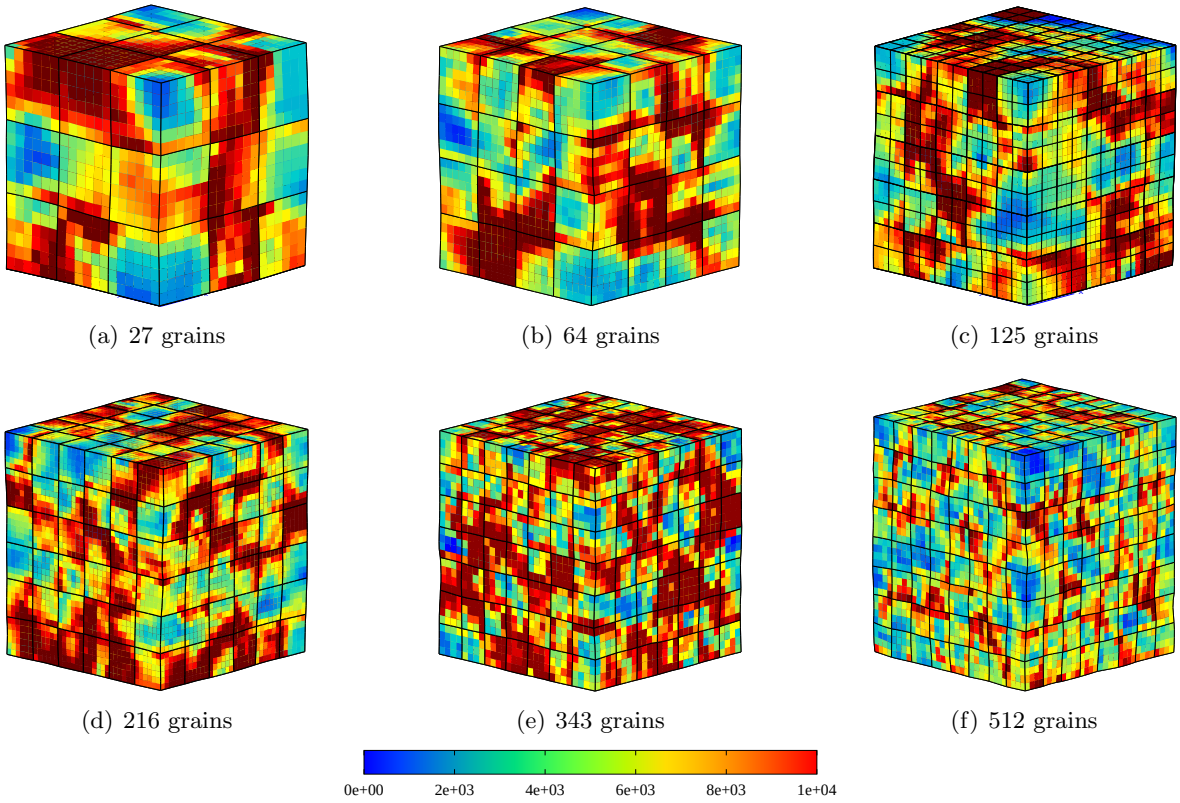

(a) 27 grains (b) 64 grains (c) 125 grains

(d) 216 grains (e) 343 grains (f) 512 grains

Figure 4.22: Dislocation density (in mm^{-2}) after 10% applied strain

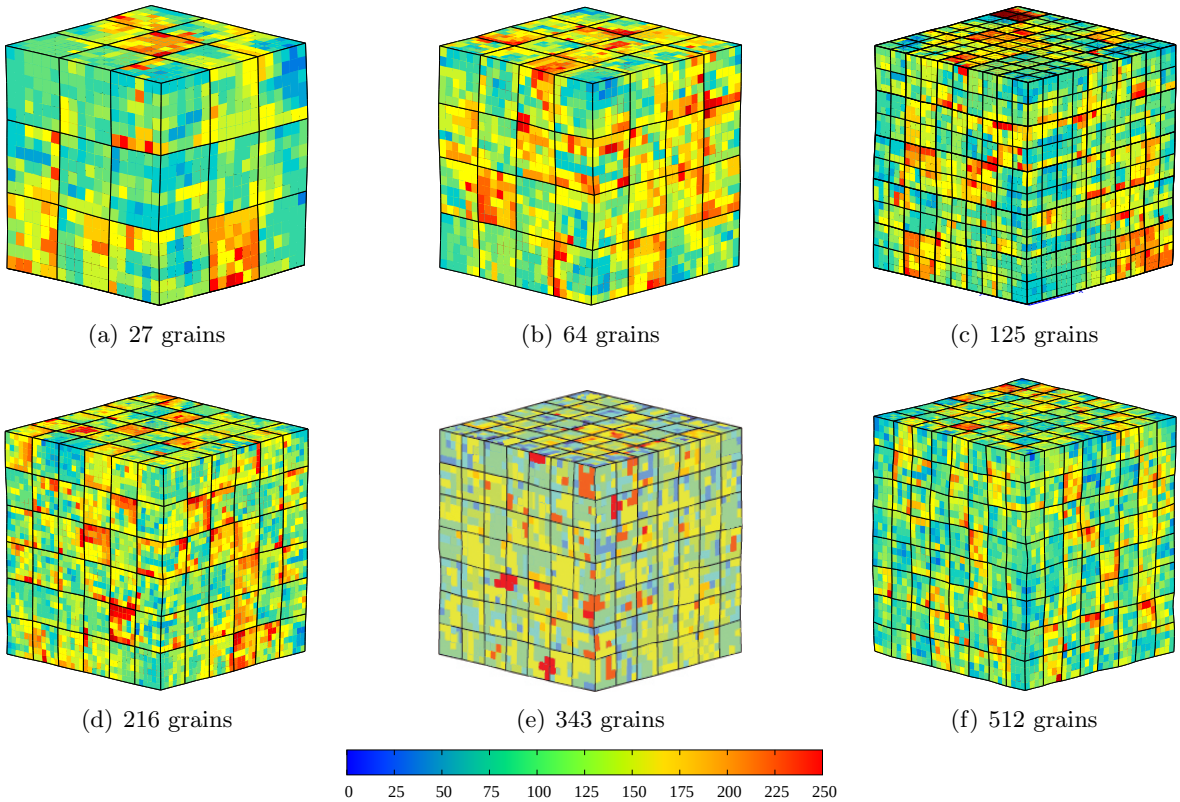

(a) 27 grains (b) 64 grains (c) 125 grains

(d) 216 grains (e) 343 grains (f) 512 grains

Figure 4.23: Von Mises stress distribution (in MPa) after 10% applied strain

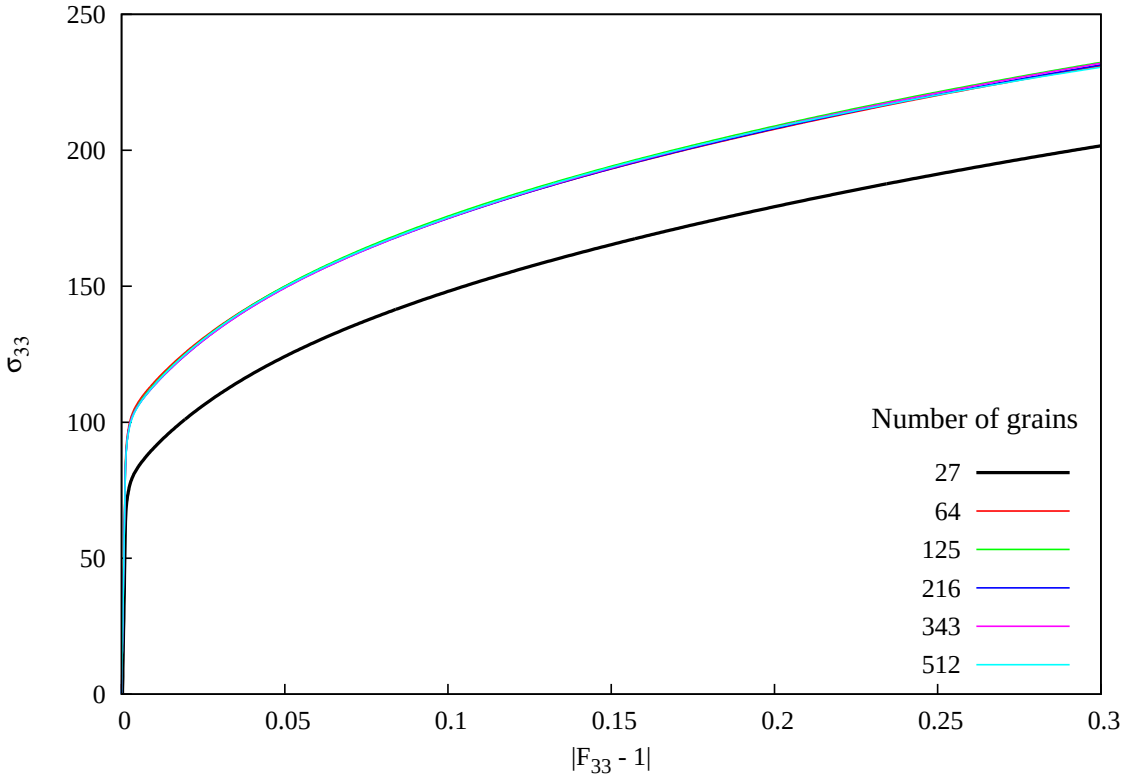

Figure 4.24: Effect of the number of considered grains on the overall tensile curve (σ_{33} in MPa).

First observations confirm deformed bands with a size close to those of the grains. These deformed bands are oriented at 45° from the axial tensile direction. Despite a similar distribution of angle rotations, strain field, dislocation density and von Mises stresses (see Figures 4.20, 4.21, 4.22 and 4.23), the stress–strain behaviour of the aggregate composed by 27 grains is softer than the other ones. It can be explained by a higher constrained grains in the core of larger aggregates that are less affected by free surface effects. From this study one can conclude that aggregates composed at least of 64 grains can be used to properly calibrate the crystal plasticity model parameters.

4.3.2.3 Effect of mesh refinement

In this section, the aggregates used to represent the alloy polycrystals consists of a polycrystal with 64 randomly oriented grains. The aggregate model has an initial cubic geometry and each grain has the same cuboidal morphology and size. The models are constructed using standard 20–node isoparametric 3D elements with reduced integration. The series of cubic meshes generated for the 64-grain polycrystal is shown in Figure 4.25. The coarsest mesh consisted of $4 \times 4 \times 4$ elements and subsequent mesh refinement was carried out in multiples of 8 with the finest mesh having $32 \times 32 \times 32$ elements. Note that all the meshes share identical assignments of the initial grain orientations and only differ in the number of elements used to discretise the grains. A constant value of crystal orientation was assumed inside each grain. Boundary conditions are described in Figure 4.13. A displacement leading to an average true strain rate of $10^{-4}s^{-1}$ was applied on the top surface. All simulations were carried out at a temperature of 298 K. In order to study locally the effect of mesh refinement, the grain rotation distribution (Figure 4.26), the accumulated plastic strain distribution (Figure 4.27), the dislocation density (Figure 4.28) and von Mises stress distribution (Figure 4.29) were plotted after 10% applied strain for the three polycrystals up to $16 \times 16 \times 16$ elements. The resulting average stress–strain response can be seen in Figure 4.30.

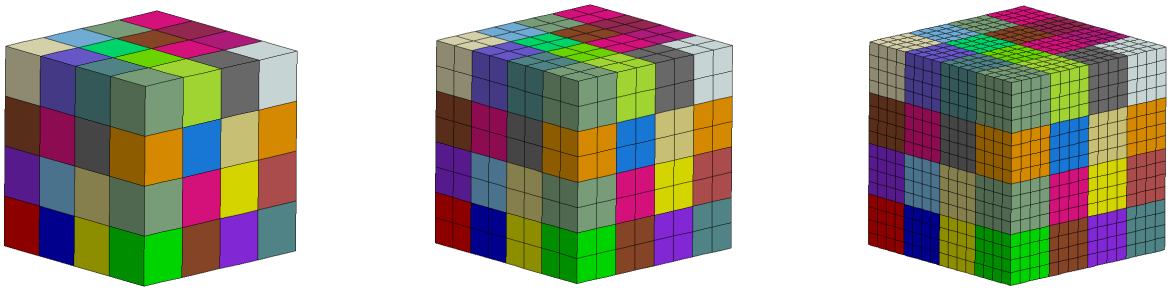

(a) $4 \times 4 \times 4$ (b) $8 \times 8 \times 8$ (c) $16 \times 16 \times 16$

Figure 4.25: Polycrystalline aggregates with a regular mesh of 64 grains with (a) 4x4x4, (b) 8x8x8 and (c) 16x16x16 elements used to evaluated mesh density on macroscopic behavior

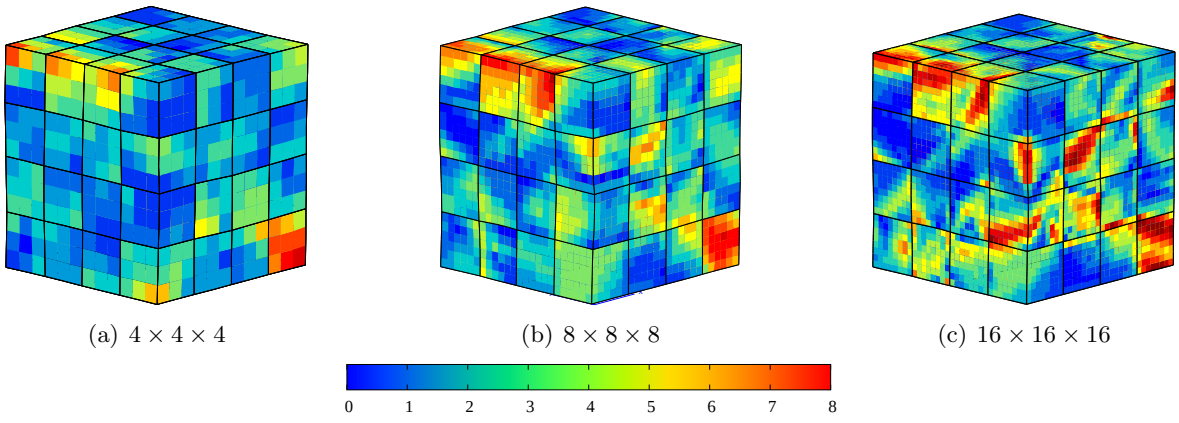

(a) $4 \times 4 \times 4$ (b) $8 \times 8 \times 8$ (c) $16 \times 16 \times 16$

Figure 4.26: Grain rotation distribution (in degrees) after 10% applied strain

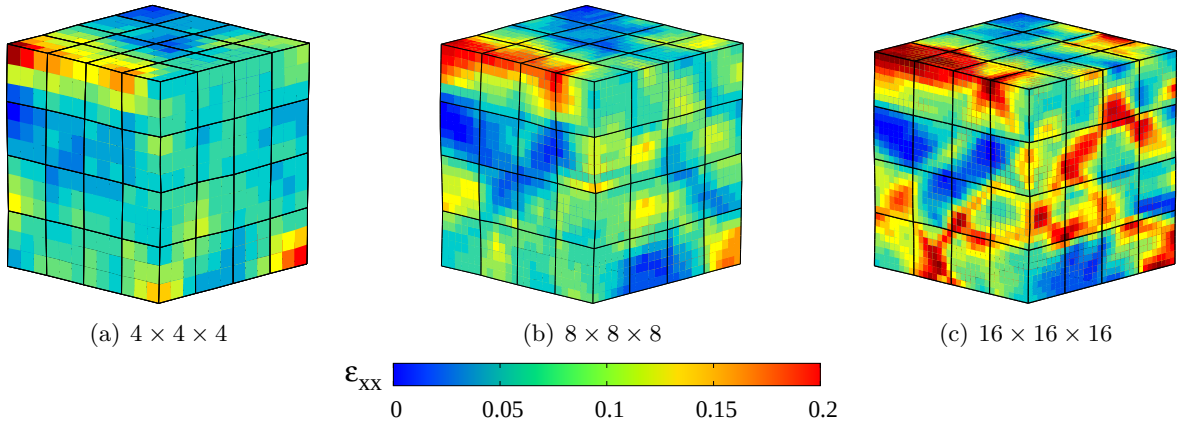

(a) $4 \times 4 \times 4$ (b) $8 \times 8 \times 8$ (c) $16 \times 16 \times 16$

Figure 4.27: Accumulated plastic strain distribution after 10% applied strain

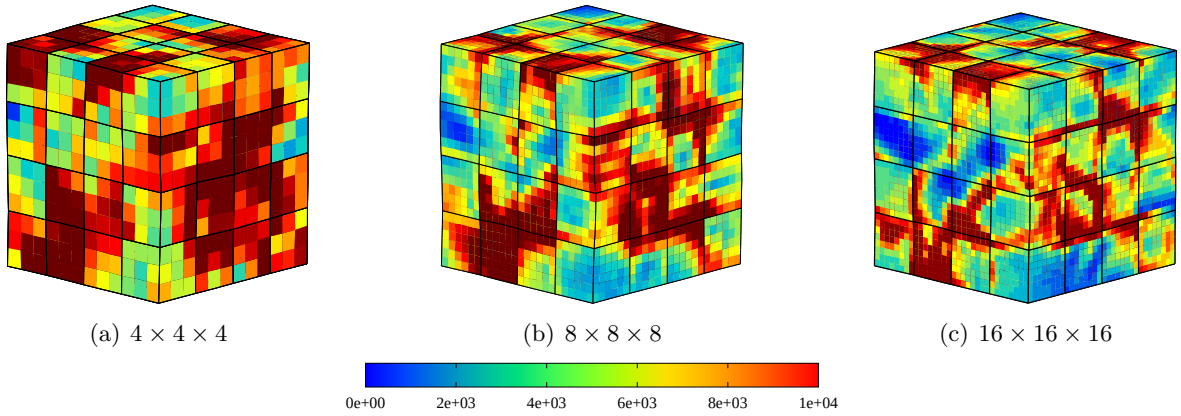

(a) $4 \times 4 \times 4$ (b) $8 \times 8 \times 8$ (c) $16 \times 16 \times 16$

Figure 4.28: Dislocation density (in mm^{-2}) after 10% applied strain

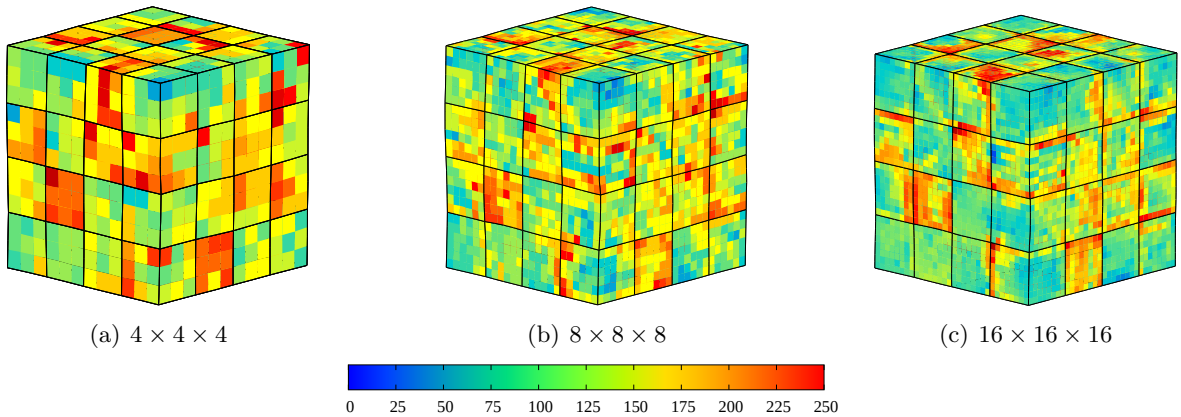

(a) $4 \times 4 \times 4$ (b) $8 \times 8 \times 8$ (c) $16 \times 16 \times 16$

Figure 4.29: Von Mises stress distribution (in MPa) after 10% applied strain

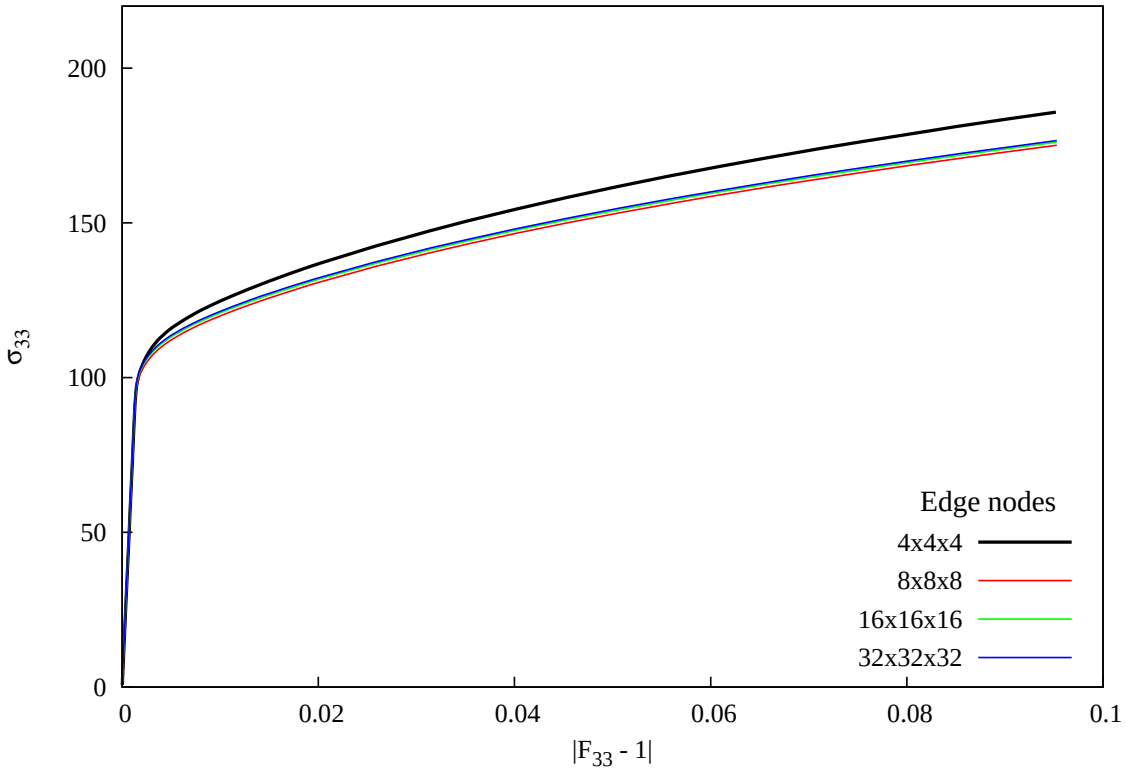

Figure 4.30: Effect of the number of elements per grain on the predicted average polycrystal response (σ_{33} in MPa).

For the two finest grains, namely $16 \times 16 \times 16$ and $32 \times 32 \times 32$ (see Figure 4.27), the predicted distribution of accumulated plastic strain is virtually mesh insensitive. However, it can be seen in Figure 4.26, that the angle rotation at the left top edge is less developed in the coarsest mesh than in the other ones. This is confirmed by the stress–strain response higher than for more finely meshed grains (see Figure 4.30). It should be noted that the harder predicted response of the 64-grains polycrystal with the coarsest mesh can be linked to the lack of integration points (e.g. volume representativity) needed to describe dislocation interactions in the model.

4.3.2.4 Effect of free surfaces

The effect of free surfaces was investigated using an embedded cell approach to evaluate the macroscopic and local behavior obtained with a aluminium polycrystalline aggregate. In this section, the aggregate used to represent the alloy polycrystal consists of a polycrystal with 512 randomly oriented grains. The models are constructed using standard 20–noded isoparametric 3D elements with reduced integration. The series of cubic meshes post generated from the same 512-grains polycrystal is shown in Figure 4.31. The aggregate is considered in post calculation for 37.5%, 50 %, 62.5 %, 75 %, 87.5 % and 100 % of the parent edge size. Boundary conditions are described in Figure 4.13. All simulations were carried out at a temperature of 298 K. In order to study localy the effect of mesh refinement at the local scale, the grain rotation distribution (Figure 4.32), the accumulated plastic strain distribution (Figure 4.33), the dislocation density (Figure 4.34) and von Mises stress distribution (Figure 4.35) were plotted after 5% applied strain for the three polycrystals. The resulting stress–strain response can be seen in Figure 4.30.

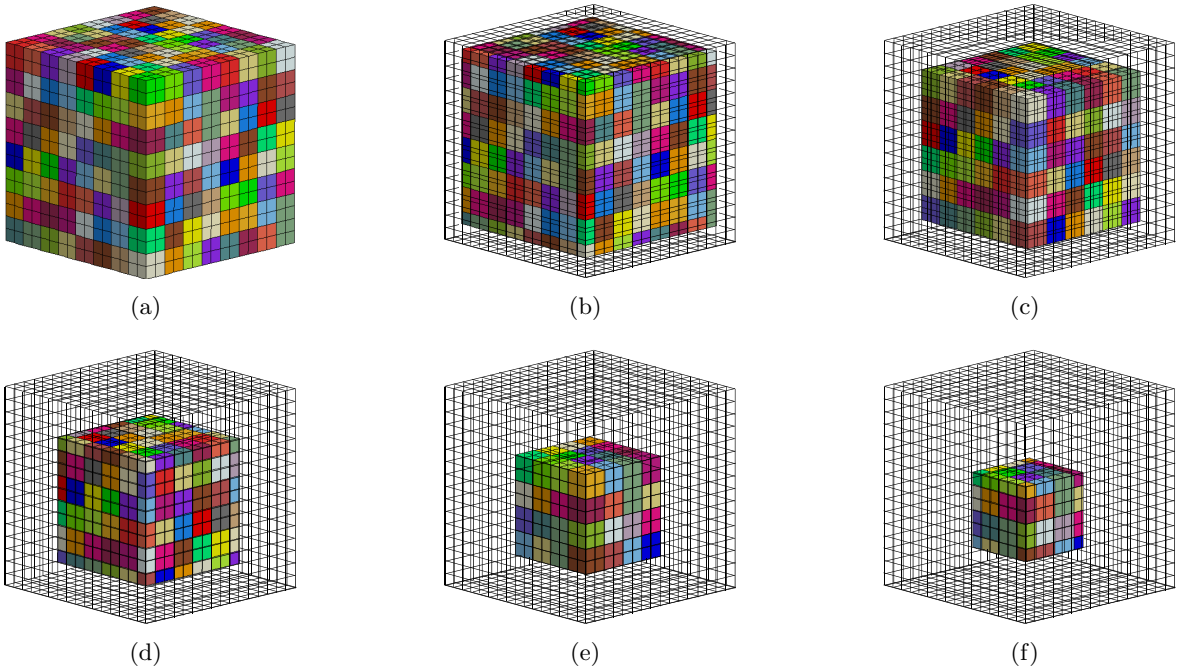

Figure 4.31: (a) 512 grains parent cubic aggregate and extracted volume of (b) 87.5 %, (c) 75 %, (d) 62.5 %, (e) 50 % and (f) 37.5% of the parent edge size

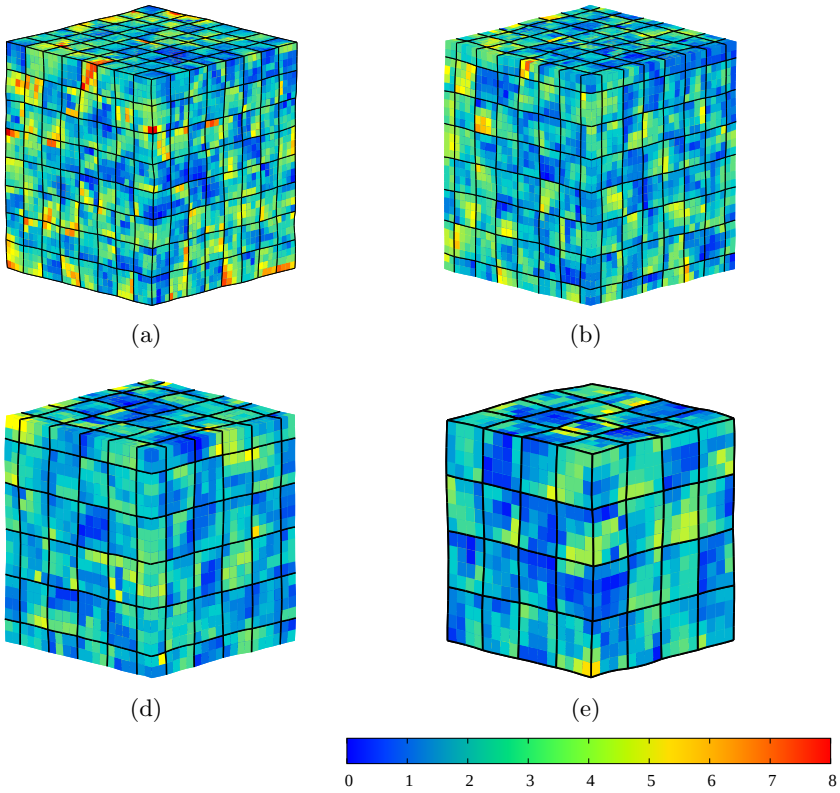

Figure 4.32: Grain rotation distribution (in degrees) after 10% tensile strain

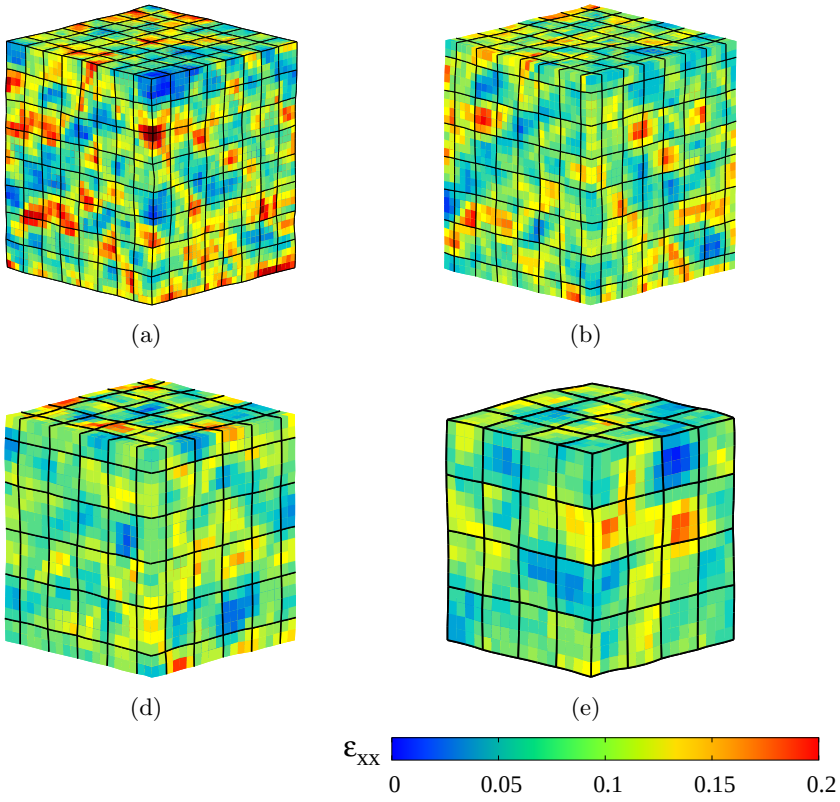

Figure 4.33: Accumulated plastic strain distribution after 10% tensile strain

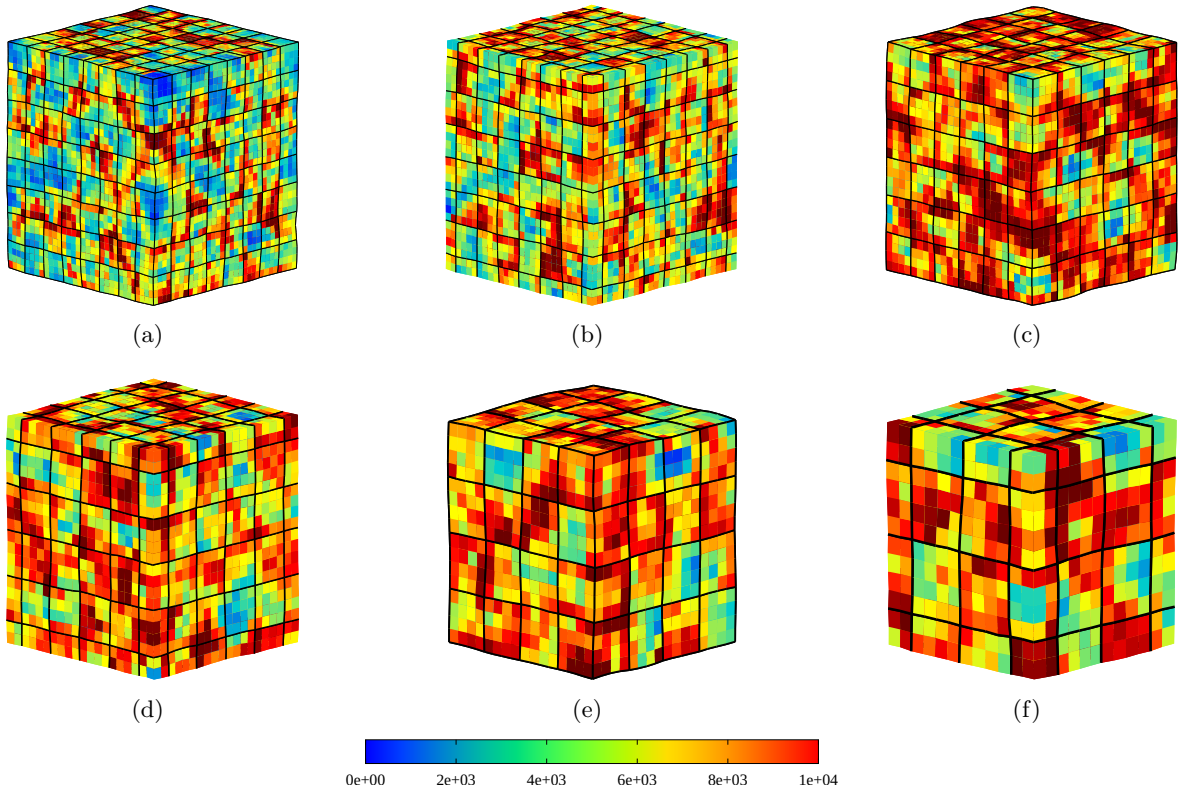

Figure 4.34: Distribution of all dislocation densities (in mm^{-2}) after 10% tensile strain

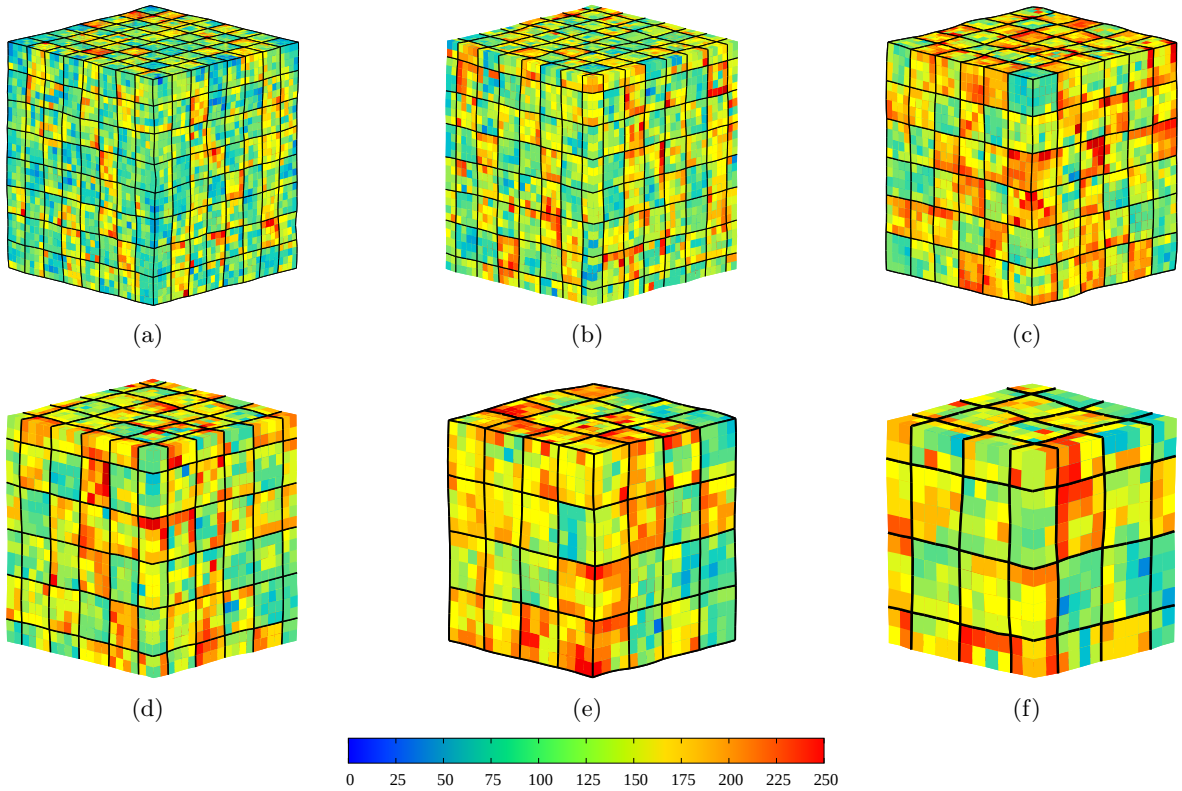

Figure 4.35: Von Mises stress distribution (in MPa) after 10% tensile strain

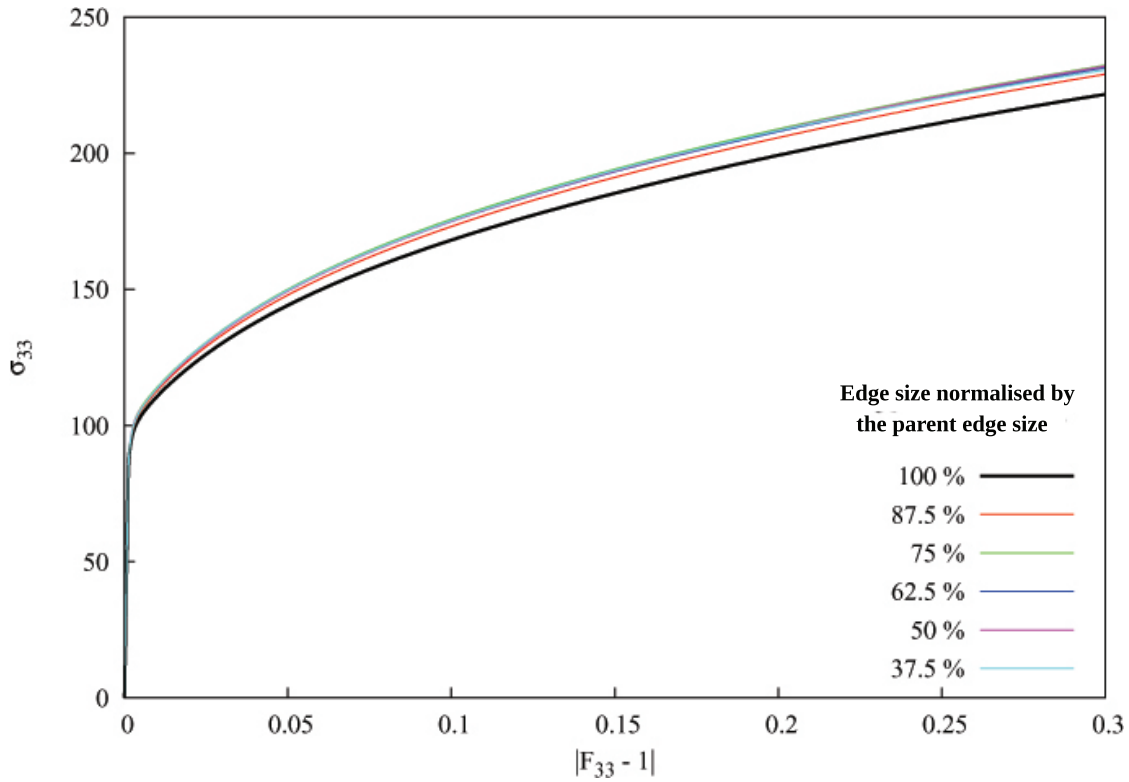

Figure 4.36: Effect of free surfaces on the macroscopic behaviour. (σ_{33} in MPa)

In Figure 4.36, only when the entire volume is considered the resulting stress-strain response is significantly different from the others. Plotted distributions of the grain rotation distribution (Figure 4.32), accumulated plastic strain distribution (Figure 4.33), dislocation density (Figure 4.34) and Von Mises stress distribution (Figure 4.35) show clearly that in the volume distributions are not affected by the absence of prescribed boundary conditions. Thus, in this work the parameter calibration will be done with an edge size of 87.5 % of the parent fraction to ensure accurancy of results.

As a summary, a parent aggregate of $8 \times 8 \times 8$ (512) grains with $2 \times 2 \times 2$ elements per grain was used and the average behaviour was calculated by removing the first layer of elements (i.e. with a cube of 87.5 % of the parent cube size).

4.3.3 Determination of model parameters

4.3.3.1 Effect of slip rate gradients with the non-local formulation

This section reports the differences in the deformed features predicted by the introduction of GNDs in the model. Then particular calculations were carried out with Voronoi aggregate in the order to investigate local responses. Two simulations were performed, one without the introduction of GNDs and the other one with GNDs. Figure 4.37 shows similar rotation distributions, the rotation heterogeneities are not stronger when GND hardening is accounted for. Moreover, distribution of total dislocation density (Figure 4.38) is similar and not affected by GNDs introduction. However the GNDs are expected to accommodate the lattice incompatibilities and therefore increase the aggregate strengthening.

It is known that for each grain size, the build up of strain gradients lead to the accumulation of GNDs during deformation affecting significantly the hardening behavior of polycrystalline aggregates. Nevertheless, a significative plastic deformation is needed in order to create strain gradient, which is not significative for low average amout of strain e.g. $\leq$5% (Abrivard 2009). Moreover, strain gradients are effective for grain sizes lower than 30 µm, these observations were deeply dicussed by Abrivard (2009).

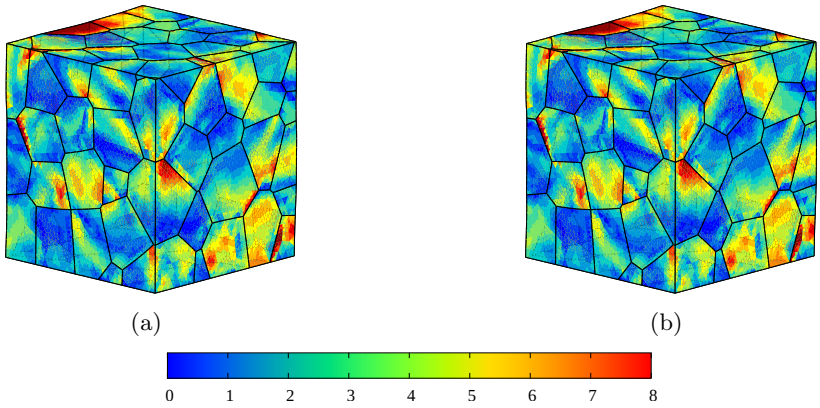

Figure 4.37: Accumulated grain rotation distributions (in degrees) after 5% tensile strain: (a) with and (b) without introduction of GNDs

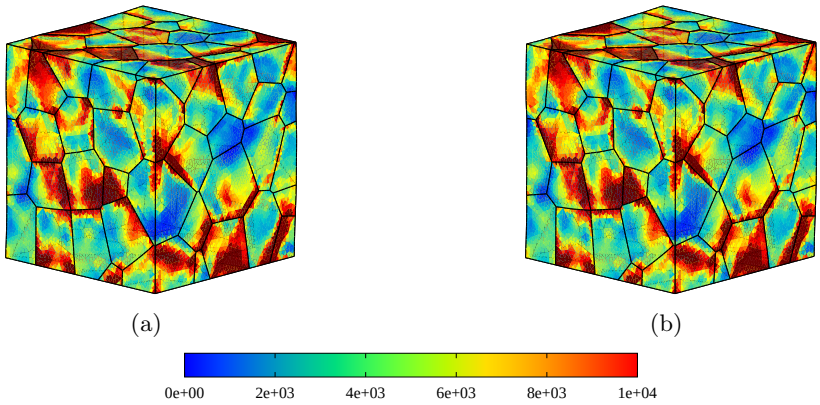

Figure 4.38: Distribution of all dislocation densities (in mm^{-2}) after 5% tensile strain: (a) with and (b) without introduction of GNDs

4.3.3.2 Solid solution effect of magnesium

The solid solution strengthening effect of magnesium atoms was investigated for magnesium concentrations ranging from 0.2 % to 5.0 % (see Table 4.4) and compared with experimental data. The Al-Mg polycrystalline aggregate identified in Section 4.4 was used. Boundary conditions remain the same and are described in Figure 4.13. In order to take into account the work hardening imparted by forming processes for alloys considered in Lyman (1972) the initial dislocation density is increased from 8000 mm^{-2} to 10^6 mm^{-2}. Note that this value of initial dislocation density is in good agreement with the literature for cold-worked aluminum alloys (Chastel 2010).

Numerical stress-strain curves for commercial aluminium-magnesium alloys of Lyman (1972) are plotted in Figure 4.39. Stress-strain curves from the model prediction highlight a linear increase in proof stress with increasing amout of magnesium. The comparison between model prediction and experimental data is shown in Figure 4.40. Despite a significative difference between experimental data and model prediction in the slope of the linear relation between wt% Mg and values of proof stress, proof stress values predicted by the model are close to experimental data in the range of 2 - 5 wt% Mg.

Table 4.4: Contribution of solid solution effects with S_{ss}^{α}

Al-Mg alloys designation	1200	5457	5050	5052	5154	5086	5083	5056
wt% Mg	0.2	1.0	1.5	2.5	3.5	4.0	4.5	5.0
S_{ss} (MPa)	1.51	7.55	11.33	18.88	26.43	30.2	33.98	37.76

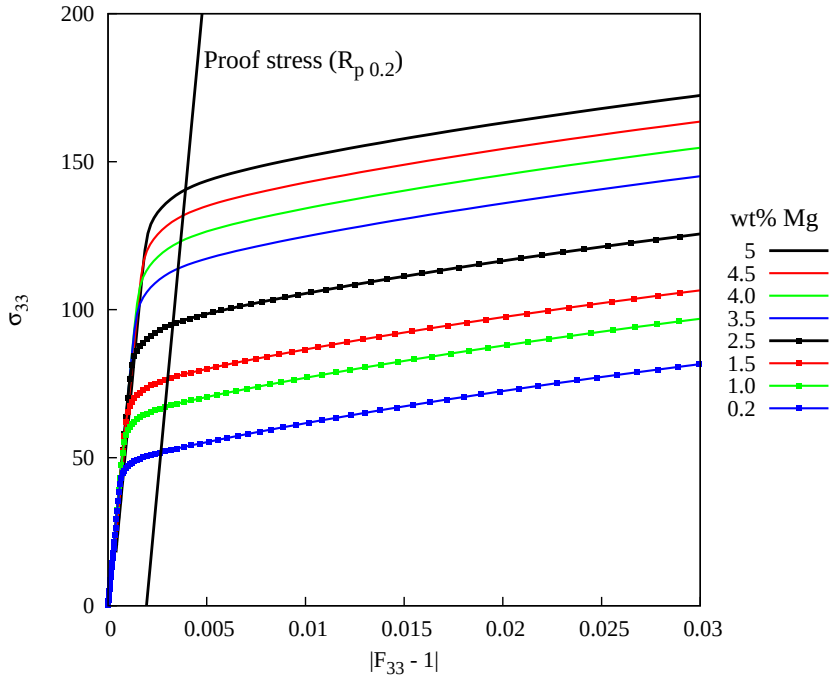

Figure 4.39: Predicted stress-strain curves for cold-worked aluminium-magnesium alloys (σ_{33} in MPa).

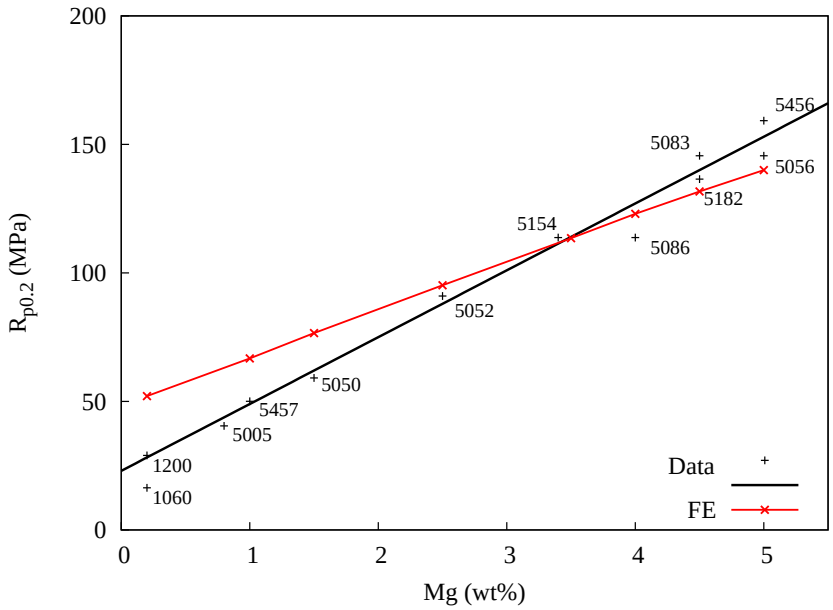

Figure 4.40: Comparison of experimental data from Lyman (1972) and Al-Mg aggregates behaviour: effect of the magnesium content on the 0.2% proof stress

4.3.3.3 Modelling of Al-Mg 5083 macroscopic behaviour

With the aid of the identified representative volume element of aggregates model parameters were modified in order to fit the experimental macroscopic behavior of the studied material. The value of 34 MPa calculated for a S_{ss} corresponding to 4.5 wt%Mg in solid solution over estimates the macroscopic strain-stress behavior of the studied material. However, only a correction of 1 MPa on S_{ss} allows for a good prediction macroscopic strain-stress behavior. This substitution of 1 MPa on S_{ss} is equivalent to a wt% Mg of 0.05 wt % that is attributable to the scatter in the solution heat treatement.

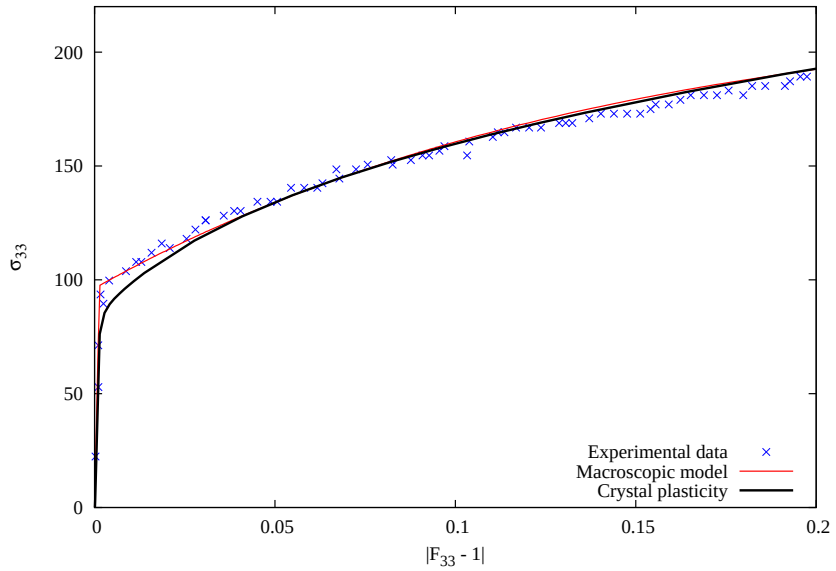

Figure 4.41: Comparison of Experimental Data and Al-Mg aggregates behaviour after heat treatment

Results depicted in Figure 4.41 are in good agreement with both the predicted by macroscopic model and experimental data. Thus, further simulations of local strain field should be close to those measured experimentally. Local strain does not exceed 5 % i.e. remains within the validated domain of the crystal plasticity model (Figure 4.41).

4.4 Modelling of the Actual Microstructure of the In-Situ Tensile Specimen

The aim of this section is to obtain in terms of local strain field accurate FE results validated with experimental strain field measurements. To reach this goal simulations of 2D microstructures were chosen to take as many experimental observations as possible into account. To do that, the microstructures are generated such that they respect the morphological and crystallographic textures obtained from an EBSD analysis. Boundary conditions for FE model were set from displacement measured by digital image correlation.

4.4.1 FE meshing from EBSD maps

The meshing of the aggregates obtained by experimental techniques implies some difficulties due to the non-convexity of the grains. EBSD analysis allows us to obtain the crystallographic (crystal orientations) and morphological (grain size, shape factors and orientations) distributions of the sample surface. Some Fe– and Mn–rich precipitates close to grain boundaries hindered grain boundary detection. Nevertheless the grain boundary description made of 10 equidistant distributed points was considered to be accurate enough to study local behaviour of grain boundaries.

To mesh automatically the region of interest, namely Region (b) in Figure 4.42(a) and (b), an arbitrary grain color map was first plotted. To this aim, grains were defined as sets of at least 10 pixels in size with a misorientation between neighbouring pixels of at most 5 degrees. From this map, triple junctions were first identified using an in-house developed image processing method. Then, grain boundaries were revealed using both triple junctions and colour gradient detection. The grain boundary discretisation was carried out by dividing them into small segments while taking their local curvatures into account (Figure 4.42). Finally, grains were meshed using 6-noded generalised plain strain triangular elements to allow for a proper geometric description of grain boundaries. Other approaches relying on square meshing based on EBSD scan step or on correlation microgrid were not deemed to be appropriate as regular meshing can result in an overestimation of the strains and stresses at grain boundaries (e.g. see (Barbe et al. 2001a)). Here, two meshes were shown, the larger one being composed of 22,590 elements (Figure 4.43(a)) and the smaller one of 15,230 elements (Figure 4.43(b)). This density of elements was chosen considering both the spatial resolution of the EBSD measurements, the description of grain boundary morphologies and the convergence of the computations.

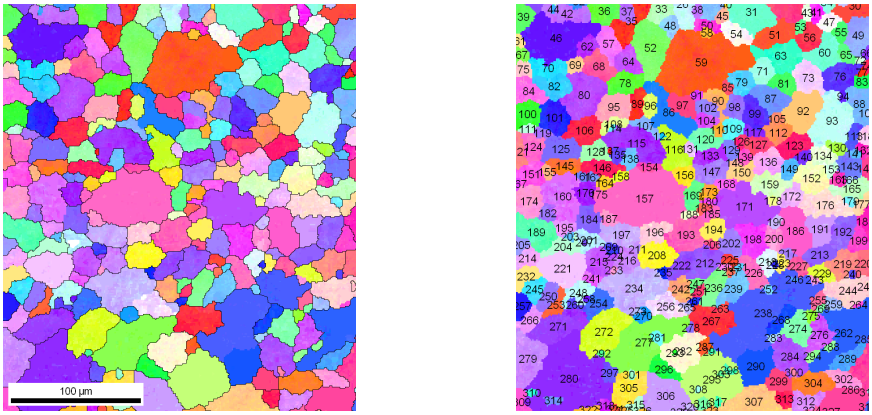

(a) (b)

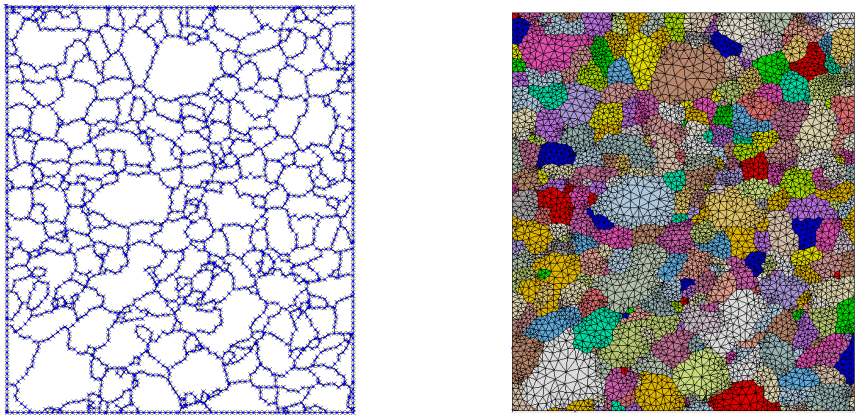

(c) (d)

Figure 4.42: For an aggregate of 400 grains (a) EBSD map, (b) colour map, (c) grain boundaries discretisation, (d) initial mesh

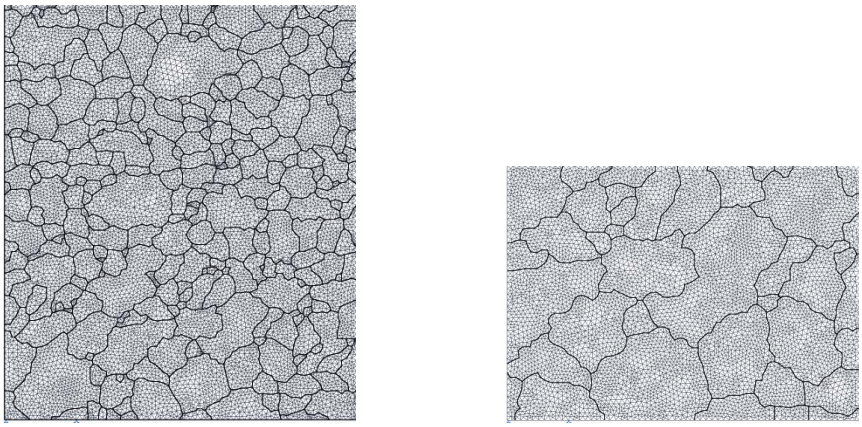

(a) (b)

Figure 4.43: Final mesh for FE model made of (a) 400 grains and 22,590 elements and (b) 40 grains with 15,210 elements

4.4.2 Boundary conditions

The microstructure below the surface can be accessed only by using a destructive method, such as successive polishing, or by X-ray synchrotron 3D analysis (DCT). These two techniques will be explained and used in Chapter 6. Nevertheless, here the objective is to take into account the influence of the subsurface grains, in terms of 2D FE mesh and boundary conditions to apply in the out-of-plane direction, in order to be the most representative of the material. To that propose two FE calculations have been performed. The first one for an aggregate of 40 grains and the second one for an aggregate of 400 grains.

Most of the time in the field of FE calculations in micromechanics boundary conditions are homogeneous or periodic (Barbe et al. 2001a;b). In order to compare numerical and experimental results, the influence of the neighbouring grains on the simulated microstructure has to be taken into account. Surronding grains can affect the mechanical behaviour, till 10 times the average grain size (Doumalin et al. 2003). This is the consequence of the length of the localisation strain bands, as mentioned in Chapter 3. In order to take this effet into account, the measured displacements of each node of the mesh edges, obtained by image correlation, were corrected from rigid body motion and then applied as boundary conditions (referred to later as experimental BC) see Figure 4.44.

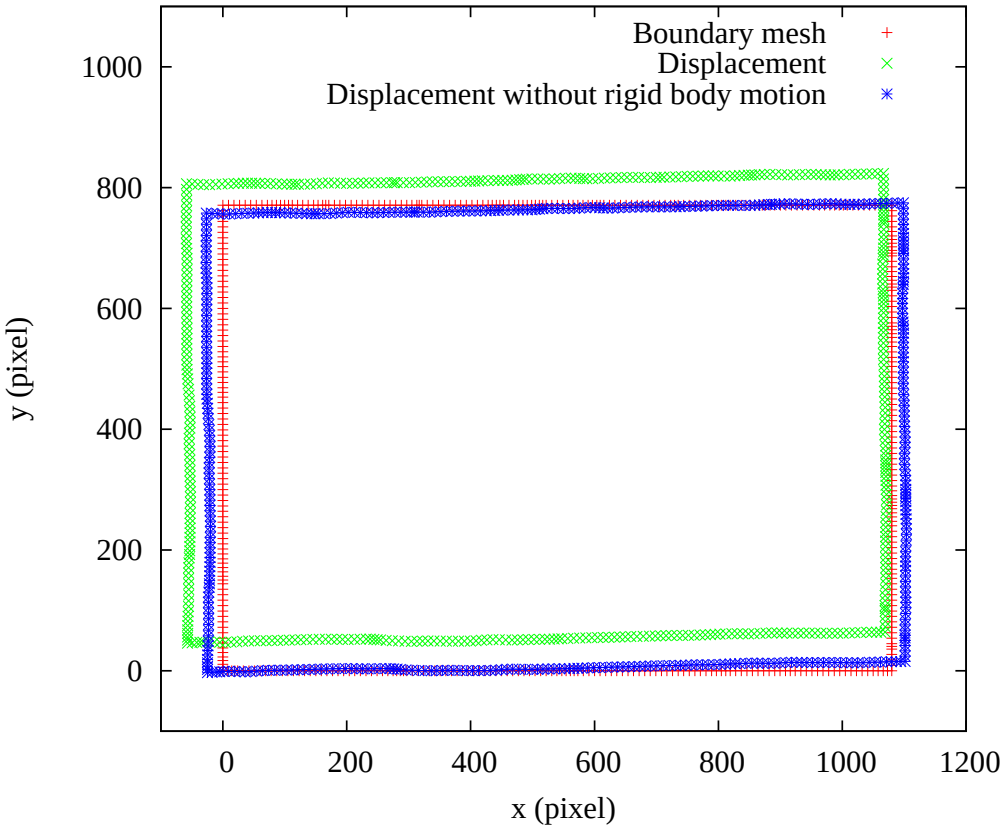

Figure 4.44: Applied boundary conditions from experimental measurements.

4.4.3 Numerical predictions of local stress and strain fields

Figures 4.45(a) and (b) and 4.46(a) and (b) show experimental and predicted strain fields for Specimen (I), after 0.45% applied macroscopic strain. Even through, strain bands appear in both strain fields, high level of strain are not localised in the same grains. Thus, the smaller model Figure 4.46(b) was used to predict the correct strain field inside grains.

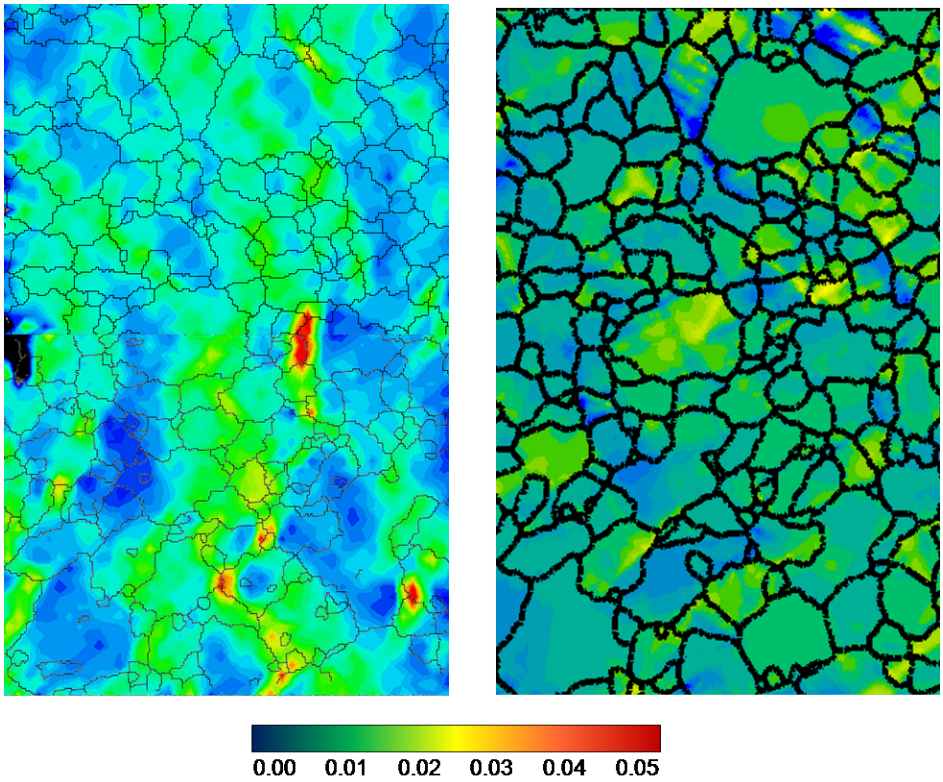

Figure 4.45: (a) Measured and (b) predicted axial strain fields after an average tensile strain of 0.0045 . The load is applied along the x axis.

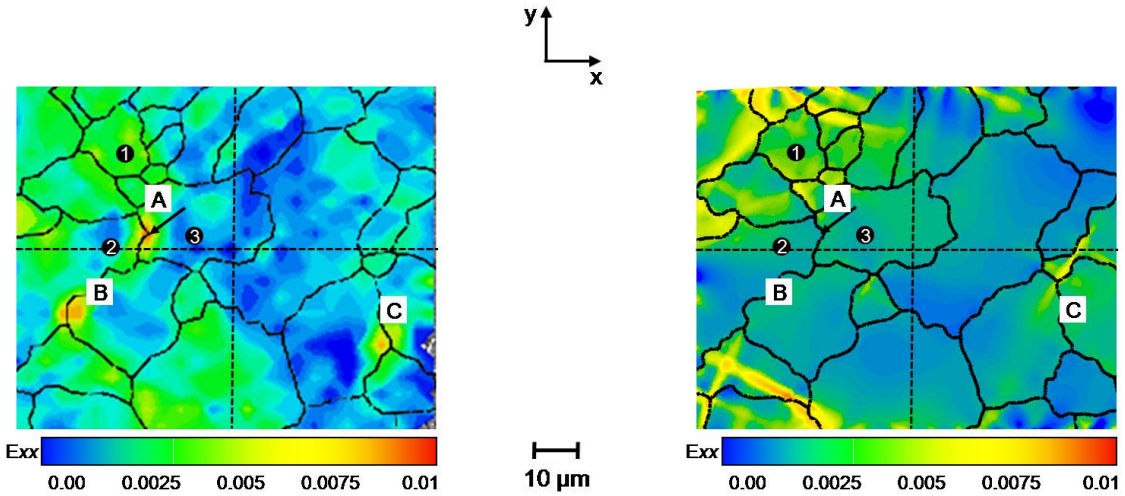

(a) (b)

Figure 4.46: (a) Measured and (b) predicted axial strain fields after an average tensile strain of 0.0045. The load is applied along the x axis.

In regions A, B and C of Figure 4.46 the high axial elongation is due to initiation of cracks, which was only detectable by digital image correlation. The spatial resolution of the scanning electron microscopy image was not high enough for the crack to be observed for an average axial strain less than 0.1%.

Figure 4.47 shows both predicted and measured axial strain profiles along the two dotted lines Figure 4.46 (a) and (b). Along the vertical line model predictions are in satisfactory agreement with measurements. Along the horizontal line, for d higher than 60 μm the model overestimated the local axial strain. The model predicts very low Exx over 4 μm close to the crack, but still higher than experimental measurements, which can be due to a stress redistribution after crack opening. The very high value of Exx measured at the crack at 18 μm is attributed to crack opening (and not to localised strain) as discussed before. For $d = 0$ (both lines) and $d = 60$ μm (vertical line) the experimental measurements was prescribed as boundary condition in the model, model predictions and experimental measurement coincide, along the horizontal line at $d = 68\,\mu$m model predictions and experimental measurements do not coincide because the size of the region studied by digital image correlation is smaller than the region studied by the model, so that boundary conditions are prescribed farther in the model.

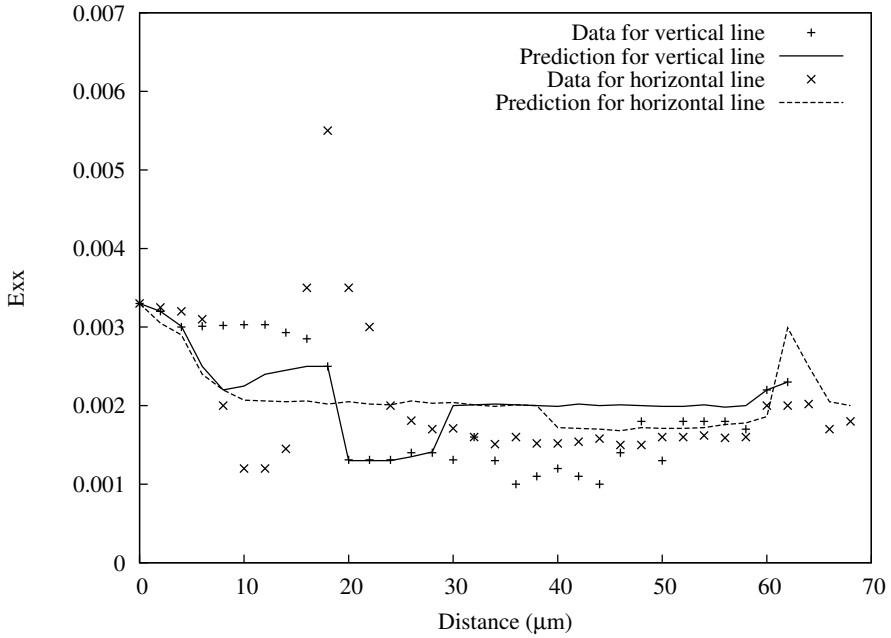

Figure 4.47: Comparison between measured and predicted axial strain profiles along dashed lines of Figure 4.46 after 0.0045 applied macroscopic strain.

From the above results one can conclude that the axial strain field is well predicted by the model, at least close to the boundary which is the first to fail. Consequently, the model was then used to estimate stress fields just before crack initiation in order to derive a criterion for crack initiation and propagation.

4.5 Conclusions

It was found in this chapter that aggregates composed of at least 64 cubic grains of 8×8×8 elements each, with a random texture can be used to properly calibrate the behaviour of considered aluminium-magnesium alloy. Moreover, it was found that the solid solution strengthening effect due to magnesium can be rather accurately predicted through an additional function expressed in terms of the magnesium concentration in the rate-dependent flow stress at the level of each individual slip system in the single crystal model. On the other hand, introduction of strain rate gradient in the model does not impact local fields (e.g. accumulated plastic strain, total dislocation density) due to the low level of plastic strain and rather coarse grain size that are considered in this work.

Finally, the accuracy of model prediction decrease when the number of grains increases. Even though the model only accounted for the deformation in the centre gauge section of the tensile specimen, it was able to accurately predict the overall macroscopic stress–strain response of the specimen. At the local level and for small aggregates (e.g. $\approx$ 40 grains), the prediction of the accumulated plastic axial strain distribution was in agreement with experimental trend. Based on these results, the model was considered as a valuable tool to estimate the stress field next to grain boundaries in order to derive a grain boundary cracking criterion.

Résumé

Ce chapitre a été dédié à la description et à la mise en œuvre du modèle de plasticité cristalline. Il a été montré qu'un agrégat constitué d'au moins 64 grains cubiques composés chacun de 128 éléments quadratiques est suffisant pour représenter la réponse macroscopique moyenne du modèle et ainsi calibrer les paramètres du modèle de plasticité cristalline par rapport aux prédictions du modèle macroscopique mis en place dans le chapitre 2.

Fondé sur des paramètres identifiés dans le cas d'un alliage d'aluminium à 0.045% de magnésium, le modèle de plasticité cristalline existant pour l'aluminium pur a été enrichi afin de prendre en compte, pour chaque système de glissement, l'effet de solution solide (force de friction) en fonction de la concentration en magnésium. D'autre part, il a été montré que l'introduction de gradient du second ordre n'influence pas l'intensité des champs mécaniques locaux. Cela s'explique par le fait que notre étude se cantonne à de faible niveaux de déformation totale (<5%) et pour une taille de grains de l'ordre de 30 µm, peu sensible aux effets de gradients.

Il a également été montré dans ce chapitre, à l'aide de simulations 2D avec des conditions de type déformations planes généralisées que plus le nombre de grains modélisé était important plus l'écart entre les champs de déformations numérique et expérimentaux diminue. Une bonne correspondance a été obtenue entre les champs de déformation numérique et expérimentaux pour un agrégat 2D de 40 grains. Grâce à ces résultats il a été possible d'établir la valeur de la contrainte normale critique ("traction" au joint de grains) du critère de rupture. Cette valeur sera exploitée dans le chapitre suivant pour modéliser l'ouverture de fissure.

Chapter 5

Intergranular Crack Initiation and Propagation

Contents

5.1 Introduction

It was shown in the experimental part of this work that grain boundary cracking occurs on boundaries oriented normally to the applied tensile stress when the average local strain is as low as 0.45 %. In addition, failed grain boundaries were found to be between grains that undergo very limited plastic deformation despite being embedded in large deformation bands. From these results, a failure criterion for intergranular cracking was proposed by considering that the grains at either side of the failed grain boundary develop high normal tractions. Thus, it is assumed here that crack initiation is controlled by a critical normal grain boundary traction.

The main objectives of this chapter are to predict the critical normal grain boundary traction and then use this value in an appropriate model formulation in order to simulate the mechanism of hydrogen induced enbrittlement in an aluminium alloy.

Two methods will be used to determine the critical normal grain boundary traction, namely one based on an analytical Eshelby-type approach and the other on a finite element model of the polycrystal using plasticity concepts. Appropriate numerical methods to simulate hydrogen induced enbrittlement mechanism will be first reviewed. In agreement with both experimental results obtain in Chapter 3 and results obtained elsewhere (El-Houdaigui et al. 2011) at a finer scale, reasons for the selection of a cohesive zone modelling approach will be presented. The chosen cohesive model will be calibrated with the critical normal grain boundary tractions obtained from the simulation of the actual polycrystalline microstructure of in-situ tensile specimens.

Finally, a numerical study of intergranular crack initiation is carried out by introducing cohesive zone elements in the actual microstructure of the in-situ tensile specimen. The predictions are then compared to local experimental observations and measurements presented in Chapter 3. The adopted approach will be also tested with Voronoi type meshes in order to simulate intergranular crack propagation in a large representative volume element.

5.2 Identification of the Intergranular Fracture Criterion

5.2.1 Simplified traction based grain boundary failure criterion

A first approximation to the normal tractions needed to fracture a given grain boundary, σ_d, is obtained by solving an Eshelby problem consisting of a "hard" spherical elastic inclusion embedded in an "softer" infinite elasto-viscoplastic matrix (as illustrated in Figure 5.1(b)). It will be assumed that the grain boundary belongs to two "hard" grains that behave elastically, very much as the grain boundary in Figure 5.1(b) elastic inclusion. Under this assumption, it can be shown that the solution to this problem yields uniform stresses within the inclusion, and that the maximum principal stress is given by (Beremin 1981),

$$\sigma_{xx} = \Sigma_{xx} + k(\Sigma_{eq} - \sigma_y) \tag{5.1}$$

where Σ_{xx} is the average axial stress in the polycrystal at the moment the first grain boundary fails. This value can be approximated from the stress-strain curves shown in Figure 5.2, Point A, which yields Σ_{xx}= 120 MPa. Also, σ_y is the material yield stress (= 85 MPa), and Σ_{eq} the average von Mises stress in the inclusion. From the FE calculations, the average von Mises stress in Grains B and C (see Figure 5.3) was found to be Σ_{eq} = 140 MPa at point A of Figure 5.2. Figure 5.4 shows the von Mises stress distribution at point A of Figure 5.2. Finally, the parameter k in Equation (5.1) is a function of the inclusion shape, equal to 1 for the spherical particle assumed here (Pineau and François 2001). With these values, Equation (5.1) yields σ_{xx} = 175 MPa. This value will henceforth be used as the critical grain boundary traction, σ_d, required to fracture a grain boundary.

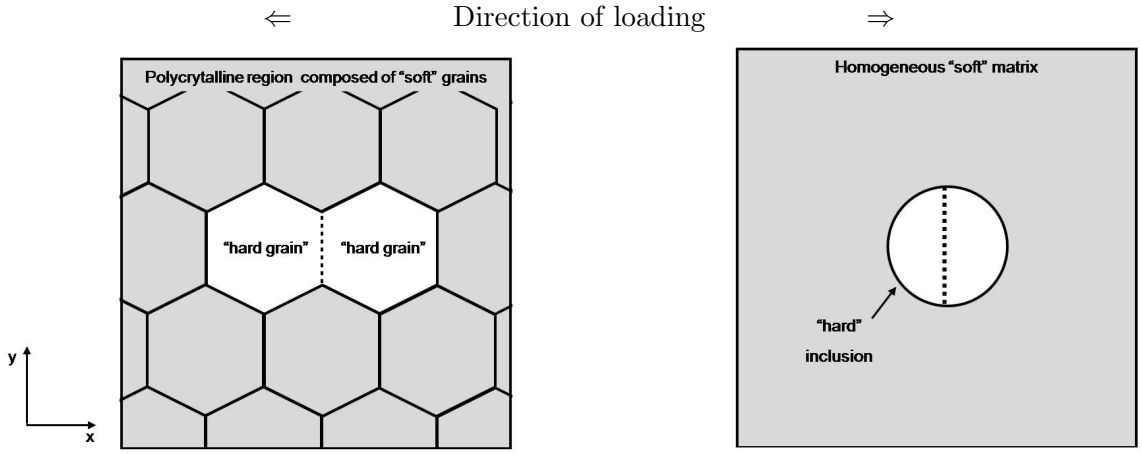

(a) (b)

Figure 5.1: Schematics of the typical grain configuration observed around a cracked grain boundary (indicated by the dashed line): (a) polycrystalline region and (b) idealised configuration to be used in the simplified model. The dashed line delimits the boundary that is assumed to fail.

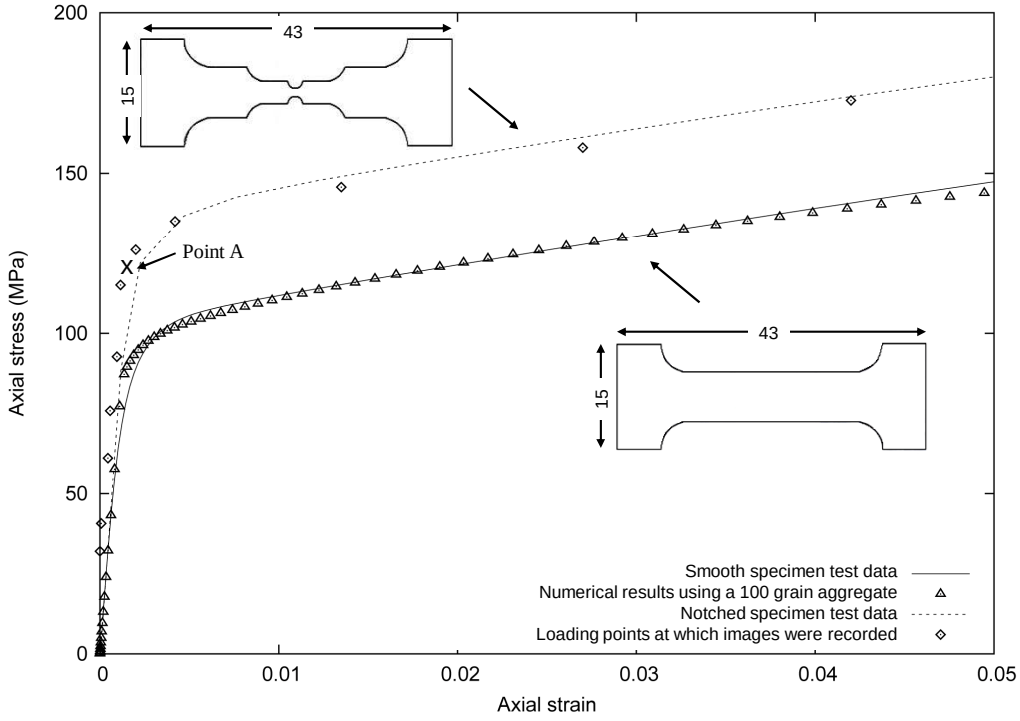

Figure 5.2: Measured and predicted tensile stress-strain curves and specimen geometries (dimensions in mm).

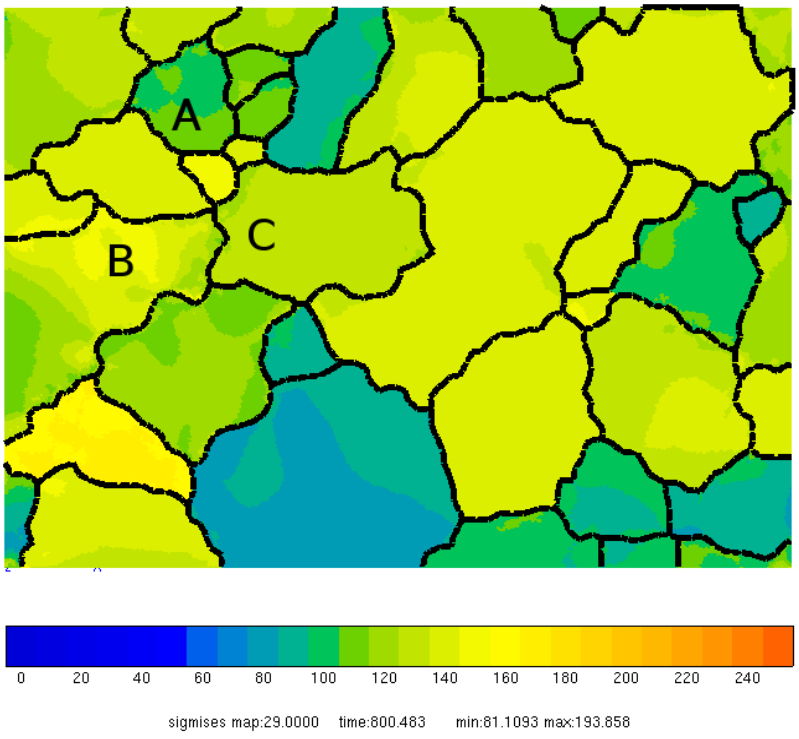

Figure 5.3: Von Mises stress distribution after 0.45% applied stress corresponding to point A in Figure 5.1

5.2.2 Critical grain boundary tractions predicted by full FE analyses of the 2D crystal aggregate

The predictions obtained from the previous section were validated against local normal tractions obtained from the numerical simulations of the crystal aggregate. Here, the normal grain boundary tractions were determined by rotating the local stress tensor along a direction normal to the grain boundary.

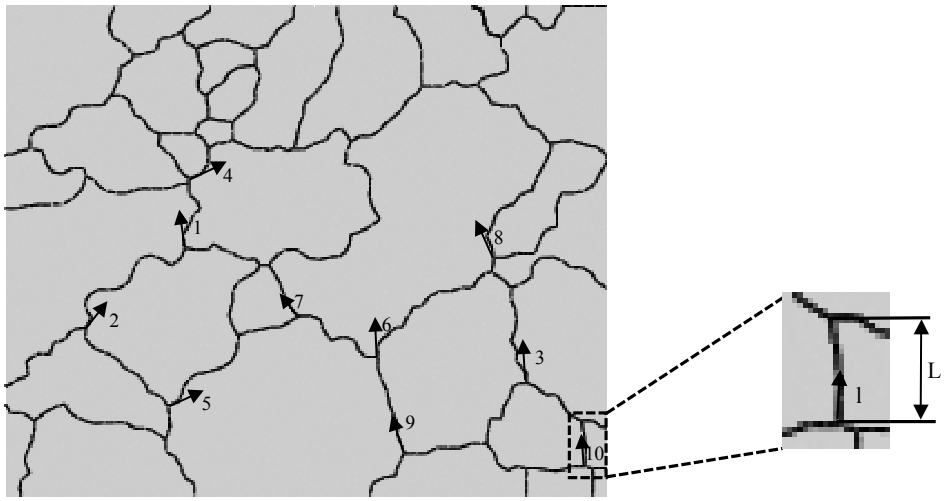

(a)

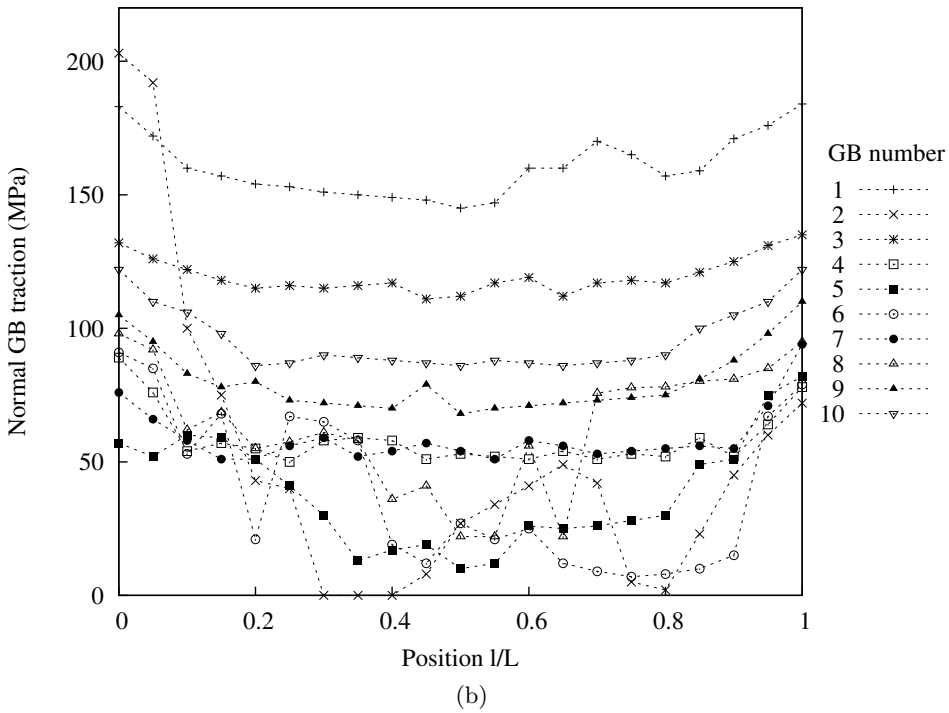

(b)

Figure 5.4: (a) Identification of the grain boundaries analysed, with the arrows indicating the triple junctions or origin of the grain boundary coordinate l used in (b), which shows the computed normal grain boundary tractions along the grain boundaries labelled to 1 to 10 in (a). Grain boundaries 1, 2 and 3 are the only ones found to have cracked when the test was stopped at 0.45% applied macroscopic strain

The predicted normal tractions along some of the most highly stressed grain boundaries within the region studied by DIC, labelled to 1 to 10 in Figure 5.4(a), are shown in Figure 5.4(b). Here, the tractions are expressed in terms of the distance along the boundary of interest from a triple point, l, normalised by the overall grain boundaries length, L. It can be seen that the normal grain boundary tractions tend to be higher in the vicinity of triple junctions, as also reported elsewhere (Masayuki et al. 2007),due to the complex deformation constraints imposed by the surrounding material on the triple junctions.

It worth noting from Figures. 5.4(a) and (b) that, out of the 10 grain boundary regions along which their normal tractions were calculated, only those numbered 1 to 3 failed during this particular test. It should also be recalled that these three failed grain boundaries were already identified in Chapter 3 in Figure 3.22(a). The predicted tractions shown in Figure 5.4(b) reveal that, at the onset of cracking, the tractions in Grain Boundaries 1 to 3 vary between an upper bound of 205 MPa to a lower bound of 135 MPa. The critical tractions in these grain boundaries can then be written in terms of their mean value as 170±35 MPa. This numerical prediction is close to the one obtained analytically in the previous section using a simplified model based on an extension of Eshelby's theory, namely 175 MPa. This good correlation is encouraging as far as the suitability of the configuration considered in Figure 5.1 to describe intergranular crack initiation due to hydrogen embrittlement is concerned.

5.3 Intergranular Crack Propagation Approaches

Over the last decades, several numerical methods have been developed to predict intergranular fracture mechanisms in brittle and quasi-brittle materials. In order to overcome difficulties in describing the evolution of microcrack patterns in brittle solids, continuum damage mechanics has been used to model the failure processes of brittle materials. Continuum damage mechanics, regarded as a continuous description of the internal strengh degradation, was first introduced by Kachanov (1958) and enriched later by Lemaitre (1985) and Chaboche (1988a;b) amongst others. The effect of damage on the deformation processes is taken into account through a damage variable which is introduced into the constitutive equations at the local damaged region. Other authors have proposed the asymptotic method called eXtended Finite Element Method (XFEM) (Belytschko and Black 1999, Moës et al. 1999). This method is based on an enrichement of the standard FE approximations with the introduction of known information about discontinuities in the shape functions, such as the strain and displacement discontinuities seen across crack surfaces. Therefore, in XFEM based approaches, cracks can propagate through elements. A different technique to simulate crack initiation and crack growth is based on so–called cohesive laws. Cohesive models originate from the concept of a cohesive zone, which was first introduced by Dugdale (1960) and Barenblatt (1962). The implementation of cohesive zones into numerical analyses takes the form of cohesive elements, which explicitly simulate the crack process zone.

5.3.1 Continuum damage mechanics models

Appropriate continuum damage mechanics models can be used to describe microstructural failure mechanisms. Instead of reproducing the fine details of micro-cracking patterns, continuum damage mechanics attempts to formulate a theory that will reflect the influence of defects in an approximate manner. In the framework of continuum thermodynamics Lemaitre (1996) and Besson et al. (2001) introduced the Helmholtz free energy as a state potential (Ψ). With this formulation, a coupling between the elastic behaviour, damage and hardening can be established. Besson et al. (2001) introduce the damage variable D in the hardenning Ψ_p. Three cases were distingished. One without coupling between damage and hardening, an other based on the Cordebois Sidoroff theory with the intoduction of a specific term for damages and a third case with an explicit introduction of D in the hardenning term Ψ_p.

This type of approachs was used by Diard et al. (2002) for intergranular damage, but without hardenning coupling:

$$\Psi = \Psi_e(\varepsilon^{\mathbf{e}}, D) \tag{5.2}$$

Introducing only one scalar variable, D, representing damage, the classical approach (Lemaitre 1985; 1996) proposes a modification of the elasticity related part of the free energy, so that:

$$\rho\psi_e = \frac{1}{2}(1-D)(\varepsilon^{\mathbf{e}} - \mathbf{k}\Delta T) : \mathcal{C} : (\varepsilon^{\mathbf{e}} - \mathbf{k}\Delta T) \tag{5.3}$$

where $\mathcal{C}$ is the fourth-order anisotropic elasticity tensor $\mathcal{C}$ and $\mathbf{k}$ is the tensor of thermal dilatation. The variable Y is energetically conjugated with D and obtained by taking the opposite of the partial derivative of $\rho\psi_e$ with respect to D:

$$Y = -\rho \frac{\partial \Psi_e}{\partial D} \tag{5.4}$$

Due to the specific role of normal and shear stresses in D (σ_n and σ_t respectively), (Diard et al. 2002) introduced an equivalent stress for damage as a quadratic form of σ_n and σ_t:

$$\sigma_d = \frac{\sqrt{\langle \sigma_n^2 \rangle + \beta \sigma_t^2}}{1+\beta} \tag{5.5}$$

where the parameter β is used to control the effect of shear stress on damage. For a zero value of β, damage will be driven by the normal stress only.

In the described model, inelastic flow can start without any damage. Opening and shear are not coupled as long as no damage exists. With this damage model, positive normal stresses or shear stresses can develop damage, and have an influence on the sliding and opening rate. However, some authors consider the grain boundary as a distinct material with a given thickness, which is a purely numerical and empirical parameter at the continuum level (e.g Diard et al. (2002)).

The grain boundary was considered by *two layers*, one in each grain. Figure 5.5 illustrates the important difference originating from this concept. Each grain has now its core and grain boundary region. This idea can be found in Evers et al. (2002) (see Figure 5.5). Here, the concept is used for a polycrystal model. Introducing the concept explicitly into the finite element model incorporating real-shaped grains boundaries elements.

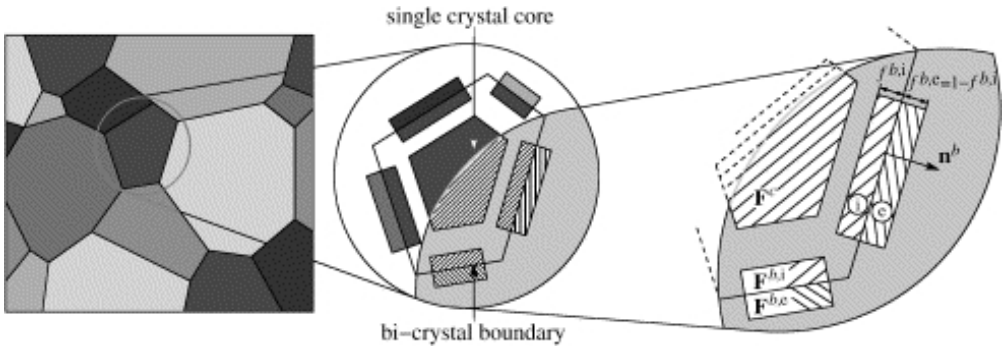

Figure 5.5: From a polycrystal assembly, each crystal is decomposed into constituent parts, representing its core and its boundaries (Evers et al. 2002).

Continuum damage concepts based on a theory of Kachanov (1958) and Lemaitre (1985) (see also work on intergranular cracking by Diard et al. (2002) and Musienko and Cailletaud (2009)) remained anecdotal compared to cohesive zone models to study intergranular crack propagation. The main disadvantage of this method is that the grain boundary has to be meshed explicitily. A grain boundary thikness cannot be considered as a physical length scale at the continuum level. Moreover, the threshold traction at which the grain boundaries fail is not expressed explicitly as a model parameter. Nevertheless, a threshold traction value is the most important material parameter input in the work for intergranular cracking simulation.

5.3.2 XFEM formulation

The standard finite element method is well suited for cases with smooth model solutions. However, the presence of discontinuities and singularities such as cracks creates convergence problems in its use. For singularities and high gradients, a solution is discontinuous and thus mesh refinement is needed. The extended finite element method (XFEM) (Belytschko and Black 1999, Moës et al. 1999) has the advantage to overcome these problems without mesh refinement near singularities. Thus, since several years, XFEM was used to study cohesive crack propagation in quasi-brittle materials (Wells and Sluys 2001, Moës and Belytschko 2002). Application of the XFEM to fracture mechanics requires special enrichment functions to capture discontinuities along the crack path and the singularity at the crack-tip. Remmers et al. (2003) studied successfully cohesive segments that can arise at arbitrary locations and in arbitrary directions and thus enable the resolution of complex crack problems (e.g. crack nucleation at multiple locations, followed by growth and coalescence). Sukumar and Srolovitz (2004) have used such extended form to study quasi-static crack propagation in polycrystalline microstructures in isotropic elasticity (see Figure (5.6)).

A common XFEM approximation for fracture problems consists of a standard local FE displacement approximation around the crack enriched with a discontinuous function for the cracked domain, and the asymptotic crack-tip fields at nodes surrounding the cohesive crack tip using the framework of partition of unity (Melenk and Babuska 1996). The XFEM approximation for displacements $u^h(x)$ and $v^h(x)$ in a 2-dimensional domain $\Omega \in \mathbb{R}^2$ is given as:

$$\left\{ \begin{array}{c} u^h(x) \\ v^h(x) \end{array} \right\} = \sum_{i \in I} N_i(x) \left\{ \begin{array}{c} u_{0i} \\ v_{0i} \end{array} \right\} + \sum_{j \in J \cap I} N_i(x) \cdot S(x) \left\{ \begin{array}{c} a_{1j} \\ a_{2j} \end{array} \right\} + \sum_{k=1}^{m} \sum_{i \in M_k} N_i(x) \cdot B_k(x) \left\{ \begin{array}{c} b_1^k \\ b_2^k \end{array} \right\} \tag{5.6}$$

where $N_i(x)$ is the standard FE shape function for node i, u_{0i} and v_{0i} are the unknown of the continuous part at node i (e.g regular degrees of freedom), I is the set of all nodes in the element, $N_j(x)$ is a partition of unity function of node j, $S(x)$ is the step enrichment function, (a_1^k, a_2^k) are the unknowns of the enrichment at node j and J is the set of nodes whose shape function support is cut by the crack surface. Also, m is the number of enrichment terms, $B(x)$ is the crack-tip enrichment function, M_k is the subset of nodes that are enriched around the cohesive crack tip k with the asymptotic displacements b_1^k and b_2^k. b_1^k and b_2^k are the nodal enriched degree of freedom and can be associated with the elastic asymptotic crack-tip functions (Sukumar and Srolovitz 2004).

For the $S(x)$ function in Equation 5.6, a typical enrichment function is the sign-enrichment (Xiao et al. 2007). Note that the Heaviside function is also communly employed (assumes the value +1 above the crack and -1 below the crack) ; (Moës and Belytschko 2002, Abbas and Fries 2010).

For the crack-tip enrichment function $B_k(x)$ in the case of brittle fracture, a classical enrichment function in isotropic elasticity expressing asymptotic functions of the displacement field at the crack-tip is:

$$B(x) = \left\{ \sqrt{r}\sin\frac{\theta}{2}, \sqrt{r}\cos\frac{\theta}{2}, \sqrt{r}\sin\frac{\theta}{2}\sin\theta, \sqrt{r}\cos\frac{\theta}{2}\sin\theta \right\}, \tag{5.7}$$

where (r,θ) are polar coordinates in the local crack-tip coordinate system. The enrichment functions in the above form have infinite derivatives with respect to r at the crack-tip. Thus depicting the stress singularity at the crack-tip in the case of brittle fracture. However, the enrichment functions (Equation (5.7)) are not valid for cohesive cracks, and other enrichment functions have to be introduced (Meschke and Dumstorff 2007).

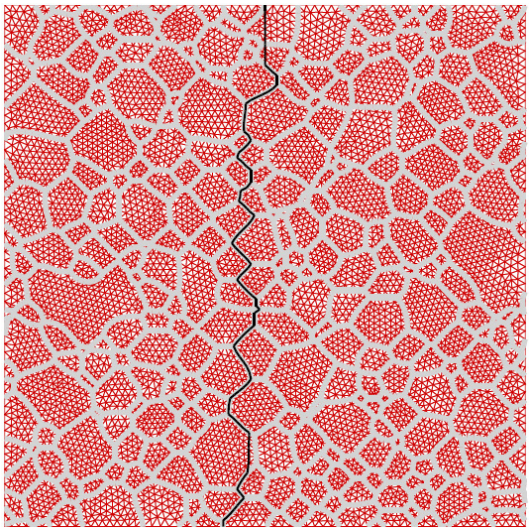

Figure 5.6: Example of crack propagation in a polycrystalline material predicted using XFEM (Sukumar and Srolovitz 2004).

The main advantage of the XFEM approach is that cracks can propagate through ordinary elements and thus the crack path does not need to be defined beforehand. In the intergranular case of hydrogen induced embrittlement, the crack path is known and is intergranular. The use of undefined preliminary crack paths is therefore not essential. Although, the XFEM approach renders smooth crack paths with no remeshing procedures, discontinuities must be introduced in the shape functions in order to model cracked elements. The method can become very cumbersome when multiple cracks initiate and interact. Moreover, the asymptotic function in our case (e.g. quasi-brittle fracture for crystal plasticity) is not yet well established. Moreover, XFEM is generally limited to elasticity problems. In X-FEM the scale at which fracture occurs is equal to the scale at which the structure is evaluated. Therofore a method like XFEM is therefore not suitable for one problem at hand.

5.3.3 Cohesive zone models

The basis of cohesive zone models can be traced back to Dugdale (1960), Barenblatt (1962) and Hillerborg et al. (1976). The approach from which cohesive zone models treat fracture as a gradual phenomenon in which separation takes place across an extended cohesive crack zone, and is resisted by cohesive tractions was proposed by Needleman (1987). The particularity of cohesive zone elements is that they do not explicity represent any physical material, but describe the cohesive energy releases during material separation. The constitutive behaviour of cohesive zone models describe then the tractions as a function of crack tip separation. A large variety of traction separation laws can be find in the literature (Chandra et al. 2002), which exhibit globaly more or less the same behaviour. In typical cohesive laws, the traction increases until a maximum is reached and then decreases to zero as the cohesive surfaces separates. This leads to a complete separation of interfaces.

In the cohesive zone model approach, potential crack surfaces are considered as internal surfaces. In the finite element formulation, the mechanical equilibrium equations include the contribution of the cohesive zone as integral over internal surfaces S_{int} as shown in Figure 5.7. The principle of virtual work can be written as follows:

$$\int_V s : \partial F dV - \int_{S_{int}} T_{CZ} \cdot \partial \Delta dS = \int_{S_{ext}} T_e \partial u dS \tag{5.8}$$

with the nominal stress tensor, $\mathbf{s}$, the deformation gradient, $\mathbf{F}$, the displacement vector, $\mathbf{u}$ and the traction vector, T_e, on the external surface, S_{ext}, of the body. The nominal stress tensor is calculated by $\mathbf{s} = \mathbf{F} - det(F)\sigma$, with, σ, the Cauchy stress. Tractions are related to σ by $T = n\sigma$, with n being the surface normal.

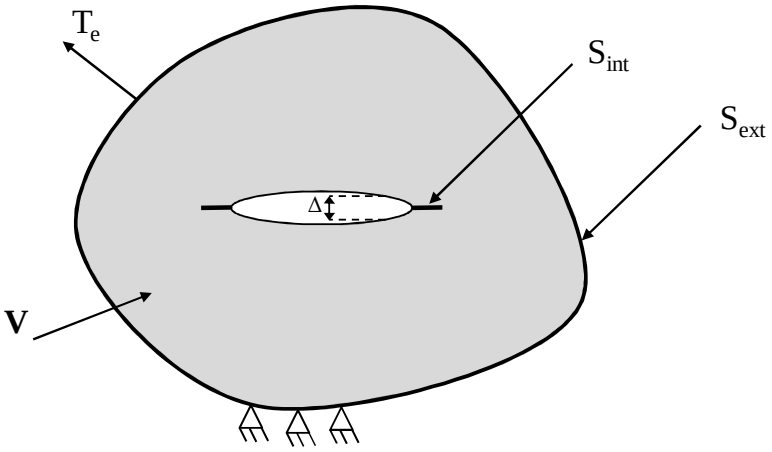

Figure 5.7: Schematic drawing of the conceptual framework of CZM.

On the internal surfaces, S_{int}, the cohesive zone tractions and the material separation Δ characterise the state of the cohesive zone material separation, $\Delta = \Delta n + \Delta t$, is computed from the displacements $(u+)$ and $(u-)$ at the crack tip.

$$T_{CZ} = \partial \Phi(\Delta)/\partial(\Delta) \quad \text{with} \quad \Delta = (\Delta_n, \Delta_t), \tag{5.9}$$

Based on the cohesive surface model of Xu and Needleman (1994), the energy potential

ϕ is given by Equation (5.10). Note that the choise of the energy potential formulation will be discuss in Section 5.4.2:

$$\Phi = \Phi_n + \Phi_n \exp\left(-\frac{\Delta_n}{\delta_n}\right)\left[\left(1-\chi+\frac{\Delta_n}{\delta_n}\right)\frac{1-q}{\chi-1} - \left(q+\frac{\chi-q}{\chi-1}\frac{\Delta_n}{\delta_n}\right)\exp\left(-\frac{\Delta_t^2}{\delta_t^2}\right)\right] \quad (5.10)$$

where $q = \Phi_t/\Phi_n$ and $\chi = \Delta_n/\delta_n$, Φ_n and Φ_t are the normal and tangential works of separation, δ_n and δ_t are two characteristic lengths of normal and shear separation. Material parameters q and χ govern the coupling between the normal and tangential response. q will be taken equal to one and χ equal to zero. The resulting equations for the normal and shear tractions T_n and T_t are obtained by combining Equations 5.9 and 5.10:

$$T_n = \frac{\phi_n}{\delta_n}\exp\left(-\frac{\Delta_n}{\delta_n}\right)\left\{\frac{\Delta_n}{\delta_n}\exp\left(-\frac{\Delta_t^2}{\delta_t^2}\right) + \frac{1-q}{r-1}\left[1-\exp\left(-\frac{\Delta_t^2}{\delta_t^2}\right)\right]\left[r-\frac{\Delta_n}{\delta_n}\right]\right\} \quad (5.11)$$

$$T_t = 2\left(\frac{\phi_n \Delta_t}{\delta^2 t}\right)\left\{q+\left(\frac{r-q}{r-1}\right)\frac{\Delta_n}{\delta_n}\exp\left(-\frac{\Delta_n}{\delta_n}\right)\exp\left(-\frac{\Delta_t^2}{\delta_t^2}\right)\right\} \quad (5.12)$$

Assuming that $T_n = T_n(\Delta_n; \Delta_t = 0)$ and $T_t = T_t(\Delta_n = 0; \Delta_t)$, then uncoupled tractions are obtained. Using $T_n(\delta_n) = \sigma_{max}$ and $T_t(\delta_t/\sqrt{2}) = \tau_{max}$, the following relationships for ϕ_n and ϕ_t are obtained,

$$\phi_n = \sigma_{max}\exp(1)\delta_n, \quad \phi_t = \sqrt{\exp(1)/2}\tau_{max}\delta_t \quad (5.13)$$

Figure 5.8 shows the normalised traction curves for uncoupled normal and shear separations. Here, $T_n = \sigma_{max}$ and $T_t = \tau_{max}$ are the dimensionless normal and shear tractions, and $\Delta_n = \delta_n$ and $\Delta t = \delta_t$ represent the dimensionless normal and shear openings respectively. When the cohesive zone is given in the negative direction, the traction becomes more negative in order to prevent penetration. For shear traction separation in the negative direction is opposite to those for a positive Δt.

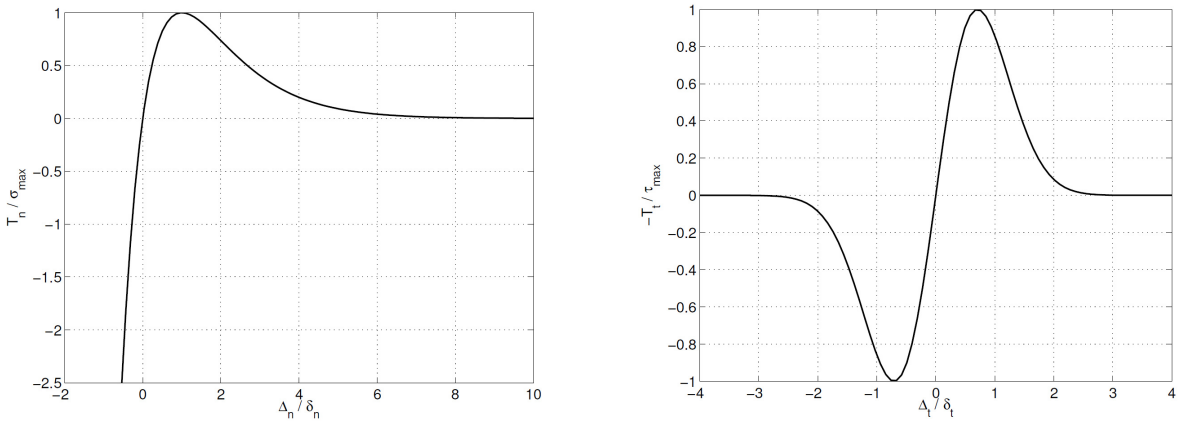

(a) (b)

Figure 5.8: (a) Normal and (b) shear traction curves for uncoupled normal and shear separations.

The two dimensions framework presented here can be extended to three dimensions by adding a new tangential traction to the set of equations (Equations (5.9) and (5.10)). This

new traction will be perpendicular to the other two (Goncalves et al. 2000).

Chaboche et al. (2001) pointed out a problem of stability in the solution, which can occur while using a rate independent cohesion law. Let us consider a simple 2D example with one interface element and one elastic plate element. The total displacement control is at the position BB' and the total displacement U is a sum of the interface separation u and the elastic elongation of a plate element:

$$U = u + \frac{L}{U_0} T \tag{5.14}$$

Here, T, is the applied stress, E_0, the Young's modulus and L, the length of the elastic part. The behavior of the interface is described as:

$$T = E \cdot F(u/\delta) \cdot u/\delta \tag{5.15}$$

If the stiffness $k = E_0/L$ is high enough, one can expect the solution jump from u_a to u_b, see Figure 5.9. To avoid this problem one could use a rate-dependent interface model (Attouch 1996) or, as is the case in this work, one could introduce a sufficiently fine mesh at grain boundaries.

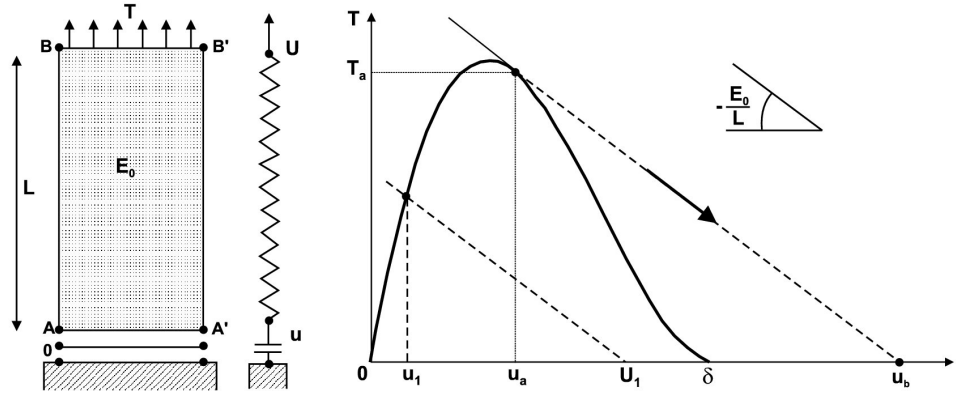

Figure 5.9: Simple uniaxial configuration that illustrates the "solution jumps": (a) the plate and interface elements and (b) the interface nodes response, applied traction (**T**) versus displacement (**U**), see (Chaboche et al. 2001)

Cohesive law approaches have been broadly used in crack propagation simulations. The implementation of cohesive zone models into numerical analyses takes the form of cohesive elements, which simulate a crack process zone. Since the crack path can only follow these elements, but is not a disavantage for intergranular modelling because cracks are known to develop in grain boundaries that are explicily defined in the polycrystal model. Thus, fracture can occur at physical interfaces. Another main advantage of cohesive zone models is that only few parameters are needed and can be identify.

5.4 Proposed Crack Propagation Model

Two test cases of modelling of crack propagation are considered. The first case is a direct application of the results obtained in Section 4.4 with the addition of a cohesive zone model at grain boundaries (see Figure 5.10). It is used to verify that the identifed intergranular fracture mechanism is in agreement with the observed experimental cracking patterns. Secondly, a cohesive zone model is incorporated in a microstructure generated by Voronoi tesselation (see Figure 5.11). This last case will be used (a) to massily propagate cracks in the microstructure and (b) to deduce what the effect is of not taking into account the bulk of the material that has not been embrittlled by hydrogen.

5.4.1 Mesh and boundary conditions

The first numerical study with cohesive zones consider the actual microstructure of the in-situ tensile specimen given in Chapter 3. The mesh is made of 13,257 triangular solid elements for the crystalline regions and the interface is composed of 530 cohesive prismatic elements. The bulk uses reduced quadratic elements and the interface fully quadratic elements. The resulting problem reaches a size of 108,000 degrees of freedom. Furthermore, the grain orientations are defined based on the results of EBSD measurements. Boundary conditions are imposed based on the displacement measurement obtained from the digital image correlation results shown in Chapter 3. Geometry and boundary conditions are defined in Figure 5.10.

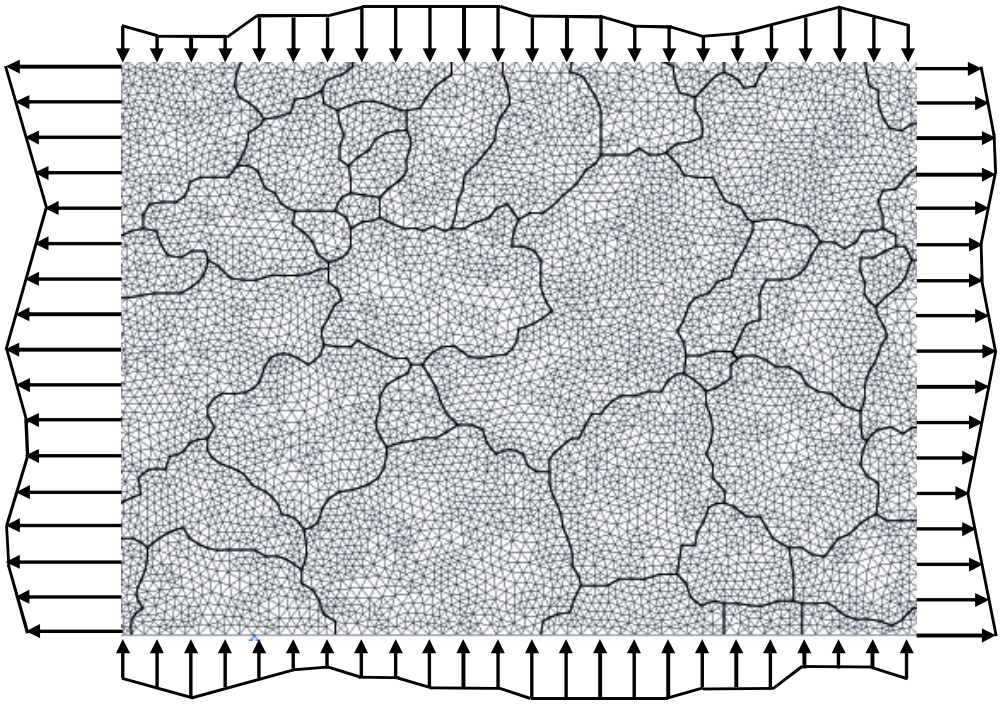

Figure 5.10: Mesh of the actual microstructure in the region of interest defined in Chapter 3 and a schematics of the applied boundary conditions.

The second application of cohesive zone models is an aggregate mesh generated by Voromoi tesselation. The mesh is made of 25,500 prismatic elements for crystals and the interface is composed of 2,500 cohesive prismatic elements, with the same shape functions defined previously. The resulting problem reaches a size of 1,080,000 dof. Grain orientation is assigned ramdomly and the boundary conditions are homogeneous. The aggregate mesh and homogeneous boundary conditions are illustrated in Figure 5.11.

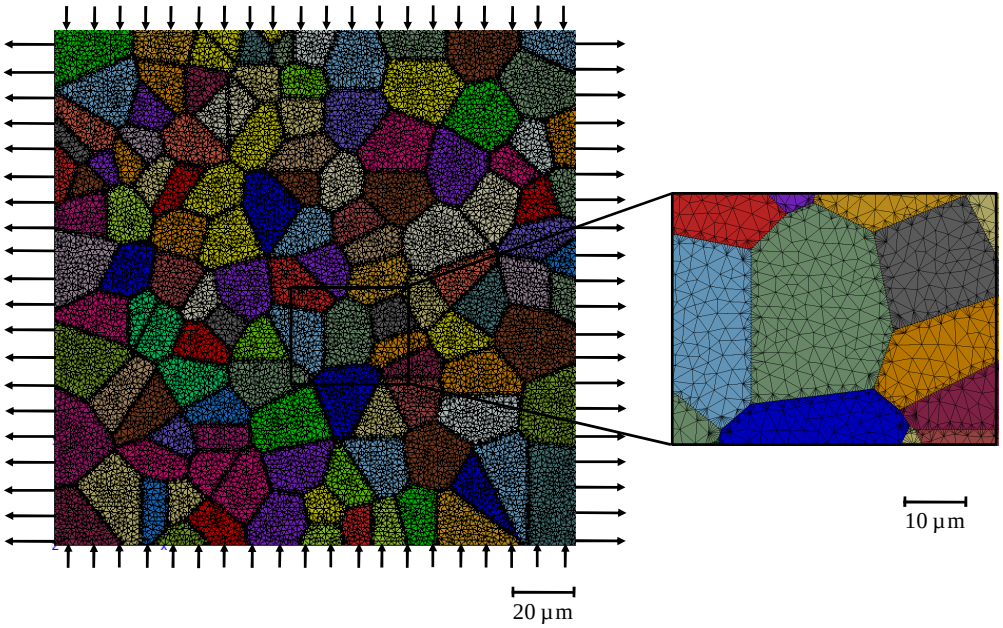

Figure 5.11: Aggregate mesh of 125 grains showing a zoomed region of grain boundary mesh.

5.4.2 Model calibration

The cohesive zone properties are assumed uniform along the interface with the traction separation laws shown in Figure 5.8(a), as originaly proposed by Xu and Needleman (1994). For quasi-brittle fracture, the shape of the traction separation law as well as the parameters of the cohesive zone are very important. The assumption of an exponential law for the traction separation law (Xu and Needleman 1994) is consistent with experimental results obtained in brittle fracture cases. The traction separation law used by El-Houdaigui et al. (2011) is used in this work to introduce the effects of hydrogen induced embrittlement.

The cohesive zone parameters were conditioned by the critical grain boundary tractions calculated from the FE analyses of the crystal aggregate presented in the previous section. Thus, the maximum cohesive force, σ_c, was fund to be equal to 175 MPa. δ_n, the opening at the onset of debonding was adjusted to be 100 nm which is the minimum size for FE mesh. The resulting work of separation $\phi = \exp(1)\sigma_{max}\delta_n$ was fond to be equal to 45.1 J/m^2 . This value is resonable for quasi-brittle fracture in alluminum alloys and in agreement with micro-ductile cavities shown in Chapter 1 Figure 2.6. The length of the cohesive zone, $L_{cohesive}$ can be estimated by Rice's formula (Rice 1980):

$$L_{cohesive} = \frac{9\pi}{32}\frac{E}{1-\nu^2}\frac{G_c}{\sigma_c^2} \tag{5.16}$$

where $G_c = 2\phi$ is the fracture energy. Using the values for the material parameters of aluminum alloy (see Table 2.2), the size of the cohesive zones is estimated to be 230 nm. This value has to be slightly less than the edge size of the elements around cracks path. As quadratic elements are used, it corresponds to the node-to-node distance. To avoid the problem of instability in the solution (Chaboche et al. 2001) for a brittle material, it is recommended that 2-5 elements are necessary to resolve the cohesive zone. It is the reason why particular attention was paid to the grain boundary mesh refinement shown in Figure 5.11.

5.4.3 Comparison between observed and predicted cracking patterns

Experimental strain field and predicted ones are plotted in Figure 5.12(a)(b)(c) and in Figure 5.12(d)(e)(f) respectively, at 0.45%, 1.6%, 2.6% applied strain. Figure 5.12(g)(h)(i) show high concentration of stresses in the principal loading direction at each triple boundary of the cracked grain boundary. It can be assumed that stresses at triple grain boundaries play a non negligeable role in the intergranular fracture mechanism.

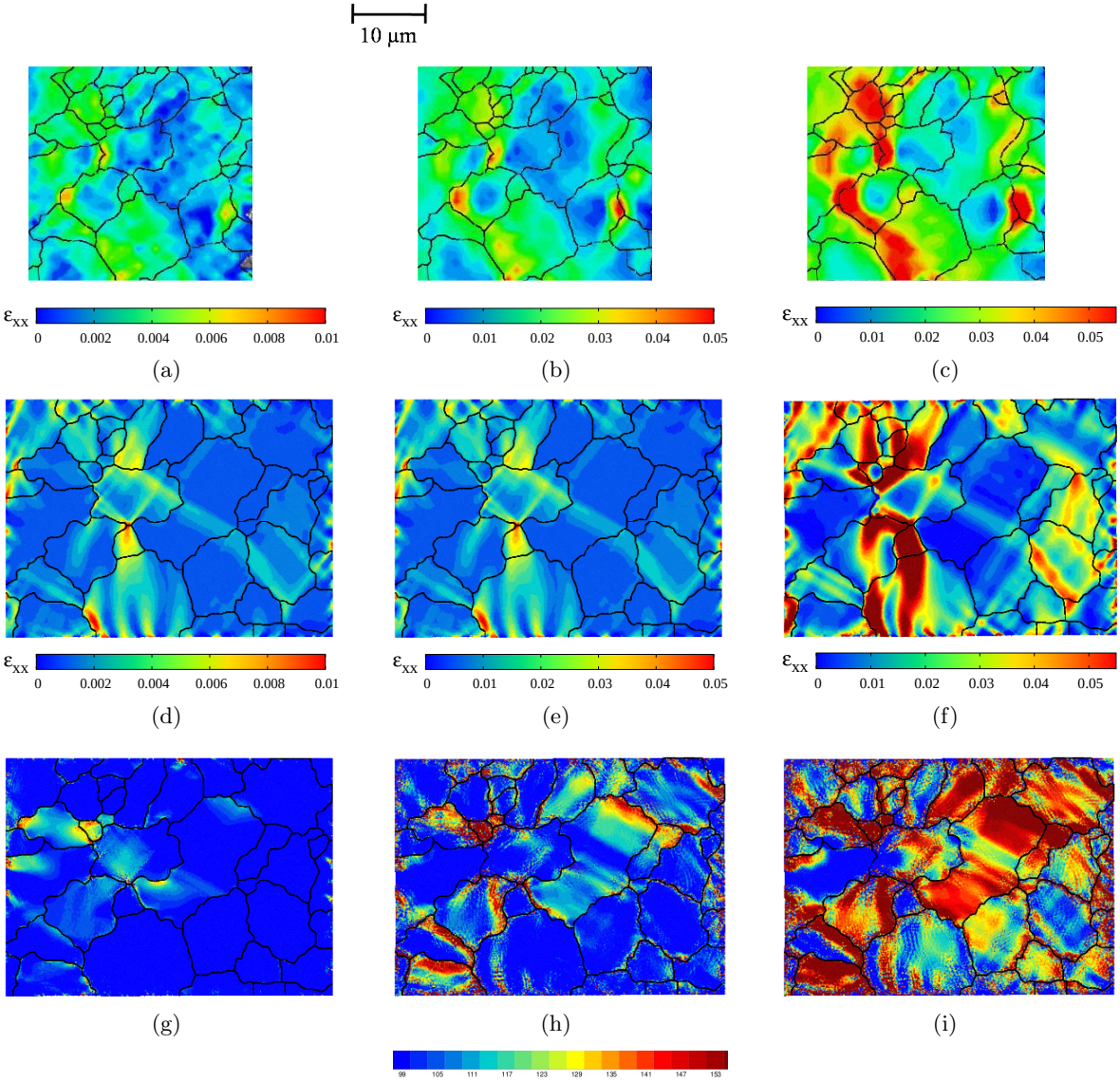

Figure 5.12: (a), (b), (c) experimental strain fields, (d), (e), (f) predicted strain fields and (g), (h), (i) maximum principal stress fields

Despite some differences in the strain field predictions, the model was able to predict the onset of cracking of the correct cracked grain boundary observed experimentally. Additionally it can be see in Figure 5.13 that the crack opening seems to be close to those predicted.

Experimentally three cracks was observed in the studied region of Figure 5.12, however only one of the three is well described in the model. The 2D model presented is able to describe only one crack: the first crack to be formed could be considered to be "through-

thickness" in 3D, which is not the case experimentally (the depth of the embrittled layer is much lower than the specimen thickness). Thus, only first boundary to crack could be predicted in the model. Unfortunately, SEM observations did not reveal which of the three cracks was the first to nucleate Figure 5.13.

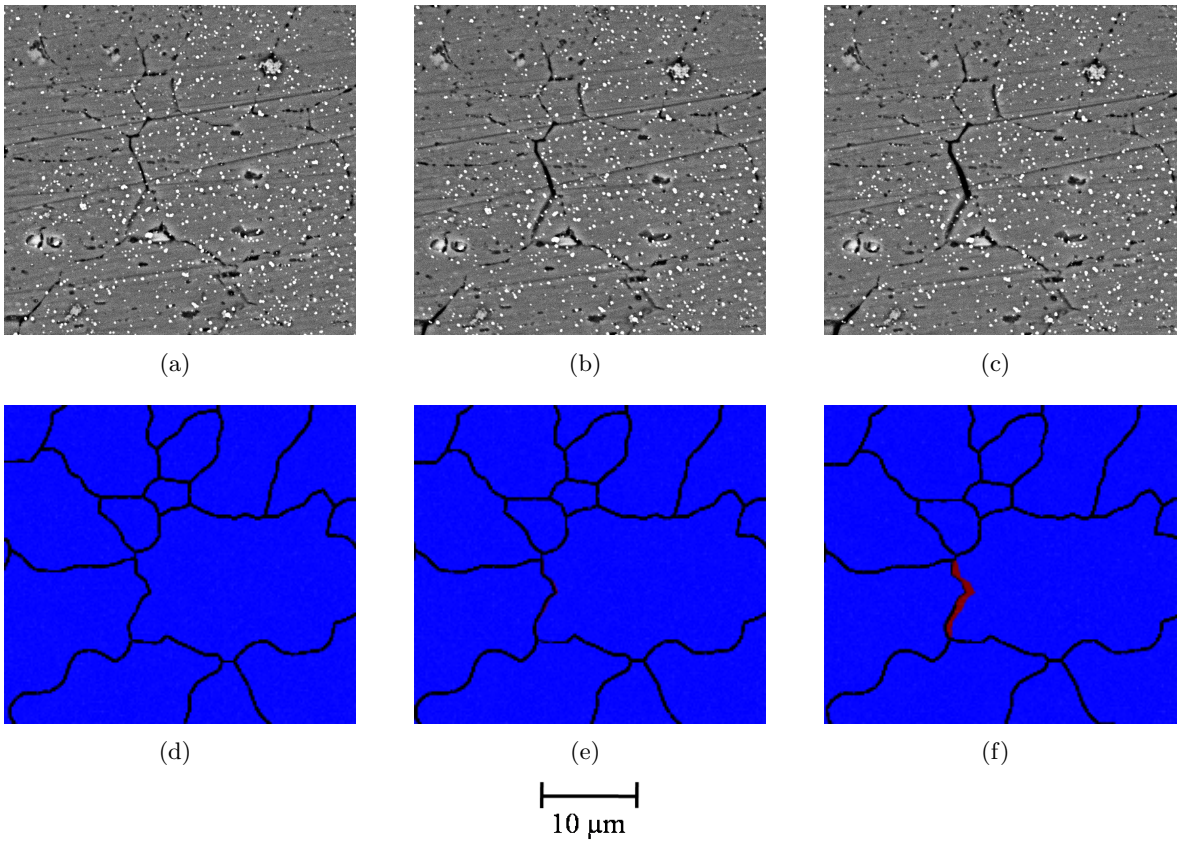

Figure 5.13: Crack opening (a), (b), and (c) micrographs, (d), (e), and (f) numerical prediction (crack in red) at 0.45%, 1.6%, 2.6% applied strain.

For the large aggregate simulation, it can be seen in Figure 5.14 at point (a) that the crack appears in the microstrure after 0.6% tensile strain. This is in good agreement with experimental observations shown in Chapter 3. On the other hand, the first cracks progate through the microstructure, are shown in Figure 5.14 (a) to (f) before the iniation of another crack. Moreover, the second crack is created inside the deformed band induced by the first one. However, experimental results exhibit multiple crack iniations in the microstructure in opposition to only 2 cracks in the quasi 2D-simulation. 3 cracks in 50 grains on average were observed experimentaly (see Figure 3.22) and 2 cracks were created by the model made of 125 grains. This can be explained by the fact that in such model the load transfert is not taken into account. Due to the quasi-2D assumption, numerical cracks can go through the microstructure and induce a loss of strengthening of the model. This is illustrated by the difference between the behaviour of a sound model and a model using cohesive zones in Figure 5.14.

Figure 5.15 shows the distribution of all dislocation densities. It can be seen that the cracks appear in a grain boundary which is below or behind a grain in which the dislocation density is very high, see Figure 5.15(c) for the first crack and Figure 5.15(k) for the second crack.

This observation is confirmed when plotting the accumulated plastic strain distributions in Figure 5.16(c) for the first crack and Figure 5.16(k) for the second crack.

It was found in Figure 5.16(c) that close to failed grain boundaries the cumulated plastic strain is higher than elsewhere and equal to 0.06 % before crack opening at 0.045 % applied strain. This result is in agreement with strain fields measurements of largest deformed grains close to failed grains boundaries (i.e Figure 3.20(f)).

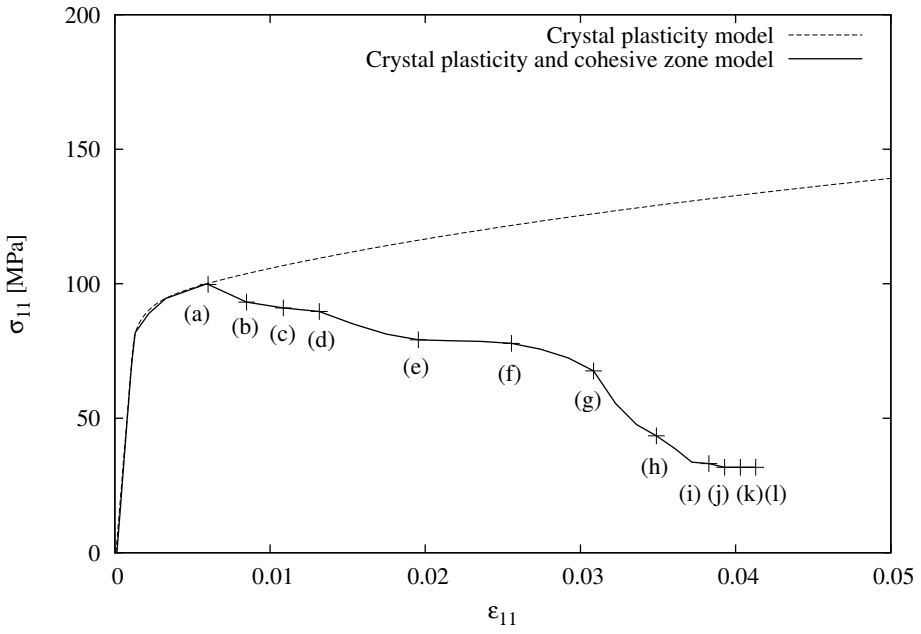

Figure 5.14: Stress-strain curves (a) with and (b) without cohesive zone model. Here, (a),(b),(c),(d),(e),(f),(g),(h),(i),(j) correspond to the maps shown in Figures 5.15 and 5.16.

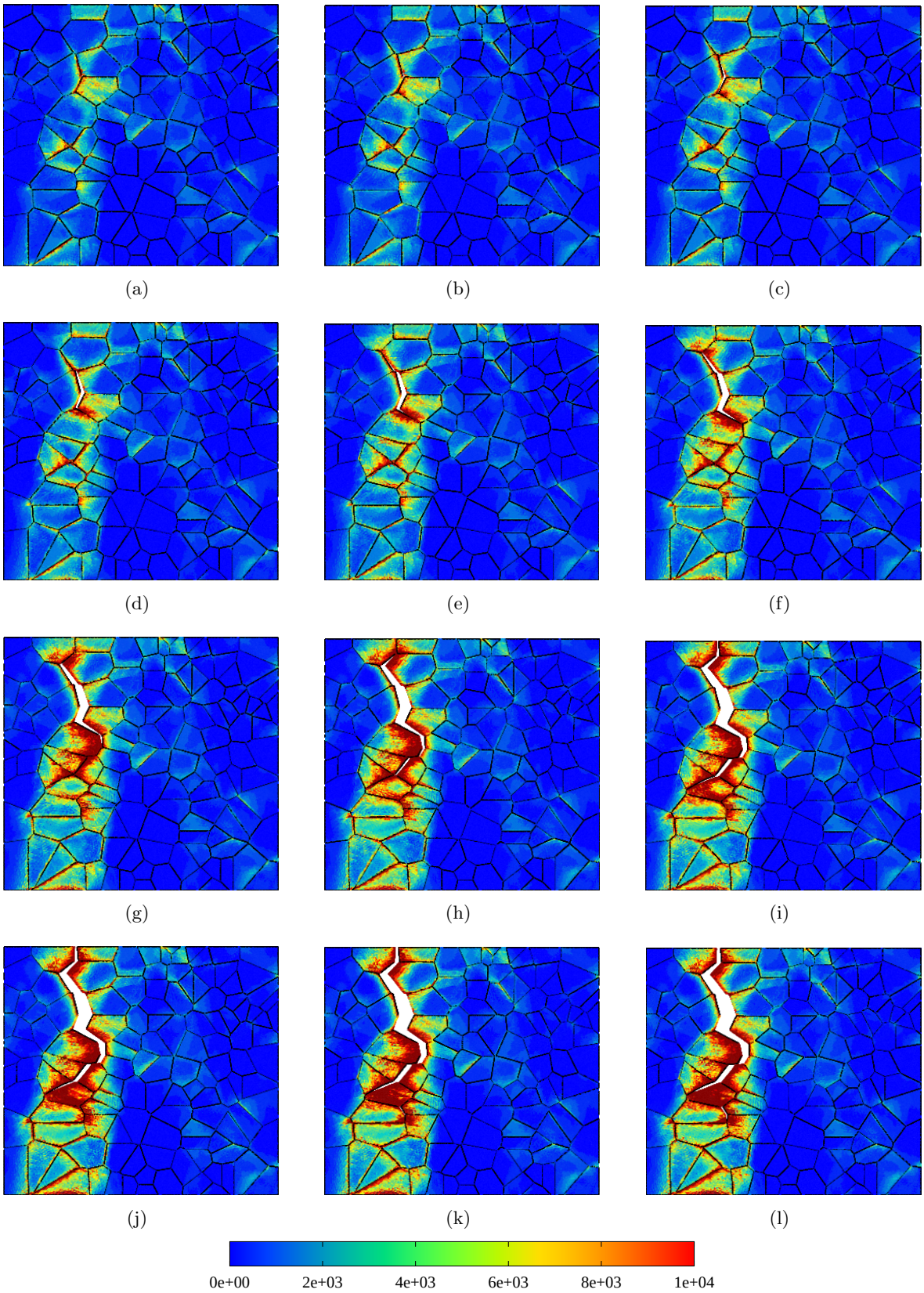

Figure 5.15: Distribution of the total dislocation densities (i.e. over all slips system). Corresponding applied tensile strains are those reported in Figure 5.14.

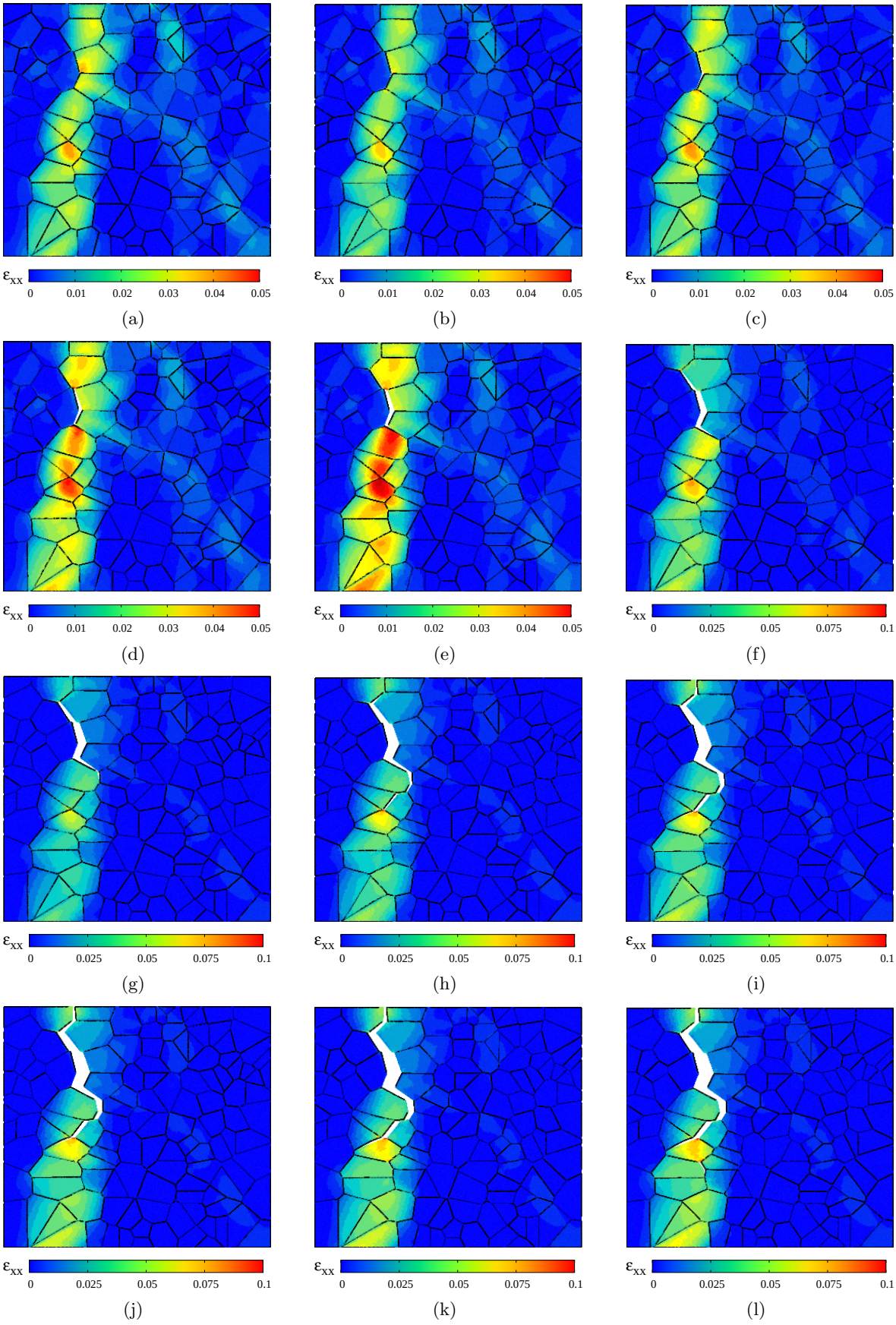

Figure 5.16: Accumulated plastic strain distributions. Corresponding applied tensile strains are those reported in Figure 5.14

5.5 Conclusions

The results obtained in this chapter show that the critical local grain boundary tractions obtained from an analytical Eshelby-type approach, which was based on "hard" inclusion embedded in a "softer" matrix, of 175MPa was consistent with the numerical prediction of 170±35 MPa obtained from a finite element model of the polycrystal using crystal plasticity concepts.

To model the effects of HIE in polycrystalline materials, a crystal-plasticity model for the grain bulk has been coupled with a cohesive zone model for the grain-boundary behaviour. The model accounts for critical tractions at the grain boundaries. This computational method was able to quantitatively study the deformation and fracture response of the polycrystalline Al-Mg alloy under simple and multiaxial tension. The results from the simulations confirm the major features of the experimentally observed strain fields and the dominant fracture mechanisms in this metalic alloy (see Chapter 3).

The simulations show that the stress concentrations at the tips of the grain-boundary cracks and at grain-boundary triple junctions cause a limited amount of plastic deformation inside the grains. This proves that the fracture mechanism is mainly due to the deformation of surrounding grains. Additionaly, the simulations show that the high normal tractions at grain boundaries are the most important driving force responsible for intergranular cracking.

The simulations with the actual microstructure and with Voronoi aggregate are both limited in the modelling of intergranular cracking mechanism. This is due to the lost of strengthening of the finite element modelling due to the crack opening through the calculated microstructure. This is due to the quasi 2D simulations used in these models. The effect of bulk of the material which has not been embrittled by hydrogen is not taken into account. For this reason, the number of failed grain boundaries is smaller than that observed experimentaly. Moreover, the critical tractions calculated with the model in quasi 2D model does not take into account the influence of the substrate. Much work remains to be done to account for grain boundary morphologie to elucidate the effects of the interplay between grain-boundary geometry and grain bulk deformation in polycrystalline materials. Three dimensional analyses will be done in the next chapter to study these effects on intergranular cracking.

Finally, it should be noted that the modelling approach used in this work should also be useful to represent the inelastic deformation and fracture response of other materials with little plasticity, such as other brittle metals, ceramics and rock materials, where grain boundary separation arises at the early stages of plastic deformation.

Résumé

Les résultats obtenus dans ce chapitre montrent que la contrainte normale critique au joint de grain calculée à partir d'une approche analytique de type Eshelby est égale à 175±35 MPa. Cette approche fondée sur le concept d'une sphère "dure" dans un milieu "mou" est cohérente avec les résultats obtenus par modélisation par éléments finis de polycristaux utilisant les concepts de plasticité cristalline.

Pour modéliser les effets d'HIE dans le matériau polycristallin, un couplage a été réalisé en incorporant un modèle de zone cohésive à tous les joints de grains en plus du comportement de plasticité cristalline dans les grains. Cette méthode de calcul permet à la fois une étude quantitative des champs de déformation et des mécanismes de rupture intergranulaire. Les champs de déformation et le mécanisme de rupture obtenus grâce aux simulations numériques sont cohérents avec les résultats expérimentaux.

Les simulations présentées dans ce chapitre montrent également une concentration de contrainte sur les pointes de fissures et près des points triples. Cela s'explique par la faible capacité des grains environnants à accommoder la déformation plastique. On montre ainsi que le mode de rupture du joint de grain est très dépendant des grains environnants, notamment ceux dont le joint de grain à rompu.

Cependant, dû au fait de l'utilisation de simulations quasi 2D (i.e. avec des conditions de chargement hors plan de type déformation plane généralisée) le matériau non-fragilisé composant l'ensemble de la matière sous jacente au matériau fragilisé, n'est pas pris en compte dans ce type de calcul. C'est la raison pour laquelle le nombre de fissures obtenues numériquement est inférieur à celui obtenu expérimentalement. Pour prendre en compte l'effet de substrat il sera nécessaire d'engager une campagne de calculs dans lequel le substrat serait modélisé avec le modèle macroscopique dans un premier temps, puis avec le modèle de plasticité cristalline dans un second temps. C'est pour cette raison que le chapitre suivant se concentre sur la modélisation d'agrégat dont la morphologie et la texture ont été caractérisées expérimentalement.

Chapter 6

Application to Intergranular Fracture of an Actual 3D Alloy Aggregate

Contents

6.1 Introduction

In order to improve the accuracy of the calculated grain boundary tractions in Chapter 4, and to account for the effects of bulk in the prediction of strain-stress fields at the specimen surface, a 3D representation of the considered microstructure is needed. The microstructure morphology in the third dimension plays a dominant role on the deformation of the material measured at the surface (see Chapter 3). As it can be seen through this work, grain boundaries have many sharp angles that introduce locally high stresses (see Chapter 4). A 3D description of such sharp angles will account for this problem more clearly than the 2D models from Chapter 4. Despite previous work that tried to model 3D microstructures based on EBSD data (e.g St-Pierre et al. (2008)), no single classical approach has yet been developed that can deal with both sophisticated experimental databases and nonlinear numerical analysis (Dillard et al. 2004).

For these reasons, it was decided to improve the methodology of finite element 3D mesh generation from 3D experimental microstructure description. Two experimental procedures were used here. First, EBSD mapping and X-Ray microtomography were combined to describe both the free surface and bulk microstructure morphology respectively. In a complementary approach 3D microstructural characterisation of the full microtexture was achieved through serial sectioning from EBSD mapping. Resulting 3D microstructures were analysed to reveal the 3D geometry of cracked grain boundaries.

Once the 3D microstructure was properly described, a set of algorithms was used to provide a complete microstructure description to the mesh generation step. The mesh generation step in turn produced a good quality 3D mesh as input for the finite element code and maintains mesh quality as the simulation proceeds.

6.2 Characterisation of an Actual 3D Alloy Aggregate

6.2.1 Polycrystals characterised using X-Ray tomography after liquid gallium infiltration

X-ray microtomographic experiments have been performed using a synchrotron light source at the European Synchrotron Radiation Facility (ESRF) in Grenoble. The large distance between the source and the experimental end station (ID19) provides a very high spatial beam that is able to produce high quality images. A white beam becomes coherent with a set of optical tools such as slits and monochromated parallel silicon single crystals to reduce beam hardening artifacts.

A sample is fixed on a rotating stage between the X-ray source and the detection unit that records the transmitted X-rays. A fluorescent screen, coupled with a low noise 2048 $\times$ 2048 pixels CCD camera (Fast REadout LOw Noise), is used to detect the projections of the parallel beam. The resulting images, which are function of the local linear attenuation coefficient, μ, are retrieved in grey-level tone. The atomic number, Z, and the material density, ρ, for a given photon energy, E, are linked to the attenuation coefficient, μ, through the relationship determined by Attix and Roesch (1968):

$$\mu \approx \rho \frac{Z^4}{E^3} \tag{6.1}$$

The sample is step by step under the beam from 0 to 180° to provide a set of 1980 2D images. Intensity inhomogeneities and variations of the X-ray beam are then eliminated by subtraction of a reference image recorded every 10 slides. The high photon flux delivered by the ESRF allows to reduce the exposure time to 1 second per radiography and thus minimise noise from the X-ray variation.

The beam energy is set to 30 keV and two values of spatial resolution were chosen, one of 0.75 µm to allow for fine microstructural analysis and another of 2 µm to permit a larger microstructural volume to be characterised. The 2 µm resolution gives statistical data at the grain scale, whereas the 0.75 µm resolution provides detailed observations of intergranular cracks. This choice of the resolution dictates the possible sample width. For example, the largest dimension of the sample must be lower than 2 mm for a 2 µm resolution, due to the limited number of pixels in the camera (2048 × 2048). As a result, all the material is illuminated by the beam for each value of the rotation angle. Note that in the case where the sample is larger than the field of view, the projections are truncated and the reconstruction is known as "local tomography" (Baruchel et al. 2000).

6.2.1.1 3D image analyses

3D image analysis of the aluminium alloy is a complicated task because of the 3D segmentation of the grains. To compute morphological parameters, the grains of the aluminium alloy have to be isolated first. But, their separation is not easy to perform numerically.

The 3D starting volume, derived from one reconstructed volume, is divided into a set of 2D grey level slices. Due to the large differences between the linear attenuation coefficients of gallium and aluminium, the grey-level distribution of the images appears bimodal. Thus, simple threshold, which takes the lowest grey-level, is applied to generate binary images and the hollow struts in the "gallium-free" part of the image are filled in by straight forward morphological operations.

The 3D segmentation method is divided into two main stages. First, the distance map image of the grains is computed and the position of the ultimate eroded sets, called markers, is determined. Second, the watershed is constructed from these markers with the help of the distance function. This procedure results in grains that are closed and they do not interpenetrate. A 2D section of the aluminium alloy and its segmentation results are represented, respectively, in Figure 6.1. This segmentation allows to directly find the value of some morphometric parameters. For instance, the volume of each grain can be determined by stacking the 2D slices of that grain into 3D volume. However, other morphometric parameters require the knowledge of the 3D skeleton (one voxel thick) of grain boundaries revealed by gallium. For that purpose, the 3D resulting watershed, formed by one or two voxels thick, is made thinner.

The difference between the simulated microstructure and the experimental one, corresponding to the bright grain boundaries, is now negligible as shown in Figure 6.1 for a 2D case and in Figure 6.2 for a 3D case. In order to combine information about crystal microstructure and microtexture, resulting crystallographic orientation obtained by

EBSD maps before microtomography can be assigned to corresponding grains as illustrated in Figure 6.3.

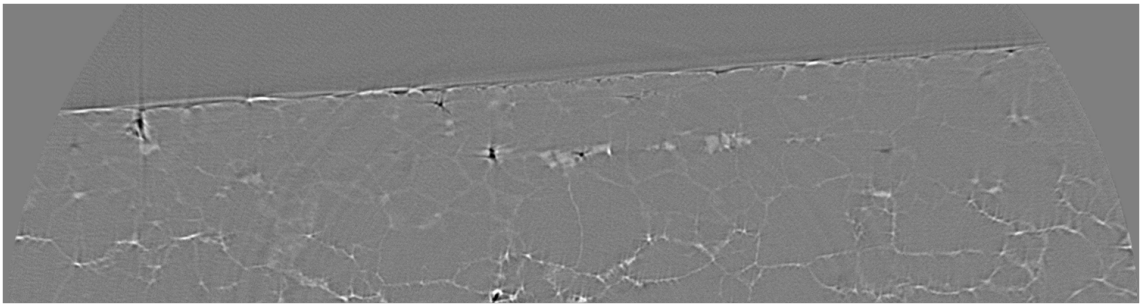

(a)

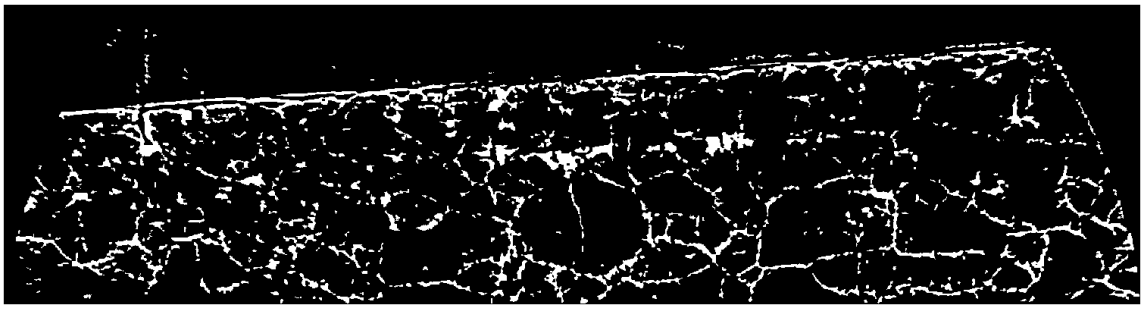

(b)

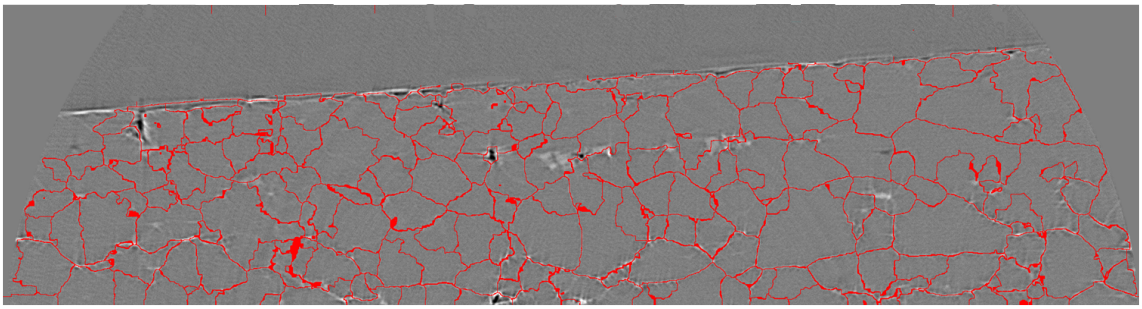

(c)

Figure 6.1: 2D segmentation of the Al-Mg alloy :(a) gray-level slice, (b) binary slice with markers, and (c) closed grains

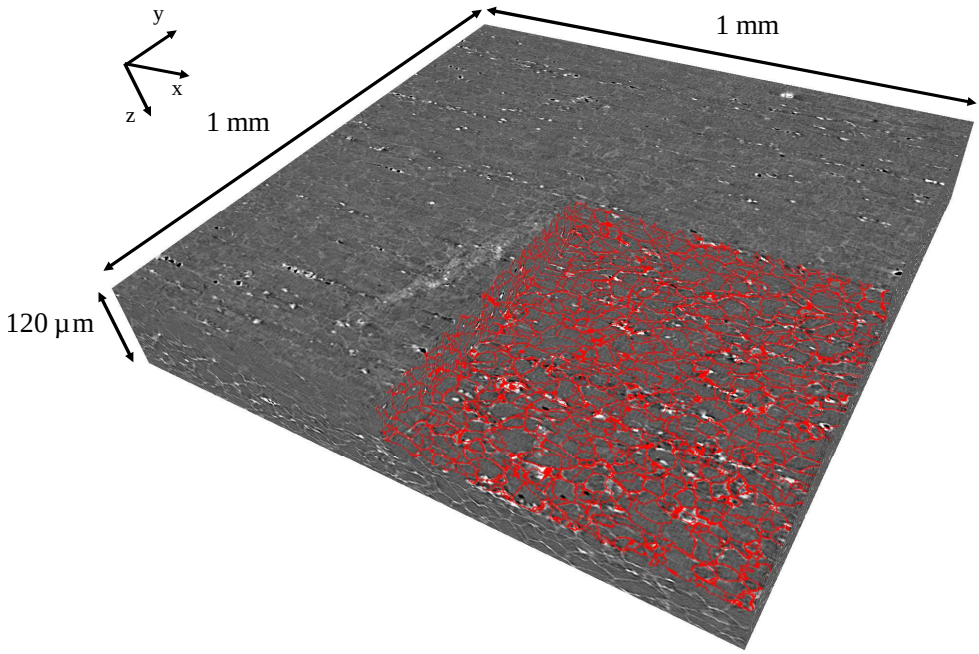

(a)

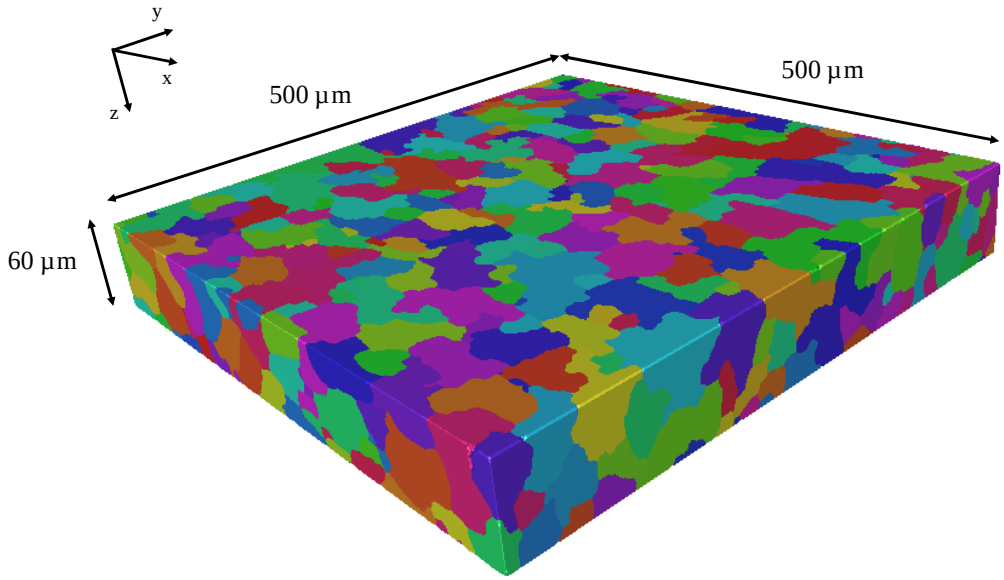

(b)

Figure 6.2: (a) part of a volume obtained by microtomography and grain boundaries identified in red and (b) corresponding recorded volume.

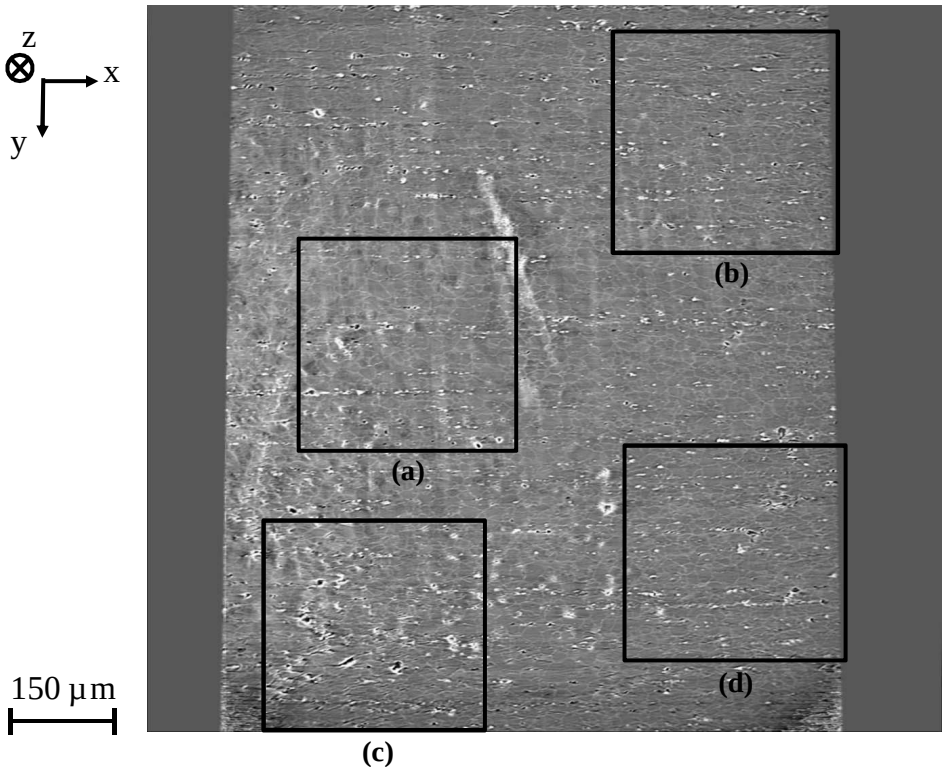

(a)

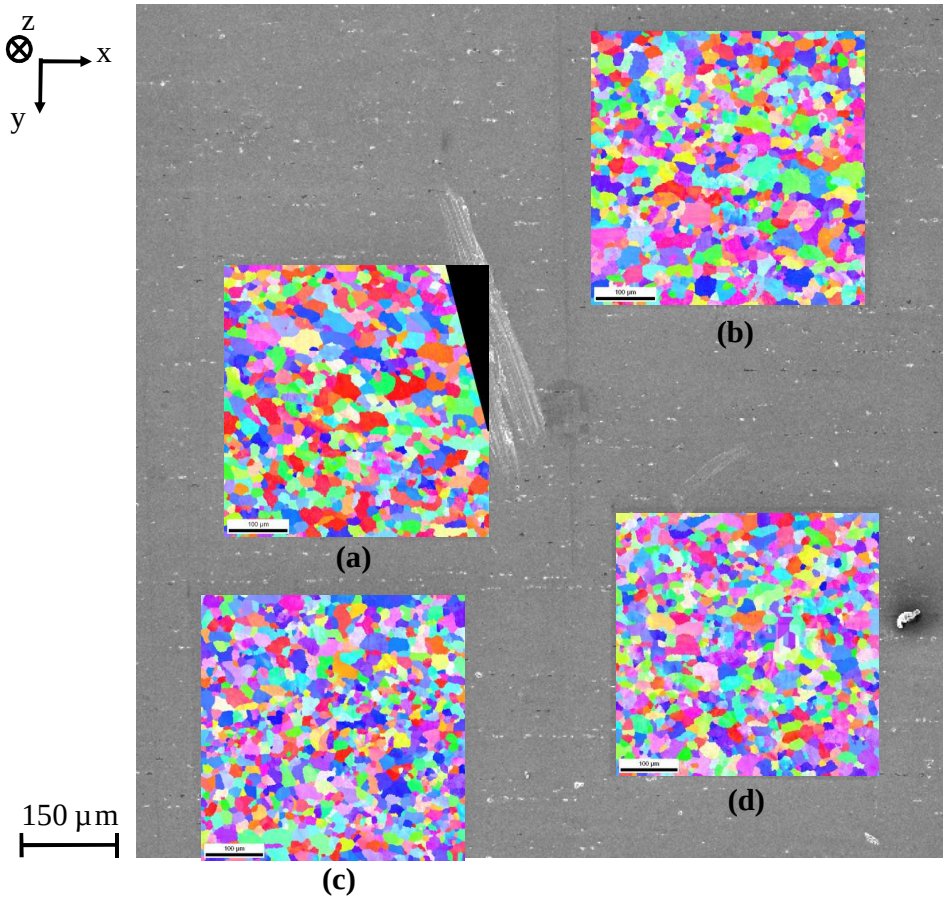

(b)

Figure 6.3: (a) surface slice obtained by microtomography and (b) corresponding EBSD maps and SEM micrographs. Here, the link between this two analysis tools was made with the central scratch as a fiducial mark.

6.2.2 Polycrystals obtained from 3D EBSD analyses

As many traditional metallographic techniques, EBSD, is usually performed on 2D sections of a sample. The serial sectioning technique used here involves the serial removing of layers, recording the microtexture of the newly exposed surface and then reconstructing the 3D structure by stacking of the recorded images. The main challenges associated with these methods are controlling the sectioning depth, obtaining flat and parallel surfaces, and correctly re-detecting and aligning the observation region.

In this work serial chemical-mechanical polishing by colloidal silica was used to reveal the 3D microstructure of the alloy in the studied region. In order to control the depth and ensure parallel surfaces between scanned surfaces 9 fiducial indentations recorded were engraved around the studied region. At the end of each polishing step the length of indentation marks was recorded. Thus, the distance in depth from the previous scanned plane and the planarity of the actual plane can be known. The use of a vibratory polisher that ensures planar surfaces, obtained surfaces were not rigorously parallel. To overcome this difficulty an image registration method was applied for non parallel surfaces.

Image registration is the process of overlaying images of the same object taken at different times, from different views, and/or by different sensors. This technique was adapted to connect not parallel surfaces in the stack of EBSD scans before 3D reconstruction.

The registration method used in this study consisted of the following four steps (see Figure 6.4) :

- Control points selection for further processing. Control points can be closed-boundary regions, edges, contours, line intersections or mathematical objects such as centers of gravity and line endings. Here, triple grain boundaries were used as control points (red circles in Figure 6.4)
- Establishing of feature matching points. Here, the objective is to link points between the reference image (Figure 6.4(a)) and the deformed image (Figure 6.4(b)).
- Transform model estimation. The type and parameters of the mapping functions, aligning the deformed image with the reference image, are estimated. The parameters of the mapping functions are computed by means of the established correspondence.
- Image resampling and transformation. The deformed image is transformed by means of the mapping functions (Figure 6.4(c)) . Image values in non-integer coordinates are computed by an interpolation function.

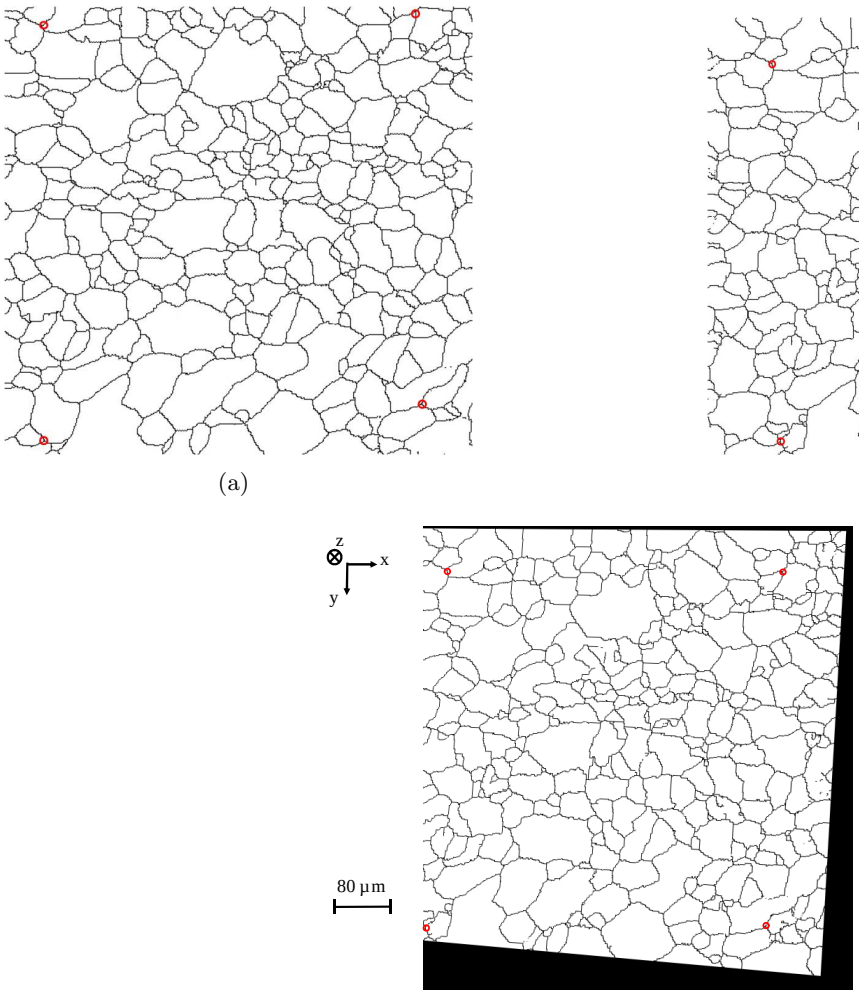

(a) (b) (c)

Figure 6.4: Feature matching control points (the corresponding pairs are marked by red circles) (a) reference image, (b) deformed image and (c) image resampling.

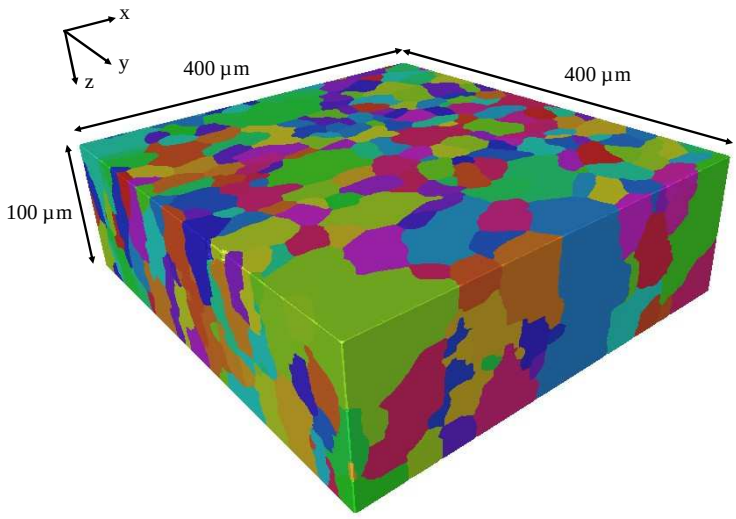

Figure 6.5: Recorded microstructure with a serial sectioning of 3 µm per step.

6.3 3D Orientation of Embrittled Grain Boundaries

It was shown in Chapter 3 that at the surface of the specimen, cracks appear oriented perpendicular to the loading axis. Amongst such grain boundaries oriented perpendicular to the loading axis at the specimen surface, four grain boundaries have been examined from the surface and in the bulk material. Figure 6.6 shows analysed grain boundaries (a) in the registered polycrystal, (b) in a micrograph after 4.5% applied strain. Adjacent grains containing two of the cracked grain boundary and two non cracked ones are identified in Figure 6.7. Grain surfaces have been plotted with a transparent shape in 3D which allows grain boundary visualisation.

It can be seen from Figure 6.7 that, in the z direction, cracked grain boundaries are not necessarily that perpendicular to the loading direction. However, amongst these ten cracked grain boundaries observed in Figure 6.6(b), only one is not perpendicular to the loading direction, see (2) in Figure 6.6. The same observation can be made with grain boundaries that have not cracked. Some of them are oriented perpendicular to the loading direction (e.g grain boundary (3) in Figure 6.7) and others without any particular preferential orientation (e.g grain boundary (4) in Figure 6.7).

This result proves that, even if the orientation of grain boundary could make its failure easier, being perpendicular to the applied local, it is not a necessary condition for grain boundary failure even at the specimen surface. Moreover, the 3D morphology of GBs in this alloy is very complex, so that the GB orientation may not be properly defined. Concerning the cracking criterion, these observations reveal that the local stress state at grain boundaries is not correlated with a particular morphology of the grain boundary but a result of mechanism coming from a larger scale involving a higher number of grains.

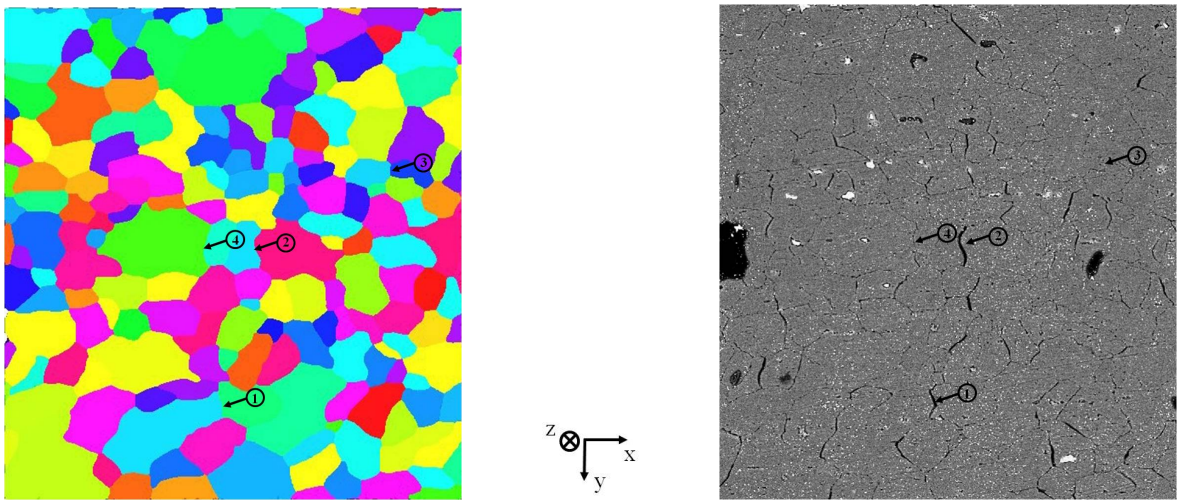

(a) (b)

Figure 6.6: (a) free surface of the recorded volume and (b) SEM micrograph After 4.5 % applied strain. Grain boundaries (1), (2), (3) and (4) are those characterised in Figure 6.7. The loading direction is horizontal.

(a) Grain boundary (1)

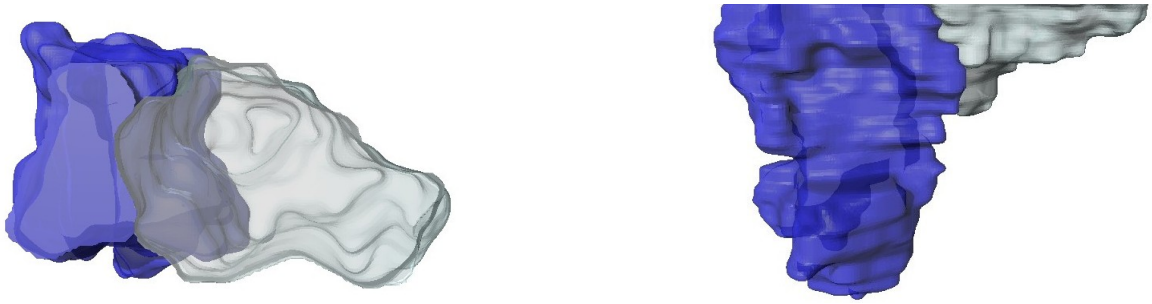

(b) Grain boundary (2)

(c) Grain boundary (3)

(d) Grain boundary (4)

Figure 6.7: 3D morphology: (a) and (b) cracked grain boundaries, (c) and (d) non cracked grain boundaries (grain boundaries (1) to (4) are identified in Figure 6.6. The loading direction: **x**.

6.4 FE Meshing Procedure

Once the 3D microstructure has been segmented, the next step in the model reconstruction is the surface generation. The surface must not have topology errors such as holes and intersections between grains. In this way, realistic high-quality meshes can be obtained in the next step. The algorithm calculates a triangular approximation of the interfaces between grains. In order to keep main topological characteristics of the 3D microtextures, the resulting surfaces have a large amount of triangles (see Figure 6.8) and the amount of triangles is only reduced in later resampling steps.

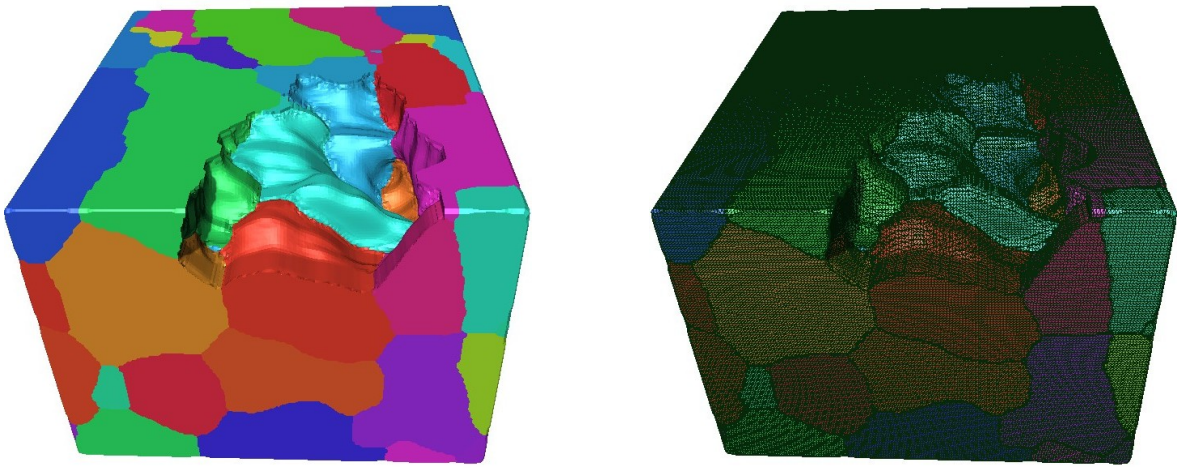

(a) (b)

Figure 6.8: (a) registered volume and (b) first surface mesh (880000 triangles). Some "surface" grains have been removed to illustrate the 3D morphology of inner boundaries.

The next step consists in improving the mesh to reduce the number of triangles and maintain the grain topological properties (see Figure 6.9(a)). In addition, the quality and the number of triangles have to be controlled so as to ensure the flexibility of the problem solution in terms of final mesh size. Triangles with bad aspect ratios (i.e long edges and low angles between vertices) have to be removed to enable for 3D mesh generation. Two algorithms of surface remeshing have been tested (Zilske et al. 2008), one based on an explicit regularisation of the triangles around a vertex which leads to triangular surfaces with high vertex regularities (i.e. a mesh for which vertices have 6 neighbours)(see Figure 6.9(b)). The second approach uses Lloyd relaxation and does not explicitly regularise the vertex connectivity. The main advantage of the latter approach is a better isotropic placement than standard remeshing techniques (see Figure 6.9(c)). Results shown in Figure 6.9 revealed that the high regularity approach introduces too many elements with bad aspect ratios compared to the more efficient "isotropic vertex placements". Therefore, the best "isotropic vertex placement" technique was chosen in the present case to generate 3D mesh in this work. Note that the edges of the corner will be recall on linear plane during 3D mesh generation.

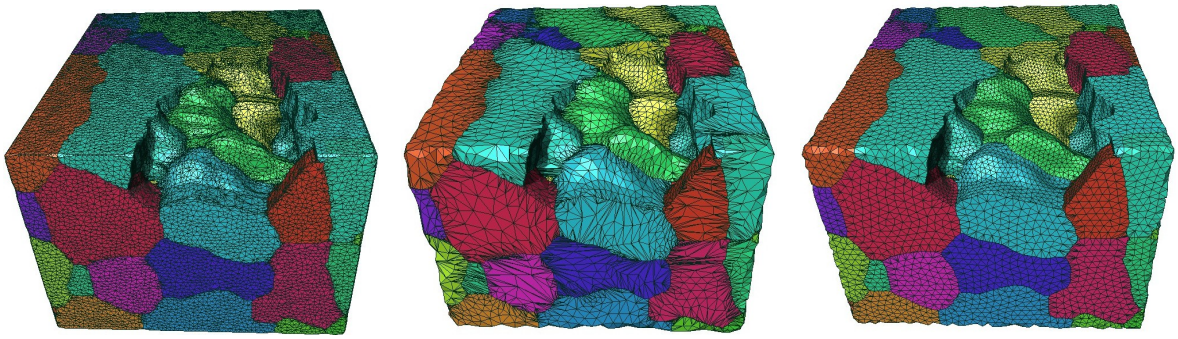

(a) (b) (c)

Figure 6.9: (a) simplified red surfaces (220.000 triangles), (b) remeshed model of (a) with high vertex regularities (72.500 triangles) and (c) remeshed model with best isotropic vertex placement (101.000 triangles). Same view as in Figure 6.8

The last step of the mesh generation in Figure 6.9 consists in the creation of procedures through volumetric tetrahedral grids suitable for 3D finite-element simulations. Again, special care is taken to generate high quality meshes. The mesh generation algorithm is a variation of the constrained Delaunay type method. A constrained tetrahedralization is a decomposition of a three-dimensional domain into a tetrahedral mesh, such that the boundary is prescribed in the faces of the mesh. The main difficulty here is to preserve the complex shape of the internal (i.e. grain) boundaries. This problem is known in literature as *boundary mesh generation* or *boundary conformity*.

The variation of constrained Delaunay type method used to generate 3D aggregate mesh is described by Si and Gärtner (2005). This algorithm extends the segment recovery algorithm proposed by Si and Gärtner (2004). The main difference with the respect to other constrained Delaunay tetrahedralization algorithms (Shewchuk 2002; 2003, Si and Gärtner 2004) is the practical workable of a strongly constrained Delaunay tetrahedralization existence condition that requires no local degeneresence in the set of vertices of the three-dimensional domain.

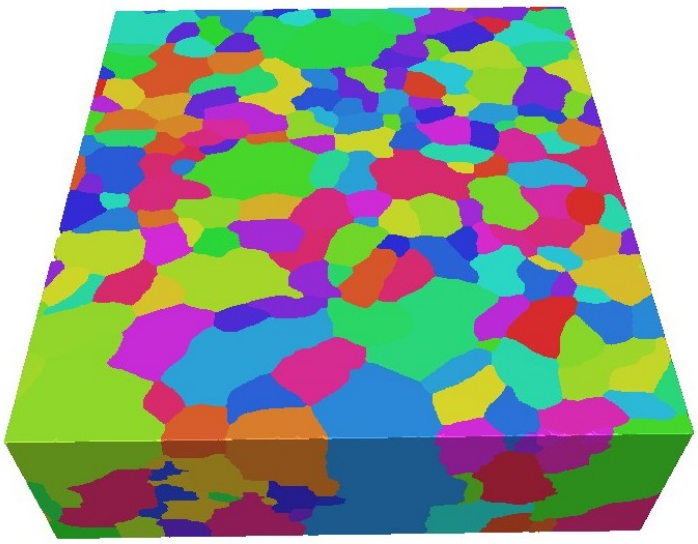

(a)

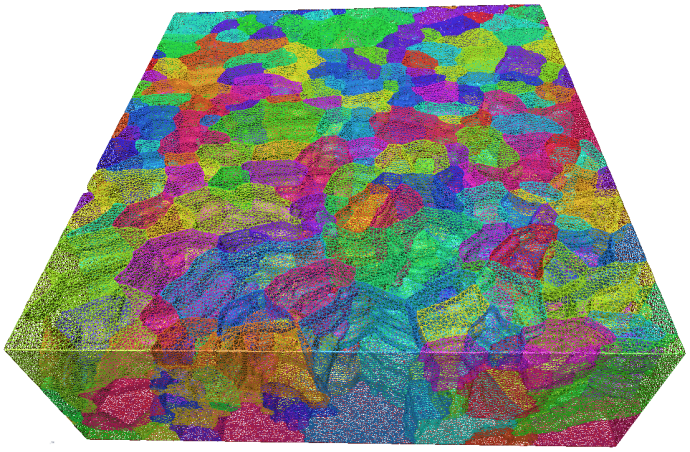

(b)

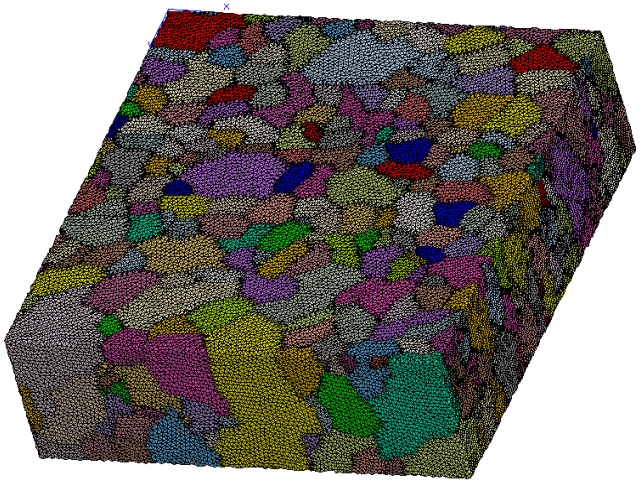

(c)

Figure 6.10: For the volume studied in Figure (3.16): (a) Recorded volume (b) surface mesh and (c) volume mesh (i.e. 8,8M elements).

6.5 Relative Accuracy of 2D Assumptions to an Elastic Approximation to Polycrystal Behaviour

An exploratory elastic analysis has been done with the actual 3D Polycrystals studied experimentally and numerically in Chapter 3 and 4. The mesh obtained with the procedure explained previously is composed by 40000 tetrahedric elements (Figure 6.11(a)). However, the crystal orientation is not assisted by computational algorithm. Boundary conditions are derived from simulations made with "the macroscopic model" on the in-situ specimen.

One can conclude that from comparison between 3D with 524 grains aggregate, 2D with 400 grains and 2D with 40 grains validaded experimentaly in Chapter (3) aggregate that despite agreement of stress and strain averages, the surface aggregate of 40 grains is not in agreement with the 3D aggregate and with the surface aggregate made of 400 grains. In order to obtain more accurate linking between 3D aggregate and surface aggregate future work is needed.

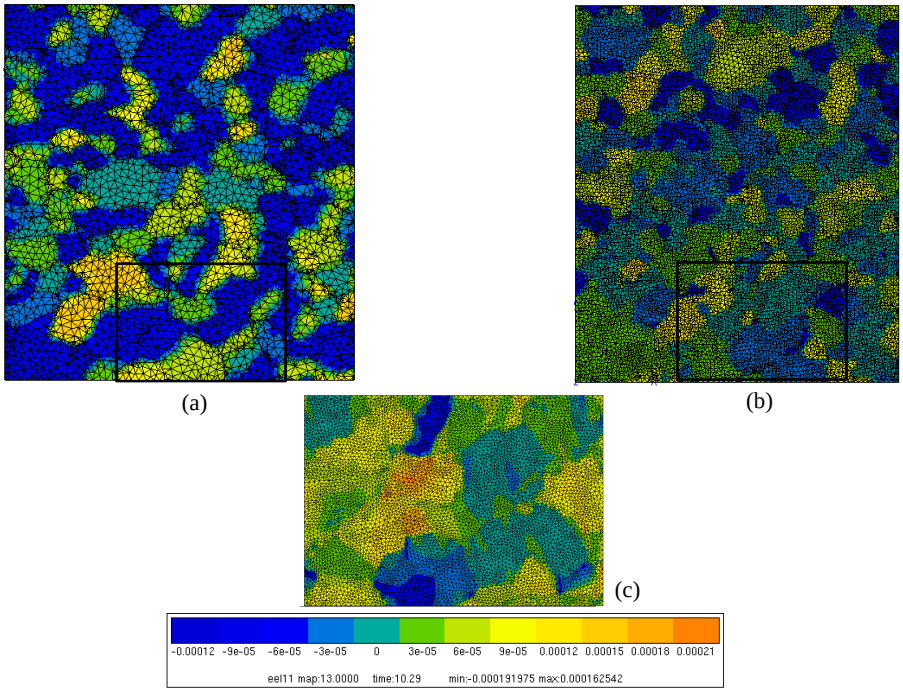

Figure 6.11: For the surface studied here: (a) top surface 3D aggregate (b) surface of 400 grains (c) surface of 40 grains

6.6 Conclusions

Despite the fact that the EBSD serial sectioning methods tend to be extremely tedious, it allows for the reconstruction of large microstructures with both the crystallographic orientation of each grain and the actual microstructural morphology. By following several key steps, volumic meshing can be generated for complex morphologies such as those of the considered aluminium alloy. Thus, numerical simulations of the actual crystal aggregate can be performed with a full description of the material behaviour (i.e. crystal plasticity), microstructure (i.e. grain shape) and microtexture (i.e. crystallographic orientation). Nevertheless, the coupling of surface EBSD analyses and microtomography enables a first description of microstructures including the crystallographic orientation of surface grains. It is, however, destructive. This method can be very useful to study the surface, important in applications such as wear.

It was found in this chapter that failed grain boundaries are not necessarily perpendicular to the loading direction. This can be due to the heterogeneous nature of the polycrystal, local tractions at purely perpendicular grain boundaries can be greater than those at boundary perpendicular to the loading axis.

Concerning the modelling of polycrystals, it was shown that small 2D aggregates loaded with experimental measured displacements where found to be in average in agreement with a full 3D model of the same aggregates. In order to obtain accurate linking between 3D aggregate and surface aggregate future work is needed to assign crystal orientation of each grains.

Résumé

Malgré le fait que l'analyse 3D de microstructure à l'aide de cartographie EBSD par coupes sériées soit très fastidieuse, cette technique reste à ce jour la référence pour la reconstruction de gros agrégats polycristallins (i.e. supérieure à une centaine de grains) pour des matériaux composés de grains présentant une taille de quelques microns.

En respectant plusieurs étapes clés, des maillages libres volumiques adéquats au calcul par élément fini ont été générés. Ainsi il devient possible de réaliser des simulations avec une description complète du matériau comprenant le comportement en plasticité cristalline, la morphologie des grains et l'orientation cristalline. Il a été également montré que le couplage d'analyses en EBSD de la surface et de microtomographie en volume permet une première description qui prend en compte la morphologie des grains et leur orientation en surface.

Il a été mis en évidence dans ce chapitre que les joints de grains rompus ne sont pas nécessairement perpendiculaires à la direction du chargement mécanique. Cela peut être du à la morphologie des polycristaux. Les surfaces des joints de grains étant très sinueuses de fortes contraintes normales peuvent apparaître localement sur des joints de grains qui ne sont pas préférentiellement orientés perpendiculairement à l'axe de traction.

Concernant les simulations sur les polycristaux en 3D, ce chapitre montre qu'il est possible de réaliser des calculs incorporant une description complète du matériau à l 'échelle microscopique. Malgré des premiers résultats de calcul encourageants, un effort devra être fait sur le type de conditions aux limites à appliquer pour permettre la validation des champs de déformations numériques comparés à ceux obtenus expérimentalement.

Chapter 7

Conclusions and Recommendations for Future Work

Contents

7.1 Conclusions

The main objective of the thesis was to study the effects of local plasticity and crack initiation at the grain scale due to hydrogen induced embrittlement in aluminium magnesium alloys. To achive that purpose, an in-situ tensile testing procedure was set up to investigate intergranular fracture due to hydrogen embrittlement at the free surface. Results obtained from a combination of in-situ tests, local EBSD analyses, strain field measurements by digital image correlation techniques have led to the following conclusions:

- In spite of the fact that many studies of intergranular brittle fracture identify local strain incompatibility as the main factor responsible for the microcrack initiation, it was found in this work that this fracture mechanism is not in agreement with our case of intergranular cracking. Relevant strain incompatibility is here rather a long range one than a short range one.

- At the specimen free surface grain boundary cracking occurs on boundaries normally oriented to the applied tensile stress when the average local axial strain is as low as 0.45%. However, these failed grain boundaries were found to be neither straight nor fully normal to the loading axis. Nevertheless, cracks were found to form always between grains that undergo very limited plastic deformation despite being embedded in large deformation bands.

- From these observations, it can be concluded that intergranular cracking due to hydrogen embrittlement in the aluminium alloy is locally triggered by high tensile grain boundary tractions.

In order to obtain a critical value of the traction needed to crack a grain boundary, a combination of in-situ 2D strain field, EBSD measurements, and finite element simulations of the observed specimen regions using crystal plasticity concepts was relied upon. From the extensive study carried out in this thesis, it was found that:

- Aggregates composed of at least 64 cubic grains with a random texture constitute a representative volume element large enough to properly describe the average behaviour of the aluminium alloy. Moreover, it was found that the solid solution strengthening effect due to magnesium can be accurately predicted through an additional function expressed in terms of the magnesium concentration in the rate-dependent flow stress at the level of each individual slip system in the single crystal model.

- The predicted deformation behaviour of small 2D polycrystal aggregates subjected to experimentally measured displacements was found to be locally in agreement with both those predicted with a full 3D model of the same aggregates and strain fields measured experimentally. In contrast, the large 2D model is not in agreement with 3D modelling since surface strain and stress fields are constrained by the bulk material substrate behaviour.

- The critical value of the local grain boundary traction obtained from an analytical Eshelby-type approach, which was based on a ”hard” inclusion embedded in a ”softer” matrix, of 175 MPa was consistent with the numerical prediction of 170±35 MPa obtained from the finite element model of the polycrystal.

Finally, to model the effects of hydrogen induced embrittlement in polycrystalline materials, the crystal-plasticity model used to describe the behaviour of each grain was coupled with a cohesive zone type model to introduce explicitly intergranular cracking into the finite element model for grain-boundary interfaces. The model accounts for the critical tractions at the grain boundaries prior to failure and a fracture energy consistent with the microductility observed on cracked grain boundary surfaces. This thesis has shown that the proposed computational framework quantitatively describes the deformation and fracture response of the polycrystalline aluminium alloy. Furthermore, the simulations reflect the major features of the experimentally measured strain fields and the dominant fracture mechanism of hydrogen induced embrittlement in aluminium-magnesium alloys.

7.2 Recommendations for Future Work

Concerning intergranular fracture modelling, additional studies need to be carried out to further validate the previous results, in particular substrat effects have to be assessed more precisely. One possibility could be to introduce a substrate in the finite element model which could be for instance the average material described by the macroscopic model and to reassess the critical grain boundary traction. Thus, the constitutive model could be able to predict multiple grain boundary cracking as observed experimentally due to load transfer thanks to the substrate. Note this type of approach was not achieved yet due to the lack of computation power.

The aluminium alloy investigated in the present study exhibits a high stacking fault energy, which prevents it from twinning during annealing. This behaviour strongly limits the possibility of increasing the intrinsic grain boundary resistance to environmentally assisted cracking through the use of grain boundary engineering. The results of this study suggests that, in such cases, grain boundary cracking sensitivity can be limited or reduced provided the in-service mechanical loading conditions are well–known. This approach, which could be referred to as ”computer-assisted texture engineering”, should enable for the tailoring of the crystallographic texture of a material so as to lower the probability of finding clusters of ”harder grains” embedded in a softer surrounding.

New opportunities for 3D materials science of polycrystalline materials at the micrometer lengthscale are and will be found in the combined use of X-ray imaging (Ludwig et al. 2009) and 3D volume correlation to study complex heterogeneous deformation and fracture phenomena. At present, constitutive models are calibrated from measured macroscopic behaviour of the material of interest. In order to increase the accuracy of crystal plasticity models, parameter calibration should be based on tools capable of comparing numerical and future experimental 3D strain fields.

Appendix A : Local Integration Algorithm

The time rate of change of the plastic deformation gradient, $\dot{\underset{\sim}{\mathbf{F}}}^p$, is defined by:

$$\dot{\underset{\sim}{\mathbf{F}}}^p = \underset{\sim}{\mathbf{L}}^p \underset{\sim}{\mathbf{F}}^p \tag{7.1}$$

Integrating the last equation, we have the following integration scheme:

$$\underset{\sim}{\mathbf{F}}^p_{n+1} = \underset{\sim}{\mathbf{F}}^p_n \exp(\underset{\sim}{\mathbf{L}}^p \Delta t) = \underset{\sim}{\mathbf{F}}^p_n \exp(\Delta\gamma^\alpha \underset{\sim}{\mathbf{N}}^\alpha_{n+1}) \tag{7.2}$$

let us consider:

$$\underset{\sim}{\mathbf{F}}^* = \underset{\sim}{\mathbf{F}}_{n+1} \underset{\sim}{\mathbf{F}}^{p-1}_n \tag{7.3}$$

and by definition:

$$\underset{\sim}{\mathbf{F}}^e_{n+1} = \underset{\sim}{\mathbf{F}}_{n+1} \underset{\sim}{\mathbf{F}}^{p-1}_{n+1} \tag{7.4}$$

we get:

$$\underset{\sim}{\mathbf{F}}^* = \underset{\sim}{\mathbf{F}}^e_{n+1} \exp(\Delta\gamma^\alpha \underset{\sim}{\mathbf{N}}^\alpha) \approx \underset{\sim}{\mathbf{F}}^e_{n+1} (\underset{\sim}{\mathbf{I}} + \Delta\gamma^\alpha \underset{\sim}{\mathbf{N}}^\alpha_{n+1}) \tag{7.5}$$

In order to write a relationship with the elastic strain, we form:

$$\underset{\sim}{\mathbf{F}}^{*T} \underset{\sim}{\mathbf{F}}^* = (\underset{\sim}{\mathbf{I}} + \Delta\gamma^\alpha \underset{\sim}{\mathbf{N}}^\alpha_{n+1})^T \underset{\sim}{\mathbf{F}}^{eT}_{n+1} \underset{\sim}{\mathbf{F}}^e_{n+1} (\underset{\sim}{\mathbf{I}} + \Delta\gamma^\alpha \underset{\sim}{\mathbf{N}}^\alpha_{n+1}) \tag{7.6}$$

development at the first order:

$$\underset{\sim}{\mathbf{F}}^{*T} \underset{\sim}{\mathbf{F}}^* = \underset{\sim}{\mathbf{F}}^{eT}_{n+1} \underset{\sim}{\mathbf{F}}^e_{n+1} + 2\Delta\gamma^\alpha (\underset{\sim}{\mathbf{N}}^\alpha_{n+1} \underset{\sim}{\mathbf{C}}^e_{n+1}) \tag{7.7}$$

Using the expression of Lagrangian strain, an equation with elastic and plastic parts is developed:

$$\underset{\sim}{\mathbf{E}}^* = \underset{\sim}{\mathbf{E}}^e_{n+1} + \Delta\gamma^\alpha (\underset{\sim}{\mathbf{N}}^\alpha_{n+1} \underset{\sim}{\mathbf{C}}^e_{n+1}) \tag{7.8}$$

For the implicit scheme, 4 internal variables: $\underset{\sim}{\mathbf{E}}^e$, γ^α, ρ^α_e, ρ^α_s. Finally, 4 residual equations for the θ -method:

$$r_E = -\underset{\sim}{\mathbf{E}}^* + \underset{\sim}{\mathbf{E}}^e_{n+1} + \sum_{\alpha=1}^{N} \Delta\gamma^\alpha (\underset{\sim}{\mathbf{N}}^\alpha_{n+1} \underset{\sim}{\mathbf{C}}^e_{n+1}) \tag{7.9}$$

$$r_{\gamma^\alpha} = \Delta\gamma^\alpha - \dot{\gamma}_0 \exp\left[-\frac{F_0}{kT} \left\{ 1 - \left\langle \frac{|\tau^\alpha_{n+1}| - S^\alpha_{n+1}}{\widehat{\tau}} \right\rangle^p \right\}^q \right] sgn(\tau^\alpha) \Delta t \tag{7.10}$$

$$r_{\rho_e^\alpha} = \Delta\rho_e^\alpha - \frac{C_e}{b^\alpha}\left[K_e\sqrt{\sum_{\beta=1}^{N}\rho_{T_{n+1}}^{\beta}} - 2d_e\rho_{e_{n+1}}^{\alpha}\right]\Delta\gamma^\alpha sgn(\tau^\alpha) \tag{7.11}$$

$$r_{\rho_s^\alpha} = \Delta\rho_s^\alpha - \frac{C_s}{b^\alpha}\left[K_s\sqrt{\sum_{\beta=1}^{N}\rho_{T_{n+1}}^{\beta}} - \rho_{s_{n+1}}^{\alpha}\left(\pi d_s^2 K_s\sqrt{\sum_{\beta=1}^{N}\rho_{T_{n+1}}^{\beta}} + 2d_s\right)\right]\Delta\gamma^\alpha sgn(\tau^\alpha) \tag{7.12}$$

The resolved shear stress is expressed as:

$$\tau^\alpha = (\underset{\sim}{\mathbf{F}}^{eT}\underset{\sim}{\mathbf{F}}^{e}\Lambda\underset{\sim}{\mathbf{E}}^{e}) : \underset{\sim}{\mathbf{N}}^{\alpha} \tag{7.13}$$

However, since the elastic stretch for metallic materials is unsignificant, we can simplify the resolved shear stress as:

$$\tau^\alpha = (\Lambda\underset{\sim}{\mathbf{E}}^{e}) : \underset{\sim}{\mathbf{N}}^{\alpha} \tag{7.14}$$

Calculation steps: Zebulon Architecture

• PreStep at the beginning of each increment :

$$\underset{\sim}{\mathbf{F}}^{*} = \underset{\sim}{\mathbf{F}}_{n+1}\underset{\sim}{\mathbf{F}}_{n}^{p-1} \tag{7.15}$$

$$\underset{\sim}{\mathbf{E}}^{*} = \frac{1}{2}(\underset{\sim}{\mathbf{F}}^{*T}\underset{\sim}{\mathbf{F}}^{*} - \underset{\sim}{\mathbf{I}}) \tag{7.16}$$

At the beginning of the step, the plastic deformation gradient is used in order to obtain the elastic strain. $\underset{\sim}{\mathbf{F}}^{p}$ needs to be conserved during the increment, it is an auxiliary variable.

• StrainPart in order to calculate Cauchy Stress and to update the auxialiary variables after convergence:

$$\underset{\sim}{\mathbf{F}}_{n+1}^{p} = \underset{\sim}{\mathbf{F}}_{n}^{p}\exp(\Delta\gamma^\alpha\underset{\sim}{\mathbf{N}}^{\alpha}) \tag{7.17}$$

$$\underset{\sim}{\mathbf{F}}_{n+1}^{e} = \underset{\sim}{\mathbf{F}}_{n+1}\underset{\sim}{\mathbf{F}}_{n+1}^{p-1} \tag{7.18}$$

$$\underset{\sim}{\mathbf{T}}_{n+1} = \Lambda : \underset{\sim}{\mathbf{E}}_{n+1}^{e} \tag{7.19}$$

$$\sigma_{n+1} = (1/J)\underset{\sim}{\mathbf{F}}_{n+1}^{e}\underset{\sim}{\mathbf{T}}_{n+1}\underset{\sim}{\mathbf{F}}_{n+1}^{eT} \tag{7.20}$$

• CalcGradF enables for the resolution by Newton's method:

First, we calculate:

$$C_{n+1}^{e} = 2\underset{\sim}{\mathbf{E}}_{n+1}^{e} + \underset{\sim}{\mathbf{I}} \tag{7.21}$$

$$\underset{\sim}{\mathbf{T}}_{n+1} = \Lambda : \underset{\sim}{\mathbf{E}}_{n+1}^{e} \tag{7.22}$$

Second, we calculate all the partial derivatives for each integration variables:
$*$ elastic strain:

$$\frac{\partial r_e}{\partial \Delta \underset{\sim}{\mathbf{E}}^e} = \underset{\approx}{\mathbf{I}} + 2\sum_{\alpha=1}^{N} \left\{ N^\alpha \underset{\approx}{\mathbf{I}} \right\} \Delta\gamma^\alpha \tag{7.23}$$

$$\frac{\partial r_e}{\partial \Delta\gamma^\alpha} = \left\{ N^\alpha C^e_{n+1} \right\} \tag{7.24}$$

$$\frac{\partial r_e}{\partial \Delta\rho^\alpha_e} = 0 \tag{7.25}$$

$$\frac{\partial r_e}{\partial \Delta\rho^\alpha_s} = 0 \tag{7.26}$$

$*$ slip:

$$\frac{\partial r_{\gamma^\alpha}}{\partial \Delta\gamma^\gamma} = \delta_{\alpha\gamma} \tag{7.27}$$

$$\begin{aligned} \frac{\partial r_{\gamma^\alpha}}{\partial \Delta \underset{\sim}{\mathbf{E}}^e_e} = & - \dot{\gamma}_0 \exp\left[- \frac{F_0}{kT} \left\{ 1 - \left\langle \frac{|\tau^\alpha_{n+1}| - S^\alpha_{n+1}}{\widehat{\tau}} \right\rangle^p \right\}^q \right] \frac{F_0 pq}{kT} \left\{ 1 - \left\langle \frac{|\tau^\alpha_{n+1}| - S^\alpha_{n+1}}{\widehat{\tau}} \right\rangle^p \right\}^{q-1} sgn(\tau^\alpha) \\ & \times \left\langle \frac{|\tau^\alpha_{n+1}| - S^\alpha_{n+1}}{\widehat{\tau}} \right\rangle^{p-1} \frac{sgn(\tau^\alpha)}{\widehat{\tau}} \frac{\partial \tau^\alpha}{\partial \Delta \underset{\sim}{\mathbf{E}}^e_{n+1}} \Delta t \end{aligned} \tag{7.28}$$

$$\begin{aligned} \frac{\partial r_{\gamma^\alpha}}{\partial \Delta\rho^\gamma_e} = & - \dot{\gamma}_0 \exp\left[- \frac{F_0}{kT} \left\{ 1 - \left\langle \frac{|\tau^\alpha_{n+1}| - S^\alpha_{n+1}}{\widehat{\tau}} \right\rangle^p \right\}^q \right] \frac{F_0 pq}{kT} \left\{ 1 - \left\langle \frac{|\tau^\alpha_{n+1}| - S^\alpha_{n+1}}{\widehat{\tau}} \right\rangle^p \right\}^{q-1} sgn(\tau^\alpha) \\ & \times \left\langle \frac{|\tau^\alpha_{n+1}| - S^\alpha_{n+1}}{\widehat{\tau}} \right\rangle^{p-1} \frac{1}{\widehat{\tau}} \frac{\partial \Delta S^\alpha_T}{\partial \Delta\rho^\gamma_e} \Delta t \end{aligned} \tag{7.29}$$

$$\begin{aligned} \frac{\partial r_{\gamma^\alpha}}{\partial \Delta\rho^\gamma_s} = & - \dot{\gamma}_0 \exp\left[- \frac{F_0}{kT} \left\{ 1 - \left\langle \frac{|\tau^\alpha_{n+1}| - S^\alpha_{n+1}}{\widehat{\tau}} \right\rangle^p \right\}^q \right] \frac{F_0 pq}{kT} \left\{ 1 - \left\langle \frac{|\tau^\alpha_{n+1}| - S^\alpha_{n+1}}{\widehat{\tau}} \right\rangle^p \right\}^{q-1} sgn(\tau^\alpha) \\ & \times \left\langle \frac{|\tau^\alpha_{n+1}| - S^\alpha_{n+1}}{\widehat{\tau}} \right\rangle^{p-1} \frac{1}{\widehat{\tau}} \frac{\partial \Delta S^\alpha_T}{\partial \Delta\rho^\gamma_s} \Delta t \end{aligned} \tag{7.30}$$

let us consider for computational integration that:

$$glis = \dot{\gamma}_0 \exp\left[- \frac{F_0}{kT} \left\{ 1 - \left\langle \frac{|\tau^\alpha_{n+1}| - S^\alpha_{n+1}}{\widehat{\tau}} \right\rangle^p \right\}^q \right] sgn(\tau^\alpha) \tag{7.31}$$

$$deriv = glis \frac{F_0 pq}{kT} \left\{ 1 - \left\langle \frac{|\tau^\alpha_{n+1}| - S^\alpha_{n+1}}{\widehat{\tau}} \right\rangle^p \right\}^{q-1} \left\langle \frac{|\tau^\alpha_{n+1}| - S^\alpha_{n+1}}{\widehat{\tau}} \right\rangle^{p-1} \Delta t \tag{7.32}$$

we get:

$$\frac{\partial r_{\gamma^\alpha}}{\partial \Delta \underset{\sim}{\mathbf{E}}^e} = -deriv \frac{sgn(\tau^\alpha)}{\widehat{\tau}} \frac{\partial \tau^\alpha}{\partial \Delta \underset{\sim}{\mathbf{E}}^e_{n+1}} \tag{7.33}$$

$$\frac{\partial r_{\gamma^\alpha}}{\partial \Delta\gamma^\gamma} = \delta_{\alpha\gamma} \tag{7.34}$$

$$\frac{\partial r_{\gamma^\alpha}}{\partial \Delta\rho_e^\gamma} = \frac{deriv}{\widehat{\tau}} \frac{\partial \Delta S_T^\alpha}{\partial \Delta\rho_e^\gamma} \tag{7.35}$$

$$\frac{\partial r_{\gamma^\alpha}}{\partial \Delta\rho_s^\gamma} = \frac{deriv}{\widehat{\tau}} \frac{\partial \Delta S_T^\alpha}{\partial \Delta\rho_s^\gamma} \tag{7.36}$$

with:

$$\frac{\partial \tau^\alpha}{\partial \Delta \underset{\sim}{\mathbf{E}}^e_{n+1}} = \Lambda \underset{\sim}{\mathbf{N}}^\alpha \tag{7.37}$$

$$\frac{\partial \Delta S_T^\alpha}{\partial \Delta\rho_e^\gamma} = \frac{\lambda\mu b h^{\alpha\gamma}}{2\sqrt{\sum_{\beta=1}^N h^{\alpha\beta}(\rho^\beta_{e_{n+1}} + \rho^\beta_{s_{n+1}})}} \tag{7.38}$$

$$\frac{\partial \Delta S_T^\alpha}{\partial \Delta\rho_s^\gamma} = \frac{\lambda\mu b h^{\alpha\gamma}}{2\sqrt{\sum_{\beta=1}^N h^{\alpha\beta}(\rho^\beta_{e_{n+1}} + \rho^\beta_{s_{n+1}})}} \tag{7.39}$$

$*$ edge dislocation density:

$$\frac{\partial r_{\rho_e^\alpha}}{\partial \Delta \underset{\sim}{\mathbf{E}}^e} = 0 \tag{7.40}$$

$$\frac{\partial r_{\rho_e^\alpha}}{\partial \Delta\gamma^\gamma} = -\frac{C_e}{b^\alpha}\left[K_e\sqrt{\sum_{\beta=1}^N \rho^\beta_{T_{n+1}}} - 2d_e\rho^\alpha_{e_{n+1}}\right]\delta_{\alpha\gamma} sgn(\tau^\alpha) \tag{7.41}$$

$$\frac{\partial r_{\rho_e^\alpha}}{\partial \Delta\rho_e^\gamma} = -\frac{C_e K_e}{b^\alpha}\frac{\Delta\gamma^\alpha sgn(\tau^\alpha)}{2\sqrt{\sum_{\beta=1}^N \rho^\beta_{T_{n+1}}}} + \left(1 + \frac{2C_e d_e}{b^\alpha}\Delta\gamma^\alpha sgn(\tau^\alpha)\right)\delta_{\alpha\gamma} \tag{7.42}$$

$$\frac{\partial r_{\rho_e^\alpha}}{\partial \Delta\rho_s^\gamma} = -\frac{C_e K_e}{b^\alpha}\frac{\Delta\gamma^\alpha sgn(\tau^\alpha)}{2\sqrt{\sum_{\beta=1}^N \rho^\beta_{T_{n+1}}}} \tag{7.43}$$

$*$ screw dislocation density:

$$\frac{\partial r_{\rho_s^\alpha}}{\partial \Delta \underset{\sim}{\mathbf{E}}^e} = 0 \tag{7.44}$$

$$\frac{\partial r_{\rho_s^\alpha}}{\partial \Delta\gamma^\gamma} = -\frac{C_s}{b^\alpha}\left[K_s\sqrt{\sum_{\beta=1}^N \rho^\beta_{T_{n+1}}} - \rho^\alpha_{s_{n+1}}(\pi d_s^2 K_s\sqrt{\sum_{\beta=1}^N \rho^\beta_{T_{n+1}}} + 2d_s\right]\delta_{\alpha\gamma} sgn(\tau^\alpha) \tag{7.45}$$

$$\frac{\partial r_{\rho_s^\alpha}}{\partial \Delta\rho_e^\gamma} = -\frac{C_s}{b^\alpha}\left[\frac{K_s}{2\sqrt{\sum_{\beta=1}^N \rho^\beta_{T_{n+1}}}} - \rho_s^\alpha\frac{\pi d_s^2 K_s}{2\sqrt{\sum_{\beta=1}^N \rho^\beta_{T_{n+1}}}}\right]\Delta\gamma^\alpha sgn(\tau^\alpha) \tag{7.46}$$

$$\frac{\partial r_{\rho_s^\alpha}}{\partial \Delta \rho_s^\gamma} = -\frac{C_s}{b^\alpha}\left[\frac{K_s}{2\sqrt{\sum_{\beta=1}^{N}\rho_{T_{n+1}}^{\beta}}} - \rho_{s_{n+1}}^{\alpha}\frac{\pi d_s^2 K_s}{2\sqrt{\sum_{\beta=1}^{N}\rho_{T_{n+1}}^{\beta}}}\right]\Delta\gamma^\alpha sign(\tau^\alpha) + \left[1 + \frac{C_s}{b^\alpha}\left(\pi d_s^2 K_s\sqrt{\sum_{\beta=1}^{N}\rho_{T_{n+1}}^{\beta}} + 2d_s\right)\Delta\gamma^\alpha sign(\tau^\alpha)\right]\delta_{\alpha\gamma} \tag{7.47}$$

References

Abbas S. and Fries T.P. (2010). *A unified enrichment scheme for fracture problems.* In : IOP Conference Series: Materials Science and Engineering, vol. 10, pp 12–45. IOP Publishing.

Abrivard A. (2009). *A Coupled Crystal Plasticity - Phase Field Formulation To Describe Microstructural Evolution In Polycrystalline Aggregates During Recrystallisation.* PhD thesis, École Nationale Supérieure des Mines de Paris.

Acharya A., Bassani J.L., and Beaudoin A. (2003). *Geometrically necessary dislocations, hardening, and a simple gradient theory of crystal plasticity.* Scripta Materialia, vol. 48 n° 2, pp 167–172.

Acharya A. and Beaudoin A.J. (2000). *Grain-size effect in viscoplastic polycrystals at moderate strains.* Journal of the Mechanics and Physics of Solids, vol. 48 n° 10, pp 2213–2230.

Adams B.L. (1993). *Orientation imaging microscopy: application to the measurement of grain boundary structure.* Materials Science and Engineering A, vol. 166, pp 59–66.

Arsenlis A. and Parks D.M. (1999). *Crystallographic aspects of geometrically–necessary and statistically–stored dislocation density.* Acta Materialia, vol. 47 n° 5, pp 1597–1611.

Arsenlis A. and Parks D.M. (2002). *Modeling the evolution of crystallographic dislocation density in crystal plasticity.* Journal of the Mechanics and Physics of Solids, vol. 50 n° 9, pp 1979–2009.

Asaro R. J. and Rice J. R. (1977). *Strain localization in ductile single crystals.* Journal of the Mechanics and Physics of Solids, vol. 25 n° 5, pp 309–338.

Ashby M.F. (1970). *The deformation of plastically non-homogeneous materials.* Philosophical Magazine, vol. 21, pp 399–424.

Attix F.H.R. and Roesch W.C. (1968). *Radiation Dosimetry.* Academic Press.

Attouch H. (1996). *Viscosity solutions of minimization problems.* SIAM Journal on Optimization, vol. 6, pp 769.

Balasubramanian S. and Anand L. (2002). *Elasto-viscoplastic constitutive equations for polycrystalline fcc materials at low homologous temperatures.* Journal of the Mechanics and Physics of Solids, vol. 50 n° 1, pp 101–126.

Barbe F., Decker L., Jeulin D., and Cailletaud G. (2001a). *Intergranular and intragranular behavior of polycrystalline aggregates. Part I: FE model.* International Journal of Plasticity, vol. 17 n° 4, pp 513–536.

Barbe F., Forest S., and Cailletaud G. (2001b). *Intergranular and intragranular behavior of polycrystalline aggregates. Part II: Results.* International Journal of Plasticity, vol. 17 n° 4, pp 537–566.

Barbe F., Quey R., Musienko A., and Cailletaud G. (2009). *Three-dimensional characterization of strain localization bands in high-resolution elastoplastic polycrystals.* Mechanics Research Communications, vol. 36 n° 7, pp 762–768.

Barenblatt G.I. (1962). *The mathematical theory of equilibrium cracks in brittle fracture.* Advances in applied mechanics, vol. 7, pp 55–129.

Barnes A.J. (1994). . Material Science Forum, vol. 701, pp 170–172.

Baruchel J., Buffière J.-Y., Maire E., Merle P., and Peix G. (2000). *X-ray Tomography in Material Science.* Hermès.

Bassani J.L. (1990). *Single Crystal Hardening.* Adv. Applied Mech., vol. 45, pp 320.

Beachem C. D. (1976). *Hydrogen Damage.* ASM International.

Belytschko T. and Black T. (1999). . International Journal for Numerical Methods in Engineering, vol. 45, pp 601–620.

Ben Ali N., Tanguy D., and Estevez R. (2011). *Effects of microstructure on hydrogen-induced cracking in aluminum alloys.* Scripta Materialia, vol. 65, pp 210–213.

Beremin F. M. (1981). *Cavity formation from inclusions in ductile fracture of A508 steel.* Metallurgical and Materials Transactions A, vol. 12 n° 5, pp 723–731.

Bergonnier S., Hild F., and Roux S. (2005). *Digital image correlation used for machanical tests on crimped glass wool samples.* Journal of Strain Analysis for Engineering Design, vol. 40 n° 2, pp 185–197.

Besnard G., Hild F., and S. Roux (2006). *Finite-Element Displacement Fields Analysis from Digital Images: Application to Portevin Le Chatelier Bands.* Experimental Mechanics, vol. 46, pp 789–803.

Besson J., Cailletaud G., Chaboche J.L., and Forest S. (2001). *Mécanique non linéaire des matériaux.* Hermès.

Birnbaum HK (1994). *Hydrogen effects on deformation relation between dislocation behavior and the macroscopic stress–strain behavior.* Scripta Metallurgica et Materialia, vol. 31 n° 2.

Birnbaum H.K and Sofronis P. (1994). *Hydrogen-enhanced localized plasticity–a mechanism for hydrogen-related fracture.* Materials Science and Engineering: A, vol. 176 n° 1-2, pp 191–202.

Bornert B., Bretheau T., and Gilormini P. (2001). *Homogénéisation en mécanique des matériaux, volumes 1 et 2.* Hermes Sciences Publications.

Bruck H.A., McNeill S.R., Sutton M.A., and Peters W.H. (1989). *Digital image correlation using Newton–Raphson method of partial differential corrections.* Exp. Mech., vol. 29, pp 261–267.

Bunge H.J. and Morris P.R. (1982). *Texture analysis in materials science: mathematical methods.* Butterworths London.

Burgers J.M. (1939). *Some considerations on the fields of stress connected with dislocation in a regular crystal lattice I.* Proceedings of the Koninklijke Nederlandse Akad. Wetenschappen, vol. 42 n° A, pp 293–325.

Busso E.P. (1990). *Cyclic deformation of monocrystalline nickel aluminide and high temperature coatings.* PhD thesis, MIT.

Busso E.P. and Cheong K.S. (2001). *Length Scale Effects on the Macroscopic Behaviour of Single and Polycrystalline FCC Materials.* Journal de Physique IV, vol. 11, pp 161–170.

Busso E.P. and Cheong K.S. (2005). *A study of microstructural length scale effects on the behaviour of FCC polycrystals using strain gradient concepts.* International Journal of Plasticity, vol. 21 n° 9, pp 1797–1814.

Busso E.P. and McClintock F.A. (1994). *Mechanisms of cyclic deformation of NiAl single crystals at high temperatures.* Acta Metallurgica et Materialia, vol. 42 n° 10, pp 3263–3275.

Busso E. P., Liu Y.P., McClintock F. A., and Allen S.M. (1992). *Stable Configurations of Dislocations in Homogenized Nickel-Aluminide Single Crystals* . Philosophical Magazine A, vol. 66, pp 1065–1080.

Busso E. P. and McClintock F. A. (1996). *A dislocation mechanics-based crystallographic model of a B2-type intermetallic alloy.* International Journal of Plasticity, vol. 12 n° 1, pp 1–28.

Busso E. P., Meissonnier F. T., and O'Dowd N. P. (2000). *Gradient-dependent deformation of two-phase single crystals.* Journal of the Mechanics and Physics of Solids, vol. 48 n° 11, pp 2333–2361.

Cailletaud G. (1988). *Micromechanical approach of polycrystalline behavior.* Revue de Physique Appliquée, vol. 23 n° 4, pp 353–365.

Cailletaud G. (1992). *A micromechanical approach to inelastic behaviour of metals.* International Journal of Plasticity, vol. 8, pp 55–73.

Caron D. (2000). *Influence de l'hydrogène sur la vitesse de propagation des fissures de corrosion sous containte dans l'alliage 600 en milieu primaire des réacteurs nucléaire à eau sous pression.* PhD thesis, Institut National des Sciences Appliquées de Lyon.

Chaboche J.L. (1988a). *Continuum damage mechanics. I: General concepts.* Journal of applied mechanics, vol. 55 n° 1, pp 59–64.

Chaboche J.L. (1988b). *Continuum damage mechanics: Part II–Damage growth, crack initiation, and crack growth.* Journal of Applied Mechanics, vol. 55, pp 65.

Chaboche JL, Feyel F., and Monerie Y. (2001). *Interface debonding models: a viscous regularization with a limited rate dependency.* International journal of solids and structures, vol. 38 n° 18, pp 3127–3160.

Chandra N., Li H., Shet C., and Ghonem H. (2002). *Some issues in the application of cohesive zone models for metals–ceramic interfaces.* International Journal of Solids and Structures, vol. 39, pp 2827–2855.

Chastel Y. (2010). *Lecture: Mechanismes physiques de la déformation.* Mines ParisTech.

Cheong K.S. and Busso E.P. (2004). *Discrete Dislocation Density Modelling of Single Crystal FCC Polycrystals.* Acta Materialia, vol. 52, pp 5665–5675.

Cheong K.S. and Busso E.P. (2006). *Effects of Lattice Misorientations on Strain Heterogeneities in FCC Polycrystals.* Journal of the Mechanics and Physics of Solids, vol. 54, pp 671–689.

Crussard C. (1950). *Métaux et Corrosion.* book, vol. 25, pp 203.

Cuitifio A.M. and Ortiz M. (1992). *Computational Modelling of Single Crystals.* Modelling Simul. Mater. Sci. Eng., vol. 1, pp 225.

Cuitifio A.M. and Ortiz M. (1993). *Constitutive Modelling of $L1_2$ Intermetallic Crystals.* Mater. Sci. Eng. A, vol. 170, pp 111.

Dai H. and Parks D. (1997). *Geometrically-necessary dislocation density and scaledependent crystal plasticity.* In : Proceedings of Plasticity '97, vol. 1, pp 17–18.

Devincre B., Hoc T., and Kubin L.P. (2005). *Collinear interactions of dislocations and slip systems.* Materials Science and Engineering A, vol. 400, pp 182–185.

Diard O., Leclercq S., Rousselier G., and Cailletaud G. (2002). *Distribution of normal stress at grain boundaries in multicrystals: application to an intergranular damage modeling.* Computational Materials Science, vol. 25 n° 1-2, pp 73–84.

Dillard T., N'Guyen F., Forest S., Bienvenu Y., Bartout J.-D., Salvo L., Dendievel R., Maire E., and Cloetens P. (2004). *In-situ observation of tensile deformation of open–cell nickel foams by means of X–ray microtomography.* Philosophical Magazine, vol. 85, pp 2147–2175.

Dix E.H. (1940). *Acceleration of the rate of corrosion by high constant stresses.* Transactions American Institute of Mining and Metallurgical Engineers, vol. 137, pp 11–40.

Doumalin P., Bornert M., and Crépin J. (2003). *Caractérisation de la répartition de la déformation dans les matériaux hétérogènes.* Mécanique & Industries, vol. 4 n° 6, pp 607–617.

Dugdale D.S. (1960). *Yielding of steel sheets containing slits.* Journal of the Mechanics and Physics of Solids, vol. 8 n° 2, pp 100–104.

El-Houdaigui F., Ben Ali N., Estevez R., and Tanguy D. (2009). *Cohesive zone model for hydrogen embrittlement of grain boundaries in Al 5XXX alloys.* In : Proceedings of the International Hydrogen Conference.

El-Houdaigui F., Benali N., Estevez R., and Tanguy D. (2011). *Cohesive zone model for hydrogen embrittlement of grain boundaries in Al 5xxx alloys.* Proceedings of the 2008 International Hydrogen Conference, vol. 1, pp 604–612.

Evans U.R. (1948). *An Introduction to Metallic Corrosion.* Faraday Society.

Evers L.P., Parks D.M., Brekelmans W.A.M., and Geers M.G.D. (2002). *Crystal plasticity model with enhanced hardening by geometrically necessary dislocation accumulation.* Journal of the Mechanics and Physics of Solids, vol. 50 n° 11, pp 2403–2424.

Fahrat C. and Roux F.-X. (1991). *A Method of Finite Element Tearing and Interconnecting and its Parallel Solution Algorithm.* Int. J. Numer. Meth. Engng, vol. 32, pp 1205–1227.

Feyel F. (1998). *Application du calcul parallèle aux modèles á grand nombre de variables internes.* PhD thesis, École Nationale Supérieure des Mines de Paris.

Forest S., Boubidi P., and Sievert R. (2001). *Strain localization patterns at a crack tip in generalized single crystal plasticity.* Scripta Materialia, vol. 44 n° 6, pp 953–958.

Forquin P., Rota L., Charles Y., and Hild F. (2004). *A method to determine the toughness scatter of brittle materials.* Int. J. Fract., vol. 125, pp 171–187.

Franciosi P., Berveiller M., and Zaoui A. (1980). *Latent hardening in copper and aluminium single crystals.* Acta Metallurgica, vol. 28, pp 273–283.

Frankel J. (1926). *Zur theorie der elastizitätsgrenze und der festigkeit kristallinischer körper.* Zeitschrift fur Physik, vol. 37, pp 572–609.

Friedel J. (1965a). *Dislocations pp 360.* Pergamon Gauthier Villars London.

Friedel J. (1965b). *Dislocations pp 362.* Pergamon Gauthier Villars London.

Frost H.J. and Ashby M.F. (1982). *Deformation-mechanism maps.* Pergamon Press.

Gest R. J. and Troiano A. R. (1974). *Stress corrosion and hydrogen embrittlement in an aluminum alloy.* Corrosion-Nace, vol. 30, pp 274–279.

Gitman I.M., Askes H., and Sluys L.J. (2007). *Representative volume : Existence and size determination.* Engineering Fracture Mechanics, vol. 74, pp 2518–2534.

Gourgues A.F. (2002). *Electron backscatter diffraction and cracking.* Materials Science and Technology, vol. 18 n° 2, pp 119–133.

Gruhl W. (1984). *Stress corrosion cracking of high strengh aluminum alloys.* Z. Metallkde, vol. 75, pp 819.

Hall E.0. (1951). *The deformation and ageing of mild steel.* Proceedings of the Physical Society, vol. 64, pp 747–753.

Hansen N. (1977). *Effect of grain–size and strain on tensile flow–stress of aluminium at room–temperature.* Acta Metallurgica, vol. 25 n° 8, pp 863–869.

Harder J. (1934). *Gitterstorung die einem kristall plastisch machen konnte.* Zeitschrift fur Physik, vol. 89, pp 660–664.

Hefti L. (2007). *Commercial Airplane Applications of Superplastically Formed AA5083 Aluminum Sheet.* Journal of Materials Engineering and Performance, vol. 16 n° 2, pp 136–141.

Hild F., Raka B., Baudequin M., Roux S., and Cantelaube F. (2002). *Multiscale displacement field measurements of compressed mineral–wool samples by digital image correlation.* Applied optics, vol. 41 n° 32, pp 6815–6828.

Hill R. (1965). *Continuum Micro–Mechanisms of Elastoplastic Polycrystals.* JMPS, vol. 13, pp 89–101.

Hillerborg A., Modéer M., and Petersson P.E. (1976). *Analysis of crack formation and crack growth in concrete by means of fracture mechanics and finite elements.* Cem Concr Res, vol. 6, pp 773–82.

Hirth J.P. (1972). *The influence of grain boundaries on mechanical properties.* Metallurgical and Materials Transactions B, vol. 3 n° 12, pp 3047–3067.

Hollinsworth E. H. and Hunsicker H.Y. (1987). *Metals Handbook.* ASM, Metals Park OH, vol. 13, pp 581–609.

Honeycombe R.W.K (1968). *The plastic deformation of metals.* Edward Arnold Publishers Ltd.

Hosford Jr., Fleischer R.L., and Backofen W.A. (1960). *Tensile deformation of aluminum single crystals at low temperatures.* Acta Metallurgica, vol. 8, pp 187–199.

Johnson W. H. (1875). *Hydrogen.* Proceedings of the Royal Society, vol. 23 n° 1, pp 168.

Jones R.H., Baer D.R., Danielson M.J., and Vetrano J.S. (2001). *Role of Mg in the stress corrosion cracking of an Al–Mg alloy.* Metallurgical and Materials Transactions A, vol. 32, pp 1699–1711.

Jones R.H. and Danielson M.J. (2003). *Role of Hydrogen in Stress Corrosion Cracking of Low Strength Al–Mg alloys.* Corrosion/2003, NACE, Houston, TX, vol. , pp Paper 03513.

Jones R. H., Gertsman V. Y., Vetrano J. S., and Windisch C. F. (2004). *Crack-particle interactions during intergranular stress corrosion of AA5083 as observed by cross-section transmission electron microscopy.* Scripta Materialia, vol. 50, pp 1355–1359.

Jordan H.J., Shi S., and K.P. Walker (1993). *The Viscoplastic Behaviour of Hastelloy–X Single Crystal.* Int. J. Plast., vol. 9, pp 119.

Kachanov L. (1958). *Rupture Time Under Creep Conditions.* International Journal of Fracture, vol. 97, pp 11–18. 10.1023/A:1018671022008.

Kanit T., Forest S., Galliet I., Mounoury V., and Jeulin D. (2003). *Determination of the size of the representative volume element for random composites: statistical and numerical approach.* International Journal of Solids and Structures, vol. 40, pp 3647–3679.

Kocks U.F. (1977). *The theory of an obstacle-controlled yield strength-Report after an international workshop.* Materials Science and Engineering, vol. 27, pp 291–298.

Kocks U.F. and Brown T.J. (1966). *Latent hardening in aluminum.* Acta Metallurgica, vol. 14, pp 87–98.

Kumar A.V. and Yang C.H. (1999). *Study of work hardening models for single crystals using three dimensional finite element analysis.* International Journal of Plasticity, vol. 15 n° 7, pp 737–754.

Kuntz M., Jolin M., Bastien J., Perez F., and Hild F. (2006). *Digital image correlation analysis of crack behavior in a reinforced concrete beam during a load test.* Canadian Journal of Civil Engineering, vol. , pp 1418–1425.

Lemaitre J. (1985). *A continuous damage mechanics model for ductile fracture.* Journal of Engineering Materials and Technology, vol. 107, pp 83.

Lemaitre J. (1996). *A Course of Damage Mechanics.* Springer Verlag.

Li X. (2000). *Spatial Characterization of Unstable Plastic Flows in Two Aluminum Alloys.* Ph.D. Thesis., vol. .

Lu Gang and Kaxiras Efthimios (2005). *Hydrogen Embrittlement of Aluminum: The Crucial Role of Vacancies.* Physical Review Letters, vol. 94 n° 15, pp 155501.

Lu Gang, Orlikowski Daniel, Park Ickjin, Politano Olivier, and Kaxiras Efthimios (2002). *Energetics of hydrogen impurities in aluminum and their effect on mechanical properties.* Physical Review B, vol. 65 n° 6, pp 064102.

Lu Gang, Zhang Qing, Kioussis Nicholas, and Kaxiras Efthimios (2001). *Hydrogen-Enhanced Local Plasticity in Aluminum: An Ab Initio Study.* Physical Review Letters, vol. 87 n° 9, pp 095501.

Ludwig W., King A., Reischig P., Herbig M., Lauridsen EM, Schmidt S., Proudhon H., Forest S., Cloetens P., Roscoat S., et al. (2009). *New opportunities for 3D materials science of polycrystalline materials at the micrometer lengthscale by combined use of X-ray diffraction and X-ray imaging.* Materials Science and Engineering: A, vol. 524 n° 1-2, pp 69–76.

Lyman T. (1972). *Metals handbook: Atlas of microstructures of industrial alloys*, vol. 7. American Society for Metals.

Ma A. and Roters F. (2004). *A constitutive model for fcc single crystals based on dislocation densities and its application to uniaxial compression of aluminium single crystals.* Acta Materialia, vol. 52 n° 12, pp 3603–3612.

Mackenzie J. K. (1958). *Second Paper on Statistics Associated with the Random Disorientation of Cubes.* Biometrika, vol. 45, pp 229–240.

Madec R., Devincre B., Kubin L., Hoc T., and Rodney D. (2003). *The role of collinear interaction in dislocation-induced hardening.* Science, vol. 301 n° 5641, pp 1879.

Mader S. (1957). *Elektronmikroskopische Untersuchung der Gleitlinienbildung auf Kupfereinkristallen.* Z. Phys., vol. 149, pp 73–102.

Maeng D.Y., Lee J.H., Kim T.S., Son H.T., Hong S.J., Won C.W., Cho S.S., and Chun B.S. (2001). *The mechanical properties and microstructure of Al composite bar manufactured by using stone mill crushed rapidly solidified Al-Al2O3-TiC.* Materials Science and Engineering, vol. 304, pp 564–568.

Magnin T., Chambreuil A., and Bayle B. (1996). *The corrosion-enhanced plasticity model for stress corrosion cracking in ductile fcc alloys.* Acta Materialia, vol. 44 n° 4, pp 1457–1470.

Malis T. and Chaturvedi M.C. (1982). *Grain–boundary segregation in an Al–8 wt % Mg alloy.* Journal of Materials Science, vol. 17, pp 1479–1486.

Mandel J. (1973). *Equations constitutives et directeurs dans les milieux plastiques et viscoplastiques.* IJSS, vol. 9, pp 725–740.

Masayuki K., Yoshihiro K., and Takayuki K. (2007). *Three–dimensional local stress analysis on grain boundaries in polycrystalline material* . International Journal of Solids and Structures, vol. 44 n° 10, pp 3267–3277.

McNeill S.R., Peters W.H., and Sutton M.A. (1987). *Estimation of stress intensity factor by digital image correlation.* Eng. Fract. Mech., vol. 28.

Meissonnier F. T., Busso E. P., and O'Dowd N. P. (2001). *Finite element implementation of a generalised non-local rate-dependent crystallographic formulation for finite strains.* International journal of plasticity, vol. 17 n° 4, pp 601–640.

Melenk J.M. and Babuska I. (1996). *The partition of unity finite element method: basic theory and applications.* Computer methods in applied mechanics and engineering, vol. 139 n° 1-4, pp 289–314.

Meric L., Poubanne P., and Cailletaud G. (1991). *Single Crystal Modelling for Structural Calculations: Part 1 – Model Presentation.* J. Eng. Mat. Tech., vol. 113, pp 162.

Meschke G. and Dumstorff P. (2007). *Energy-based modeling of cohesive and cohesionless cracks via X-FEM.* Computer methods in applied mechanics and engineering, vol. 196 n° 21-24, pp 2338–2357.

Mika D.P. and Dawson P.R. (1998). *Effects of grain interaction on deformation in polycrystals.* Materials Science and Engineering A, vol. 257, pp 62–76.

Moës N. and Belytschko T. (2002). *Extended finite element method for cohesive crack growth.* Engineering Fracture Mechanics, vol. 69, pp 813–833.

Moës N., Dolbow J., and Belytschko T. (1999). . International Journal for Numerical Methods in Engineering, vol. 46, pp 131–150.

Musienko A. and Cailletaud G. (2009). *Simulation of inter- and transgranular crack propagation in polycrystalline aggregates due to stress corrosion cracking.* Acta Materialia, vol. 57 n° 13, pp 3840–3855.

Nabarro F. R. N. (1947). *Dislocations in a simple cubic lattice.* Proceedings of the Physical Society, vol. 59, pp 256.

Nakamachi E., Tam N.N., and Morimoto H. (2007). *Multi-scale finite element analyses of sheet metals by using SEM-EBSD measured crystallographic RVE models.* International Journal of Plasticity, vol. 23, pp 450–489.

Needleman A. (1987). *A continuum model for void nucleation by inclusion debonding.* Journal of Applied Mechanics, vol. 54, pp 525.

Nye J. (1953). *Some geometrical relations in dislocated crystals.* Acta Metallurgica, vol. 1, pp 153–162.

Ohnishi T. and Higashi K. (1981). *Aluminium.* Aluminium, vol. 8 n° 5, pp 558–590.

Orowan E. (1934). *Zur kristallplastizitat III. uber den mechanismus des gleitvorganges.* Zeitschrift fur Physik, vol. 89, pp 634–659.

Orowan E. (1940). *Problems of plastic gliding.* Proceedings of the Physical Society, vol. A 52, pp 8–22.

Peierls R. (1940). *The size of a dislocation.* Proceedings of the Physical Society, vol. 52, pp 34.

Peirce D., Asaro R.J., and Needleman A. (1983). *Material Rate Dependence and Localized Deformation of Crystalline Solids.* Acta Metallurgica, vol. 31, pp 1951.

Pérez-Prado MT, González-Doncel G., Ruano OA, and McNelley TR (2001). *Texture analysis of the transition from slip to grain boundary sliding in a discontinuously recrystallized superplastic aluminum alloy.* Acta materialia, vol. 49 n° 12, pp 2259–2268.

Petch N.J. (1953). *The cleavage strength of polycrystals.* J. Iron and Steel Inst., vol. 174, pp 25–28.

Pineau A. and François D. (2001). *Fracture of metals. Part II: ductile fracture. In: Physical Aspects of Fracture.* (Edited by Bouchaud, E., Jeulin, D., Prioul, C. and Roux, S.) Kluwer, Dordrecht.

Rastogi P.K. (2000). *Photomechanics.* Springer.

Rebstock H. (1957). *Kombinierte Zug-und Torsionsverformung von Kupbfer-Einkristallrohen.* Z. Metallk., vol. 48, pp 206–220.

Remmers J.J.C, de Borst R., and Needleman A. (2003). *A cohesive segments method for the simulation of crack growth.* Computational Mechanics, vol. 31, pp 69–77.

Ren Z.Y. and Q.S. Zheng (2002). *A Quantitative study of minimum sizes of representative volume elements of cubic polycrystals-numerical experiments.* Journal of the Mechanics and Physics of Solids, vol. 50, pp 881–893.

Réthoré J., Morestin F., and Gravouil A. (2005). *Estimation of mixed-mode stress intensity factors using digital image correlation and an interaction integral.* Int. J. Fract., vol. 132, pp 65–79.

Rice J.R. (1980). *The mechanics of earthquake rupture.* In : Proceedings of International School of Physics Enrico Fermi. In: Dziewonski AM, Boschi E, editors. Physics of the Earth's Interior, pp 555–649.

Rios R., Magnin T., Noel D., and de Bouvier O. (1995). *Critical analysis of Alloy 600 stress corrosion cracking mechanisms in primary water.* Metallurgical and Material Transactions: A, vol. 26A, pp 925–939.

Roters F., Raabe D., and Gottstein G. (2000). *Work hardening in heterogeneous alloys – A microstructural approach based on three internal state variables.* Acta Materialia, vol. 48 n° 17, pp 4181–4189.

Roux S. and Hild F. (2006). *Stress intensity factor measurements from digital image correlation: post-processing and integrated approaches.* Int J Fract, vol. .

Rozenak P., Sirois E., Ladna B., Birnbaum H.K., and Spooner S. (2005). *Characterization of hydrogen defects forming during chemical charging in the aluminum.* Journal of Alloys and Compounds, vol. 387 n° 1–2, pp 201–210.

Rupil J., Roux S., Hild F., and Vincent L. (2011). *Fatigue microcrack detection with digital image correlation.* The Journal of Strain Analysis for Engineering Design, vol. 46 n° 6, pp 492–509.

Saada G. (1968). *Limite élastique et durcissement dessolutions solides.* Pont à Mousson, vol. 16, pp 255–269.

Scamans G. M. (1978). *Hydrogen bubbles in embrittled Al-Zn-Mg alloys.* Journal of Materials Science, vol. 13, pp 27–36.

Scamans G. M., Alani R., and Swann P. R. (1976). *Pre–exposure embrittlement and stress corrosion failure in Al–Zn–Mg Alloys.* Corrosion Science, vol. 16, pp 443–459.

Schreier H.W., Braasch J.R., Sutton M.A., Roux S., and Cantelaube F (2000). *Systematic errors in digital image correlation caused by intensity interpolation.* Opt Eng, vol. 39 n° 11, pp 2915–2921.

Schroeter B.M. and McDowell D.L. (2003). *Measurement of deformation fields in polycrystalline OFHC copper.* International Journal of Plasticity, vol. 19 n° 9, pp 1355–1376.

Schroth J.G., Taleff E.M., Friedman P.A., Krajewski P.E., and Mishra R.S. (2004). *Advances in Superplasticity and Superplastic Forming.* J.G. Schroth (Eds.), vol. 1, pp 9.

Schwartz A.J., Kumar M., and Adams B.L. (2000). *Electron Backscatter Diffraction in Material Science.* Kluwer Academic, vol. .

Searles JL, Gouma P.I., and Buchheit RG (2001). *Stress corrosion cracking of sensitized AA5083 (Al-4.5 Mg-1.0 Mn).* Metallurgical and Materials Transactions A, vol. 32 n° 11, pp 2859–2867.

Sheh M.Y. and Stouffer D.C. (1990). *A Crystallographic Model for the Tensile and Fatigue Response for Rene–N4 at 982 °C.* J. Appl. Mech., vol. 57, pp 25.

Shewchuk J.R. (2002). *Constrained Delaunay Tetrahedralizations and Provably Good Boundary Recovery.* In : Eleventh International Meshing Roundtable (Ithaca, New York), Sandia National Laboratories, pp 193–204.

Shewchuk J.R. (2003). *Updating and Constructing Constrained Delaunay Tetrahedralizations by Flips. Proceeding of 19th Annual Symposium on Computational Geometry.* In : Proceeding of 19th Annual Symposium on Computational Geometry.

Shewmon P.G. (1985). *Hydrogen attack of pressure-vessel steels.* Materials Science and Technology, vol. 1 n° 1, pp 2–11.

Si H. and Gärtner K. (2004). *An Algorithm for Three-Dimensional Constrained Delaunay Tetrahedralizations.* In : Proceeding of the Fourth International Conference on Engineering Computational Technology, Lisbon, Portugal.

Si H. and Gärtner K. (2005). *Meshing Piecewise Linear Complexes by Constrained Delaunay Tetrahedralizations.* In : Proceeding of the 14th International Meshing Roundtable.

Simmons G. and Wang H. (1971). *Single Crystal Elastic Constants and Calculated Aggregate Properties.* M.I.T Press, Cambridge.

Smith B.W., Li X., and Tong W. (1998). *Error assessment for strain mapping by digital image correlation.* Exp. Tech., vol. 22 n° 4, pp 19–21.

St-Pierre L., Héripré E., Dexet M., Crépin J., Bertolino G., and Bilger N. (2008). *3D simulations of microstructure and comparison with experimental microstructure coming from O.I.M analysis.* International Journal of Plasticity, vol. 24, pp 1516–1532.

Sukumar N. and Srolovitz DJ (2004). *Finite element-based model for crack propagation in polycrystalline materials.* Computational and Applied Mathematics, vol. 23 n° 2-3, pp 363–380.

Sutton M.A., McNeill S.R., Helm J.D., and Chao V. (2000). *Advances in two-dimensional and three-dimensional computer vision.* Photomechanics, vol. , pp 323–372.

Takeda Y. and McMahon CJ (1981). *Strain controlled vs stress controlled hydrogen induced fracture in a quenched and tempered steel.* Metallurgical and Materials Transactions A, vol. 12 n° 7, pp 1255–1266.

Tanguy D. (2001). *Effets de l'hydrogène lors de la CSC des alliages base Al-5Mg en milieu NaCl 30G/L.* PhD thesis, INP Grenoble.

Tanguy D., Bayle B., Dif R., and Magnin T.h. (2002). *Hydrogen effects during IGSCC of pure Al-5Mg Alloy in NaCl media.* Corrosion Science, vol. 44, pp 1163–1175.

Tanguy D., Razafindrazaka M., and Delafosse D. (2008). *Multiscale simulation of crack tip shielding by a dislocation.* Acta Materialia, vol. 56 n° 11, pp 2441–2449.

Taylor G.I. (1934). *The mechanism of plastic deformation of crystals Part I - Theoritical.* Proc. Royal Society London, vol. 145 n° A, pp 362–387.

Tong W. (1997). *Detection of plastic deformation patterns in a binary aluminum alloy.* Exp. Mech., vol. 37 n° 4, pp 452–459.

Vamvakopoulos Emmanouil and Tanguy Döme (2009). *Equilibrium vacancy concentrations in $Al\Sigma_{33}[1\bar{1}0]$ by grand canonical Monte Carlo simulations.* Physical Review B, vol. 79, pp 11.

Van der Ven A. and Ceder G. (2003). *Impurity-induced van der Waals transition during decohesion.* Physical Review B, vol. 67 n° 6, pp 060101.

Vehoff H. and Klameth H.K. (1985). *Hydrogen embrittlement and trapping at crack tips in Ni-single crystals.* Acta Metallurgica, vol. 33 n° 6, pp 955–962.

Vehoff H. and Rothe W. (1983). *Gaseous hydrogen embrittlement in FeSi-and Ni-single crystals.* Acta Metallurgica, vol. 31 n° 11, pp 1781–1793.

Vendroux G. and Knauss W.G. (1998). *Submicron deformation field measurements, Part 2. Improved digital image correlation.* Exp. Mech., vol. 38 n° 2, pp 86–91.

Wang Z., Hu T., Xia Y., and Yang Q. (1986). -. Chinese Journal of Metal Science and Technology, vol. 2 n° 1, pp 1763.

Wells G.N. and Sluys L.J (2001). *A new method for modelling cohesive cracks using finite elements.* International Journal for Numerical Methods in Engineering, vol. 50, pp 2667–2682.

West E.A. and Was G.S. (2010). *A Model for the Normal Stress Dependence of Intergranular Cracking of Irradiated 316L Stainless Steel in Supercritical Water.* Journal of Nuclear Materials, vol. .

Xiang Q., Cao S., Sun D., Li J., and Jiang Y. (2010). *Characterization and cathode electrophoresis deposition of Cerium modified films on Al 5083.* Acta Metallurgia Sinica, vol. 46, pp 352–357.

Xiao Q.Z., Karihaloo B.L., and Liu X.Y. (2007). *Incremental-secant modulus iteration scheme and stress recovery for simulating cracking process in quasi-brittle materials using XFEM.* International Journal For Numerical Methods in Engineering, vol. 69, pp 2606–2635.

Xu X. and Needleman A. (1994). *Numerical simulations of fast crack growth in brittle solids.* Journal of the Mechanics and Physics of Solids, vol. 42, pp 1397–1434.

Zapffe C.A. and Sims C. (1941). *Hydrogen Embrittlement and Defects in Steels.* Transactions in American Institute of Mining, Metallurgical and Petroleum Engineers, vol. 145, pp 225.

Zhong W.M., Esperance G. L, and Suery M. (1996). *Effect of thermomechanical processing on the microstructure and mechanical properties of AI-Mg (5083) SiCp and AI-Mg (5083) A12Ogp composites. Part 2: Tensile properties at different temperatures.* Materials Science and Engineering, vol. A93, pp 93–103.

Zienkievicz O.C. and Taylor R.L. (1989). *The finite element method, 4th edn.* McGraw-Hill, London (UK).

Zikry M.A. and Kao M. (1996). *Dislocation based multiple-slip crystalline constitutive formulation for finite-strain plasticity.* Scripta Materialia, vol. 34 n° 7, pp 1115–1121.

Zilske M., Lamecker H., and S. Zachow (2008). *Adaptive remeshing of non-manifold surfaces.* In : Eurographics 2008, Annex to the conference proceedings, pp 207–211.

Rupture intergranulaire induite par l'hydrogène dans les alliages Aluminium-Magnesium

RESUME : L'objectif principal de cette étude est de comprendre le rôle spécifique de la plasticité à l'échelle cristalline sur la rupture intergranulaire dans un alliage d'aluminium préalablement fragilisé par l'hydrogène. Afin de remplir cet objectif, des outils expérimentaux, numériques et de couplage entre ces deux types d'approches ont été développés. Les résultats de mesures de champs de déformation locaux et de l'évolution de l'orientation cristalline, obtenus lors d'essais de traction in-situ, ont mis en avant une configuration particulière de l'environnement granulaire à l'origine de la rupture des joints de grains. Les premières fissures s'amorcent entre des grains qui se déforment peu ou pas dans un environnement granulaire relativement déformé. Ces joints de grains vont de fait subir des contraintes intergranulaires particulièrement élevées. A partir de ces observations expérimentales, un critère de rupture basé sur la contrainte normale au joint de grains a pu être proposé. Afin d'obtenir la valeur de contrainte seuil donnant lieu à la rupture intergranulaire, des simulations numériques sur les surfaces étudiées expérimentalement ont été entreprises. Ces simulations composées de maillages de microstructures réelles, d'un modèle de plasticité cristalline préalablement calibré et des conditions aux limites extraites des mesures expérimentales, ont permis d'évaluer une contrainte seuil de 175±35 MPa. Cette contrainte a ensuite été utilisée dans une loi de type zone cohésive pour décrire numériquement le comportement à rupture des joints de grains.

Mots clés : Rupture intergranulaire, Alliage d'aluminium, Fragilisation par hydrogène, Essais in-situ, Plasticité cristalline, Zone cohésive, Microstructure 3D

Hydrogen-induced intergranular fracture of Aluminium-Magnesium alloys

ABSTRACT: The main goal of this work was the study of local plasticity on the mechanism of hydrogen-induced intergranular fracture of an aluminium-magnesium alloy. An experimental procedure based on in-situ tensile tests was developed to measure the evolution of local strain fields at microstructural scales and of lattice orientation. From these observations, it was established that interfaces between two grains which have undergone little amount of deformation but lying within a neighbourhood of significantly deformed grains are the first to develop micro-cracks. To determine the role of local plasticity on the mechanisms of intergranular fracture, a dislocation mechanics based crystal plasticity model was employed to describe the constitutive behaviour of each grain in the finite element model of the in-situ experiment. Measured EBSD maps were relied upon to define the orientation of the discrete grain regions of the in-situ specimens in the corresponding multi-scale finite element (FE) models. From the FE results, a threshold value of 175±35 MPa was identified to be the normal grain boundary tractions needed to initiate intergranular cracks. Finally, a cohesive zone model calibrated with the critical grain boundary tractions and typical surface energies was added to the FE model of the polycrystal.

Keywords: Intergranular fracture, Aluminium alloys, Hydrogen embrittlement, In situ tensile tests, Crystal plasticity modelling, Cohesive zone, 3D microstructural characterisation

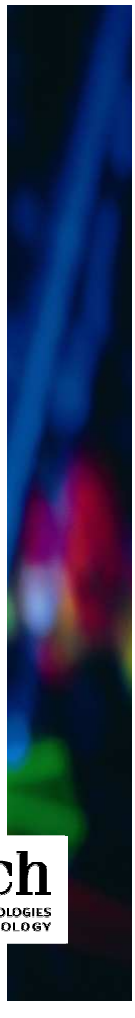

MINES ParisTech

ParisTech
INSTITUT DES SCIENCES ET TECHNOLOGIES
PARIS INSTITUTE OF TECHNOLOGY